Synthesis of nano heterodimers by laser photodeposition of metal nanodots on TiO2 nanoparticles

Qingguo Bai

▶ To cite this version:

Qingguo Bai. Synthesis of nano heterodimers by laser photodeposition of metal nanodots on TiO2 nanoparticles. Material chemistry. Université de Bordeaux, 2019. English. NNT : 2019BORD0129 . tel-02943887

HAL Id: tel-02943887
https://theses.hal.science/tel-02943887

Submitted on 21 Sep 2020

université
de BORDEAUX

THÈSE PRÉSENTÉE

POUR OBTENIR LE GRADE DE

DOCTEUR DE

L'UNIVERSITÉ DE BORDEAUX

ÉCOLE DOCTORALE DES SCIENCES CHIMIQUES

SPÉCIALITÉ: PHYSICO-CHIMIE DE LA MATIERE CONDENSEE

Par Qingguo BAI

Synthesis of nano heterodimers by laser photodeposition of metal nanodots on TiO₂ nanoparticles

Sous la direction de: Dr. Marie-Hélène DELVILLE,
Co-directeur: Dr. Jean-Pierre DELVILLE

Soutenue le: 20 septembre 2019

Membres du jury :

M. TOUPANCE, Thierry	Professeur	University of Bordeaux	Président
M. PAROLA, Stéphane	Professeur	University of Lyon	Rapporteur
M. HESEMANN, Peter	Directeur de recherche	CNRS-Montpellier	Rapporteur
M. DURUPTHY, Olivier	Professeur	University of Paris	Examinateur
Mme DELVILLE Marie-Hélène	Directeur de recherche	CNRS-Bordeaux	Directeur de thèse
M. DELVILLE Jean-Pierre	Directeur de recherche	CNRS-Bordeaux	Co-Directeur de thèse

Acknowledgements

Comme mentionné dans le titre de cette thèse, l'objectif de ce travail est la synthèse de nano hétérodimères à base de nanodots métalliques photodéposés sur des nanoparticules de TiO₂. Ces objets peuvent également être appelés particules Janus, car ces types de particules présentent deux matériaux constitutifs différents, et les performances sont donc nettement compartimentées sur la même particule. Ils portent le nom du dieu romain «Janus» dont les deux visages se tournent vers l'un vers le passé et l'autre vers le futur. Le premier exemple de particules Janus remonte à 1988, lorsque Casagrande et al. ont employé le terme «perles Janus» pour décrire une sphère de verre avec des surfaces à moitié hydrophiles et à moitié hydrophobes.[1] Le terme a ensuite été avancé par Pierre-Gilles de Gennes lors de sa conférence Nobel en 1992, lorsqu'il a mis en évidence leurs comportements physiques et chimiques anisotropes.[2] Depuis lors, nous avons assisté à une explosion des synthèses et des applications de particules Janus avec des géométries, des formes et des compositions particulières.[3-9] Les nanoparticules Janus ont suscité l'intérêt pour une gamme d'applications potentielles telles que les textiles hydrofuges, les capteurs, les nanomoteurs.,[10-13] la détection optique, stabilisation des émulsions, imagerie de champ magnétique et dispositifs de détection optiques.[8, 14-16] Récemment, des recherches sur la photocatalyse hétérogène ont également porté sur les particules Janus parmi lesquelles les nanoparticules Janus de type semi-conducteur sont devenues un sujet d'intérêt au cours des dernières décennies.

Les métaux nobles (Ag, Au et Pt) sont les plus étudiés en raison de leur inertie chimique dans un environnement organique. Lorsque les clusters métalliques forment un contact étroit avec le semi-conducteur, il en résulte une jonction Schottky.[17] Cette jonction permet de séparer les porteurs de charge photogénérés en jouant le rôle de réservoir d'électrons.[17-18] Cela réduit la probabilité de recombinaison, permettant ainsi à des espèces plus chargées de migrer vers la surface et d'initier la catalyse. Par conséquent, leur incorporation tente également de réduire le surpotentiel pour les réactions électrochimiques de surface. Enfin, la disponibilité abondante d'électrons libres conducteurs à l'interface métal / eau permet à ces clusters métalliques d'afficher des résonances de surface des plasmons (SPR en Anglais).[19] Ces «électrons chauds» dus à l'effet SPR peuvent surmonter la barrière de la jonction Schottky et peuvent être utilisés pour des réactions de réduction de surface. La SPR et la catalyse plasmonique sont un domaine en pleine croissance et le lecteur peut consulter les excellents articles cités en référence pour plus d'informations.[19-20]

En bref, les nanoclusters les plus couramment employés sont basés sur Ag, Au et Pt, tandis

que les semi-conducteurs incluent TiO$_2$, CdS, ZnO et WO$_3$.[19-21] Bien que les matériaux catalyseurs de type métal-semi-conducteur aient été étudiés de manière approfondie en termes de métal[22-29] ou type de semi-conducteur, [21] méthode de synthèse, [30-31] teneur en métal[32-37] et structure hybride, [38-40] un nombre limité de travaux ont étudié l'effet du nombre de clusters de métaux et de la taille des particules de métal sur les réactions catalytiques. [41-44]

En contrôlant la méthode de thermoréduction et de photoréduction, Menagen a réussi à fabriquer les bâtonnets de CdS avec des décorations en Au, soit avec de multiples points Au sur toute la surface, soit un gros plot d'Au à la pointe.[41] Dinh a suggéré que la population d'argent à la surface de TiO$_2$ puisse être contrôlée par le degré d'hydrophobie occupé par l'acide oléique (AO), les particules d'argent multiples se sont transformées en un plot lors de l'augmentation de l'occupation de l'AO sur la surface de TiO$_2$.[45] Cependant, aucun d'eux n'a encore effectué d'essai de catalyse.

Dans une étude récente, Nakibli a obtenu des bâtonnets CdSe @ CdS décorés de Pt sur lesquels il était capable de contrôler le nombre de points de Pt (un, deux et plusieurs). Il a constaté que, dans le cas d'une réaction multiélectronique telle que la réduction de l'hydrogène, les bâtonnets décorés avec un seul catalyseur de platine étaient plus actifs que les bâtonnets comportant deux points de platine ou de multiples points.[42] L'auteur a souligné l'importance d'un seul catalyseur en corrélation avec le nombre d'électrons impliqués dans le processus. Kalisman, du même groupe de recherche, a même constaté une efficacité de production record photons-hydrogène de 100% pour la réduction photocatalytique par fractionnement de l'eau avec un bâtonnet CdSe @ CdS à une seule extrémité en Pt, alors que le co-catalyseur à double Pt n'atteignait que 58,5%.[43]

Figure 1(a) Efficacité quantique photocatalytique pour la demi-réaction de réduction de l'hydrogène obtenue avec les photocatalyseurs nanobâtonnets C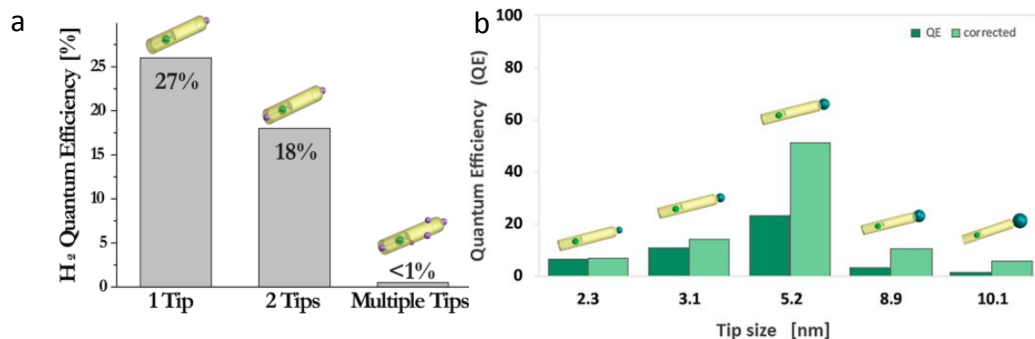dSe @ CdS décorés avec un, deux ou plusieurs sites de réduction du Pt.[42] (b) Efficacité quantique photocatalytique pour la demi-réaction de réduction de l'eau obtenue avec les photocatalyseurs nanobâtonnets CdSe @ CdS décorés avec des extrémités de Ni de tailles différentes.[44]

Outre le nombre de dépôts métalliques sur le semi-conducteur, la taille du cocatalyseur métallique joue également un rôle clé dans l'optimisation des matériaux.[44] Un ensemble de nanobâtonnets CdSe @ CdS décorés de Ni et présentant différentes tailles de pointe ont été examinés et une taille de métal optimale de 5,2 nm a été obtenue. La nature de la jonction entre le semi-conducteur et la nanoparticule métallique est sensible à la taille du composant métallique, comme en témoigne l'activité rapport à la production d'hydrogène, le rendement quantique d'émission et le taux de séparation de charges.[44] Les travaux de Ben-Shahar confirment encore cette idée, montrant que les matériaux hybrides de type CdS-Au avec des pointes d'Au de taille importante, sont plus efficaces pour le transfert d'électrons vers le centre métallique[46-48] Pour un autre semi-conducteur TiO_2, Oros-Ruiz et al. ont confirmé que la taille des particules d'or déposées sur les particules de TiO_2 avait un effet important sur le taux de photodégradation du 4-chlorophénol.[30]

Il ressort de ces études que non seulement la taille des nanoparticules métalliques sur les semi-conducteurs, mais également le nombre de ces NPs peuvent constituer un paramètre crucial et que la controverse n'est pas encore terminée dans la littérature. [30, 42-44, 46-48]

En ce qui concerne le TiO_2 en tant que substrat, outre le brevet de Delville et al. [49], deux articles concernant la synthèse d'hétérodimères ont été découverts dans la littérature.[50-51] En 2009, Pradhan a préparé des nanoparticules d'hétérodimères de type bonhomme de neige Au-TiO_2 par une synthèse sol-gel de surface de TiO_2 sur des nanoparticules Janus en or pré-modifiées avec deux groupes fonctionnels différents.[50] En 2013, Byeon a affirmé pouvoir synthétiser des hétérodimères ultra-fins Au-TiO_2 en utilisant une décharge étincelle hétérogène ambiante[51] même si les illustrations fournies ne semblent pas convaincantes.

Dans cette thèse, en utilisant TiO_2 comme substrat semi-conducteur, nous introduisons ici une méthode de photodéposition utilisant un faisceau laser focalisé comme source de lumière, pour générer des structures Janus de type M-TiO_2 (M = Ag, Pd, Au) avec un seul point métallique par NP de TiO2, formant ainsi une nanoparticule de type hétérostructure. Un modèle de prévision de la croissance du métal photodéposé sur la surface de TiO_2 est proposé et justifié par les résultats expérimentaux. Les grandes lignes de la thèse sont les suivantes:

Dans le chapitre 1, nous décrivons la recherche documentaire sur les principes, les mécanismes et les applications de la photodéposition. Cela démontrera que la photodéposition est une technique qui a été utilisée massivement pour charger des

nanoparticules métalliques sur diverses nanoparticules, mais que, d'un point de vue fondamental, certaines données manquent encore. À titre d'exemple dans cette thèse, nous allons, dans la ligne droite d'un premier travail initial effectué en laboratoire[52] nous concentrer sur la mise en œuvre d'un laser UV focalisé pour générer des nanodots métalliques à la surface du TiO_2 afin de mettre en évidence l'avantage de cette méthode de photodéposition pour la synthèse de particules dimères hétérogènes. Nous y abordons successivement les principes de la photodéposition de nanoparticules à la surface du semi-conducteur avec les applications de la photodéposition et leur comparaison à d'autres méthodes. Nous évoquons la photodéposition de nanoparticules à la surface de TiO_2 dont celle de nanodots (NDs) d'argent d'or de palladium et d'autres métaux, avant de parler de la photodéposition de particules sur d'autres semi-conducteurs. Nous consacrons également une partie à l'étude de la photodéposition induite par laser.

Le chapitre 2 est consacré à la synthèse du substrat: nanoparticules de TiO_2 de type anatase de formes et de tailles variées. La synthèse de l'anatase TiO_2 est basée et adaptée à partir des méthodes décrites dans la littérature.[53-57] L'influence du pH du système réactionnel et de la température de traitement sur la morphologie finale du cristal est discutée, ainsi que l'influence des agents structurants. Sont ainsi obtenus les nanoobjets illustrés ci-dessous (Figures 2-5).
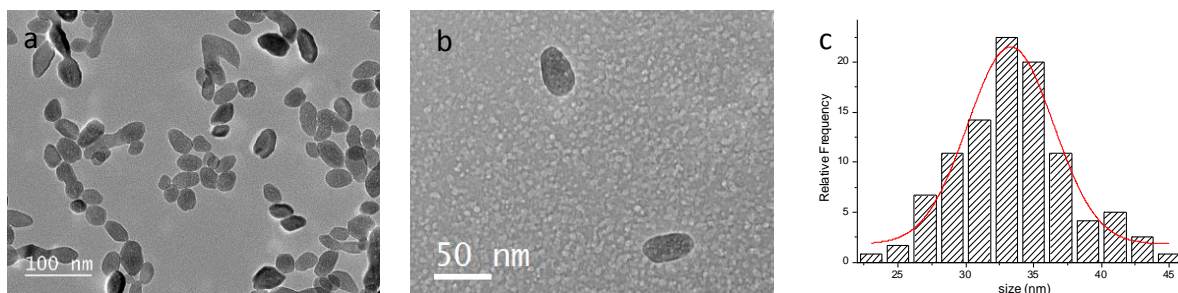
Figure 2 (a)(b) Images TEM de polyèdres TiO₂, (c) distribution statistique de taille de TiO₂.
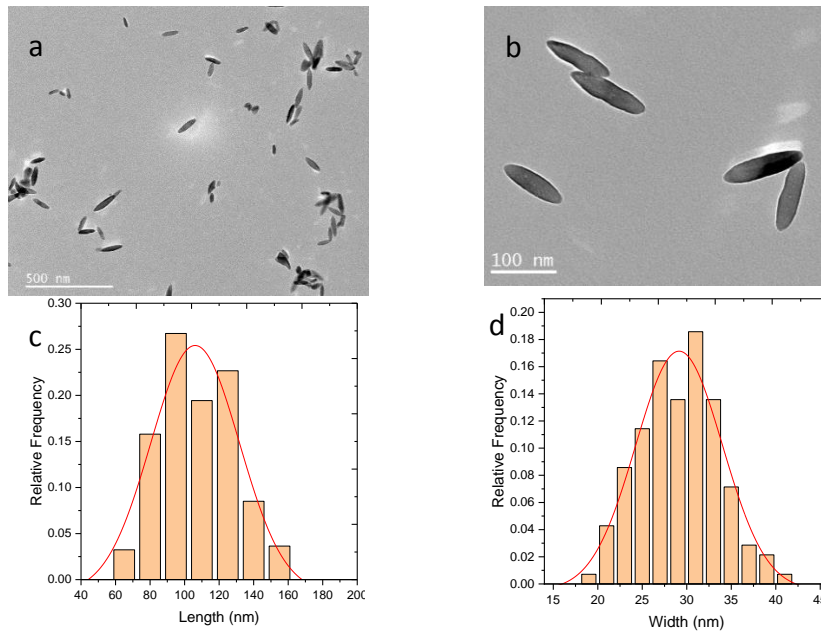
Figure 3. Images TEM à (a) faible et (b) fort grossissement; l'histogramme de taille en(c) longueur et en(d) largeur.
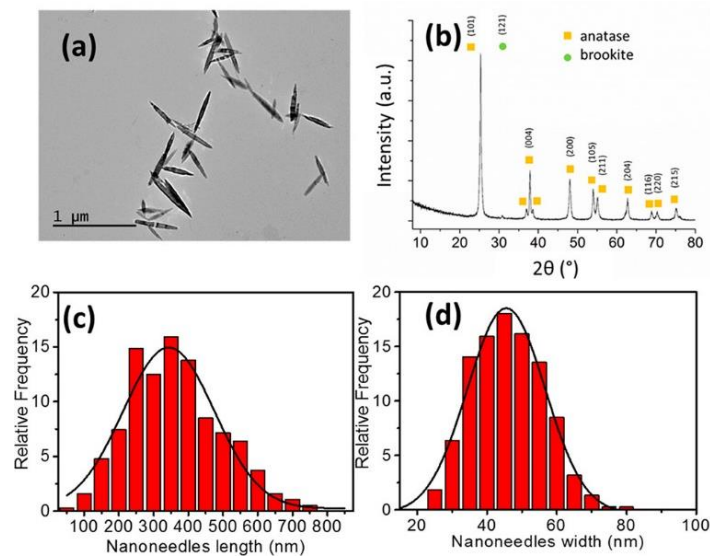
Figure 4 (a) Image TEM et (b) diffraction des rayons X de nanoaiguilles de TiO_2; (c, d) distribution statistique des longueurs et des largeurs de nanoaiguilles, respectivement. [57]
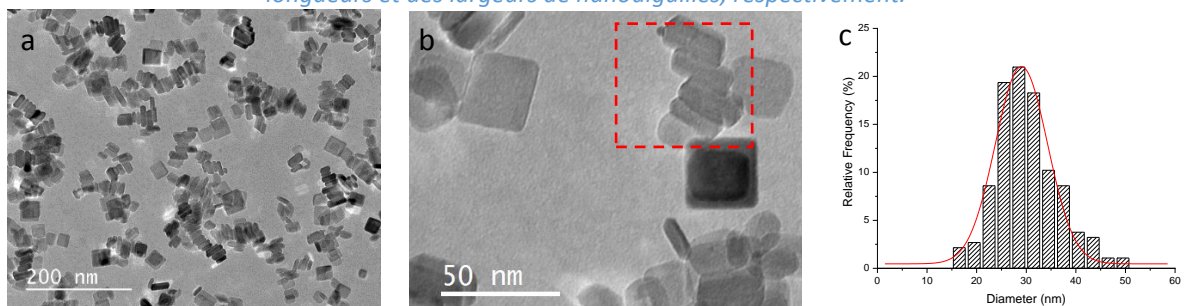
Figure 5 (a) (b) Images TEM de particules de nanoplaquettes d'anatase et (c) leurs distributions de taille correspondantes.

Avant d'aborder plus avant les études de photodéposition, le chapitre 3 présente les trois configurations différentes construites et utilisées pour effectuer le dépôt photochimique des dots métalliques sur les nanoparticules semi-conductrices (Figure 6). Une description des paramètres spécifiques et des configurations est décrite en détail. Les comparaisons seront mentionnées en termes d'intensité laser, et de durée d'irradiation.
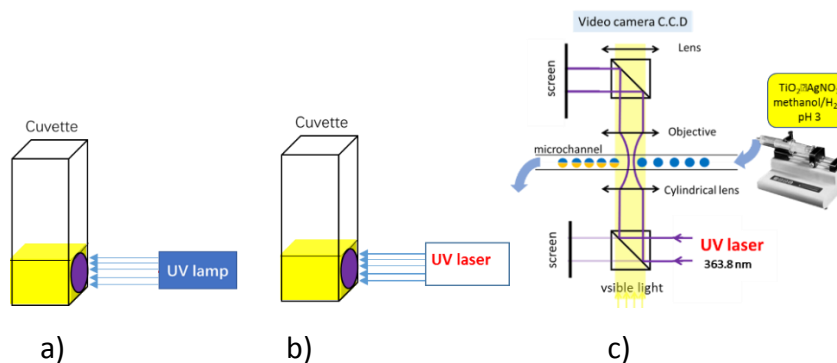
Figure 6 (a) cuve Hellma irradiée pr une lampe UV (b) cuve Hellma irradiée pr un laser UV (c) microcanal irradié par un lase UV.

Au chapitre 4 et au chapitre 5, quatre précurseurs métalliques avec différents états de valence, à savoir les ions Ag (I), Au (III), Pd (II) et Pt (IV), sont photochimiquement réduits à la surface de TiO_2. On obtient des nano-hétérodimères avec un plot d' Ag, Au, Pd et Pt par TiO_2, ce qui montre que le dépôt par laser semble être beaucoup plus efficace dans ce cas que celui de la photodéposition par lampe UV habituelle, suggérant que le flux de photons compte beaucoup plus que l'énergie déposé . Les nanoparticules d'hétérodimères Ag-TiO_2 sont synthétisées avec succès par les deux méthodes de dépôt par voie laser. Le nombre et la distribution de taille des points Ag dépendent des capteurs de trous, du pH et du précurseur de métal. Un modèle de croissance prédit bien la variation de la taille de l'argent dans le processus de photodéposition. La taille de l'argent se comporte comme $P^{1/6}$ en puissance, $[Ag^+]^{1/6}$ concentration et $t^{1/3}$ en temps. Le taux de réduction de l'argent dans le processus de photodéposition est également déduit et correspond au même ordre que les valeurs rapportées dans la littérature.[58-59]

Nous avons également étudié les effets d'autres paramètres sur le processus de photodéposition. Deux types de piégeurs de trous, le méthanol et le formiate (HCOONa), ont été étudiés et se sont révélés conduire à un taux élevé de dépôts d'argent à la surface de TiO_2. HCOONa offre de bien meilleurs rendements en hétérodimères, tandis que l'utilisation de méthanol peut entraîner la présence de multi nanodots d'argent. Plusieurs valeurs de pH, comprises entre 3 et 5, ont été utilisées pour en étudier le rôle dans le processus de

photodéposition. Nous avons constaté qu'un pH plus faible facilite la synthèse d'hétérodimères, alors que des environnements à pH relativement élevé induisent une nucléation à multidots à la surface de TiO_2. Au-delà des expériences réalisées avec la configuration à microcanaux, la photodéposition a également été étudiée dans une configuration de cuvettes, éclairée soit par le même laser UV, soit par une lampe UV à haute pression. Des expériences sur des cuvettes utilisant le laser UV ont montré un dépôt de nanoparticules simples ou multiples sur la surface de TiO_2 en fonction des conditions expérimentales, tandis que les expériences avec une lampe UV conduisaient systématiquement à la nucléation de minuscules points de diamètre inférieur à 3 nm. Enfin, en fonction de la nature du précurseur métallique, l'acétate d'argent induit une gamme de tailles beaucoup plus réduite que l'$AgNO_3$ habituellement considéré, il est suggéré que la plus petite valeur de K_A pour l'AgOAc induit une plus petite taille d'argent.

L'extension de la synthèse à d'autres précurseurs de métaux ($KAuCl_4$, Na_2PdCl_4 et H_2PtCl_6) à l'aide des deux configurations est décrite explicitement au chapitre 5 et conduit à la formation d'hétérodimères à base de TiO_2 à base d'or, de palladium et de platine. La loi de croissance de l'or peut aussi être raisonnablement prédite, bien qu'elle ne soit pas aussi bonne que dans le cas de l'Ag, alors que notre modèle ne fonctionne pas dans le cas de Pd et de Pt.

Enfin, dans le chapitre 6, nous avons discuté des nanoobjets bimétalliques cœur-écorce structurés (Au @ M) -TiO_2 (M = Ag, Pd, Au et Pt) synthétisés par une simple méthode de dépôt au laser UV en deux étapes dans la configuration de la cuvette.

L'or métallique est d'abord photodéposé à la surface de TiO_2, puis il est procédé à un second photodépôt d'un autre métal sur Au-TiO_2 par introduction d'un autre sel métallique dans la solution (Figure 7).
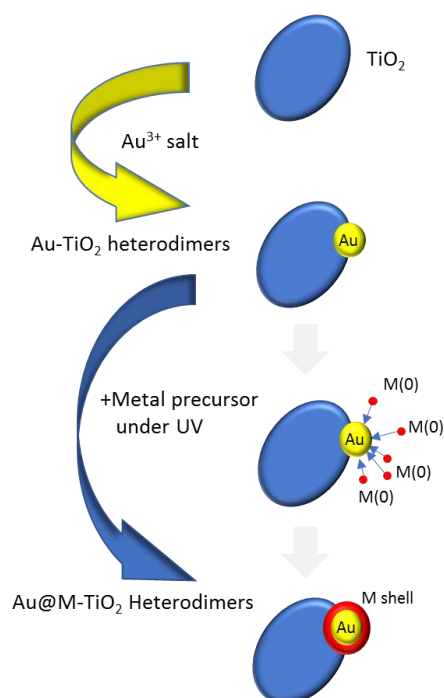
Figure 7 Principe de la synthèse de nanoobjets bimétalliques cœur-écorce structurés (Au @ M) -TiO₂ (M = Ag, Pd, Au et Pt) par une simple méthode de dépôt au laser UV en deux étapes dans une cuve Hellma.

Les techniques telles que la cartographie TEM, XPS et EDS ont confirmé l'existence d'une structure cœur-écorce pour la plupart d'entre elles. Pour les systèmes Au @ Au et Au @ Ag, une coquille fine d'environ 1 nm d'épaisseur est formée sur le noyau en Au, en raison de leurs constantes de réseau similaires entre Ag et Au, alors que, dans le cas de Pd et de Pt, conditions conduisaient à une coquille moins définie dans le cas du Pd et à une configuration en étoile dans le cas du Pt. L'extension des nanoparticules monométalliques aux bimétalliques pourra favoriser les études de conception et de synthèse de composites structurés hybrides et l'étude des applications potentielles dans le futur.

Cette thèse se termine par des Conclusions et Perspectives avec une réflexion sur les résultats obtenus et les améliorations possibles pour des recherches ultérieures. Le lecteur peut se référer à l'Annexe pour une meilleure compréhension des informations détaillées concernant l'absorption et l'effet de chauffage par laser UV (Annexe 1), le modèle proposé (Annexe 2) et la prédiction théorique de la taille du métal (Annexe 3).

Réferences

1.   Casagrande, C.; Fabre, P.; Raphaël, E.; Veyssié, M., "Janus Beads": Realization and Behaviour at Water/Oil Interfaces. *Europhysics Letters* **1989,** *9*, 251-255,

2.   de Gennes, P. G., Soft matter. *Reviews of Modern Physics* **1992,** *64*, 645-648,

3.   Walther, A.; Müller, A. H. E., Janus Particles: Synthesis, Self-Assembly, Physical Properties, and Applications. *Chemical Reviews* **2013,** *113*, 5194-5261,

4.   Yi, Y.; Sanchez, L.; Gao, Y.; Yu, Y., Janus particles for biological imaging and sensing. *Analyst* **2016,** *141*, 3526-3539,

5.   Kirillova, A.; Marschelke, C.; Synytska, A., Hybrid Janus Particles: Challenges and Opportunities for the Design of Active Functional Interfaces and Surfaces. *ACS Applied Materials & Interfaces* **2019,** *11*, 9643-9671,

6.   Loget, G.; Kuhn, A., Bulk synthesis of Janus objects and asymmetric patchy particles. *Journal of Materials Chemistry* **2012,** *22*, 15457-15474,

7.   Hu, J.; Zhou, S.; Sun, Y.; Fang, X.; Wu, L., Fabrication, properties and applications of Janus particles. *Chemical Society Reviews* **2012,** *41*, 4356-4378,

8.   Perro, A.; Reculusa, S.; Ravaine, S.; Bourgeat-Lami, E.; Duguet, E., Design and synthesis of Janus micro- and nanoparticles. *Journal of Materials Chemistry* **2005,** *15*, 3745-3760,

9.   Liang, F.; Zhang, C.; Yang, Z., Rational Design and Synthesis of Janus Composites. *Advanced Materials* **2014,** *26*, 6944-6949,

10.   Ebbens, S. J.; Howse, J. R., In pursuit of propulsion at the nanoscale. *Soft Matter* **2010,** *6*,

11.   Rodríguez-Fernández, D.; Liz-Marzán, L. M., Metallic Janus and Patchy Particles. *Particle & Particle Systems Characterization* **2013,** *30*, 46-60,

12.   Xu, L.; Mou, F.; Gong, H.; Luo, M.; Guan, J., Light-driven micro/nanomotors: from fundamentals to applications. *Chem Soc Rev* **2017,** *46*, 6905-6926,

13.   Guix, M.; Weiz, S. M.; Schmidt, O. G.; Medina-Sánchez, M., Self-Propelled Micro/Nanoparticle Motors. *Particle & Particle Systems Characterization* **2018,** *35*, 1700382,

14.   Du, J.; O'Reilly, R. K., Anisotropic particles with patchy, multicompartment and Janus architectures: preparation and application. *Chemical Society Reviews* **2011,** *40*, 2402-2416,

15.   Synytska, A.; Khanum, R.; Ionov, L.; Cherif, C.; Bellmann, C., Water-Repellent Textile via Decorating Fibers with Amphiphilic Janus Particles. *ACS Applied Materials & Interfaces* **2011,** *3*, 1216-1220,

16.   Lattuada, M.; Hatton, T. A., Synthesis, properties and applications of Janus nanoparticles. *Nano Today* **2011,** *6*, 286-308,

17.   Clavero, C., Plasmon-induced hot-electron generation at nanoparticle/metal-oxide interfaces for photovoltaic and photocatalytic devices. *Nature Photonics* **2014,** *8*, 95-103,

18.   Bai, S.; Li, X.; Kong, Q.; Long, R.; Wang, C.; Jiang, J.; Xiong, Y., Toward Enhanced Photocatalytic Oxygen Evolution: Synergetic Utilization of Plasmonic Effect and Schottky Junction via Interfacing Facet Selection. *Adv Mater* **2015,** *27*, 3444-52,

19.   Hou, W.; Cronin, S. B., A Review of Surface Plasmon Resonance-Enhanced Photocatalysis. *Advanced Functional Materials* **2013,** *23*, 1612-1619,

20.   Zhang, X.; Chen, Y. L.; Liu, R.-S.; Tsai, D. P., Plasmonic photocatalysis. *Reports on Progress in Physics* **2013,** *76*, 046401,

21.   Wenderich, K.; Mul, G., Methods, Mechanism, and Applications of Photodeposition in Photocatalysis: A Review. *Chemical Reviews* **2016,** *116*, 14587-14619,

22.   Pan, X.; Xu, Y.-J., Defect-Mediated Growth of Noble-Metal (Ag, Pt, and Pd) Nanoparticles on TiO2 with Oxygen Vacancies for Photocatalytic Redox Reactions under Visible Light. *The Journal of Physical Chemistry C* **2013,** *117*, 17996-18005,

23.   Chen, S. F.; Li, J. P.; Qian, K.; Xu, W. P.; Lu, Y.; Huang, W. X.; Yu, S. H., Large scale photochemical synthesis of M@TiO2 nanocomposites (M = Ag, Pd, Au, Pt) and their optical properties, CO oxidation performance, and antibacterial effect. *Nano Research* **2010,** *3*, 244-255,

24.   Taing, J.; Cheng, M. H.; Hemminger, J. C., Photodeposition of Ag or Pt onto TiO2 Nanoparticles Decorated on Step Edges of HOPG. *ACS Nano* **2011,** *5*, 6325-6333,

25.   Diak, M.; Grabowska, E.; Zaleska, A., Synthesis, characterization and photocatalytic activity of noble metal-modified TiO2 nanosheets with exposed {001} facets. *Applied Surface Science* **2015,** *347*, 275-285,

26.   Melvin, A. A.; Illath, K.; Das, T.; Raja, T.; Bhattacharyya, S.; Gopinath, C. S., M–Au/TiO$_2$ (M = Ag, Pd, and Pt) nanophotocatalyst for overall solar water splitting: role of interfaces. *Nanoscale* **2015,** *7*, 13477-13488,

27.   Shoaib, A.; Ji, M.; Qian, H.; Liu, J.; Xu, M.; Zhang, J., Noble metal nanoclusters and their in situ calcination to nanocrystals: Precise control of their size and interface with TiO$_2$ nanosheets and their versatile catalysis applications. *Nano Research* **2016,** *9*, 1763-1774,

28.   Zheng, Z.; Huang, B.; Qin, X.; Zhang, X.; Dai, Y.; Whangbo, M.-H., Facile in situ synthesis of visible-light plasmonic photocatalysts M@TiO2 (M = Au, Pt, Ag) and evaluation of their photocatalytic oxidation of benzene to phenol. *Journal of Materials Chemistry* **2011,** *21*, 9079-9087,

29.   Dozzi, M. V.; Saccomanni, A.; Selli, E., Cr(VI) photocatalytic reduction: Effects of simultaneous organics oxidation and of gold nanoparticles photodeposition on TiO$_2$. *Journal of Hazardous Materials* **2012,** *211-212*, 188-195,

30.   Oros-Ruiz, S.; Pedraza-Avella, J. A.; Guzmán, C.; Quintana, M.; Moctezuma, E.; del Angel, G.; Gómez, R.; Pérez, E., Effect of Gold Particle Size and Deposition Method on the Photodegradation of 4-Chlorophenol by Au/TiO$_2$. *Topics in Catalysis* **2011,** *54*, 519-526,

31.   You, X.; Chen, F.; Zhang, J.; Anpo, M., A novel deposition precipitation method for preparation of Ag-loaded titanium dioxide. *Catalysis Letters* **2005,** *102*, 247-250,

32.   López-Tenllado, F. J.; Hidalgo-Carrillo, J.; Montes, V.; Marinas, A.; Urbano, F. J.; Marinas, J. M.; Ilieva, L.; Tabakova, T.; Reid, F., A comparative study of hydrogen photocatalytic production from glycerol and propan-2-ol on M/TiO2 systems (M=Au, Pt, Pd). *Catalysis Today* **2017,** *280*, 58-64,

33.   Melián, P. E.; Díaz, G. O.; Rodríguez, J. M.; Colón, G.; Navío, J. A.; Macías, M.; Peña, P. J., Effect of deposition of silver on structural characteristics and photoactivity of TiO$_2$-based photocatalysts. *Applied Catalysis B: Environmental* **2012,** *127*, 112-120,

34.   Sreethawong, T.; Yoshikawa, S., Impact of photochemically deposited monometallic Pt and bimetallic Pt–Au nanoparticles on photocatalytic dye-sensitized H2 production activity of mesoporous-assembled TiO2–SiO2 mixed oxide nanocrystal. *Chemical Engineering Journal* **2012,** *197*, 272-282,

35.   Iliev, V.; Tomova, D.; Bilyarska, L.; Eliyas, A.; Petrov, L., Photocatalytic properties of TiO2 modified with platinum and silver nanoparticles in the degradation of oxalic acid in aqueous solution. *Applied Catalysis B: Environmental* **2006,** *63*, 266-271,

36.   Wang, D.; Bi, Q.; Yin, G.; Wang, P.; Huang, F.; Xie, X.; Jiang, M., Photochemical Preparation of Anatase Titania Supported Gold Catalyst for Ethanol Synthesis from CO$_2$ Hydrogenation. *Catalysis Letters* **2018,** *148*, 11-22,

37.   Herrmann, J.-M.; Disdier, J.; Pichat, P.; Fernández, A.; González-Elipe, A.; Munuera, G.; Leclercq, C., Titania-supported bimetallic catalyst synthesis by photocatalytic codeposition at ambient temperature: Preparation and characterization of Pt   Rh, Ag   Rh, and Pt   Pd couples. *Journal of Catalysis* **1991,** *132*, 490-497,

38.   Aronovitch, E.; Kalisman, P.; Mangel, S.; Houben, L.; Amirav, L.; Bar-Sadan, M., Designing Bimetallic Co-Catalysts: A Party of Two. *J Phys Chem Lett* **2015,** *6*, 3760-4,

39.   Zaleska-Medynska, A.; Marchelek, M.; Diak, M.; Grabowska, E., Noble metal-based bimetallic nanoparticles: the effect of the structure on the optical, catalytic and photocatalytic properties. *Advanced Colloid Interface Science* **2016,** *229*, 80-107,

40.   Jones, W.; Su, R.; Wells, P. P.; Shen, Y.; Dimitratos, N.; Bowker, M.; Morgan, D.; Iversen, B. B.; Chutia, A.; Besenbacher, F.; Hutchings, G., Optimised photocatalytic hydrogen production using core-shell AuPd promoters with controlled shell thickness. *Phys Chem Chem Phys* **2014,** *16*, 26638-44,

41.   Menagen, G.; Macdonald, J. E.; Shemesh, Y.; Popov, I.; Banin, U., Au Growth on Semiconductor Nanorods: Photoinduced versus Thermal Growth Mechanisms. *Journal of the American Chemical Society* **2009,** *131*, 17406-17411,

42.   Nakibli, Y.; Kalisman, P.; Amirav, L., Less Is More: The Case of Metal Cocatalysts. *J Phys Chem Lett* **2015,** *6*, 2265-8,

43.   Kalisman, P.; Nakibli, Y.; Amirav, L., Perfect Photon-to-Hydrogen Conversion Efficiency. *Nano Letters* **2016,** *16*, 1776-1781,

44.   Nakibli, Y.; Mazal, Y.; Dubi, Y.; Wachtler, M.; Amirav, L., Size Matters: Cocatalyst Size Effect on Charge Transfer and Photocatalytic Activity. *Nano Lett* **2018,** *18*, 357-364,

45.   Dinh, C.-T.; Nguyen, T.-D.; Kleitz, F.; Do, T.-O., A New Route to Size and Population Control of Silver Clusters on Colloidal TiO_2 Nanocrystals. *ACS Applied Materials & Interfaces* **2011,** *3*, 2228-2234,

46.   Ben-Shahar, Y.; Banin, U., Hybrid Semiconductor–Metal Nanorods as Photocatalysts. *Topics in Current Chemistry* **2016,** *374*, 54,

47.   Ben-Shahar, Y.; Scotognella, F.; Kriegel, I.; Moretti, L.; Cerullo, G.; Rabani, E.; Banin, U., Optimal metal domain size for photocatalysis with hybrid semiconductor-metal nanorods. *Nature Communications* **2016,** *7*, 10413,

48.   Ben-Shahar, Y.; Philbin, J. P.; Scotognella, F.; Ganzer, L.; Cerullo, G.; Rabani, E.; Banin, U., Charge Carrier Dynamics in Photocatalytic Hybrid Semiconductor–Metal Nanorods: Crossover from Auger Recombination to Charge Transfer. *Nano Letters* **2018,** *18*, 5211-5216,

49.   Delville, M.-H.; Delville, J.-P.; Vauriot, L. Particules de TiO_2 dissymétriques (Particules de Janus) et leur procédé de synthèse par photodéposition. FR2999452, 2012.

50.   Pradhan, S.; Ghosh, D.; Chen, S., Janus Nanostructures Based on Au–TiO_2 Heterodimers and Their Photocatalytic Activity in the Oxidation of Methanol. *ACS Appl. Mater. Interfaces* **2009,** *1*, 2060-2065,

51.   Byeon, J. H.; Kim, Y.-W., Au-TiO_2 Nanoscale Heterodimers Synthesis from an Ambient Spark Discharge for Efficient Photocatalytic and Photothermal Activity. *ACS Appl. Mater. Interfaces* **2014,** *6*, 763-767,

52.   Vauriot, L. Synthèse microfluidique de nanomatériaux multifonctionnels par laser. 2012.

53.   Menzel, R.; Duerrbeck, A.; Liberti, E.; Yau, H. C.; McComb, D.; Shaffer, M. S. P., Determining the Morphology and Photocatalytic Activity of Two-Dimensional Anatase Nanoplatelets Using Reagent Stoichiometry. *Chemistry of Materials* **2013,** *25*, 2137-2145,

54.   Kanie, K.; Sugimoto, T., Shape control of anatase TiO2 nanoparticles by amino acids in

a gel–sol system. *Chemical Communications* **2004**, 1584-1585,

55.   Dinh, C. T.; Nguyen, T. D.; Kleitz, F.; Do, T. O., Shape-controlled synthesis of highly crystalline titania nanocrystals. *ACS Nano* **2009,** *3*, 3737-43,

56.   Zhuang, M.; Zheng, Y.; Liu, Z.; Huang, W.; Hu, X., Shape-dependent performance of TiO2 nanocrystals as adsorbents for methyl orange removal. *RSC Advances* **2015,** *5*, 13200-13207,

57.   Bai, Q.; Lavenas, M.; Vauriot, L.; Le Tréquesser, Q.; Hao, J.; Weill, F.; Delville, J.-P.; Delville, M.-H., Hydrothermal Transformation of Titanate Scrolled Nanosheets to Anatase over a Wide pH Range and Contribution of Triethanolamine and Oleic Acid to Control the Morphology. *Inorganic Chemistry* **2019,** *58*, 2588-2598,

58.   Janata, E.; Henglein, A.; Ershov, B. G., First Clusters of Ag+ Ion Reduction in Aqueous Solution. *The Journal of Physical Chemistry* **1994,** *98*, 10888-10890,

59.   Kull, M.; Coutaz, J.-L., Intensity-dependent absorption and luminescence in semiconductor-doped glasses. *Journal of the Optical Society of America B* **1990,** *7*, 1463-1472,

Table of Contents

General Introduction

As mentioned in the title, the objective of this thesis is the synthesis of nano heterodimers based on metal nanodots photodeposited on TiO_2 nanoparticles. These objects may also be called Janus particles since these types of particles have two different constituent materials, and thus performances are distinctly compartmented on the same particle. They are named after the Roman god "Janus" whose two faces look to the past and the future. The first example of Janus particles can be traced back to 1988 when Casagrande *et al.* employed the term "Janus beads" to describe a glass sphere with half hydrophilic and half hydrophobic surfaces.[1] The term was further advanced by Pierre-Gilles de Gennes in his Nobel lecture in 1992, which highlighted their anisotropic physical and chemical behaviours.[2] Since then, we have witnessed a blooming of the syntheses and applications of Janus particles with particular geometries, shapes and compositions.[3-9] Janus nanoparticles have attracted interest for a range of potential applications such as water-repellent textiles, sensors, nanomotors,[10-13] optical sensing, stabilisation of emulsions, magnetic field imaging, and optical sensing devices.[8, 14-16] Recently, researches in heterogeneous photocatalysis[17] have also considered Janus particles and initial studies have reported promising results, which will be discussed in the subsequent sections. Among these Janus nanoparticles, metal-semiconductor type Janus nanoparticles have become a subject of interest over the last decades as illustrated below.

Noble metals (Ag, Au and Pt) are the most studied due to their chemical inertness in an organic environment. When the metal clusters form a close-contact with the semiconductor, it gives rise to a Schottky junction.[18] This junction allows for the separation of photogenerated charge carriers by acting as an electron reservoir.[18, 19] This lowers the probability of recombination, thereby allowing more charged species to migrate to the surface and initiate catalysis. Hence, their incorporation also attempts to reduce the overpotential for surface electrochemical reactions. Finally, the abundant availability of freely conducting electrons at the metal/water dielectric interface allows these metal clusters to display surface plasmon resonances (SPR).[20] These "hot-electrons" due to the SPR effect can overcome the barrier of the Schottky junction and can be used for surface reduction reactions. SPR and plasmonic catalysis are a growing field, and the reader is directed to the excellent articles for further information.[20, 21]

In brief, the most commonly employed nanoclusters are based on Ag, Au, and Pt, while the semiconductors included TiO_2, CdS, ZnO and WO_3.[20-22] Although metal-semiconductor catalyst materials have been extensively studied in terms of metal[23-30] or semiconductor type[22], synthesis method,[31, 32] metal content[33-38] and hybrid structure[39-41], a limited number of works

3

investigated the effect of the number of metal cluster and metal particle size on the catalytic reactions.[42-45]

By the control of thermal and photoreduction method, Menagen succeeded in fabricating the Au decorating CdS rods, with either multi Au dots on the body or a large Au at the tip.[42] Dinh suggested that the population of silver clusters on TiO_2 surface can be controlled by the degree of hydrophobicity occupied by oleic acid (OA), the multi silver particles turned to be a single dot when increasing the OA occupation on TiO_2 surface.[46] However, neither of them further performed any catalysis test.

In a recent study, Nakibli et al.[43] obtained Pt-decorated CdSe@CdS rods in which he was able to control the number of Pt dots (one, two and multiple). In the case of hydrogen reduction, rods decorated with a single Pt dot catalyst were found to be more active than the rods having two or more Pt dots. The author emphasized the importance of a single dot catalyst in correlation with the number of electrons involved in the process. Kalisman in the same research group even found a record 100 % efficiency of photon-to-hydrogen production for water splitting reduction using a single Pt tipped CdSe@CdS rod, while the double Pt co-catalyst achieved at only 58.5%.[44]
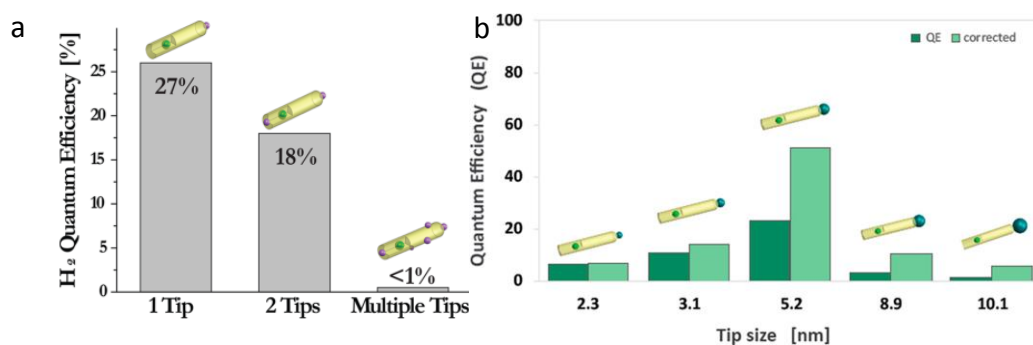
Figure (a) Photocatalytic quantum efficiency for the hydrogen reduction half-reaction obtained with CdSe@CdS nanorod photocatalysts decorated with a single, double, or multiple Pt reduction sites.[43] (b) Photocatalytic quantum efficiency for the water reduction half-reaction obtained with CdSe@CdS nanorod photocatalysts decorated with different-sized Ni tips.[45]

In addition to the number of metal dots on semiconductor, the size of the metal cocatalyst also plays a key role in the optimization of materials.[45] A set of Ni-decorated CdSe@CdS nanorods with various sizes of metal tip were examined, and an optimal size of 5.2 nm was obtained. The nature of junction between the semiconductor and metal nanoparticle is sensitive to the size of the metal component, as reflected in the activity toward hydrogen

4

production, emission quantum yield and the quantity of charge separation.[45] This is further confirmed by Ben-Shahar's work, showing that hybrid materials, CdS-Au, with large Au tips are advantageous for electron transfer to metal domain.[47-49] For another semiconductor TiO_2, Oros-Ruiz et al. confirmed that the gold particle size on TiO_2 has a strong effect on the photodegradation rate of 4-Chlorophenol.[31]

From these studies, it appears that not only the size of the metal on semiconductor but also the number of these metal NPs can be a crucial parameter and that the controversy is not over yet in the literature.[31, 43-45, 47-49]

As far as TiO_2 as a substrate is concerned, besides the patent by Delville et al.,[50] two papers concerning the synthesis of heterodimers were found.[51, 52] Pradhan et al. in 2009 prepared Au-TiO_2 snowman-like heterodimer nanoparticles by a surface sol-gel synthesis of TiO_2 on gold Janus nanoparticles pre-modified with two different functional groups.[51] Byeon et al. in 2013 claimed he was able to synthesize ultrafine Au-TiO_2 heterodimers using ambient heterogeneous spark discharge,[52] even if the provided illustrations do not seem convincing.

In this thesis, using TiO_2 as a semiconductor substrate, we here introduce a photodeposition method using a focusing laser beam as a light source, to generate M-TiO_2 (M = Ag, Pd, Au) Janus structure with a single metal dot per TiO_2 NP, thus forming a heterostructure nanoparticle. A growth prediction model of the metal photodeposited on TiO_2 surface will be proposed, and will be justified by the experimental results. The outline of the thesis is the following:

In **Chapter 1**, we will describe the literature research on the principles, mechanisms and applications of photodeposition. It will demonstrate that photodeposition is a technique that has been massively used to load metal NPs on various semiconductors, but that from a fundamental point of view, some data are still missing. As an example in this thesis, we will, following the initial work performed in the laboratory, focus on the implementing a focused UV laser to generate metal nanodots on TiO_2 surface to highlight the advantage in heterogeneous particle synthesis using photodeposition method.

Chapter 2 is dedicated to the synthesis of the substrate: anatase TiO_2 nanoparticles with varied shapes and sizes. The synthesis of anatase TiO_2 is based and adapted from methods depicted in the literature.[53-56] The influence of the pH of the reaction system and treatment temperature on the final crystal morphology is discussed, as well as the influence of surface directing agents.

Before further photodeposition studies are discussed, In **Chapter 3**, we will introduce the three different setups which are built and used to perform the photodeposition of the metal dots onto the semiconductor nanoparticles. A description of specific parameters and configuration of the setups will be fully described. Comparisons will be mentioned in terms of laser intensity, irradiation duration and also the initial photodeposition results.

In **Chapter 4** and **Chapter 5**, four metal precursors with different valence states, i.e. Ag(I), Au (III), Pd(II) and Pt(IV) ions, are photochemically reduced on the surface of TiO_2. Nano-heterodimers with one Ag, Au and Pd nanodot per TiO_2 are obtained showing that laser deposition seems to be much more efficient in this case than of the usual UV lamp photodeposition, suggesting that the flux of photons matters much more than the deposited energy. Ag-TiO_2 heterodimer nanoparticles are successfully synthesized by the two laser deposition methods. The number and size distribution of Ag dots are dependent on hole scavengers, pH and metal precursor. A growth model well predicted the silver size variation in the photodeposition process. Extending the synthesis to other metal precursors ($KAuCl_4$, Na_2PdCl_4 and H_2PtCl_6) using both setups is described explicitly in chapter 5, and leads to the formation of gold, palladium and platinum-based heterodimers with TiO_2. The growth law of gold can reasonably be predicted as well, although it is not as good as in the case of Ag, while our model did not work in the case of Pd and Pt.

Finally, in **Chapter 6,** we discussed bimetallic core-shell structured (Au@M)-TiO_2 (M=Ag, Pd, Au and Pt) nanoobjects synthesized by a simple two-step UV laser deposition method in the cuvette setup.

This thesis ends up with **Conclusions and Perspectives** with a reflection about the as-obtained results and some possible improvements for further research.

One may refer to **Appendix** for a better understanding of the detailed information concerning absorption and heating effect by UV laser (Appendix 1), the proposed model (Appendix 2), the theoretical prediction of the metal size (Appendix 3) and the characterization techniques (Appendix 4).

Bibliography

1.	Casagrande, C.; Fabre, P.; Raphaël, E.; Veyssié, M., "Janus Beads": Realization and Behaviour at Water/Oil Interfaces. *Europhys. Lett.* **1989,** *9*, 251-255.
2.	de Gennes, P. G., Soft matter. *Rev. Mod. Phys.* **1992,** *64*, 645-648.
3.	Walther, A.; Müller, A. H. E., Janus Particles: Synthesis, Self-Assembly, Physical Properties, and Applications. *Chem. Rev.* **2013,** *113*, 5194-5261.
4.	Yi, Y.; Sanchez, L.; Gao, Y.; Yu, Y., Janus particles for biological imaging and sensing. *Analyst* **2016,** *141*, 3526-3539.
5.	Kirillova, A.; Marschelke, C.; Synytska, A., Hybrid Janus Particles: Challenges and Opportunities for the Design of Active Functional Interfaces and Surfaces. *ACS Appl. Mater. Interfaces* **2019,** *11*, 9643-9671.
6.	Loget, G.; Kuhn, A., Bulk synthesis of Janus objects and asymmetric patchy particles. *J. Mater. Chem.* **2012,** *22*, 15457-15474.
7.	Hu, J.; Zhou, S.; Sun, Y.; Fang, X.; Wu, L., Fabrication, properties and applications of Janus particles. *Chem. Soc. Rev.* **2012,** *41*, 4356-4378.
8.	Perro, A.; Reculusa, S.; Ravaine, S.; Bourgeat-Lami, E.; Duguet, E., Design and synthesis of Janus micro- and nanoparticles. *J. Mater. Chem.* **2005,** *15*, 3745-3760.
9.	Liang, F.; Zhang, C.; Yang, Z., Rational Design and Synthesis of Janus Composites. *Adv. Mater.* **2014,** *26*, 6944-6949.
10.	Ebbens, S. J.; Howse, J. R., In pursuit of propulsion at the nanoscale. *Soft Matter* **2010,** *6*.
11.	Rodríguez-Fernández, D.; Liz-Marzán, L. M., Metallic Janus and Patchy Particles. *Part. Part. Syst. Char.* **2013,** *30*, 46-60.
12.	Xu, L.; Mou, F.; Gong, H.; Luo, M.; Guan, J., Light-driven micro/nanomotors: from fundamentals to applications. *Chem. Soc. Rev.* **2017,** *46*, 6905-6926.
13.	Guix, M.; Weiz, S. M.; Schmidt, O. G.; Medina-Sánchez, M., Self-Propelled Micro/Nanoparticle Motors. *Part. Part. Syst. Char.* **2018,** *35*, 1700382.
14.	Du, J.; O'Reilly, R. K., Anisotropic particles with patchy, multicompartment and Janus architectures: preparation and application. *Chem. Soc. Rev.* **2011,** *40*, 2402-2416.
15.	Synytska, A.; Khanum, R.; Ionov, L.; Cherif, C.; Bellmann, C., Water-Repellent Textile via Decorating Fibers with Amphiphilic Janus Particles. *ACS Appl. Mater. Interfaces* **2011,** *3*, 1216-1220.
16.	Lattuada, M.; Hatton, T. A., Synthesis, properties and applications of Janus nanoparticles. *Nano Today* **2011,** *6*, 286-308.
17.	Chauhan, A.; Rastogi, M.; Scheier, P.; Bowen, C.; Kumar, R. V.; Vaish, R., Janus nanostructures for heterogeneous photocatalysis. *Appl. Phys. Rev.* **2018,** *5*, 041111.
18.	Clavero, C., Plasmon-induced hot-electron generation at nanoparticle/metal-oxide interfaces for photovoltaic and photocatalytic devices. *Nature Photonics* **2014,** *8*, 95-103.
19.	Bai, S.; Li, X.; Kong, Q.; Long, R.; Wang, C.; Jiang, J.; Xiong, Y., Toward Enhanced Photocatalytic Oxygen Evolution: Synergetic Utilization of Plasmonic Effect and Schottky Junction via Interfacing Facet Selection. *Adv. Mater.* **2015,** *27*, 3444-3452.
20.	Hou, W.; Cronin, S. B., A Review of Surface Plasmon Resonance-Enhanced Photocatalysis. *Adv. Funct. Mater.* **2013,** *23*, 1612-1619.
21.	Zhang, X.; Chen, Y. L.; Liu, R.-S.; Tsai, D. P., Plasmonic photocatalysis. *Rep. Prog. Phys.* **2013,** *76*, 046401.
22.	Wenderich, K.; Mul, G., Methods, Mechanism, and Applications of Photodeposition in Photocatalysis: A Review. *Chem. Rev.* **2016,** *116*, 14587-14619.
23.	Pan, X.; Xu, Y., Defect-Mediated Growth of Noble-Metal (Ag, Pt, and Pd) Nanoparticles on TiO_2 with Oxygen Vacancies for Photocatalytic Redox Reactions under Visible Light. *J. Phys. Chem. C* **2013,** *117*, 17996-18005.
24.	Chen, S. F.; Li, J. P.; Qian, K.; Xu, W. P.; Lu, Y.; Huang, W. X.; Yu, S. H., Large scale photochemical

synthesis of M@TiO$_2$ nanocomposites (M = Ag, Pd, Au, Pt) and their optical properties, CO oxidation performance, and antibacterial effect. *Nano Res.* **2010,** *3*, 244-255.

25. Taing, J.; Cheng, M. H.; Hemminger, J. C., Photodeposition of Ag or Pt onto TiO$_2$ Nanoparticles Decorated on Step Edges of HOPG. *ACS Nano* **2011,** *5*, 6325-6333.

26. Diak, M.; Grabowska, E.; Zaleska, A., Synthesis, characterization and photocatalytic activity of noble metal-modified TiO$_2$ nanosheets with exposed {001} facets. *Appl. Surf. Sci.* **2015,** *347*, 275-285.

27. Melvin, A. A.; Illath, K.; Das, T.; Raja, T.; Bhattacharyya, S.; Gopinath, C. S., M-Au/TiO$_2$ (M=Ag, Pd, and Pt) nanophotocatalyst for overall solar water splitting: role of interfaces. *Nanoscale* **2015,** *7*, 13477-13488.

28. Shoaib, A.; Ji, M.; Qian, H.; Liu, J.; Xu, M.; Zhang, J., Noble metal nanoclusters and their in situ calcination to nanocrystals: Precise control of their size and interface with TiO$_2$ nanosheets and their versatile catalysis applications. *Nano Res.* **2016,** *9*, 1763-1774.

29. Zheng, Z.; Huang, B.; Qin, X.; Zhang, X.; Dai, Y.; Whangbo, M.-H., Facile in situ synthesis of visible-light plasmonic photocatalysts M@TiO$_2$ (M = Au, Pt, Ag) and evaluation of their photocatalytic oxidation of benzene to phenol. *J. Mater. Chem.* **2011,** *21*, 9079-9087.

30. Dozzi, M. V.; Saccomanni, A.; Selli, E., Cr(VI) photocatalytic reduction: Effects of simultaneous organics oxidation and of gold nanoparticles photodeposition on TiO$_2$. *J. Hazard Mater.* **2012,** *211-212*, 188-195.

31. Oros-Ruiz, S.; Pedraza-Avella, J. A.; Guzmán, C.; Quintana, M.; Moctezuma, E.; del Angel, G.; Gómez, R.; Pérez, E., Effect of Gold Particle Size and Deposition Method on the Photodegradation of 4-Chlorophenol by Au/TiO$_2$. *Top. Catal.* **2011,** *54*, 519-526.

32. You, X.; Chen, F.; Zhang, J.; Anpo, M., A novel deposition precipitation method for preparation of Ag-loaded titanium dioxide. *Catal. Lett.* **2005,** *102*, 247-250.

33. López-Tenllado, F. J.; Hidalgo-Carrillo, J.; Montes, V.; Marinas, A.; Urbano, F. J.; Marinas, J. M.; Ilieva, L.; Tabakova, T.; Reid, F., A comparative study of hydrogen photocatalytic production from glycerol and propan-2-ol on M/TiO$_2$ systems (M=Au, Pt, Pd). *Catal. Today* **2017,** *280*, 58-64.

34. Melián, P. E.; Díaz, G. O.; Rodríguez, J. M.; Colón, G.; Navío, J. A.; Macías, M.; Peña, P. J., Effect of deposition of silver on structural characteristics and photoactivity of TiO$_2$-based photocatalysts. *Appl. Catal., B* **2012,** *127*, 112-120.

35. Sreethawong, T.; Yoshikawa, S., Impact of photochemically deposited monometallic Pt and bimetallic Pt-Au nanoparticles on photocatalytic dye-sensitized H$_2$ production activity of mesoporous-assembled TiO$_2$-SiO$_2$ mixed oxide nanocrystal. *Chem. Eng. J.* **2012,** *197*, 272-282.

36. Iliev, V.; Tomova, D.; Bilyarska, L.; Eliyas, A.; Petrov, L., Photocatalytic properties of TiO$_2$ modified with platinum and silver nanoparticles in the degradation of oxalic acid in aqueous solution. *Appl. Catal. B* **2006,** *63*, 266-271.

37. Wang, D.; Bi, Q.; Yin, G.; Wang, P.; Huang, F.; Xie, X.; Jiang, M., Photochemical Preparation of Anatase Titania Supported Gold Catalyst for Ethanol Synthesis from CO$_2$ Hydrogenation. *Catal. Lett.* **2018,** *148*, 11-22.

38. Herrmann, J.-M.; Disdier, J.; Pichat, P.; Fernández, A.; González-Elipe, A.; Munuera, G.; Leclercq, C., Titania-supported bimetallic catalyst synthesis by photocatalytic codeposition at ambient temperature: Preparation and characterization of Pt-Rh, Ag-Rh, and Pt-Pd couples. *J. Catal.* **1991,** *132*, 490-497.

39. Aronovitch, E.; Kalisman, P.; Mangel, S.; Houben, L.; Amirav, L.; Bar-Sadan, M., Designing Bimetallic Co-Catalysts: A Party of Two. *J. Phys. Chem. Lett.* **2015,** *6*, 3760-3764.

40. Zaleska-Medynska, A.; Marchelek, M.; Diak, M.; Grabowska, E., Noble metal-based bimetallic nanoparticles: the effect of the structure on the optical, catalytic and photocatalytic properties. *Adv. Colloid Interface Sci.* **2016,** *229*, 80-107.

41. Jones, W.; Su, R.; Wells, P. P.; Shen, Y.; Dimitratos, N.; Bowker, M.; Morgan, D.; Iversen, B. B.; Chutia, A.; Besenbacher, F.; Hutchings, G., Optimised photocatalytic hydrogen production using core-shell AuPd promoters with controlled shell thickness. *Phys. Chem. Chem. Phys.* **2014,** *16*, 26638-26644.

42. Menagen, G.; Macdonald, J. E.; Shemesh, Y.; Popov, I.; Banin, U., Au Growth on Semiconductor Nanorods: Photoinduced versus Thermal Growth Mechanisms. *J. Am. Chem. Soc.* **2009,** *131*, 17406-

8

17411.

43.   Nakibli, Y.; Kalisman, P.; Amirav, L., Less is more: the case of metal cocatalysts. *J. Phys. Chem. Lett.* **2015,** *6*, 2265-2268.

44.   Kalisman, P.; Nakibli, Y.; Amirav, L., Perfect Photon-to-Hydrogen Conversion Efficiency. *Nano Lett.* **2016,** *16*, 1776-1781.

45.   Nakibli, Y.; Mazal, Y.; Dubi, Y.; Wachtler, M.; Amirav, L., Size Matters: Cocatalyst Size Effect on Charge Transfer and Photocatalytic Activity. *Nano Lett.* **2018,** *18*, 357-364.

46.   Dinh, C.-T.; Nguyen, T.-D.; Kleitz, F.; Do, T.-O., A New Route to Size and Population Control of Silver Clusters on Colloidal TiO_2 Nanocrystals. *ACS Appl. Mater. Interfaces* **2011,** *3*, 2228-2234.

47.   Ben-Shahar, Y.; Banin, U., Hybrid Semiconductor-Metal Nanorods as Photocatalysts. *Top. Curr. Chem.* **2016,** *374*, 54.

48.   Ben-Shahar, Y.; Scotognella, F.; Kriegel, I.; Moretti, L.; Cerullo, G.; Rabani, E.; Banin, U., Optimal metal domain size for photocatalysis with hybrid semiconductor-metal nanorods. *Nature Commun.* **2016,** *7*, 10413.

49.   Ben-Shahar, Y.; Philbin, J. P.; Scotognella, F.; Ganzer, L.; Cerullo, G.; Rabani, E.; Banin, U., Charge Carrier Dynamics in Photocatalytic Hybrid Semiconductor-Metal Nanorods: Crossover from Auger Recombination to Charge Transfer. *Nano Lett.* **2018,** *18*, 5211-5216.

50.   Delville, M.-H.; Delville, J.-P.; Vauriot, L. Particules de TiO_2 dissymétriques (Particules de Janus) et leur procédé de synthèse par photodéposition. FR2999452, 2012.

51.   Pradhan, S.; Ghosh, D.; Chen, S., Janus Nanostructures Based on Au−TiO_2 Heterodimers and Their Photocatalytic Activity in the Oxidation of Methanol. *ACS Appl. Mater. Interfaces* **2009,** *1*, 2060-2065.

52.   Byeon, J. H.; Kim, Y.-W., Au-TiO_2 Nanoscale Heterodimers Synthesis from an Ambient Spark Discharge for Efficient Photocatalytic and Photothermal Activity. *ACS Appl. Mater. Interfaces* **2014,** *6*, 763-767.

53.   Menzel, R.; Duerrbeck, A.; Liberti, E.; Yau, H. C.; McComb, D.; Shaffer, M. S. P., Determining the Morphology and Photocatalytic Activity of Two-Dimensional Anatase Nanoplatelets Using Reagent Stoichiometry. *Chem. Mater.* **2013,** *25*, 2137-2145.

54.   Kanie, K.; Sugimoto, T., Shape control of anatase TiO_2 nanoparticles by amino acids in a gel-sol system. *Chem. Commun.* **2004**, 1584-1585.

55.   Dinh, C. T.; Nguyen, T. D.; Kleitz, F.; Do, T. O., Shape-controlled synthesis of highly crystalline titania nanocrystals. *ACS Nano* **2009,** *3*, 3737-3743.

56.   Zhuang, M.; Zheng, Y.; Liu, Z.; Huang, W.; Hu, X., Shape-dependent performance of TiO_2 nanocrystals as adsorbents for methyl orange removal. *RSC Adv.* **2015,** *5*, 13200-13207.

Chapter 1

State of the art of photodeposition of metal nanodots on TiO$_2$

Table of Contents

1.1 Principles of photodeposition of nanoparticles on the semiconductor surface

Illumination of a mixture solution of semiconductor particles and a metal salt leads to the deposition of a metal or a metal oxide on the surface of the semiconductor, and this phenomenon is generally known as photodeposition. The first example of photodeposition can be dated back to 1965, when Clark et al.[1] succeeded in the formation of metallic silver on titanium dioxide (TiO$_2$), after they illuminated a solution of TiO$_2$ containing silver nitrate (AgNO$_3$) and first used infrared spectroscopy to identify metallic silver. However, the fast-growing interest in photodeposition has sparked since Kraeutler et al.[2] published their report in 1978. In their study, when the reaction mixture containing the TiO$_2$ powder and the platinizing solution was irradiated with a Hg-Xe lamp, its initially bright orange solution largely faded, and the greyish power significantly darkened, implying the platinum loading on TiO$_2$. Since the beginning of this century, expanded interest has focused on photodeposition (Figure 1.1).
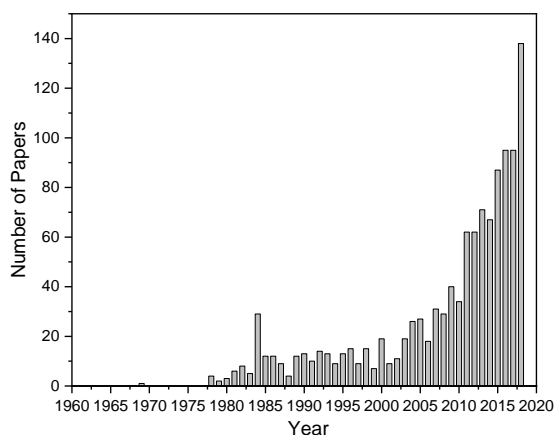
Figure 1.1 Overview of the number of papers published on "photodeposition" as a function of years, as searched in Scopus on April 9, 2019. Note: not all research related to photodeposition is shown in this picture, as it can also be called "photoreduction" or "photochemical deposition".

Two types of photodeposition need to be distinguished: one is reductive photodeposition, and the other is oxidative photodeposition. The difference is in the point that which kind of photon-excited charge carrier will be used to participate in the reaction with metal ions. Reductive photodeposition takes place when electrons are used to reduce the metal ions to a metallic cluster. An example[3] is given as:

15

$$Ag^{+}(aq)+e^{-} \rightarrow Ag(s)$$

Its counterpart, oxidative photodeposition is a process where the photo-excited holes oxidize the metal ions to form metal oxides. An example[4] of this is illustrated by:

$$Ru^{3+}(aq)+h^{+}+2H_{2}O \rightarrow RuO_{2}(s)+4H^{+}$$
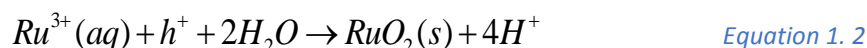
Considerations need be taken in order to initiate the photodeposition. First, the incident light needs to own enough photo-energy to induce the band-gap excitation of the semiconductors, that is $E_p \geq E_g$ as shown in Figure 1.2.
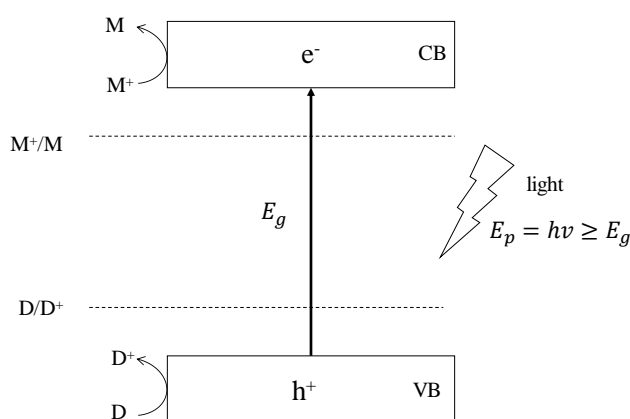
Figure 1.2 Schematic view of the metal ions reduction on a semiconductor. Excited electrons (e⁻) are used for the reduction of a metal ion, whereas holes (h⁺) are used to oxidize an electron donor D. E$_g$: band gap energy; E$_p$+: incident light photon energy; CB: conduction band; VB: valence band.

The second consideration is that the edge of the conduction band (CB) must be more negative than the reduction potential of metals, and the valence band (VB) is more positive than the oxidation potential of the species to be oxidized. Thus, the redox potential of either the reduction of metal ions or the oxidation of electron donor should be in between the band positions of CB and VB of the semiconductor (Figure 1.2). Figure 1.3 depicts the band positions of several common semiconductors on the energy scale versus either vacuum level or normal hydrogen electrode. The redox potential of several metal ions and methanol are also listed.
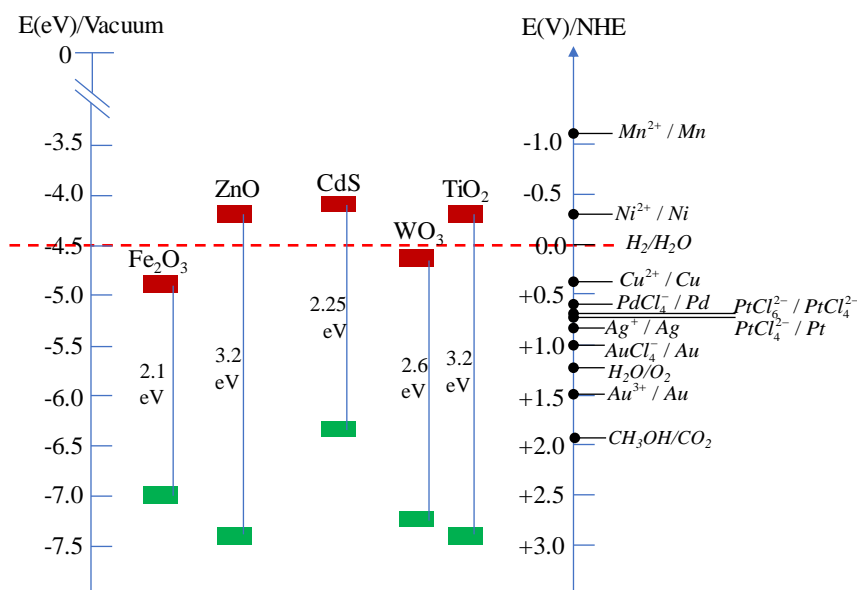
Figure 1.3 Band positions of several common semiconductors on an energy scale in electron volts with reference to vacuum level, or in volts with reference to normal hydrogen electrode (NHE). The lower edge of the conduction band (red colour) and the upper edge of the valence band (green colour) are presented along with the band gap in electron volts, and figure adapted from Gratzel's work.[5] Redox potentials of several aqueous metal solutions relevant for photodeposition are shown using NHE as a reference; the half-wave potential of methanol is also listed.[6, 7]

Take CB of TiO$_2$ as an example; electrons from the excited TiO$_2$ can reduce most metal ions except Mn^{2+}, since the reduction potential of Mn^{2+}/Mn is higher than the CB edge of TiO$_2$. Last but not least, the charge carrier separation need to be efficient to result in metal cluster formation; thus, the addition of certain hole scavengers is necessary.

1.2 Applications of photodeposition and comparison to other alternative methods

Metal (oxide) nanoparticles (NPs) on semiconductor surfaces prepared by photodeposition are predominantly utilized in applications including photocatalytic fuel generation synthesis,[8-11] water pollution treatment,[12-14] and air purification.[15, 16] Metal (oxide) NPs can significantly improve performance of semiconductors in light-stimulated reactions, including their stability.[17-19] With an appropriate loading, these hybrid materials have been proposed to function (i) as a better charge carrier separation upon photoexcitation of the semiconductor, hindering electron-hole recombination; (ii) by providing active sites for charge-transfer reactions; and (iii) by extending light absorption to visible wavelength range due to plasmonic field effects, particularly in the case of Au or Ag.[20, 21]

17

Besides photodeposition, several methods can also be applied to load metal NPs on surfaces of semiconductors, such as hydrothermal reactions,[22, 23], thermal evaporation,[24, 25] impregnation,[26] deposition–precipitation,[27] chemical reduction,[28-30]electrodeposition,[28, 31] atomic-layer deposition[32] and sputtering.[33]

The photodeposition method is one of the easiest attractive methods to synthesize noble metal/semiconductor nanocomposites by utilizing the band gap of the semiconductor. Compared with most other methods that need an elevated temperature, an additional redox agent, electric potential, or multi-step processing, the photoinduced reduction method requires only the irradiation of a light source onto a slurry or a mixture solution. Furthermore, it is easy to control the size of metal NPs by adjusting the concentration of the metal precursor, irradiating intensity and duration. The advantages of photodeposition may also include the fine control over geometrical metal distribution on facet-engineered semiconductor crystals and the material selectivity, whereby noble metal NPs are only deposited on the semiconductor.[34]

1.3 Photodeposition of nanoparticles on the surface of TiO$_2$

In this part, a short review on metal NP loaded on the surface of TiO$_2$ NPs using photodeposition method will be introduced. In some research, people could also make metal photodeposition on TiO$_2$ films,[35-38] which nonetheless will not be discussed in this part.

1.3.1 Photodeposition of silver NDs on the surface of TiO$_2$

Albiter et al.[39] studied the effect of Ag precursor on the photocatalytic properties of Ag-TiO$_2$ composites obtained by photodeposition with regards to the degradation of rhodamine B (used as a model pollutant) in aqueous solution under simulated solar light. The Ag precursors were respectively silver nitrate (AgNO$_3$), silver perchlorate (AgClO$_4$) and silver acetylacetonate (Ag(acac)). The photocatalytic reduction of Ag$^+$ ions to Ag^0 on P25 TiO$_2$ was higher with AgNO$_3$ as a precursor than with AgClO$_4$ or silver acetylacetonate. The authors stated that the Ag-TiO$_2$ hybrid materials exhibited a surface plasmon resonance effect in the visible region (400 - 530) nm, indicating that different metal particle sizes were obtained depending on the Ag precursor used. However, the author failed to explain why few silver nanodots (Ag NDs) can be observed

when using silver acetylacetonate and silver perchlorate as displayed in the TEM images.

The existence of hole scavengers in the photodepoisition process is necessary in order to improve the photodeposition rate of metals onto the surface of the semiconductor. Frequently used hole scavengers include alcohols such as methanol[40, 41], ethanol[42-44] and isopropanol[45], or an organic acid such as oxalic acid,[46] humic acid[47] and formic acid[48].

For the effect of pH, Nishimoto et al.[49] found that during the photodeposition of Ag on TiO_2, TiO_2 was deactivated when the pH of the reaction mixture decreased down to 2 with irradiation time. Ohtani et al.[50] stated that anatase TiO_2 having a high proportion of strongly acidic surface sites rather than readily protonated hydroxyls (OH groups) was favourable for the photocatalytic reactions. However, we should also bear in mind the fact that the basic solution would cause the formation of Ag_2O in solution or anchored on TiO_2, where the author may neglect this point. Optimum pH control of the aqueous reaction system would enable researchers to obtain the highest activity of semiconductor TiO_2.[49] Zhang et al.[51] performed silver photodeposition experiments under three pHs, that is, at acidic solution pH3 and pH 4 - 5, basic solution at pH11 - 12, and found a deposition of multi-NDs all over the surface of TiO_2 (Figure 1.4). However, XPS analysis confirmed a larger ratio of silver oxide in addition to metallic silver with increasing the pH values. In order to inhibit the formation of silver oxide, Cai et al.[3] built a modified protocol called dark deposition, where UV illumination was shed on TiO_2 colloidal solution for a long time before the introduction of the silver precursor. Thus the Ag^+ ions were reduced by the electrons pre-generated on the surface of TiO_2 rather than the electrons from bandgap excitation under irradiation. They thus achieved a good size distribution on the whole surface of TiO_2 but also tinier NDs than with classical photodeposition.
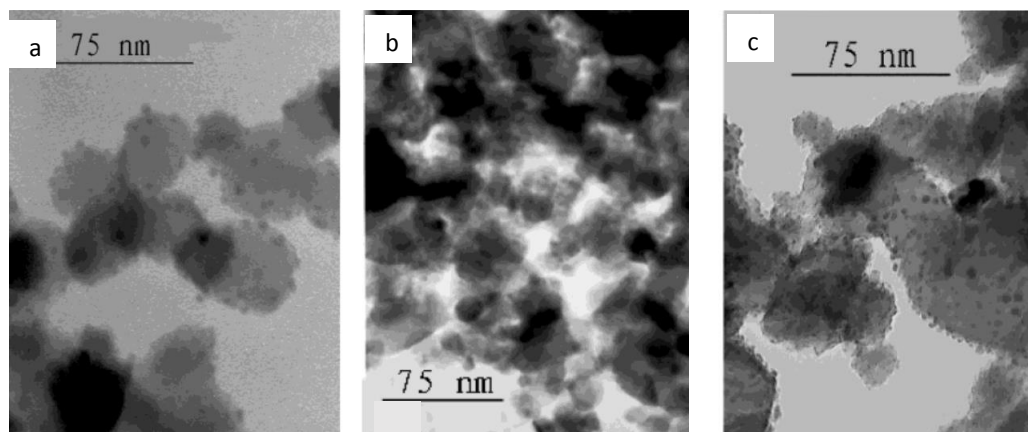
Figure 1.4 The effect of pH on the process of silver photodeposition on TiO_2.[51](a) pH 3; (b) pH 4 - 5 and (c) pH 11 - 12.

19

The surface facet of the substrate can also play a role in the photodeposition product. Jiang et al.[52] found that the Ag NDs were likely to deposit on the (101) facets of TiO$_2$ when using a traditional photodeposition method (Figure 1.5a). He performed a modified photodeposition method, in which he first coated TiO$_2$ by AgIO$_3$, then illuminated them by UV light, leading to ultrafine silver particles (~1 nm) well distributed on the surface of TiO$_2$ (Figure 1.5b) due to the low release rate of Ag$^+$ from AgIO$_3$.
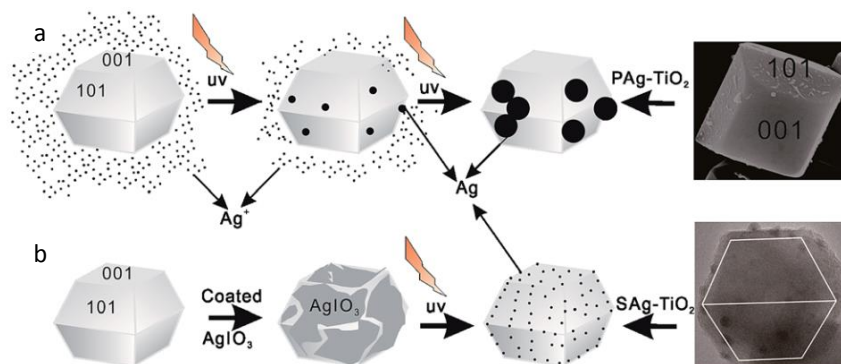
Figure 1.5 The proposed growth mechanism of Ag NDs during two preparation process: (a) traditional photodeposition method; (b)modified photodeposition method.[52]

D'Arienzo et al.[53] have studied the properties of the photogenerated defects, and in particular, their dependence on the exposed crystal faces in shape controlled anatase. They suggested that {001} surfaces could be considered essentially as oxidation sites with a critical role in the photooxidation, while the {101} surfaces provided preferential reductive sites for metal ion reduction.

The photodeposition site will also vary with the shape of the semiconductor and then the nature of the most exposed facets. As can be seen from Figure 1.6, the Ag NDs are well distributed on the whole surface of the symmetrical shaped TiO$_2$ (Figure 1.6a) or the near-tip site of the nanorods-shape TiO$_2$ (Figure 1.6b), depending on the specific facet energy of the TiO$_2$ with a particular shape.[54, 55]

References page 33
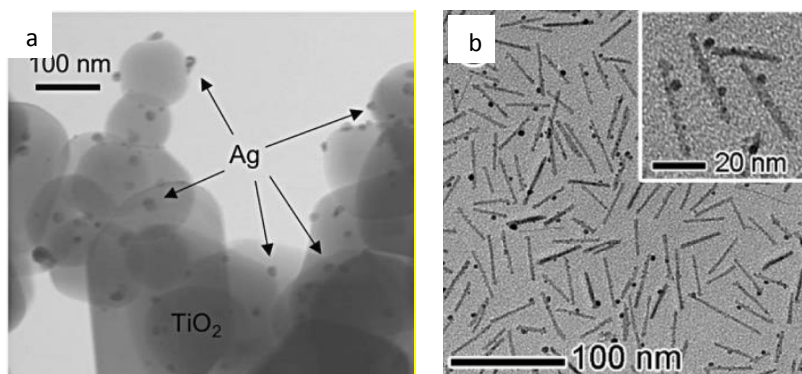
Figure 1.6 Photodeposition of Ag NDs on anatase TiO$_2$ with the shape of (a) TiO$_2$ NPs in the 300 – 500 nm range [54] and (c) TiO$_2$ nanorod[55].

The initial reaction rate of Ag photodeposition is proportional to the light intensity applied to the reaction system, implying that the second-order recombination of electrons and holes is not preponderant in the process.[56] Chan et al.[57] found that the silver size during the photodeposition process is dependent on the photon energy and durations. As shown in Figure 1.7, higher photon energy and duration resulted in larger mean size Ag NDs.
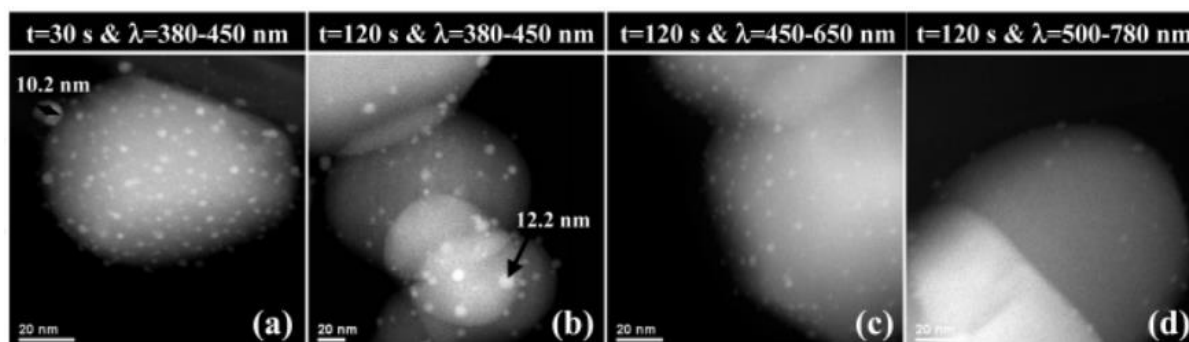
Figure 1.7 HAADF images of TiO$_2$ NPs after irradiation in an AgNO$_3$ solution at various wavelengths and times.

Most of the research concerning silver photodeposition reported on the deposition of multi silver clusters on the surface of the TiO$_2$ NPs.[29, 42, 54, 58-63] Very few are the papers which claim that the number of Ag NDs can be controlled by varying the physical or chemical conditions. Dinh et al.[42], for example, proceeded to the formation of hybrid Ag/TiO$_2$ nanocrystals in which the Ag nanodots (NDs) were uniformly deposited on the individual TiO$_2$ surface using hydrophobic surfactant (oleic acid)-capped TiO$_2$ NPs in combination with a classical photodeposition technique. The population of Ag clusters on the TiO$_2$ surface was controlled by the degree of hydrophobicity (e.g., the number of vacant sites) on the TiO$_2$ surface while their size was altered simply by varying the irradiation time. They, however, did not reach the one to one heterodimer ratio between TiO$_2$ and Ag dot. Lu et al.[55] are the first ones to claim a

21

photocatalytic strategy to synthesize colloidal Ag-TiO$_2$ composites in which each TiO$_2$ nanoparticle, in their case nanorods, exhibits a single Ag nanodot on its surface. They assume that

(i)   the photoexcitation of the TiO$_2$ nanorods under UV illumination produces electrons that reduce the Ag(I) precursor and deposit multiple small Ag NDs everywhere on the surface of the nanorods.

(ii)   The prolonged UV irradiation induces a ripening process, which dissolves the smallest NDs by photogenerated oxidative species and redeposits the "Ag" onto the larger and more stable particles attached to the TiO$_2$ nanorod through the reduction of photoexcited electrons (Figure 1.8).
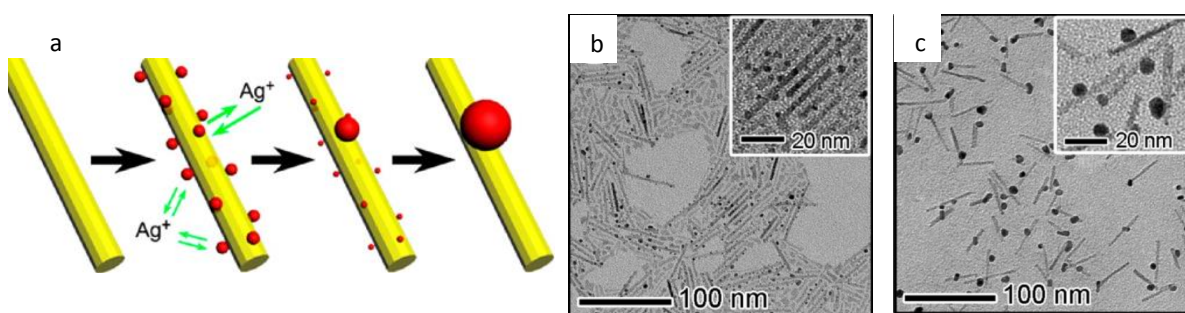
Figure 1.8 (a)Schematic mechanism of silver size evolution with increasing irradiation time. (b), (c) indicate irradiation durations of 1 h and 10 h, respectively.[55]

This is justified by the fact that the size of the Ag NDs can be precisely controlled by varying the irradiation time and the amount of alcohol additive.

1.3.2 Photodeposition of gold NDs on the surface of TiO$_2$

In general, people use AuCl$_4^-$ ions type salts as the metal precursors for the photodeposition of gold. Gartner et al. [64] synthesized gold nanodots (Au NDs) on TiO$_2$ commercial product using different Au metal salts. The highest deposition is achieved by using NaAuCl$_4$ (0.97 wt%) followed by AuCl$_3$ (0.96 wt%), AuCl (0.65 wt%) and [Au(PPh$_3$)]Cl (almost 0). The average particle size remained almost the same (3–12 nm) in all these cases.[64] Sangeetha et al.[65] also made a comparison between HAuCl$_4$ and AuCl$_3$ and found no significant difference in metal loading.

Kenens et al.[66] investigated the effect of hole scavengers on the photodeposition of Au on TiO$_2$

and found that ethylene glycol showed better efficiency than ethanol at hole consumption, making it an efficient hole scavenger. It was demonstrated that Au NDs made by photodeposition using ethanol were large (50 - 100 nm for 0.4 wt%) and aggregated, and those using ethylene glycol were small (5 - 15 nm for 0.4 wt%) and more abundant.[66]

By studying the effect of pH, Yang et al. noted that the surface property of the semiconductor substrate was related to the solution environment.[67] At low pH values (below the isoelectric point of TiO$_2$ 6.2), the surface of the TiO$_2$ is positively charged, and the species in solution are anionic. Hence an electrostatic mechanism can explain the deposition of Au. The uptake is rapid, large particles form and the catalysts have low catalytic activity. As the pH value increased, the amount of gold deposited on the support decreased.[67] However, depending on the pH of the reaction system, others noted that metal complex species in solution, such as Au(OH)$_x$Cl$_{4-x}^-$ (x = 0, 1, 2, 3, 4), could be found and provide a discrete concentration of adsorbed metal precursors on TiO$_2$.[68]

It is believed that the size control of Au NDs is vital in photocatalytic reactions.[20, 69] Wang et al.[69] found that the size of Au NDs can be easily regulated by changing the concentration of gold precursor from 0.05 to 0.25 mM or the Au loading in the range of 0.3 to 1.5 wt% using photodeposition method. Deepagan et al.[70] indicated that the size of Au NDs could be adjusted by varying the irradiation time when illuminated by a 256 nm light. An exposure time as short as 3 min resulted in the formation of unimodal small Au NDs (< 2 nm) on the surface of TiO$_2$. The exposure time of 10 min irradiation led to the appearance of large Au NDs (> 5 nm) with the coexistence of the small ones. Prolonged exposure over 12 h resulted in the growth of large Au NDs with complete disappearance of small ones (Figure 1.9). Therefore, by controlling the exposure time, the author obtained three representative composites of TiO$_2$ nanoparticle with small, bimodal and large Au NDs.[70] In another work, Wei et al.[20] emphasized the importance of the morphology of semiconductor. It was demonstrated that better morphology of titania (larger content of faceted particles) resulted in the formation of larger Au NDs, while small Au NDs were deposited on structural defects.
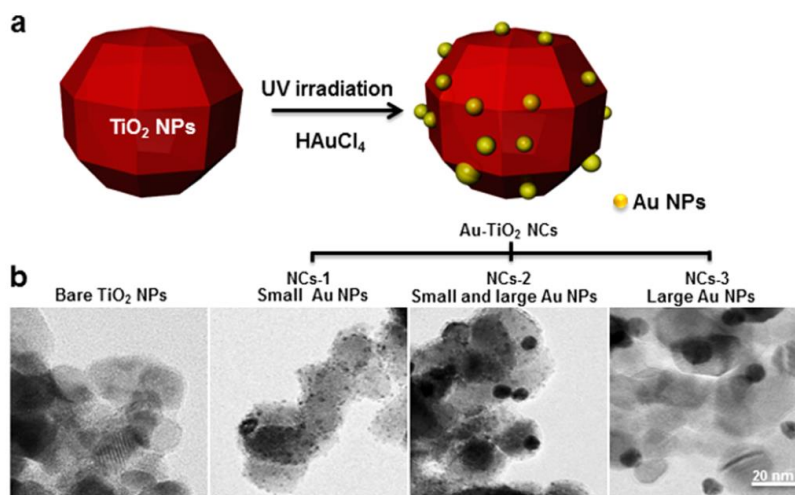
Figure 1.9 (a) Schematic photodeposition of gold on the surface of TiO$_2$; (b) TEM images of photodeposition process with increasing exposure time(from left to right).[70]

As for the number of gold deposits on the surface of TiO$_2$, most of the work concerning gold photodeposition found few Au NDs distributed on each TiO$_2$ particle, no matter the gold content loading, the kind of TiO$_2$ or its morphologies (Figure 1.10).[71-74]
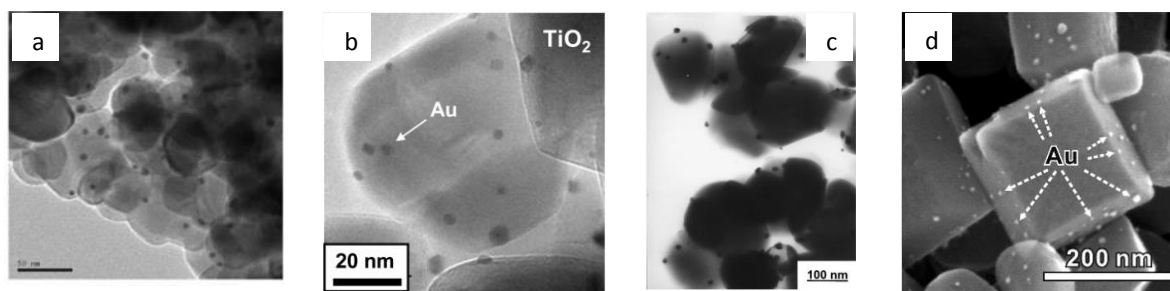
Figure 1.10 Microscopic graphes of gold deposited TiO$_2$ particles. Image are taken from references of (a) ref.[71];(b) ref.[72];(c) ref.[73]and (d) ref.[74]

The effect of the illumination source and light intensity on the photodeposition process were also an important point to study. Hidalgo et al.[75] made a comparison of the photodeposition process using either high light intensity or low light intensity. They found that the former condition led to large and heterogeneously distributed gold deposits while the latter resulted in smaller gold deposits on the surface of TiO$_2$. Hippargi et al.[76] studied the effect of the different light sources on the photodeposition of gold on the surface of TiO$_2$. It was demonstrated that Au NDs with different sizes could be photo-reduced using these three lamps, i.e., Mercury lamp, solar lamp and Tungsten lamp. It was suggested that the different characteristic wavelengths should be the primary reason for the formation of varying particle sizes, where UV radiation with λ_{max} at 254, 302, 313 nm facilitates high nucleation rate more

than the growth of gold on TiO$_2$ (Figure 1.11).[76]
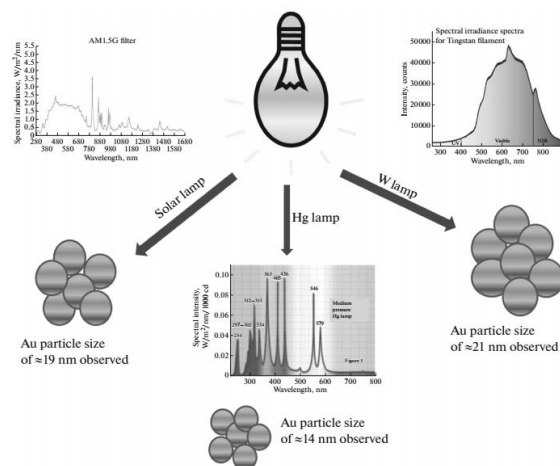
Figure 1.11 Graphical representation of light spectrum vs. particle size.[76]

In another work, the authors stated that the influence of light source intensity and was not established.[64] The effect of light source/intensity on photodeposition needs to be well established and considered in the future works.

1.3.3 Photodepositon of palladium NDs on the surface of TiO$_2$.

The photodeposition of palladium was first reported by Kelly et al. in 1975. The palladium nanodots (Pd NDs) were successfully deposited on a TiO$_2$ film when illuminated by a Mercury lamp.[77] Pd NDs can also be loaded on various semiconductors by photodeposition method.[78] It was found that the Pd size varied dramatically depending on the semiconductor, 1.8 nm Pd NDs were distributed on anatase while 51.8 nm Pd NDs on V$_2$O$_5$ substrate despite the same Pd loading. The author argued that the position of the reduction potential of each semiconductor played a crucial role in facilitating efficient deposition.

Several palladium precursors have been reported for the photodeposition of palladium.[45, 79, 80] Espino et al.[45] used Pd(NO$_3$)$_2$ to deposit Pd NDs on the surface of TiO$_2$, and found tiny metallic Pd dots on the whole surface of TiO$_2$ NPs. In Leong's work,[81] he used Na$_2$PdCl$_4$ as the metal precursor and obtained much larger palladium size in the 17 - 29 nm. Even though these two results cannot be simply compared because other parameters like the light source, the hole scavenger are different; it still seems to be surprising since the nominal metal loading was the same (1 wt% Pd-TiO$_2$) in both cases.

The effect of hole scavenger was studied. Jones et al.[82] found that the size of Pd NDs differed

25

when using methanol or triethanolamine (TEOA) as hole scavengers, owing to their difference in electronic structure. The photodeposition using methanol as a hole scavenger led to Pd size in 2 - 3 nm, while the one with TEOA gave Pd size of 4 - 7 nm, (see Figure 1.12). Dadsetan et al.[83] made a detailed work on the effect of organic alcohols on photodeposition. They tested four alcohols, i.e., methanol, ethanol, ethylene glycol, and 1-propanol, and the highest photodeposition rate was found with methanol. The results proved that the alcohols with lower carbon numbers and molar weights resulted in a higher reduction rate of Pd on TiO$_2$. Kriek et al.[84] also suggested that without any external hole scavengers it is also possible to proceed the photodeposition of Pd on TiO$_2$ surface.
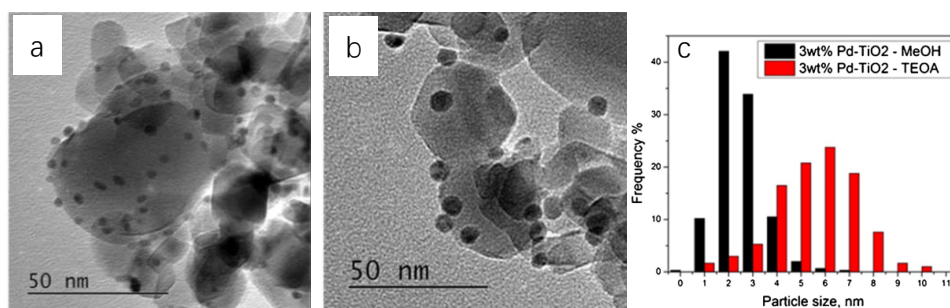
Figure 1.12 TEM images of Pd-TiO$_2$ NPs made by using (a)methanol and (b) TEOA as hole scavengers. (c) The size distribution of Pd-TiO$_2$. Images were taken from ref[82].

Borgarello studied the effect of pH values on the photodeposition rate and found the most efficient rate in the pH range 3 - 5.[85] The PdCl$_2$ solution turned turbid and a precipitate soon formed at pH > 7. It was also noticed that in the presence of hole scavenger (here methanol), the presence of O$_2$ seems to be not detrimental to the photoreduction of Pd^{2+} ions.

In situ XPS study by Fernandez demonstrated an efficient reduction of Pd ions during the photodeposition process irradiated by a Xe lamp.[86] Almost all the Pd^{2+} ions had been reduced to Pd^0 within 15 min illumination. Jacobs studied the photochemical nucleation and growth of Pd on TiO$_2$ films by a UV laser.[87, 88] It was demonstrated that a decrease in light intensity resulted in a reduction of the number of Pd particles deposited on the TiO$_2$ film. An increase of irradiation time from 3 ms to 10 ms caused the existing Pd nuclei (2 - 4 nm) to grow in size, but the density of Pd cluster only slightly increased.[87]

Dadsetan et al.[89] built a channel type quartz reactor to improve the loading amount of the metals. However, the Pd NDs made in this setup showed a large size distribution, besides large Pd particles with 8 nm, several small particles of 2.5 nm were also observed.

1.3.4 Photodeposition of other metal/particles on the surface of TiO$_2$

In addition to the three noble metals mentioned above, other works concerning metal and particles deposited onto the surface of TiO$_2$ were investigated by many researchers. In the case of platinum nanodots (Pt NDs) on TiO$_2$, one can refer to the excellent review made by Wenderich,[34] who reviewed the effect of various parameters on the photodeposition process. The concerned nanoparticles also include Cu,[90-94] Ni,[95-98] Cr[99] and Ru;[4, 19, 100, 101] metal oxides such as PbO$_2$[102] and RuO$_2$[4, 103, 104]. In some cases, photodeposition has also been employed to obtain core-shell particles,[105-107] alloy particles[108-111] or even trimetallic particles.[112, 113]

1.4 Photodeposition of particles on other semiconductors

Many other semiconductors, beside TiO$_2$, are also tested as substrates to load nanoparticles, among which the representative examples are zinc oxide (ZnO), tungsten oxide (WO$_3$) and cadmium sulfide (CdS).[34]

a) ZnO

Similar to what was discussed for TiO$_2$, the presence of a sacrificial electron donor has a strong influence on the rate of photodeposition and morphology of the metal on ZnO.[114, 115] The presence of ethanol was found to significantly improve the Ag size, from the initial size of 10 - 20 nm to huge clusters of 500 nm.[115] An opposite result was found that the silver content on ZnO using ethanol as hole scavenger is close to the one without using any hole scavenger.[114] We assumed that the nature of the substrate might also play a role in the deposit size. Some researchers observed that Ag quantities increased, with increasing irradiation time, as well as the Ag particle size.[116, 117] Ag deposits can also help to prevent photo-corrosion of ZnO, thus improving the stability of the semiconductor.[118,119] Other studies describe the photodeposition of gold[120-123] and also of palladium,[124-126] cadmium sulfide (CdS),[127, 128] copper,[129-132] platinum,[133, 134] and nickel[135, 136] on ZnO. Controlled deposition of mainly Au and Pd on ZnO was also studied, to prepare active photocatalysts. Au/ZnO catalysts have been predominantly used in CO oxidation,[137-139] dye photodegradation,[120, 140] and removal of bacteria.[140] Pd has been used for gas sensing[141, 142] and generally enhancing photocatalytic activity.[125, 126] An increase in photocatalytic activity of ZnO after deposition of Au or Pd is

attributed to enhanced charge-carrier separation and enhanced rates of electron-transfer reactions.[120, 126, 140]. Wenderich et al.[34] made a summary statement that (i) low HAuCl$_4$ concentration, (ii) high surface area of ZnO, and (iii) long illumination time are beneficial to obtain small, individual Au NDs, whereas the oxidation state usually is Au^0, irrespective of the presence of a hole scavenger.

Precursors for the photodeposition of Pd on ZnO include PdCl$_2$[125, 141, 143] and H$_2$PdCl$_4$.[126] Methanol,[141] ethanol,[143] and acetic acid[125] have been used as sacrificial agents for the photodeposition of Pd on ZnO. Interesting, Jin et al.,[126] who did not use any hole scavenger, found metallic Pd formed selectively. Gomathisankar et al.[131] focused on the deposition of Cu particles on ZnO. The stability of Cu was not discussed in detail, while oxidation of as-deposited Cu by in ZnO-generated holes is feasible.

b) WO3

WO$_3$ is another semiconductor extensively studied recently. It is nontoxic, stable under acidic conditions, and has a relatively narrow band gap.[144-146] The latter makes the material very suitable for solar-driven photocatalysis, for example, in the purification of water[147, 148] or air.[149, 150] Also of interest is the implementation of WO$_3$ in a Z-scheme for full water splitting.[146, 151, 152] WO$_3$ can be loaded through photodeposition with Pt,[149, 153-156]Pd,[157-159] Ag,[160, 161] and Au[162, 163]. In many cases, an increase in photocatalytic activity has been observed. [153, 159, 161, 162]

c) CdS

CdS is also a promising semiconductor material. Due to its instability, a hole scavenger needs to be present during the photodeposition process. Photodeposition has been applied to functionalize CdS with a variety of metal NPs. The effect of reaction conditions on Pt morphology on CdS has been investigated extensively

A surprisingly large amount of research has been performed on the formation of H$_2$ during in situ photodeposition of Pt on CdS.[164-166] Several researchers have tried to find an optimum loading of Pt on CdS for hydrogen evolution from water.[165, 167-169] For instance, the highest optimal Pt loading in H$_2$ production was found by Bao et al.[169] to be 13 wt %, whereas the lowest optimal loading was found by Li et al.[170] to be 0.025 wt %. Berr et al.[17] also investigated

the influence of photodeposition time (λ = 366 nm) on the morphology of Pt on CdS nanorods and correlated morphology to activity in H$_2$ production. The authors concluded that the photocatalytic activity was determined by the subnanometer-sized Pt particles rather than the large particles. Cocatalysts other than platinum include gold,[171-173] rhodium,[85, 174, 175]cadmium,[176] nickel (oxides),[176-178] ruthenium,[179] and palladium.[180]

1.5 Study of laser-induced photodeposition

When looking over the experimental processes involved in the photodeposition, one can find that most of the researchers used UV lamps as the light source to load metal/metal oxide on the surface of the semiconductor. A limited number of papers use another kind of light source, such as UV laser.

Jacob[87, 181] initially launched photodeposition experiments using a continuous Ar$^+$ UV laser. The wavelength of the UV laser ranged from 351.1 - 363.8 nm, with a spot size of 13 µm. Thanks to the small exposure area, the intensity can be increased up to 1.6×10^6 mW/cm^2. Pd NDs were deposited onto the surface of TiO$_2$ film under such a UV laser irradiation.[87] It was found that 3 ms irradiation time was sufficient to this high-intensity laser to induce instantaneous Pd deposition onto the surface of TiO$_2$. It was also evident that higher intensities resulted in much larger Pd size (4 nm) than lower ones. It is interesting to note that, under low light intensity, the extended irradiation time caused Pd agglomerates (5 - 25 nm), which consisted of a few smaller Pd clusters in the size of 2 - 4 nm. Copper nanodots (Cu NDs) were also photodeposited on TiO$_2$ using the same UV laser.[90] Jacobs showed the formation of small Cu$_2$O particles (< 3 nm) in the initial stage but also observed the metallic Cu when extending the irradiation time.

The photodeposition of silver on TiO$_2$ film using UV laser (257 nm) was investigated in Bade's work.[182] The evolution of the deposit spot in size was directly observed. The immediate formation of metallic Ag on the surface of TiO$_2$ was also found with a laser flash.[183] Interestingly, the authors claimed that large Ag particles formed at a low light intensity, which they attributed to an antenna effect, where Ag$^+$ is reduced by electrons transferred through TiO$_2$. Piwonski et al.[38] performed the silver photodeposition experiments on a TiO$_2$ film using two UV sources. The UV xenon lamp and the excimer laser, both operated at the same wavelength 351$\pm$5 nm. The AFM topography of Ag-TiO$_2$ nanocomposites revealed that Ag

29

NDs could be synthesized by both sources of illumination and that the photocatalysis carried out by UV light from xenon lamp illumination led to larger Ag NDs than those synthesized using the laser beam. It was found that increasing the silver ions concentration in the initial solution increased the number of Ag NDs on the titania surface, while longer irradiation times resulted in the growth of larger nanoparticle size.

CdS based semiconductors are as well used to be a substrate to load metal particles. In Banin's group, they succeeded in triggering the photodeposition of Au and Pt NDs on the surface of CdS and CdSe/CdS nanorods with the aid of a 473 nm laser.[172, 184] The light-induced Au growth leads to a selective deposition on one end of the rods; the temperature effect was investigated as well.[172] The growth of Pt NDs onto CdSe nanorods in aqueous media was demonstrated, and different morphologies could be obtained by altering the pH conditions.[184] Pt NDs with morphologies of nano-nets and nanodots were formed under acidic and basic conditions, respectively. A bunch of Pt dots (number > 20) were distributed on the surface of each CdS. Dukovic et al.,[166] however, obtained a much lower number of Pt NDs (number 1 - 6) on each CdS rod, using a UV laser at 458 nm. By contrast, most CdSe/CdS core/shell nanorods feature only one metal nanoparticle located near the CdSe core (see Figure 1.13). Furthermore, the author observed that the photodeposition process of Pt was a slow rate-limiting step, while slow oxidation or reduction steps, fast back-reactions, or inaccessibility of a CdS nanocrystal surface remain to be determined.[166]
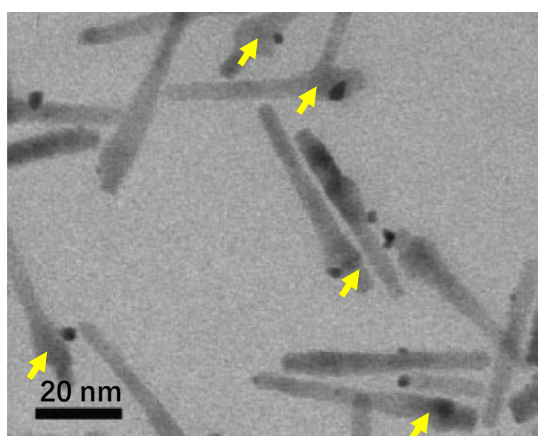
Figure 1.13 TEM image of photodeposition of Pt on CdSe/CdS core/shell nanorods. The arrows denote the position of the CdSe core.

Although light intensity can be a critical parameter in the photodeposition process, the incident laser power cannot be increased unlimitedly, because the thermal effect may be induced near the exposure area.[185] This effect will disturb the formation of deposits. For

example, the incident light may be scattered because of the bubbles formed near the laser irradiation area or the excessive heating may cause the ablation of previous deposits.

To the best of our knowledge, research using a laser as a light source for the photodeposition process has scarcely been reported except those mentioned above, which makes it a unique tool to study the photodeposition of metal on a semiconductor like TiO_2. More future works are needed to have this field well established.

1.6 Conclusions

In this chapter, a brief review was given concerning the photodeposition of metal/metal oxide on the surface of semiconductors, especially TiO$_2$. Most researchers investigating photodeposition utilized low-intensity lamp as light source, whereas few focused on lasers to excite semiconductors. In many cases, the experimental sections often failed in giving all the necessary details to reproduce the experiments (UV lamp brand, power, the distance between lamp and sample etc.), so that experiments are not necessarily reproducible. This is why in this work we wanted to establish specific detailed setups based on a UV laser as a monochromatic source to perform the further investigations which are required to explore and establish the mechanisms behind the photodeposition of metal on semiconductors, to synthesize Janus nano-heterodimers and find the conditions when this system shifts from the dimer to the multi-dots. The aim thus inspires us to build this project to address these issues.

1.7 Bibliography

1.   Clark, W. C.; Vondjidis, A. G., An infrared study of the photocatalytic reaction between titanium dioxide and silver nitrate. *J. Catal.* **1965,** *4*, 691-696.

2.   Kraeutler, B.; Bard, A. J., Heterogeneous photocatalytic preparation of supported catalysts. Photodeposition of platinum on titanium dioxide powder and other substrates. *J. Am. Chem. Soc.* **1978,** *100*, 4317-4318.

3.   Cai, T.; Liu, Y.; Wang, L.; Zhang, S.; Ma, J.; Dong, W.; Zeng, Y.; Yuan, J.; Liu, C.; Luo, S., "Dark-deposition" of Ag nanoparticles on TiO$_2$：Improve electrons storage capacity to boost "Memory Catalysis" activity. *ACS Appl. Mater. Interfaces* **2018,** *10*, 25350-25359.

4.   Mi, S.-y.; Liu, Y.-x.; Wang, W.-d., Photo-depositing Ru and RuO$_2$ on Anatase TiO$_2$ Nanosheets as Co-catalysts for Photocatalytic O$_2$ Evolution from Water Oxidation. *Chin. J. Chem. Phys.* **2016,** *29*, 585-590.

5.   Grätzel, M., Photoelectrochemical cells. *Nature* **2001,** *414*, 338.

6.   Haynes, W. M.; Lide, D. R.; Bruno, T. J., *CRC handbook of chemistry and physics a ready-reference book of chemical and physical data*. 2016.

7.   Schneider, J.; Matsuoka, M.; Takeuchi, M.; Zhang, J.; Horiuchi, Y.; Anpo, M.; Bahnemann, D. W., Understanding TiO$_2$ Photocatalysis: Mechanisms and Materials. *Chem. Rev.* **2014,** *114*, 9919-9986.

8.   Li, J.; Wu, N., Semiconductor-based photocatalysts and photoelectrochemical cells for solar fuel generation: a review. *Catal. Sci. Technol.* **2015,** *5*, 1360-1384.

9.   Ma, Y.; Wang, X.; Jia, Y.; Chen, X.; Han, H.; Li, C., Titanium dioxide-based nanomaterials for photocatalytic fuel generations. *Chem. Rev.* **2014,** *114*, 9987-10043.

10.   Li, X.; Yu, J.; Jaroniec, M.; Chen, X., Cocatalysts for Selective Photoreduction of CO$_2$ into Solar Fuels. *Chem. Rev.* **2019,** *119*, 3962-4179.

11.   Bai, Y.; Mora-Sero, I.; De Angelis, F.; Bisquert, J.; Wang, P., Titanium dioxide nanomaterials for photovoltaic applications. *Chem. Rev.* **2014,** *114*, 10095-10130.

12.   Hai, Z.; Kolli, N. E.; Uribe, D. B.; Beaunier, P.; Jose-Yacaman, M.; Vigneron, J.; Etcheberry, A.; Sorgues, S.; Colbeau-Justin, C.; Chen, J.; Remita, H., Modification of TiO$_2$ by Bimetallic Au-Cu Nanoparticles for Wastewater Treatment. *J. Mater. Chem. A* **2013,** *1*, 10829-10835.

13.   Ayati, A.; Ahmadpour, A.; Bamoharram, F. F.; Tanhaei, B.; Mänttäri, M.; Sillanpää, M., A review on catalytic applications of Au/TiO$_2$ nanoparticles in the removal of water pollutant. *Chemosphere* **2014,** *107*, 163-174.

14.   Murcia, J. J.; Ávila-Martínez, E. G.; Rojas, H.; Navío, J. A.; Hidalgo, M. C., Study of the E. coli elimination from urban wastewater over photocatalysts based on metallized TiO$_2$. *Appl. Catal., B* **2017,** *200*, 469-476.

15.   Di Paola, A.; García-López, E.; Marcì, G.; Palmisano, L., A survey of photocatalytic materials for environmental remediation. *J. Hazard Mater.* **2012,** *211-212*, 3-29.

16.   Boyjoo, Y.; Sun, H.; Liu, J.; Pareek, V. K.; Wang, S., A review on photocatalysis for air treatment: From catalyst development to reactor design. *Chem. Eng. J.* **2017,** *310*, 537-559.

17.   Berr, M. J.; Wagner, P.; Fischbach, S.; Vaneski, A.; Schneider, J.; Susha, A. S.; Rogach, A. L.; Jäckel, F.; Feldmann, J., Hole scavenger redox potentials determine quantum efficiency and stability of Pt-decorated CdS nanorods for photocatalytic hydrogen generation. *Appl. Phys. Lett.* **2012,** *100*, 223903.

18.   Kozlova, E. A.; Lyubina, T. P.; Nasalevich, M. A.; Vorontsov, A. V.; Miller, A. V.; Kaichev, V. V.; Parmon, V. N., Influence of the method of platinum deposition on activity and stability of Pt/TiO$_2$ photocatalysts in the photocatalytic oxidation of dimethyl methylphosphonate. *Catal. Communi.* **2011,** *12*, 597-601.

19.   Li, C.; Zhang, S.; Zhang, B.; Su, D.; He, S.; Zhao, Y.; Liu, J.; Wang, F.; Wei, M.; Evans, D. G.; Duan, X., Photohole-oxidation-assisted anchoring of ultra-small Ru clusters onto TiO$_2$ with excellent catalytic activity and stability. *J. Mater. Chem. A* **2013,** *1*, 2461-2467.

20.   Wei, Z.; Rosa, L.; Wang, K.; Endo, M.; Juodkazis, S.; Ohtani, B.; Kowalska, E., Size-controlled gold nanoparticles on octahedral anatase particles as efficient plasmonic photocatalyst. *Appl. Catal., B* **2017,** *206*, 393-405.

21.   Guitoume, D.; Achour, S.; Sobti, N.; Boudissa, M.; Souami, N.; Messaoudi, Y., Structural, optical and photoelectrochemical properties of TiO$_2$ films decorated with plasmonic silver nanoparticles. *Optik* **2018,** *154*, 182-191.

22.   Zhang, N.; Liu, S.; Fu, X.; Xu, Y.-J., Synthesis of M@TiO$_2$ (M = Au, Pd, Pt) Core–Shell Nanocomposites with Tunable Photoreactivity. *J. Phys. Chem. C* **2011,** *115*, 9136-9145.

23.   Wu, X.-F.; Song, H.-Y.; Yoon, J.-M.; Yu, Y.-T.; Chen, Y.-F., Synthesis of Core–Shell Au@TiO$_2$ Nanoparticles with Truncated Wedge-Shaped Morphology and Their Photocatalytic Properties. *Langmuir* **2009,** *25*, 6438-6447.

24.   Miao, J.; Hu, W.; Jing, Y.; Luo, W.; Liao, L.; Pan, A.; Wu, S.; Cheng, J.; Chen, X.; Lu, W., Surface Plasmon-Enhanced Photodetection in Few Layer MoS$_2$ Phototransistors with Au Nanostructure Arrays. *Small* **2015,** *11*, 2392-2398.

25.   Bhanu, U.; Islam, M. R.; Tetard, L.; Khondaker, S. I., Photoluminescence quenching in gold - MoS$_2$ hybrid nanoflakes. *Sci. Rep.* **2014,** *4*, 5575.

26.   Fu, Y.-s.; Li, J.; Li, J., Metal/Semiconductor Nanocomposites for Photocatalysis: Fundamentals, Structures, Applications and Properties. *Nanomaterials* **2019,** *9*, 359-.

27.   Oros-Ruiz, S.; Pedraza-Avella, J. A.; Guzmán, C.; Quintana, M.; Moctezuma, E.; del Angel, G.; Gómez, R.; Pérez, E., Effect of Gold Particle Size and Deposition Method on the Photodegradation of 4-Chlorophenol by Au/TiO$_2$. *Top. Catal.* **2011,** *54*, 519-526.

28.   Kang, J.-G.; Sohn, Y., Interfacial nature of Ag nanoparticles supported on TiO$_2$ photocatalysts. *J. Mater. Sci.* **2012,** *47*, 824-832.

29.   Shoaib, A.; Ji, M.; Qian, H.; Liu, J.; Xu, M.; Zhang, J., Noble metal nanoclusters and their in situ calcination to nanocrystals: Precise control of their size and interface with TiO$_2$ nanosheets and their versatile catalysis applications. *Nano Res.* **2016,** *9*, 1763-1774.

30.   Ma, L. L.; Cui, Z. D.; Li, Z. Y.; Zhu, S. L.; Liang, Y. Q.; Yin, Q. W.; Yang, X. J., The fabrication of SnSe/Ag nanoparticles on TiO$_2$ nanotubes. *Mater. Sci. Eng., B* **2013,** *178*, 77-82.

31.   Chen, H.; Chen, S.; Quan, X.; Yu, H.; Zhao, H.; Zhang, Y., Fabrication of TiO$_2$–Pt Coaxial Nanotube Array Schottky Structures for Enhanced Photocatalytic Degradation of Phenol in Aqueous Solution. *J. Phys. Chem. C* **2008,** *112*, 9285-9290.

32.   Su, J.; Wei, Y.; Vayssieres, L., Stability and Performance of Sulfide-, Nitride-, and Phosphide-Based Electrodes for Photocatalytic Solar Water Splitting. *J. Phys. Chem. Lett.* **2017,** *8*, 5228-5238.

33.   Murata, A.; Oka, N.; Nakamura, S.; Shigesato, Y., Visible-Light Active Photocatalytic WO$_3$ Films Loaded with Pt Nanoparticles Deposited by Sputtering. *J. Nanosci. Nanotechnol.* **2012,** *12*, 5082-5086.

34.   Wenderich, K.; Mul, G., Methods, Mechanism, and Applications of Photodeposition in Photocatalysis: A Review. *Chem. Rev.* **2016,** *116*, 14587-14619.

35.   Mills, A.; Hill, G.; Stewart, M.; Graham, D.; Smith, W. E.; Hodgen, S.; Halfpenny, P. J.; Faulds, K.; Robertson, P., Characterization of Novel Ag on TiO$_2$ Films for Surface-Enhanced Raman Scattering. *Appl. Spectrosc.* **2004,** *58*, 922-928.

36.   Tian, Y.; Tatsuma, T., Mechanisms and Applications of Plasmon-Induced Charge Separation at TiO$_2$ Films Loaded with Gold Nanoparticles. *J. Am. Chem. Soc.* **2005,** *127*, 7632-7637.

37.   Jin, S.; Shiraishi, F., Photocatalytic activities enhanced for decompositions of organic compounds over metal-photodepositing titanium dioxide. *Chem. Eng. J.* **2004,** *97*, 203-211.

38.   Piwoński, I.; Kądzioła, K.; Kisielewska, A.; Soliwoda, K.; Wolszczak, M.; Lisowska, K.; Wrońska, N.; Felczak, A., The effect of the deposition parameters on size, distribution and antimicrobial properties of photoinduced silver nanoparticles on titania coatings. *Appl. Surf. Sci.* **2011,** *257*, 7076-7082.

39.   Albiter, E.; Valenzuela, M. A.; Alfaro, S.; Valverde-Aguilar, G.; Martínez-Pallares, F. M., Photocatalytic deposition of Ag nanoparticles on TiO$_2$: Metal precursor effect on the structural and photoactivity properties. *J. Saudi Chem. Soc.* **2015,** *19*, 563-573.

40.   Sofianou, M.-V.; Boukos, N.; Vaimakis, T.; Trapalis, C., Decoration of TiO$_2$ anatase nanoplates with silver nanoparticles on the {101} crystal facets and their photocatalytic behaviour. *Appl. Catal., B* **2014,** *158-159*, 91-95.

41.   Bansal, A.; Madhavi, S.; Tan, T. T. Y.; Lim, T. M., Effect of silver on the photocatalytic degradation of humic acid. *Catal. Today* **2008,** *131*, 250-254.

42.   Dinh, C.-T.; Nguyen, T.-D.; Kleitz, F.; Do, T.-O., A New Route to Size and Population Control of Silver Clusters on Colloidal TiO$_2$ Nanocrystals. *ACS Appl. Mater. Interfaces* **2011,** *3*, 2228-2234.

43.   Takai, A.; Kamat, P. V., Capture, Store, and Discharge. Shuttling Photogenerated Electrons across TiO$_2$–Silver Interface. *ACS Nano* **2011,** *5*, 7369-7376.

44.   Grabowska, E.; Zaleska, A.; Sorgues, S.; Kunst, M.; Etcheberry, A.; Colbeau-Justin, C.; Remita, H., Modification of Titanium(IV) Dioxide with Small Silver Nanoparticles: Application in Photocatalysis. *J. Phys. Chem. C* **2013,** *117*, 1955-1962.

45.   Espino-Estévez, M. R.; Fernández-Rodríguez, C.; González-Díaz, O. M.; Araña, J.; Espinós, J. P.; Ortega-Méndez, J. A.; Doña-Rodríguez, J. M., Effect of TiO$_2$-Pd and TiO$_2$-Ag on the photocatalytic oxidation of diclofenac, isoproturon and phenol. *Chem. Eng. J.* **2016,** *298*, 82-95.

46.   Melián, P. E.; Díaz, G. O.; Rodríguez, J. M.; Colón, G.; Navío, J. A.; Macías, M.; Peña, P. J., Effect of deposition of silver on structural characteristics and photoactivity of TiO$_2$-based photocatalysts. *Appl. Catal., B* **2012,** *127*, 112-120.

47.   Bems, B.; Jentoft, F. C.; Schlögl, R., Photoinduced decomposition of nitrate in drinking water in the presence of titania and humic acids. *Applied Catalysis B: Environmental* **1999,** *20*, 155-163.

48.   Pipelzadeh, E.; Babaluo, A. A.; Haghighi, M.; Tavakoli, A.; Derakhshan, M. V.; Behnami, A. K., Silver doping on TiO$_2$ nanoparticles using a sacrificial acid and its photocatalytic performance under medium pressure mercury UV lamp. *Chem. Eng. J.* **2009,** *155*, 660-665.

49.   Nishimoto, S.-I.; Ohtani, B.; Kajiwara, H.; Kagiya, T., Photoinduced oxygen formation and silver-metal deposition in aqueous solutions of various silver salts by suspended titanium dioxide powder. *J. Chem. Soc., Faraday Trans.* **1983,** *79*, 2685-2694.

50.   Ohtani, B.; Okugawa, Y.; Nishimoto, S.; Kagiya, T., Photocatalytic activity of titania powders suspended in aqueous silver nitrate solution: correlation with pH-dependent surface structures. *J. Phys. Chem.* **1987,** *91*, 3550-3555.

51.   Zhang, F.; Guan, N.; Li, Y.; Zhang, X.; Chen, J.; Zeng, H., Control of Morphology of Silver Clusters Coated on Titanium Dioxide during Photocatalysis. *Langmuir* **2003,** *19*, 8230-8234.

52.   Jiang, Z.; Ouyang, Q.; Peng, B.; Zhang, Y.; Zan, L., Ag size-dependent visible-light-responsive photoactivity of Ag-TiO$_2$ nanostructure based on surface plasmon resonance. *J. Mater. Chem. A* **2014,** *2*, 19861-19866.

53.   D'Arienzo, M.; Carbajo, J.; Bahamonde, A.; Crippa, M.; Polizzi, S.; Scotti, R.; Wahba, L.; Morazzoni, F., Photogenerated Defects in Shape-Controlled TiO$_2$ Anatase Nanocrystals: A Probe To Evaluate the Role of Crystal Facets in Photocatalytic Processes. *J. Am. Chem. Soc.* **2011,** *133*, 17652-17661.

54.   Kowalska, E.; Wei, Z.; Karabiyik, B.; Herissan, A.; Janczarek, M.; Endo, M.; Markowska-Szczupak, A.; Remita, H.; Ohtani, B., Silver-modified titania with enhanced photocatalytic and antimicrobial properties under UV and visible light irradiation. *Catal. Today* **2015,** *252*, 136-142.

55.   Lu, Q.; Lu, Z.; Lu, Y.; Lv, L.; Ning, Y.; Yu, H.; Hou, Y.; Yin, Y., Photocatalytic Synthesis and Photovoltaic Application of Ag-TiO$_2$ Nanorod Composites. *Nano Lett.* **2013,** *13*, 5698-5702.

56.   Herrmann, J.-M.; Disdier, J.; Pichat, P., Photocatalytic deposition of silver on powder titania: Consequences for the recovery of silver. *J. Catal.* **1988,** *113*, 72-81.

57.   Chan, S. C.; Barteau, M. A., Preparation of Highly Uniform Ag/TiO$_2$ and Au/TiO$_2$ Supported Nanoparticle Catalysts by Photodeposition. *Langmuir* **2005,** *21*, 5588-5595.

58.   Guo, T.-L.; Li, J.-G.; Ping, D.-H.; Sun, X.; Sakka, Y., Controlled Photocatalytic Growth of Ag Nanocrystals on Brookite and Rutile and Their SERS Performance. *ACS Appl. Mater. Interfaces* **2014,** *6*, 236-243.

59.   Melvin, A. A.; Illath, K.; Das, T.; Raja, T.; Bhattacharyya, S.; Gopinath, C. S., M-Au/TiO$_2$ (M=Ag, Pd, and Pt) nanophotocatalyst for overall solar water splitting: role of interfaces. *Nanoscale* **2015,** *7*, 13477-13488.

60.   Yang, D.; Sun, Y.; Tong, Z.; Tian, Y.; Li, Y.; Jiang, Z., Synthesis of Ag/TiO$_2$ Nanotube Heterojunction with Improved Visible-Light Photocatalytic Performance Inspired by Bioadhesion. *J. Phys. Chem. C* **2015,** *119*, 5827-5835.

61.   Ko, S.; Banerjee, C. K.; Sankar, J., Photochemical synthesis and photocatalytic activity in simulated solar light of nanosized Ag doped TiO$_2$ nanoparticle composite. *Composites Part B* **2011,** *42*, 579-583.

35

62. Sano, T.; Negishi, N.; Mas, D.; Takeuchi, K., Photocatalytic Decomposition of N_2O on Highly Dispersed Ag^+ Ions on TiO₂ Prepared by Photodeposition. *J. Catal.* **2000,** *194*, 71-79.

63. Sclafani, A.; Mozzanega, M.-N.; Pichat, P., Effect of silver deposits on the photocatalytic activity of titanium dioxide samples for the dehydrogenation or oxidation of 2-propanol. *J. Photochem. Photobiol., A* **1991,** *59*, 181-189.

64. Gärtner, F.; Losse, S.; Boddien, A.; Pohl, M.-M.; Denurra, S.; Junge, H.; Beller, M., Hydrogen Evolution from Water/Alcohol Mixtures: Effective In Situ Generation of an Active Au/TiO₂ catalyst. *Chem. Sus. Chem* **2012,** *5*, 530-533.

65. Sangeetha, P.; Chang, L.-H.; Chen, Y.-W., Preferential Oxidation of CO in H_2 Stream on Au/TiO₂ Catalysts: Effect of Preparation Method. *Ind. Eng. Chem. Res.* **2009,** *48*, 5666-5670.

66. Kenens, B.; Chamtouri, M.; Aubert, R.; Miyakawa, K.; Hayasaka, Y.; Naiki, H.; Watanabe, H.; Inose, T.; Fujita, Y.; Lu, G.; Masuhara, A.; Uji-i, H., Solvent-induced improvement of Au photo-deposition and resulting photo-catalytic efficiency of Au/TiO₂. *RSC Adv.* **2016,** *6*, 97464-97468.

67. Yang, Y.-F.; Sangeetha, P.; Chen, Y.-W., Au/TiO₂ catalysts prepared by photo-deposition method for selective CO oxidation in H_2 stream. *Int. J. Hydrogen Energy* **2009,** *34*, 8912-8920.

68. Bamwenda, G. R.; Tsubota, S.; Nakamura, T.; Haruta, M., Photoassisted hydrogen production from a water-ethanol solution: a comparison of activities of Au-TiO₂ and Pt-TiO₂. *J. Photochem. Photobiol., A* **1995,** *89*, 177-189.

69. Wang, D.; Bi, Q.; Yin, G.; Wang, P.; Huang, F.; Xie, X.; Jiang, M., Photochemical Preparation of Anatase Titania Supported Gold Catalyst for Ethanol Synthesis from CO_2 Hydrogenation. *Catal. Lett.* **2018,** *148*, 11-22.

70. Deepagan, V. G.; You, D. G.; Um, W.; Ko, H.; Kwon, S.; Choi, K. Y.; Yi, G.-R.; Lee, J. Y.; Lee, D. S.; Kim, K.; Kwon, I. C.; Park, J. H., Long-Circulating Au-TiO₂ Nanocomposite as a Sonosensitizer for ROS-Mediated Eradication of Cancer. *Nano Lett.* **2016,** *16*, 6257-6264.

71. Yan, J.; Wu, G.; Guan, N.; Li, L., Synergetic promotion of the photocatalytic activity of TiO₂ by gold deposition under UV-visible light irradiation. *Chem. Commun.* **2013,** *49*, 11767-11769.

72. Sato, Y.; Naya, S. I.; Tada, H., A new bimetallic plasmonic photocatalyst consisting of gold(core)-copper(shell) nanoparticle and titanium(IV) oxide support. *APL Mater.* **2015,** *3*, 104502.

73. Dobosz, A.; Sobczyński, A., Water detoxification: Photocatalytic decomposition of phenol on Au/TiO₂. *Monatsh. Chem.* **2001,** *132*, 1037-1045.

74. Tong, R.; Liu, C.; Xu, Z.; Kuang, Q.; Xie, Z.; Zheng, L., Efficiently Enhancing Visible Light Photocatalytic Activity of Faceted TiO₂ Nanocrystals by Synergistic Effects of Core-Shell Structured Au@CdS Nanoparticles and Their Selective Deposition. *ACS Appl. Mater. Interfaces* **2016,** *8*, 21326-21333.

75. Hidalgo, M. C.; Murcia, J. J.; Navío, J. A.; Colón, G., Photodeposition of gold on titanium dioxide for photocatalytic phenol oxidation. *Appl. Catal., A* **2011,** *397*, 112-120.

76. Hippargi, G.; Maddigapu, P. R.; Labhsetwar, N.; Rayalu, S., Titania Gold Composite: Effect of Illumination on Size of Gold Nanoparticles with Consequent Implication on Photocatalytic Water Splitting. *Russ. J. Phys. Chem. B* **2017,** *11*, 1002-1011.

77. Kelly, J. J.; Vondeling, J. K., The Nucleation Reaction on Photosensitive TiO₂ Films. *J. Electrochem. Soc.* **1975,** *122*, 1103-1107.

78. Mori, K.; Araki, T.; Takasaki, T.; Shironita, S.; Yamashita, H., A new application of photocatalysts: synthesis of nano-sized metal and alloy catalysts by a photo-assisted deposition method. *Photochem. Photobiol. Sci.* **2009,** *8*, 652-656.

79. Hippargi, G.; Mangrulkar, P.; Chilkalwar, A.; Labhsetwar, N.; Rayalu, S., Chloride ion: A promising hole scavenger for photocatalytic hydrogen generation. *Int. J. Hydrogen Energy* **2018,** *43*, 6815-6823.

80. Fan, Q.; He, S.; Hao, L.; Liu, X.; Zhu, Y.; Xu, S.; Zhang, F., Photodeposited Pd Nanoparticles with Disordered Structure for Phenylacetylene Semihydrogenation. *Sci. Rep.* **2017,** *7*, 42172.

81. Leong, K. H.; Chu, H. Y.; Ibrahim, S.; Saravanan, P., Palladium nanoparticles anchored to anatase TiO₂ for enhanced surface plasmon resonance-stimulated, visible-light-driven photocatalytic activity. *Beilstein J. Nanotechnol.* **2015,** *6*, 428-437.

82. Jones, W.; Martin, D. J.; Caravaca, A.; Beale, A. M.; Bowker, M.; Maschmeyer, T.; Hartley, G.; Masters, A., A comparison of photocatalytic reforming reactions of methanol and triethanolamine with

36

Pd supported on titania and graphitic carbon nitride. *Appl. Catal., B* **2019,** *240*, 373-379.

83. Dadsetan, S.; Baghshahi, S.; Hadavi, S. M. M., Photodeposition of Pd nanoparticles on TiO$_2$ using sacrificial organic alcohols. *J. Aust. Ceram. Soc.* **2018,** *54*, 383-388.

84. Kriek, R. J.; Mahlamvana, F., Dependency on chloride concentration and 'in-sphere' oxidation of H$_2$O for the effective TiO$_2$-photocatalysed electron transfer from H$_2$O to [PdCl$_n$(H$_2$O)$_{4-n}$]$^{2-n}$ (n=0–4) in the absence of an added sacrificial reducing agent. *Appl. Catal., A* **2012,** *423-424*, 28-33.

85. Borgarello, E.; Serpone, N.; Emo, G.; Harris, R.; Pelizzetti, E.; Minero, C., Light-induced reduction of rhodium(III) and palladium(II) on titanium dioxide dispersions and the selective photochemical separation and recovery of gold(III), platinum(IV), and rhodium(III) in chloride media. *Inorg. Chem.* **1986,** *25*, 4499-4503.

86. Fernández, A.; González-Elipe, A. R., "In situ" XPS study of the photoassisted reduction of noble-metal cations on TiO$_2$. *Appl. Surf. Sci.* **1993,** *69*, 285-289.

87. Jacobs, J. W. M., Photochemical nucleation and growth of palladium on titanium dioxide films studied with electron microscopy and quantitative analytical techniques. *J. Phys. Chem.* **1986,** *90*, 6507-6517.

88. Jacobs, J. W. M.; Verhoeven, J. F. C. M., Specimen preparation technique for high resolution transmission electron microscopy studies on model supported metal catalysts. *J. Microsc.* **1986,** *143*, 103-116.

89. Dadsetan, S.; Baghshahi, S.; Farshidfar, F.; Hadavi, S. M. M., Photodeposition of Pd nanoparticles on TiO$_2$ utilizing a channel type quartz reactor. *Ceram. Int.* **2017,** *43*, 9322-9326.

90. Jacobs, J. W. M., Copper Photodeposition on TiO$_2$ Studied with HREM and EXAFS. *J. Electrochem. Soc.* **1989,** *136*.

91. Foster, N. S.; Lancaster, A. N.; Noble, R. D.; Koval, C. A., Effect of Organics on the Photodeposition of Copper in Titanium Dioxide Aqueous Suspensions. *Ind. Eng. Chem. Res.* **1995,** *34*, 3865-3871.

92. Kazuma, E.; Yamaguchi, T.; Sakai, N.; Tatsuma, T., Growth behaviour and plasmon resonance properties of photocatalytically deposited Cu nanoparticles. *Nanoscale* **2011,** *3*, 3641-3645.

93. Wu, G.; Guan, N.; Li, L., Low temperature CO oxidation on Cu–Cu$_2$O/TiO$_2$ catalyst prepared by photodeposition. *Catal. Sci. Technol.* **2011,** *1*, 601-608.

94. Lennox, A. J. J.; Bartels, P.; Pohl, M.-M.; Junge, H.; Beller, M., In situ photodeposition of copper nanoparticles on TiO$_2$: Novel catalysts with facile light-induced redox cycling. *J. Catal.* **2016,** *340*, 177-183.

95. Morishita, S.; Suzuki, K.-i., Photoelectrochemical Deposition of Nickel onto TiO$_2$ Particles. Formation of Nickel Patterns without Resists. *Bull. Chem. Soc. Jpn.* **1994,** *67*, 843-846.

96. Lin, W.-Y., Photocatalytic Removal of Nickel from Aqueous Solutions Using Ultraviolet-Irradiated TiO$_2$. *J. Electrochem. Soc.* **1997,** *144*, 2751.

97. Giuffrida, S.; Condorelli, G. G.; Costanzo, L. L.; Ventimiglia, G.; Nigro, R. L.; Favazza, M.; Votrico, E.; Bongiorno, C.; Fragalà, I. L., Nickel nanostructured materials from liquid phase photodeposition. *J. Nanopart. Res.* **2006,** *9*, 611-619.

98. Rodríguez, J. L.; Valenzuela, M. A.; Pola, F.; Tiznado, H.; Poznyak, T., Photodeposition of Ni nanoparticles on TiO$_2$ and their application in the catalytic ozonation of 2,4-dichlorophenoxyacetic acid. *J. Mol. Catal. A: Chem.* **2012,** *353-354*, 29-36.

99. Dozzi, M. V.; Saccomanni, A.; Selli, E., Cr(VI) photocatalytic reduction: Effects of simultaneous organics oxidation and of gold nanoparticles photodeposition on TiO$_2$. *J. Hazard Mater.* **2012,** *211-212*, 188-195.

100. Wang, F.; Zhang, S.; Li, C.; Liu, J.; He, S.; Zhao, Y.; Yan, H.; Wei, M.; Evans, D. G.; Duan, X., Catalytic behavior of supported Ru nanoparticles on the (101) and (001) facets of anatase TiO$_2$. *RSC Adv.* **2014,** *4*, 10834-10840.

101. Wojciechowska, J.; Gitzhofer, E.; Grams, J.; Ruppert, A. M.; Keller, N., Light-driven synthesis of sub-nanometric metallic Ru catalysts on TiO2. *Catalysis Today* **2018**.

102. Ohno, T.; Sarukawa, K.; Matsumura, M., Crystal faces of rutile and anatase TiO$_2$ particles and their roles in photocatalytic reactions. *New J. Chem.* **2002,** *26*, 1167-1170.

103. Uddin, M. T.; Babot, O.; Thomas, L.; Olivier, C.; Redaelli, M.; D'Arienzo, M.; Morazzoni, F.;

37

Jaegermann, W.; Rockstroh, N.; Junge, H.; Toupance, T., New Insights into the Photocatalytic Properties of RuO$_2$/TiO$_2$ Mesoporous Heterostructures for Hydrogen Production and Organic Pollutant Photodecomposition. *J. Phys. Chem. C* **2015**, *119*, 7006-7015.

104. Wang, T.; Jiang, Z.; Chu, K. H.; Wu, D.; Wang, B.; Sun, H.; Yip, H. Y.; An, T.; Zhao, H.; Wong, P. K., X‐Shaped α‐FeOOH with Enhanced Charge Separation for Visible‐Light‐Driven Photocatalytic Overall Water Splitting. *Chem. Sus. Chem* **2018**, *11*, 1365-1373.

105. Tada, H.; Suzuki, F.; Ito, S.; Akita, T.; Tanaka, K.; Kawahara, T.; Kobayashi, H., Au-Core/Pt-Shell Bimetallic Cluster-Loaded TiO$_2$. 1. Adsorption of Organosulfur Compound. *J. Phys. Chem. B* **2002**, *106*, 8714-8720.

106. Jones, W.; Su, R.; Wells, P. P.; Shen, Y.; Dimitratos, N.; Bowker, M.; Morgan, D.; Iversen, B. B.; Chutia, A.; Besenbacher, F.; Hutchings, G., Optimised photocatalytic hydrogen production using core-shell AuPd promoters with controlled shell thickness. *Phys. Chem. Chem. Phys.* **2014**, *16*, 26638-26644.

107. Naya, S. I.; Miki, S.; Yamauchi, J.; Teranishi, M.; Kobayashi, H.; Tada, H., Au (Core)-Pt (Shell) Nanocatalysts with the Shell Thickness Controlled at a Monolayer Level: Extremely High Activity for Hydrogen Peroxide Decomposition. *J. Phys. Chem. C* **2018**, *122*, 22953-22958.

108. Kuladeep, R.; Jyothi, L.; Alee, K. S.; Deepak, K. L. N.; Rao, D. N., Laser-assisted synthesis of Au-Ag alloy nanoparticles with tunable surface plasmon resonance frequency. *Opt. Mater. Express* **2012**, *2*, 161.

109. Ren, S.; Liu, W., One-step photochemical deposition of PdAu alloyed nanoparticles on TiO$_2$ nanowires for ultra-sensitive H$_2$ detection. *J. Mater. Chem. A* **2016**, *4*, 2236-2245.

110. Chen, Q.; Chen, X.; Fang, M.; Chen, J.; Li, Y.; Xie, Z.; Kuang, Q.; Zheng, L., Photo-induced Au-Pd alloying at TiO$_2$ {101} facets enables robust CO$_2$ photocatalytic reduction into hydrocarbon fuels. *J. Mater. Chem. A* **2019**, *7*, 1334-1340.

111. Zhang, X. F.; Wang, Z.; Zhong, Y.; Qiu, J.; Zhang, X.; Gao, Y.; Gu, X.; Yao, J., TiO$_2$ nanorods loaded with Au–Pt alloy nanoparticles for the photocatalytic oxidation of benzyl alcohol. *J. Phys. Chem. Solids* **2019**, *126*, 27-32.

112. Chanmanee, W.; de Tacconi, N. R.; Rajeshwar, K.; Lin, W.-Y.; Nikiel, L.; Wampler, W. A., Photocatalytically Generated Trimetallic (Pt-Pd-Au/C-TiO$_2$) Nanocomposite Electrocatalyst. *J. Electrochem. Soc.* **2012**, *159*, F226-F233.

113. Zaleska-Medynska, A.; Marchelek, M.; Diak, M.; Grabowska, E., Noble metal-based bimetallic nanoparticles: the effect of the structure on the optical, catalytic and photocatalytic properties. *Adv. Colloid Interface Sci.* **2016**, *229*, 80-107.

114. Huang, Q.; Liu, S.; Wei, W.; Yan, Q.; Wu, C., Selective synthesis of different ZnO/Ag nanocomposites as surface enhanced Raman scattering substrates and highly efficient photocatalytic catalysts. *RSC Adv.* **2015**, *5*, 27075-27081.

115. Liu, Y.; Wei, S.; Gao, W., Ag/ZnO heterostructures and their photocatalytic activity under visible light: Effect of reducing medium. *J. Hazard Mater.* **2015**, *287*, 59-68.

116. Li, R.; Han, C.; Chen, Q.-W., A facile synthesis of multifunctional ZnO/Ag sea urchin-like hybrids as highly sensitive substrates for surface-enhanced Raman detection. *RSC Adv.* **2013**, *3*, 11715-11722.

117. Lin, C.-Y.; Lai, Y.-H.; Balamurugan, A.; Vittal, R.; Lin, C.-W.; Ho, K.-C., Electrode modified with a composite film of ZnO nanorods and Ag nanoparticles as a sensor for hydrogen peroxide. *Talanta* **2010**, *82*, 340-347.

118. Xie, W.; Li, Y.; Sun, W.; Huang, J.; Xie, H.; Zhao, X., Surface modification of ZnO with Ag improves its photocatalytic efficiency and photostability. *J. Photochem. Photobiol., A* **2010**, *216*, 149-155.

119. Kislov, N.; Lahiri, J.; Verma, H.; Goswami, D. Y.; Stefanakos, E.; Batzill, M., Photocatalytic Degradation of Methyl Orange over Single Crystalline ZnO: Orientation Dependence of Photoactivity and Photostability of ZnO. *Langmuir* **2009**, *25*, 3310-3315.

120. Wu, J.-J.; Tseng, C.-H., Photocatalytic properties of nc-Au/ZnO nanorod composites. *Appl. Catal., B* **2006**, *66*, 51-57.

121. Wang, T.; Jin, B.; Jiao, Z.; Lu, G.; Ye, J.; Bi, Y., Electric field-directed growth and photoelectrochemical properties of cross-linked Au-ZnO hetero-nanowire arrays. *Chem. Commun.* **2015**, *51*, 2103-2106.

122. Yuyang, S.; Long, J.; Tian, Z.; Jin, W.; Ling, L.; Yong, J.; Zhifeng, J.; Xiaosong, S., Synthesis of Au–ZnO

hybrid nanostructure arrays and their enhanced photocatalytic activity. *New J. Chem.* **2015**, *39*, 2943-2948.

123. Fernando, J. F.; Shortell, M. P.; Noble, C. J.; Harmer, J. R.; Jaatinen, E. A.; Waclawik, E. R., Controlling Au Photodeposition on Large ZnO Nanoparticles. *ACS Appl. Mater. Interfaces* **2016,** *8*, 14271-14283.

124. Du, L.; Qian, K.; Zhu, X.; Yan, X.; Kobayashi, H.; Liu, Z.; Lou, Y.; Li, R., Interface engineering of palladium and zinc oxide nanorods with strong metal–support interactions for enhanced hydrogen production from base-free formaldehyde solution. *J. Mater. Chem. A* **2019**, *7*, 8855-8864.

125. Liqiang, J.; Baiqi, W.; Baifu, X.; Shudan, L.; Keying, S.; Weimin, C.; Honggang, F., Investigations on the surface modification of ZnO nanoparticle photocatalyst by depositing Pd. *J. Solid State Chem.* **2004**, *177*, 4221-4227.

126. Jin, Y.; Xi, J.; Zhang, Z.; Xiao, J.; Xiao, F.; Qian, L.; Wang, S., An ultra-low Pd loading nanocatalyst with efficient catalytic activity. *Nanoscale* **2015**, *7*, 5510-5515.

127. Kozytskiy, A. V.; Stroyuk, A. L.; Kuchmy, S. Y.; Streltsov, E. A.; Skorik, N. A.; Moskalyuk, V. O., Effect of the Method of Preparation of ZnO/CdS and TiO₂/CdS Film Nanoheterostructures on Their Photoelectrochemical Properties. *Theor. Exp. Chem.* **2013**, *49*, 165-171.

128. Shvalagin, V. V.; Stroyuk, A. L.; Kotenko, I. E.; Kuchmii, S. Y., Photocatalytic formation of porous CdS/ZnO nanospheres and CdS nanotubes. *Theor. Exp. Chem.* **2007,** *43*, 229-234.

129. Lu, L.; Hu, S.; Lee, H.-I.; Wöll, C.; Fischer, R. A., Photoinduced growth of Cu nanoparticles on ZnO from CuCl₂ in methanol. *J. Nanopart. Res.* **2007,** *9*, 491-496.

130. Lu, L.; Wohlfart, A.; Parala, H.; Birkner, A.; Fischer, R. A., A novel preparation of nano-Cu/ZnO by photo-reduction of Cu(OCH(Me)CH₂NMe₂)₂ on ZnO at room temperature. *Chem. Commun.* **2003**, 40-41.

131. Gomathisankar, P.; Hachisuka, K.; Katsumata, H.; Suzuki, T.; Funasaka, K.; Kaneco, S., Enhanced photocatalytic hydrogen production from aqueous methanol solution using ZnO with simultaneous photodeposition of Cu. *Int. J. Hydrogen Energy* **2013**, *38*, 11840-11846.

132. Sliem, M. A.; Hikov, T.; Li, Z. A.; Spasova, M.; Farle, M.; Schmidt, D. A.; Havenith-Newen, M.; Fischer, R. A., Interfacial Cu/ZnO contact by selective photodeposition of copper onto the surface of small ZnO nanoparticles in non-aqueous colloidal solution. *Phys. Chem. Chem. Phys.* **2010**, *12*, 9858-9866.

133. Carabineiro, S. A. C.; Machado, B. F.; Dražić, G.; Bacsa, R. R.; Serp, P.; Figueiredo, J. L.; Faria, J. L., Photodeposition of Au and Pt on ZnO and TiO₂. In *Stud. Surf. Sci. Catal.*, 2010; Vol. 175, pp 629-633.

134. Jaramillo-Páez, C. A.; Navío, J. A.; Hidalgo, M. C.; Macías, M., ZnO and Pt-ZnO photocatalysts: Characterization and photocatalytic activity assessing by means of three substrates. *Catal. Today* **2018**, *313*, 12-19.

135. Shirzad Siboni, M.; Samadi, M. T.; Yang, J. K.; Lee, S. M., Photocatalytic reduction of Cr(VI) and Ni(II) in aqueous solution by synthesized nanoparticle ZnO under ultraviolet light irradiation: a kinetic study. *Environmental Technology* **2011**, *32*, 1573-1579.

136. Yu, H.; Xie, Y.; Xu, D.; Xiang, M.; Diao, P., Preparation and photoelectrochemical water oxidation properties of ZnO/Ni-Bᵢ composite photoanodes. *Acta Aeronaut. Astronaut. Sinica* **2014**, *35*, 2865-2872.

137. Dulnee, S.; Luengnaruemitchai, A.; Wanchanthuek, R., Activity of Au/ZnO catalysts prepared by photo-deposition for the preferential CO oxidation in a H₂-rich gas. *Int. J. Hydrogen Energy* **2014**, *39*, 6443-6453.

138. Carabineiro, S. A. C.; Machado, B. F.; Bacsa, R. R.; Serp, P.; Dražić, G.; Faria, J. L.; Figueiredo, J. L., Catalytic performance of Au/ZnO nanocatalysts for CO oxidation. *J. Catal.* **2010**, *273*, 191-198.

139. Naknam, P.; Luengnaruemitchai, A.; Wongkasemjit, S., Preferential CO oxidation over Au/ZnO and Au/ZnO–Fe₂O₃ catalysts prepared by photodeposition. *Int. J. Hydrogen Energy* **2009**, *34*, 9838-9846.

140. He, W.; Kim, H.-K.; Wamer, W. G.; Melka, D.; Callahan, J. H.; Yin, J.-J., Photogenerated Charge Carriers and Reactive Oxygen Species in ZnO/Au Hybrid Nanostructures with Enhanced Photocatalytic and Antibacterial Activity. *J. Am. Chem. Soc.* **2014**, *136*, 750-757.

141. Chang, C.-M.; Hon, M.-H.; Leu, I.-C., Outstanding H₂ Sensing Performance of Pd Nanoparticle-Decorated ZnO Nanorod Arrays and the Temperature-Dependent Sensing Mechanisms. *ACS Appl. Mater. Interfaces* **2013**, *5*, 135-143.

142. Ding, J.; Zhu, J.; Yao, P.; Li, J.; Bi, H.; Wang, X., Synthesis of ZnO–Ag Hybrids and Their Gas-Sensing Performance toward Ethanol. *Ind. Eng. Chem. Res.* **2015**, *54*, 8947-8953.

143. Chang, C.-M.; Hon, M.-H.; Leu, I.-C., Improvement in CO sensing characteristics by decorating ZnO nanorod arrays with Pd nanoparticles and the related mechanisms. *RSC Adv.* **2012,** *2*, 2469-2475.

144. Zheng, H.; Ou, J. Z.; Strano, M. S.; Kaner, R. B.; Mitchell, A.; Kalantar-zadeh, K., Nanostructured Tungsten Oxide – Properties, Synthesis, and Applications. *Adv. Funct. Mater.* **2011,** *21*, 2175-2196.

145. Huang, Z. F.; Song, J.; Pan, L.; Zhang, X.; Wang, L.; Zou, J. J., Tungsten oxides for photocatalysis, electrochemistry, and phototherapy. *Adv. Mater.* **2015,** *27*, 5309.

146. Kim, J.; Lee, C. W.; Choi, W., Platinized WO$_3$ as an environmental photocatalyst that generates OH radicals under visible light. *Environ. Sci. Technol.* **2010,** *44*, 6849.

147. Arai, T.; Yanagida, M.; Konishi, Y.; Ikura, A.; Iwasaki, Y.; Sugihara, H.; Sayama, K., The enhancement of WO$_3$-catalyzed photodegradation of organic substances utilizing the redox cycle of copper ions. *Appl. Catal., B* **2008,** *84*, 42.

148. Joshi, U. A.; Darwent, J. R.; Yiu, H. H. P.; Rosseinsky, M. J., The effect of platinum on the performance of WO$_3$ nanocrystal photocatalysts for the oxidation of Methyl Orange and iso-propanol. *J. Chem. Technol. Biotechnol.* **2011,** *86*, 1018.

149. Wicaksana, Y.; Liu, S.; Scott, J.; Amal, R., Tungsten trioxide as a visible light photocatalyst for volatile organic carbon removal. *Molecules* **2014,** *19*, 17747.

150. Arai, T.; Horiguchi, M.; Yanagida, M.; Gunji, T.; Sugihara, H.; Sayama, K., Complete oxidation of acetaldehyde and toluene over a Pd/WO$_3$ photocatalyst under fluorescent- or visible-light irradiation. *Chem. Commun.* **2008,** 5565.

151. Sayama, K.; Mukasa, K.; Abe, R.; Abe, Y.; Arakawa, H., A new photocatalytic water splitting system under visible light irradiation mimicking a Z-scheme mechanism in photosynthesis. *J. Photochem. Photobiol., A* **2002,** *148*, 71.

152. Abe, R.; Higashi, M.; Domen, K., Overall water splitting under visible light through a two-step photoexcitation between TaON and WO$_3$ in the presence of an iodate-iodide shuttle redox mediator. *Chem. Sus. Chem* **2011,** *4*, 228.

153. Gunji, T.; Tsuda, T.; Jeevagan, A. J.; Hashimoto, M.; Tanabe, T.; Kaneko, S.; Miyauchi, M.; Saravanan, G.; Abe, H.; Matsumoto, F., Visible light induced decomposition of organic compounds on WO$_3$ loaded PtPb co-catalysts. *Catal. Communi.* **2014,** *56*, 96-100.

154. Gunji, T.; Jeevagan, A. J.; Hashimoto, M.; Nozawa, T.; Tanabe, T.; Kaneko, S.; Miyauchi, M.; Matsumoto, F., Photocatalytic decomposition of various organic compounds over WO$_3$-supported ordered intermetallic PtPb co-catalysts. *Appl. Catal., B* **2016,** *181*, 475.

155. Shiraishi, Y.; Sugano, Y.; Ichikawa, S.; Hirai, T., Visible light-induced partial oxidation of cyclohexane on WO$_3$ loaded with Pt nanoparticles. *Catal. Sci. Technol.* **2012,** *2*, 400.

156. Huang, Z.; Miseki, Y.; Sayama, K., Solar-light-driven photocatalytic production of peroxydisulfate over noble-metal loaded WO$_3$. *Chem. Commun.* **2019,** *55*, 3813-3816.

157. Kalanur, S. S.; Heo, J.; Yoo, I.-H.; Seo, H., 2-D WO$_3$ decorated with Pd for rapid gasochromic and electrical hydrogen sensing. *Int. J. Hydrogen Energy* **2017,** *42*, 16901-16908.

158. Shibuya, M.; Miyauchi, M., Site-selective deposition of metal nanoparticles on aligned WO$_3$ nanotrees for super-hydrophilic thin films. *Adv. Mater.* **2009,** *21*, 1373.

159. Sakai, Y.; Shimanaka, A.; Shioi, M.; Kato, S.; Satokawa, S.; Kojima, T.; Yamasaki, A., Fabrication of high-sensitivity palladium loaded tungsten trioxide photocatalyst by photodeposite method. *Catal. Today* **2015,** *241*, 2.

160. Katsumata, H.; Oda, Y.; Kaneco, S.; Suzuki, T., Photocatalytic activity of Ag/CuO/WO$_3$ under visible-light irradiation. *RSC Adv.* **2013,** *3*, 5028.

161. Sun, S.; Wang, W.; Zeng, S.; Shang, M.; Zhang, L., Preparation of ordered mesoporous Ag/WO$_3$ and its highly efficient degradation of acetaldehyde under visible-light irradiation. *J. Hazard Mater.* **2010,** *178*, 427.

162. Qamar, M.; Yamani, Z. H.; Gondal, M. A.; Alhooshani, K., Synthesis and comparative photocatalytic activity of Pt/WO$_3$ and Au/WO$_3$ nanocomposites under sunlight-type excitation. *Solid State Sci.* **2011,** *13*, 1748.

163. Karácsonyi, É.; Baia, L.; Dombi, A.; Danciu, V.; Mogyorósi, K.; Pop, L. C.; Kovács, G.; Coşoveanu, V.; Vulpoi, A.; Simon, S.; Pap, Z., The photocatalytic activity of TiO$_2$/WO$_3$/noble metal (Au or Pt)

nanoarchitectures obtained by selective photodeposition. *Catal. Today* **2013,** *208*, 19-27.

164. Xin, G.; Yu, B.; Xia, Y.; Hu, T.; Liu, L.; Li, C., Highly efficient deposition method of platinum over CdS for H$_2$ evolution under visible light. *J. Phys. Chem. C* **2014,** *118*, 21928.

165. Yu, J.; Yu, Y.; Cheng, B., Enhanced visible-light photocatalytic H$_2$-production performance of multi-armed CdS nanorods. *RSC Adv.* **2012,** *2*, 11829.

166. Dukovic, G.; Merkle, M. G.; Nelson, J. H.; Hughes, S. M.; Alivisatos, A. P., Photodeposition of Pt on Colloidal CdS and CdSe/CdS Semiconductor Nanostructures. *Adv. Mater.* **2008,** *20*, 4306-4311.

167. Wang, Y.; Wang, Y.; Xu, R., Photochemical deposition of Pt on CdS for H$_2$ evolution from water: Markedly enhanced activity by controlling Pt reduction environment. *J. Phys. Chem. C* **2013,** *117*, 783.

168. Muruganandham, M.; Kusumoto, Y.; Okamoto, C.; Muruganandham, A.; Abdulla-Al-Mamun, M.; Ahmmad, B., Mineralizer-assisted shape-controlled synthesis, characterization, and photocatalytic evaluation of CdS microcrystals. *J. Phys. Chem. C* **2009,** *113*, 19506.

169. Bao, N.; Shen, L.; Takata, T.; Domen, K., Self-templated synthesis of nanoporous CdS nanostructures for highly efficient photocatalytic hydrogen production under visible light. *Chem. Mater.* **2008,** *20*, 110.

170. Li, Y.; Tang, L.; Peng, S.; Li, Z.; Lu, G., Phosphate-assisted hydrothermal synthesis of hexagonal CdS for efficient photocatalytic hydrogen evolution. *Cryst. Eng. Comm.* **2012,** *14*, 6974.

171. Carbone, L.; Jakab, A.; Khalavka, Y.; Sönnichsen, C., Light-controlled one-sided growth of large plasmonic gold domains on quantum rods observed on the single particle level. *Nano Lett.* **2009,** *9*, 3710.

172. Menagen, G.; Macdonald, J. E.; Shemesh, Y.; Popov, I.; Banin, U., Au Growth on Semiconductor Nanorods: Photoinduced versus Thermal Growth Mechanisms. *J. Am. Chem. Soc.* **2009,** *131*, 17406-17411.

173. Singh, R.; Pal, B., Influence of Au photodeposition and doping in CdS nanorods: Optical and photocatalytic study. *Part. Sci. Technol.* **2015,** *33*, 53.

174. Rufus, I. B.; Ramakrishnan, V.; Viswanathan, B.; Kuriacose, J. C., Surface analysis of Rh/CdS. *Journal of Materials Science Letters* **1995,** *14*, 15-18.

175. Borgarello, E.; Serpone, N.; Pelizzetti, E.; Barbeni, M., Efficient photochemical conversion of aqueous sulphides and sulphites to hydrogen using a rhodium-loaded CdS photocatalyst. *J. Photochem.* **1986,** *33*, 35-48.

176. Quiroz-Cardoso, O.; Oros-Ruiz, S.; Solís-Gómez, A.; López, R.; Gómez, R., Enhanced photocatalytic hydrogen production by CdS nanofibers modified with graphene oxide and nickel nanoparticles under visible light. *Fuel* **2019,** *237*, 227-235.

177. Oros-Ruiz, S.; Hernández-Gordillo, A.; García-Mendoza, C.; Rodríguez-Rodríguez, A. A.; Gómez, R., Comparative activity of CdS nanofibers superficially modified by Au, Cu, and Ni nanoparticles as co-catalysts for photocatalytic hydrogen production under visible light. *J. Chem. Technol. Biotechnol.* **2016,** *91*, 2205-2210.

178. Kochev, S. Y.; Bubnov, Y. N.; Abramchuk, S. S.; Antonova, O. Y.; Valetsky, P. M.; Kabachii, Y. A., Photocatalytic activity of CdS nanocrystals doped with Ni and stabilized by polymer shell. *Mendeleev Commun.* **2017,** *27*, 310-312.

179. Rufus, I. B.; Ramakrishnan, V.; Viswanathan, B.; Kuriacose, J. C., Rhodium and rhodium sulfide coated cadmium sulfide as a photocatalyst for photochemical decomposition of aqueous sulfide. *Langmuir* **1990,** *6*, 565.

180. Rufus, B. I.; Ramakrishnan, V.; Viswanathan, B.; Kuriacose, J. C., Photoelectrochemical and photo-catalytic studies on Pd/CdS. *Indian J.Technol.* **1989,** *27*, 171-173.

181. Jacobs, J. W. M.; Schryvers, D., A high-resolution electron microscopy study of photodeposited Pd particles on TiO$_2$ and their oxidation in air. *J. Catal.* **1987,** *103*, 436-449.

182. Bade, K.; Karstens, O.; Michaelis, A.; Schultze, J. W., Localization of electrode reactions by a focused laser beam. *Faraday Discuss.* **1992,** *94*, 45-62.

183. Vamathevan, V.; Amal, R.; Beydoun, D.; Low, G.; McEvoy, S., Photocatalytic oxidation of organics in water using pure and silver-modified titanium dioxide particles. *J. Photochem. Photobiol., A* **2002,** *148*, 233-245.

184. Elmalem, E.; Saunders, A. E.; Costi, R.; Salant, A.; Banin, U., Growth of Photocatalytic CdSe-Pt Nanorods and Nanonets. *Adv. Mater.* **2008,** *20*, 4312-4317.

References page 33

185. Jacobs, J. W. M., Repair of transparent defects on photomasks by laser-induced metal deposition from an aqueous solution. *J. Vac. Sci. Technol., B* **1990,** *8*.

Chapter 2

TiO$_2$ Nano-objects with controlled morphologies

Table of contents

2.1 Introduction to TiO₂ as a potential material for applications

Titanium dioxide (TiO$_2$) as a nanomaterial is known for its numerous and diverse applications which range from sunscreens, pigments to photovoltaic cells, water purification photocatalysis and drug delivery.[1-6] Due to its merits, including elemental abundance, excellent stability and photo activity, TiO$_2$ has attracted keen research interest worldwide.

2.2 TiO₂ synthesis methods and crystal facet featured shapes

Developing TiO$_2$ crystals with specific morphology/facet is also necessary to finely control the TiO$_2$ based heterostructures. Facets owning different surface reactivity will exhibit distinct properties. A typical example is the selective photodeposition of Pt dots on the (110) facets and that of PbO$_2$ on the (011) facets of rutile TiO$_2$ because of the different surface energy levels of the two facets.[7]

Three main crystal phases are identified for TiO$_2$, i.e., rutile, anatase and brookite in nature. See Table 1 for their structural and thermodynamic properties.

Phase	Rutile	Anatase	Brookite
Crystal system	Tetragonal	Tetragonal	Orthorhombic
Space group	P4$_2$/mnm	I4$_1$/amd	Pbca
Unit cell (Å)	a = 4.594 Å c = 2.958 Å Z = 2	a = 3.785 Å c = 9.5143 Å Z = 4	a = 9.184 Å b = 5.447 Å c = 5.145 Å Z = 8
Distance (Ti^{4+} - O^{2-})(Å)	1.95 – 1.99	1.93 – 1.98	1.86 – 2.04
Coordination number	[Ti^{4+}] = 6 [O^{2-}] = 3	[Ti^{4+}] = 6 [O^{2-}] = 3	[Ti^{4+}] = 6 [O^{2-}] = 3
Atomic packing factor	0.705	0.645	0.655
Density (g.cm^{-3})	4.24	3.89	4.12
Hardness (Mohs)	6.0 – 6.5	5.5 – 6.0	5.5 – 6.0
Refractive index	2.61 – 2.89	2.48 – 2.56	2.58 – 2.70
Enthalpy of formation $\Delta_f H^0$ (298.15 K) (kJ.mol^{-1})	- 944.50 ± 0.96	- 939.27 ± 1.26	- 941.00
Entropy of formation $\Delta_f S^0$ (298.15 K) (kJ.mol^{-1}.K^{-1})	50.37 ± 0.21	49.95 ± 0.42	-

Structure
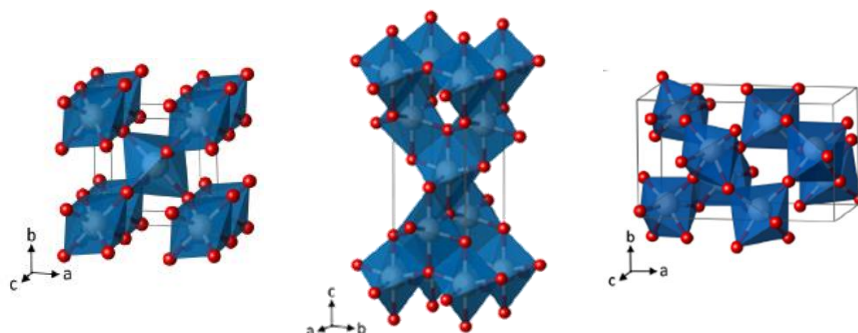
Table 1: Physical and thermodynamic properties of the three crystal phases of TiO$_2$ [8]

While rutile is the thermodynamically stable phase, anatase and brookite are metastable and irreversibly transform to rutile at high temperature (750 – 915 °C).[9] Although rutile is the most common form in nature, below 100 nm anatase becomes the most thermodynamically stable phase [10, 11] Among the three natural phases, anatase is the most studied TiO$_2$ in catalysis, photocatalysis and dye-sensitized solar cells. Most applications of anatase are sensitive to the surface properties, and numerous studies have therefore focused on controlling the shape of the anatase crystals. The equilibrium shape of an anatase crystal according to the Wulff construction is a slightly truncated bipyramid enclosed by more than 94% (101) and fewer 6% (001) facets (Figure 2.1).[12]
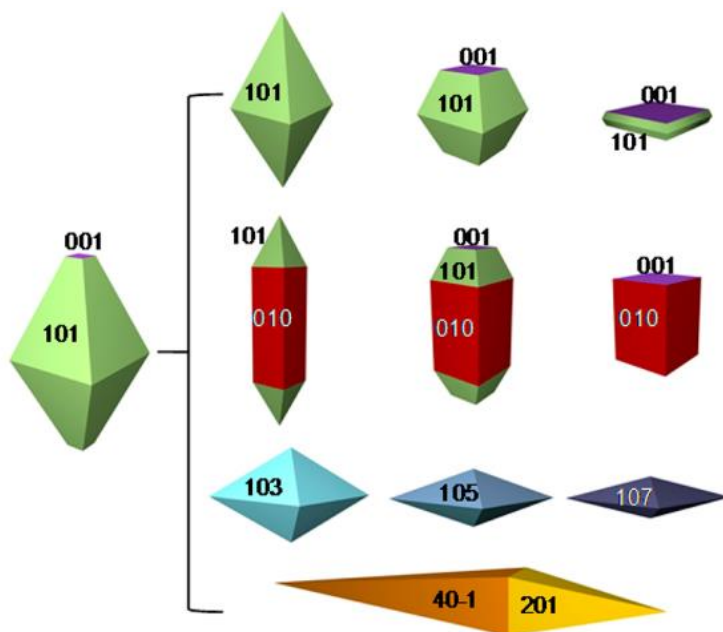
Figure 2.1 Equilibrium crystal shape of anatase TiO$_2$ according to the Wulff construction[12] and the evolved other shapes.

Our concern in this chapter will focus on the synthesis of anatase TiO$_2$, then to use it as the semiconductor substrate to load metal particles using photodeposition method, as mentioned previously (Chapter 1).

2.2.1 Common routes to synthesize TiO₂ crystals

TiO₂ nanocrystals can be synthesized by many synthesis methods[4, 13, 14 15, 16] including wet-chemistry (hydrothermal, solvothermal and nonhydrolytic), gas oxidation, topotactic transformation, crystallization transformation from amorphous TiO₂, and epitaxial growth. Among them, the hydrothermal and solvothermal methods are the most widely used to tailor the exposure of crystal facets due to easy manipulation and versatility.

The hydrothermal (or solvothermal) term refers to any reaction in an aqueous (non-aqueous) solvent under high pressure and high temperature (below the critical condition). The hydrothermal syntheses are often carried out in a sealed Teflon vessel surrounded by a stainless steel autoclave. The extreme conditions inside the autoclave allow the dissolution and the recrystallization of compounds, which are insoluble at room temperature and atmospheric pressure. As in the sol-gel process, titanium alkoxides can be used as precursors. The starting reagents are introduced in the autoclave, which is then sealed and heated in an oven. Several parameters can be controlled such as the precursor concentration, the filling ratio of the autoclave, the pH, the reaction time, and the temperature, and these parameters influence the autogenous pressure inside the autoclave if not externally controlled. The pressure inside the autoclave may play a vital role in the solubility and the crystal growth rates of the NPs in the case of low boiling point solvents. Therefore, adjusting these parameters leads to various shapes and morphologies.[11, 17] This method has been widely used to synthesize TiO₂ near-spherical nanoparticles,[18-20] nanotubes,[21-24] nanorods,[25-27] and nanoplates.[28-31]

Another method called gel-sol method was developed by Sugimoto,[32-36] based on the preparation of a metal hydroxide gel that is aged to obtain a sol in which colloidal particles are dispersed. The schematic illustration for the formation of anatase TiO₂ particles is illustrated in Figure 2.2.
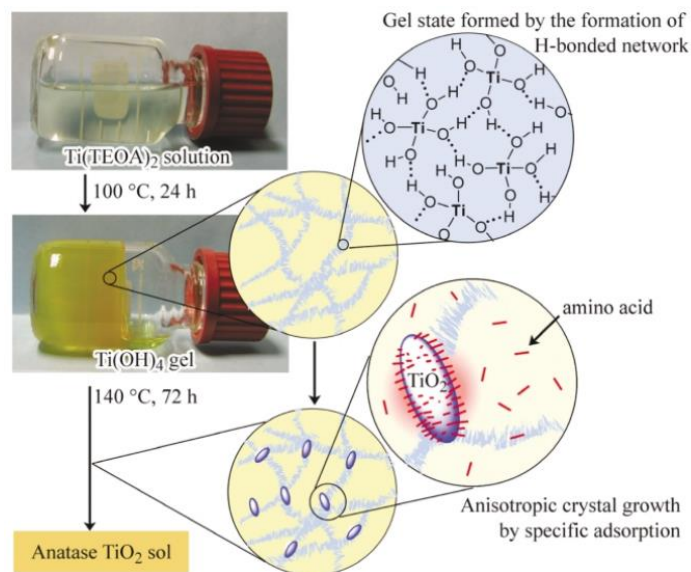
Figure 2.2 Schematic illustration for the formation of anatase TiO₂ particles by the gel-sol method.[36]

The synthesis starts with the replacement of the isopropoxy groups on titanium by the ethoxy groups of the triethanolamine generating a gel useful to slow down the hydrolysis rate. The gel is then heated to form a second gel composed mainly of titanium hydroxide, with specific ageing time, anatase particles with spherical or spindle-like morphology are finally produced. The gel-sol process is an excellent synthesis method to control the size and the morphology of nanoparticles.[33, 34] One of the main drawbacks of this method is the use of expensive precursors, such as alkoxides.

2.2.2 Crystal facet control by surface directing agents

Surface energies of the different surfaces can be effectively decreased by the selective adsorption of appropriate surface directing agents (SDA) so that the growth rates along different orientations can be controlled.[37-40] This consequently leads to the formation of crystals with tunable percentages of different facets, as indicated by Figure 2.3.

50
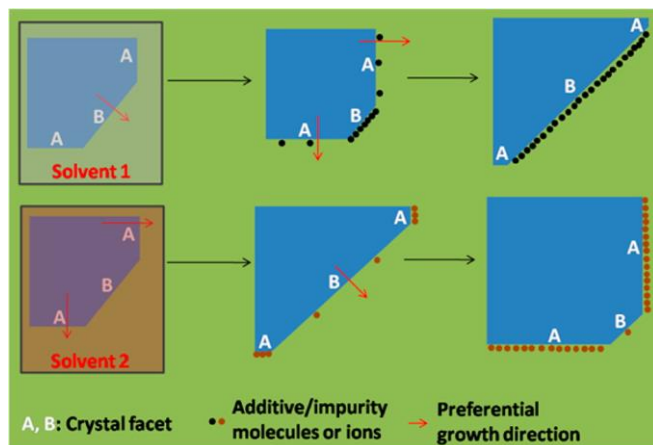
Figure 2.3 Schematic of the effect of surface directing agents on the morphological control of crystal facets.[41]

The principle of NP morphology control by SDA is the blocking of the growth of given facets in one or several directions. The SDAs are specifically adsorbed on one or several crystal surfaces inducing a steric hindrance and preventing their further growth. For instance, as shown in Figure 2.3, Solvent 1 contains certain SDAs which are prone to adsorb onto the facet "B", thus preventing the growth rate perpendicular to facet "B" while the facet "A" grows smaller meantime. In the end, the crystal formed with the dominant facet "B". Similarly, another type of SDA may cause facet "A" dominate the crystal facet as in solvent 2.

The choice of SDA is critical in controlling the facets growth of the crystals. To date, the organic agents play a predominant role in controlling the shape of TiO₂ crystals, mainly owing to the diversity of organic functions. For example, oleic acid (OA) and oleylamine (OM) with different binding strengths can act as SDAs of the anatase (001) and (101) facets, respectively (Figure 2.4).[26, 29, 42, 43]
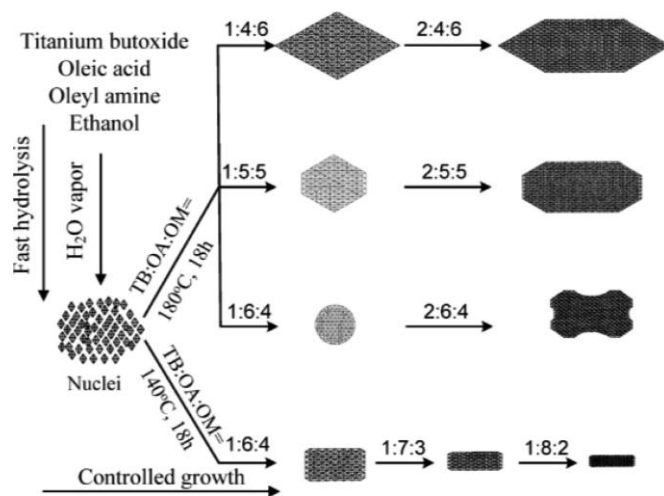
Figure 2.4 Schematic illustration of the overall formation and shape evolution of TiO2 nanocrystals.[29]

51

By varying the ratio between OA and OM, as well as the water content, it is possible to obtain TiO$_2$ with distinct morphologies such as rhombic, truncated rhombic, spherical, dog-bone, truncated and elongated rhombic, and bar.[29]

Controlling the shape of TiO$_2$ with inorganic agents, particularly for the formation of specific crystal facets, has been increasingly reported in recent years.[37, 38] One impressive example is the use of F$^-$ as a SDA to obtain a large percentage of anatase (001) facets.[37]

Another relevant parameter to modify NPs morphology is the pH modification of the reaction conditions. The pH can play a role in modifying the surface chemistry, as well as the precursor's reactivity. Figure 2.5 presents the predicted evolution of the shape of anatase as a function of pH.[39]
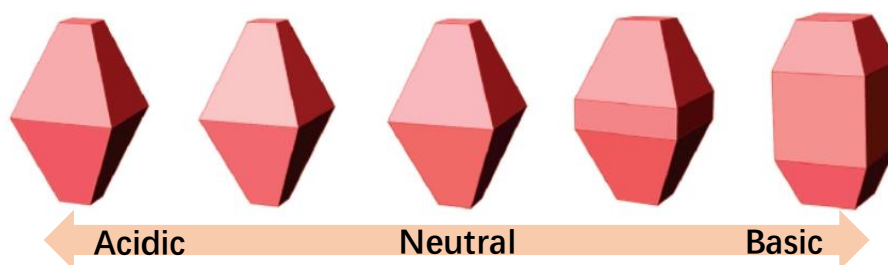
Figure 2.5 Predicted morphologies for anatase as a function of the pH.[39]

In their paper, the authors showed that when H$^+$ is dominant on the surface (acidic condition), there is little change in the shape of the nanocrystals as compared to the (neutral) water terminated nanoparticles; however, when OH or oxygen groups are dominant on the surface, the nanoparticles become elongated, which is consistent with experimental findings.[44, 45]

2.3 Synthesis methods and results

According to the literature discussed above, the morphology of TiO$_2$ can be adjusted by adding SDAs, including organic ligands, or just by pH variations. In the following part, five kinds of TiO$_2$ morphologies, *i.e.,* TiO$_2$ polyhedrons, nanoneedles, nanoplates, nanocubes and bipyramids, will be introduced to play with not only the morphology of the nanoobjects but also their size, and their aspect ratio. The synthesis methods and the results are described in the following sections.

2.3.1 TiO₂ polyhedrons

In this section, the gel-sol method[36] published by Sugimoto et al. was used to synthesize anatase TiO₂ polyhedrons with a targeted size of 30 nm with slight modifications. In short, titanium isopropoxide (TTIP) and triethanolamine (TEOA) were mixed in a molar ratio of 1:2 under an Ar atmosphere. After being stirred for 24 h, the mixture was aged at 100 ℃ for 24 h for gelation and then continued to be heated at 140 ℃ for another 72 h. The product was then washed with 30 mL of a pH 12 NaOH solution, 30 mL of a 2 M HNO₃ solution and pure water, three times for each, respectively.

TEM result (Figure 2.6a,b) showed that polyhedron-like TiO₂ nanoparticles were successfully obtained. The size distribution mainly focused in the range from 22 to 45 nm, with a mean value of 33 nm (Figure 2.6c). The shape of these nanoparticles is ill-defined and by comparison with the other ones, we decided to name them polyhedrons.
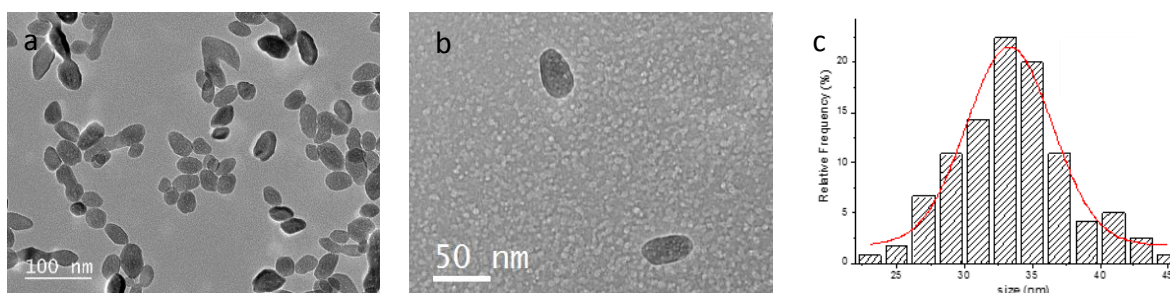
Figure 2.6 (a)(b) TEM images of TiO₂ polyhedrons, (c) statistical size distribution of TiO₂.

The X-ray diffraction (XRD) analysis was performed to check the phase structure (Figure 2.7).
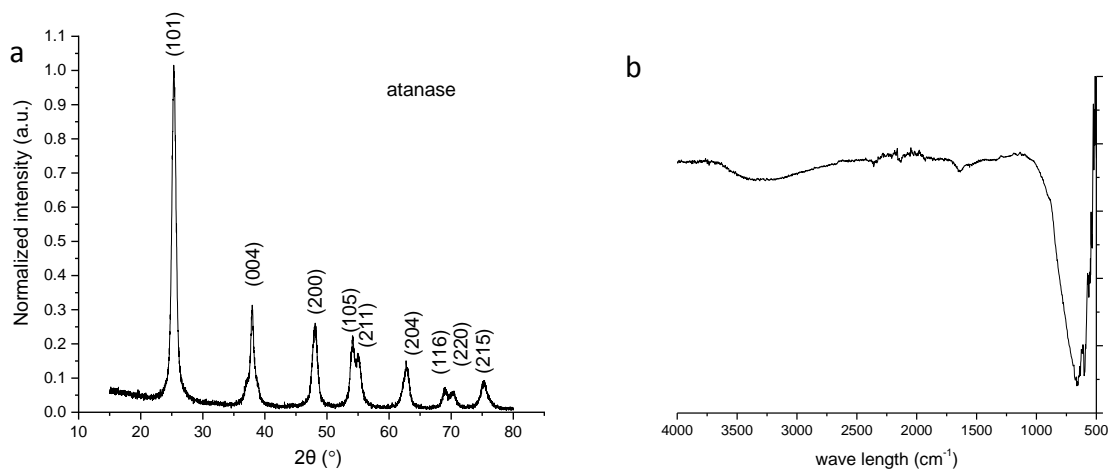
Figure 2.7 (a) XRD pattern and (b) ART spectrum of TiO₂ polyhedrons.

53

As illustrated in the XRD pattern, the peaks at 25.3°, 37.8°, 48.0°, 53.9°, 55.1°, 62.7°, 68.8°, 70.3°, and 75.1° of the sample can be indexed to anatase phase (JCPDS 21-1272) and correspond to the diffractions of (101), (004), (200), (105), (211), (204), (116), (220) and (215) planes, respectively. No other phase is detected in this sample. The ATR spectrum also showed the absence of any ligand at the surface of the particles.

The colloidal stability of theseTiO₂ polyhedrons in solution was studied by zetametry (Figure 2.8).
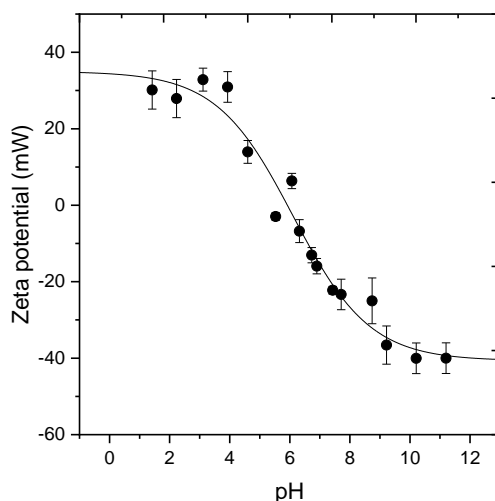
Figure 2.8 Zeta potential of colloidal anatase nanoparticles as a function of the pH.

The zero charge point of the TiO₂ polyhedrons, is found at 6.0, consistent with what is reported for TiO₂ nanoparticles in the literature[46-48] with a colloidal instability over a pH range of 2. We thus chose to keep our anatase particles in a pH 3 solution for future use.

2.3.2 TiO₂ nanoneedles

2.3.2.1 Direct synthesis of nanoneedles

TiO₂ nanoneedle particles were synthesized using two different methods, the first one is based on reference[36] with slight modifications. All the procedures are identical to those of TiO₂ polyhedrons synthesis, except that the pH of the mixture containing TTIP and TEOA is adjusted at pH 10 by addition of a NaOH solution, before the heating process at 140 °C for 24 hours. The product was washed by NaOH, HNO₃ and deionized water, each for three times, respectively. The TEM images of the TiO₂ nanoneedles are shown in Figure 2.9.

References page 63
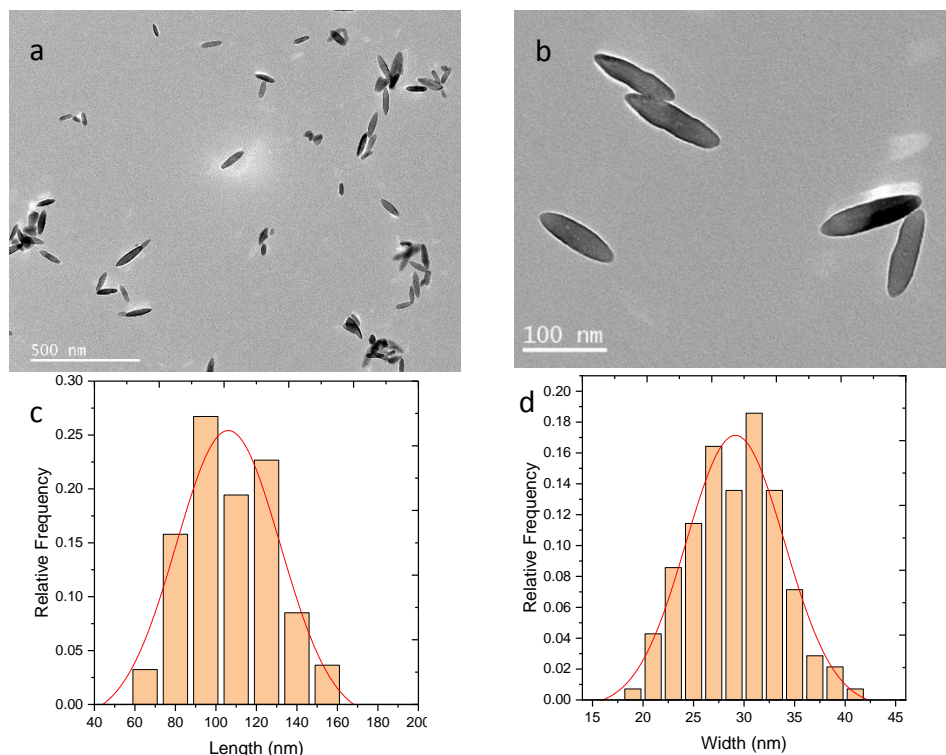
Figure 2.9 TEM images at (a) low and (b) high magnifications; the size histogram in length (c) and width (d).

Figure 2.9 a and b show that most of the particles exhibit a needle shape. The mean size of length and width are 110 and 28 nm, respectively. The aspect ratio of the TiO₂ nanoneedles is 4:1. Playing with the pH is then a helpful tool to control the size and shape of the TiO₂ polyhedrons going from 32 nm diameter particles to rods with an aspect ratio of 4.

2.3.2.2 Indirect synthesis method of TiO₂ nanoneedles

Another method to synthesize TiO₂ with nanoneedles shape consists of using a commercial nanopowder provided by Evonik (P25) as a precursor for the controlled synthesis of pure anatase nanoobjects with controlled morphologies. This powder is produced by tons and is so cheap that the smallest packaging is 5 kg. As shown in Figure 2.10. P25 is a mixture of anatase and rutile phases, which can be destroyed by a basic hydrothermal treatment at 130°C overnight.[22, 23] The general approach to making these nanoneedles from P 25 is shown below in Figure 2.10.
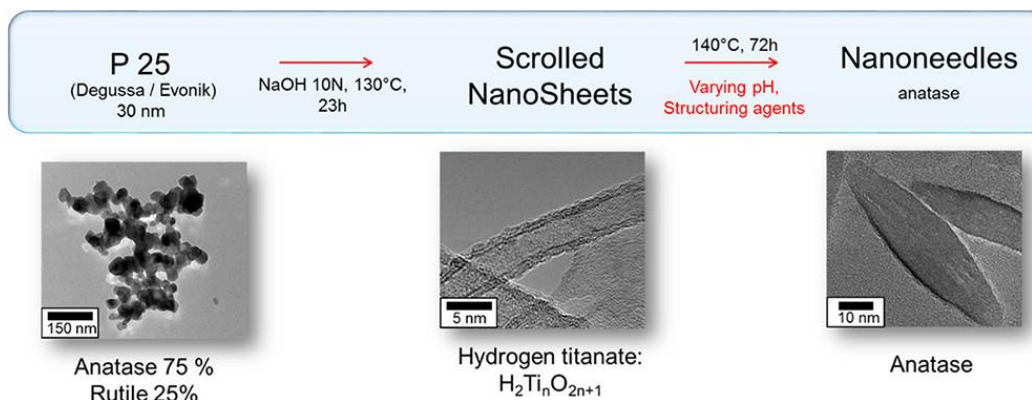
Figure 2.10 General approach to synthesize nanoneedles from P 25 through an intermediate scrolled nanosheet.

The first step is a transformation of P25 into scrolled nanosheets (SNSs). These scrolled nanosheets synthesis is adapted from the initial work by Kasuga et al..[22-24] In a 50 mL Teflon container, 2 g of TiO₂ P25 and 28 mL of a freshly prepared 10 M NaOH solution are mixed. The Teflon container is closed and manually shaken and then placed in the stainless steel autoclave and placed in an oven to heat at 130°C for 23 h.[44]

The synthesis of nanoneedles using the scrolled nanosheets previously prepared is inspired by Nian,[25] who claimed that hydrothermal treatment of titanate nanotube or scrolled nanosheet suspensions under an acidic environment resulted in the formation of single-crystalline anatase nanorods with a specific crystal-elongation direction. We recently extended the range of parameters and showed that milder hydrothermal conditions used for the treatment of titanate scrolled nanosheets (SNSs) suspensions (140 °C, 72 h) resulted in a large variety of anatase TiO₂ anisotropic nano-objects depending on the studied parameters[44]:

(i)   influence of the medium pH,

(ii)   the presence or not of surface directing agents.

We show that such a hydrothermal treatment of the SNSs, whatever the pH, resulted in the formation of single-crystalline anatase nanoneedles (NNs) with a specific crystal-elongation direction and a pH-dependent morphological anisotropy with aspect ratios (AR) from 1 to 8. The crystal size of the anatase TiO₂ obtained from this hydrothermal treatment increased with the pH of the suspensions, from 15 nm nanoparticles (NPs; AR = 1) at pH 2.2 to 500 nm NNs (AR = 8) at a pH 10.8 with a long axis systematically along the anatase [001] direction. Triethanolamine and oleic acid were used as SDAs. Their respective influence, when acting on their own, had little influence on the control of the size, shape, or polydispersity of the NNs. However, their concomitant use provided a better control of not only the size and

polydispersity, but also on (i) the shape and morphology giving rise to a controlled access to well-defined nanorods as opposed to nanoneedles and (ii) the crystal phase purity eliminating the few percent brookite still visible in the XRD patterns of samples prepared in SA-free conditions. This aspect will not be treated here, and the reader could refer to reference [44] for more information.

Our focus here was to obtain nanoneedles with a specific aspect ratio.

In order to reach the required pH, a 1M NaOH solution is added dropwise to one-third of the scrolled nanosheets suspension corresponding to 0.7 g of powder, The volume is then adjusted to 30 mL and added to a 50 mL Teflon vessel in the stainless steel autoclave. The autoclave is placed in an oven at 140 °C for 72 hours, after which the mixture is naturally cooled down and washed with distilled water until pH 7 (centrifugation steps: 9000 rpm, 10 min).

The TEM images of the intermediate product, scrolled nanosheets, are shown in Figure 2.11.
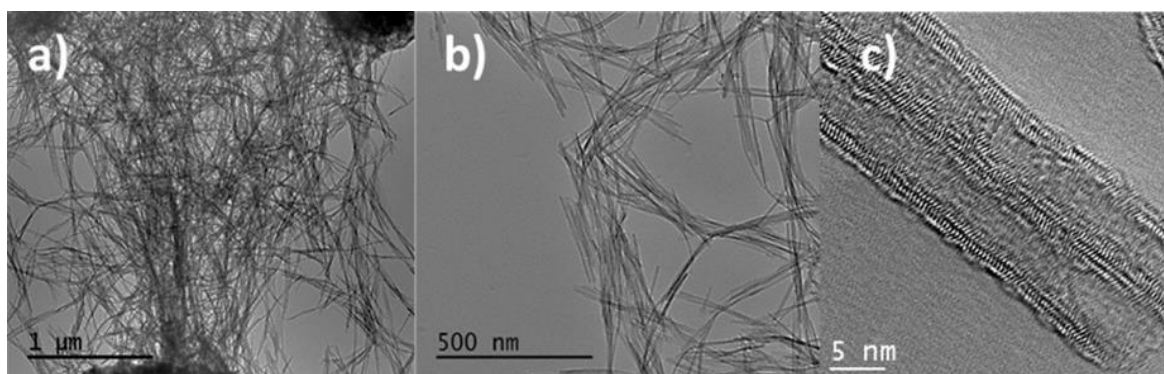
Figure 2.11 TEM images of scrolled nanosheets at three magnifications.[44]

As we can see, each scrolled nanosheet consists of a thin curved structure of several layers of a single nanosheet wrapped on itself, along with the c-axis, leading to a nanotube with an average external diameter of ~8 nm with a multiwall thickness of ~2 nm and a length of several hundred nanometers. The interlayer spacing of these nanotubes is 0.7 nm, close to the values reported in the literature.[8, 49]

When a suspension of scrolled nanosheets underwent reaction at 140 °C for 72 h at pH 9.8 treatment, nanoneedles, as shown in Figure 2.12a, are obtained. The XRD analysis (Figure 2.12b) shows the characteristic peaks of the well-crystallized anatase structure (JCPDS 21-1272) are dominant with a few per cent of brookite (JCPDS 029-1360) barely detectable.

References page 63
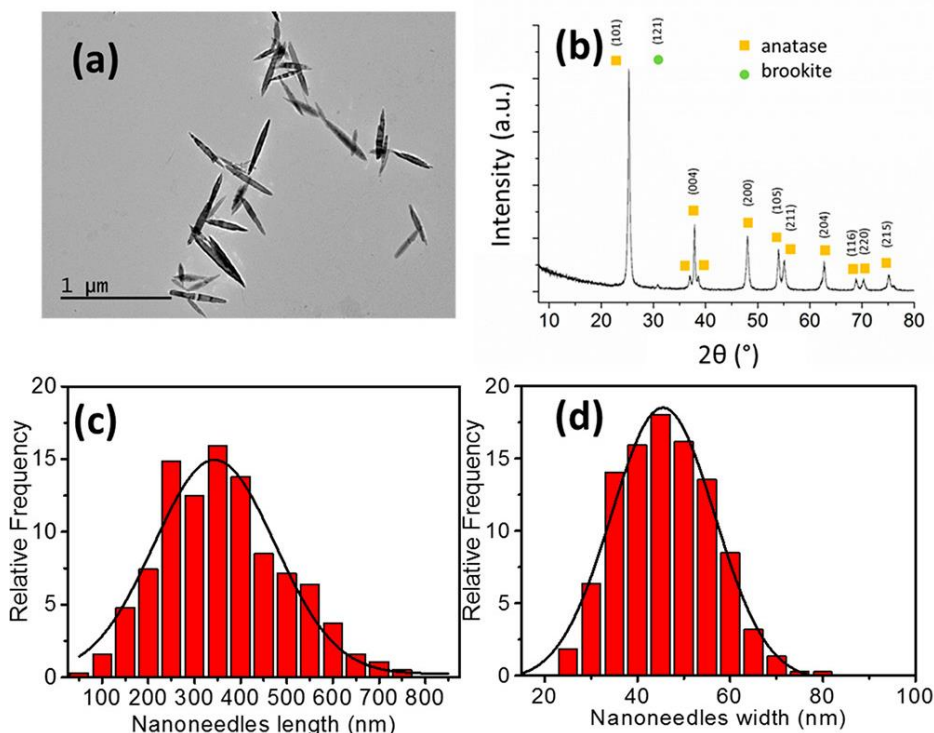
Figure 2.12 (a) TEM image and (b) XRD pattern of TiO₂ nanoneedles; (c, d) statistical distribution of nanoneedle lengths and widths, respectively. [44]

The statistical distribution of their lengths and widths measured on at least 300 nanoparticles (Figure 2.12c,d) provided an average length of 350 (± 130) nm, a width of 46 (± 10) nm, and an aspect ratio of 7.5.

2.3.3 TiO₂ nanoplates

In this part, TiO₂ nanoparticles with plate shape were fabricated to expose the (001) facets for photodeposition preferably. The synthesis method we used follows reference[30] published by Shaffer's group. In short, TTIP dissolved in isopropanol was mixed with hydrofluoric acid to get a ratio of Ti:F=1:1. The mixture was then stirred, followed by heating at 180 ℃ for 24 h in an autoclave. The white product was washed by isopropanol and water for at least three times, and finally, we kept the particles in pH 3 solution adjusted by HNO₃.

As shown in Figure 2.13, TEM results showed well-distributed plate-shape TiO₂ nanoparticles on the grid, with lateral dimensions of around 30 nm and thickness of about 9 nm, with an aspect ratio of 3. It needs to be noted that some of the plate particles tend to stack along [001] direction, forming aggregates on the grid (see Figure 2.13b).
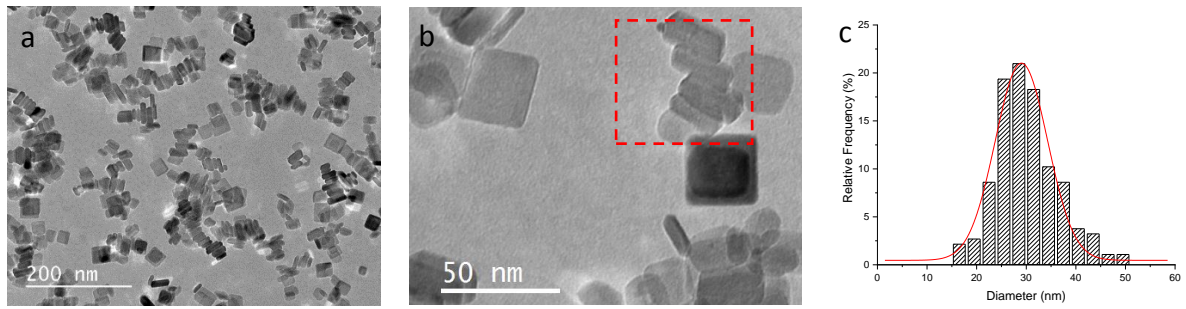
Figure 2.13 (a) (b) TEM images of nanoplate anatase particles and (c) their corresponding size distributions.

XRD analysis (Figure 2.14) confirmed that the obtained white product was highly crystalline TiO₂ anatase.
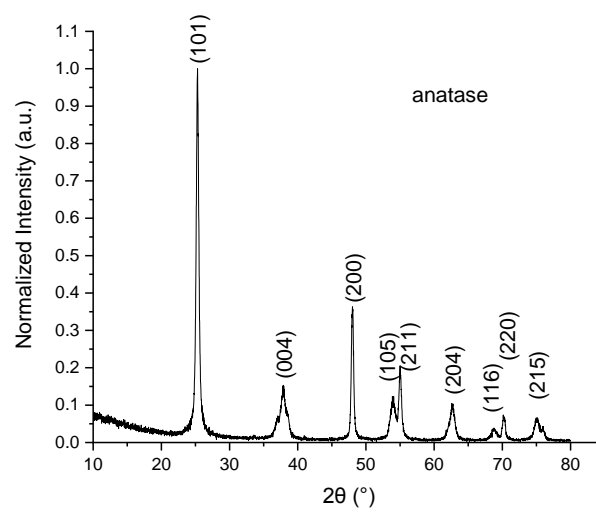
Figure 2.14 XRD pattern of plate-shape TiO₂ nanoparticles.

The zetametry experiment of nanoplates sample was made and shown in Figure 2.15.
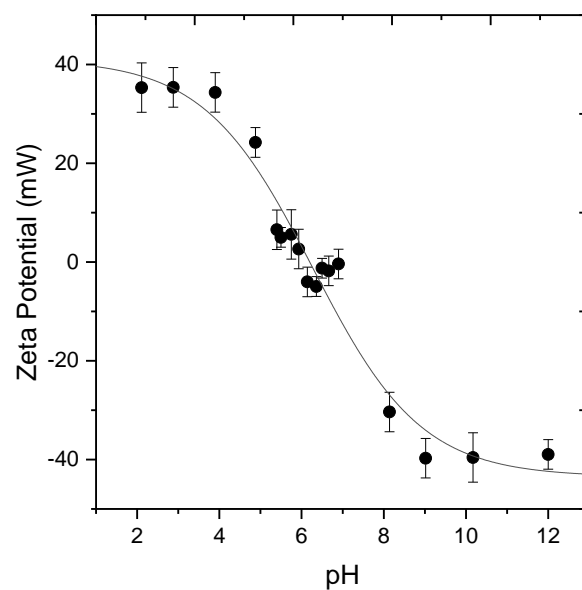
Figure 2.15 Zeta potential of plate-shape anatase nanoparticles as a function of pH.

59

The zeta potential showed a good Boltzmann fitting curve as a function of pH values. The isoelectric point is at pH 6.1, which is close to what we got for TiO$_2$ polyhedrons.

2.3.4 TiO$_2$ nanocubes

In addition to the TiO$_2$ polyhedrons and nanoplates, nanocube shape TiO$_2$ nanoparticles were also synthesized using a similar method as for nanoplates,[30] except for the ratio of Ti: F which now equals 1:0.2. The TEM results in Figure 2.16a and b have confirmed the formation of nanocubes, with the mean edge size of 12 nm, with a standard deviation of 2 nm (Figure 2.16c).
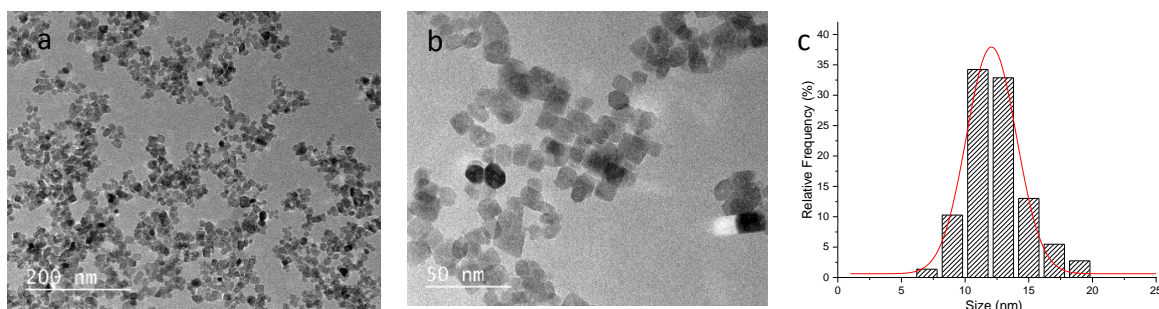
Figure 2.16 (a) (b)TEM images of anatase nanocubes and (c) the corresponding size distribution.

2.3.5 TiO$_2$ bipyramids

Bipyramid shape anatase was also made by a solvothermal method according to Liu's work in 2015.[50] In brief, Titanium butoxide (TBOT) dissolved in ethanol was mixed with oleylamine (OM). OM was proven effective as a surfactant to prepare TiO$_2$ nanosheets and rhombic-shaped TiO$_2$ nanocrystals. The well-mixed mixture was then transferred to Teflon-lined stainless steel autoclave containing water. The autoclave was then heated at 180℃ for 14 h.

The product was collected by washing the precipitate thoroughly with absolute ethanol and deionized water for at least five times to remove the residual contamination. The product particles were finally kept in solution at pH 3.

As illustrated in Figure 2.17a,b, TEM results have shown that most of the nanocrystals exhibit a shape of bipyramid.
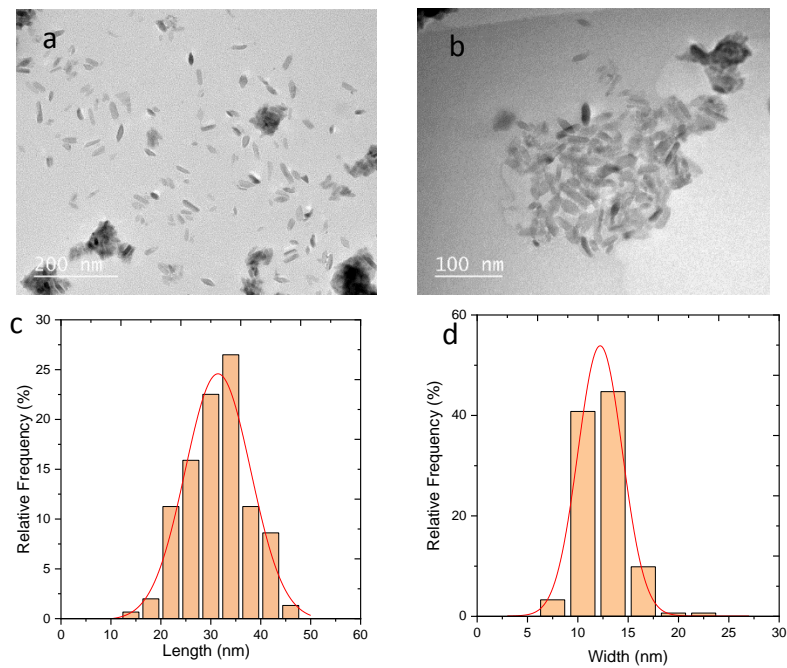
Figure 2.17 (a) (b) TEM images of TiO₂ bipyramids and (c) the corresponding size distribution.

The size of these nano-bipyramids is not uniform with a length in c-axis ranging from 20–45 nm, the mean size of which is around 31 nm (Figure 2.17c), the width is 12 (± 2)nm.

The XRD pattern (Figure 2.18) also confirmed the formation of anatase phase; no other phase was detected.
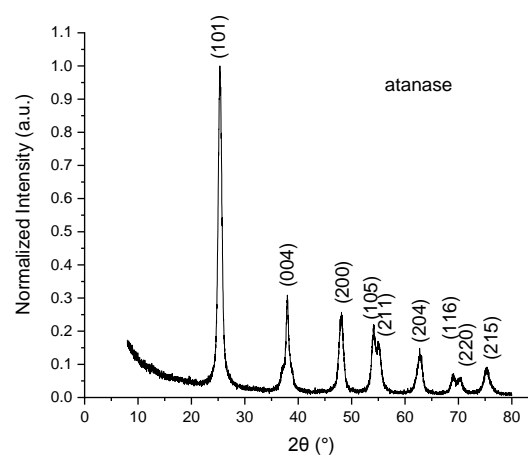
Figure 2.18 XRD pattern of TiO₂ bipyramid.

61

2.4 Conclusions

In this chapter, we have introduced and used general routes to synthesize TiO_2 nanoparticles with different morphologies. The surface directing agents have an important role in shape control of the product. First, TiO_2 polyhedrons were obtained through a gel-sol method using TEOA as a surface directing agent. Addition of NaOH solution into the mixture of TTIP and TEOA led to TiO_2 nanoneedles. In other cases, the TiO_2 nanoneedles can also be made using P25 as precursor particles through an indirect procedure with NaOH acting as shape controller. TEOA was also used as a surface directing agent, but this was not detailed here.[44] TiO_2 nanoplates and nanocubes were fabricated by a hydrothermal method, using HF as a surface directing agent. The shape can be altered by the control of the ratio between Ti^{4+} and F^- ions. Last, TiO_2 bipyramids are synthesized through a solvothermal method, using oleylamine as a surface directing agent and ethanol as the solvent. All the nano-sized TiO_2 particles are characterized by TEM technique, and most are confirmed as anatase phase by XRD analysis. The well-shaped TiO_2 nanoparticles with different morphologies provide substrates to load metal particles by photodeposition method, allowing us to study the shape effect on the preferential deposition sites during the photodeposition process, which will be mainly discussed in Chapter 4.

2.5 Bibliography

1. Kapilashrami, M.; Zhang, Y.; Liu, Y. S.; Hagfeldt, A.; Guo, J., Probing the optical property and electronic structure of TiO$_2$ nanomaterials for renewable energy applications. *Chem. Rev.* **2014,** *114*, 9662-9707.

2. Liu, K.; Cao, M.; Fujishima, A.; Jiang, L., Bio-inspired titanium dioxide materials with special wettability and their applications. *Chem. Rev.* **2014,** *114*, 10044-10094.

3. Rajh, T.; Dimitrijevic, N. M.; Bissonnette, M.; Koritarov, T.; Konda, V., Titanium dioxide in the service of the biomedical revolution. *Chem. Rev.* **2014,** *114*, 10177-10216.

4. Sang, L.; Zhao, Y.; Burda, C., TiO$_2$ nanoparticles as functional building blocks. *Chem. Rev.* **2014,** *114*, 9283-9318.

5. Li, J.; Wu, N., Semiconductor-based photocatalysts and photoelectrochemical cells for solar fuel generation: a review. *Catal. Sci. Technol.* **2015,** *5*, 1360-1384.

6. Li, X.; Yu, J.; Jaroniec, M.; Chen, X., Cocatalysts for Selective Photoreduction of CO$_2$ into Solar Fuels. *Chem. Rev.* **2019,** *119*, 3962-4179.

7. Ohno, T.; Sarukawa, K.; Matsumura, M., Crystal faces of rutile and anatase TiO$_2$ particles and their roles in photocatalytic reactions. *New J. Chem.* **2002,** *26*, 1167-1170.

8. Fujishima, A.; Hashimoto, K.; Watanabe, T., *TiO₂ photocatalysis: fundamentals and applications*. BKC Incorporated: 1999.

9. Hanaor, D. A.; Sorrell, C. C., Review of the anatase to rutile phase transformation. *J. Mater. Sci.* **2011,** *46*, 855-874.

10. Bourikas, K.; Kordulis, C.; Lycourghiotis, A., Titanium dioxide (anatase and rutile): surface chemistry, liquid-solid interface chemistry, and scientific synthesis of supported catalysts. *Chem. Rev.* **2014,** *114*, 9754-9823.

11. Chen, X.; Mao, S. S., Titanium dioxide nanomaterials: synthesis, properties, modifications, and applications. *Chem. Rev.* **2007,** *107*, 2891-2959.

12. Lazzeri, M.; Vittadini, A.; Selloni, A., Structure and energetics of stoichiometric TiO$_2$ anatase surfaces. *Phys. Rev. B* **2001,** *63*, 155409.

13. Chen, X.; Mao, S. S., Titanium Dioxide Nanomaterials: Synthesis, Properties, Modifications, and Applications. *Chem. Rev.* **2007,** *107*, 2891-2959.

14. Liu, G.; Yang, H. G.; Pan, J.; Yang, Y. Q.; Lu, G. Q.; Cheng, H.-M., Titanium Dioxide Crystals with Tailored Facets. *Chem. Rev.* **2014,** *114*, 9559-9612.

15. Schneider, J.; Matsuoka, M.; Takeuchi, M.; Zhang, J.; Horiuchi, Y.; Anpo, M.; Bahnemann, D. W., Understanding TiO$_2$ Photocatalysis: Mechanisms and Materials. *Chem. Rev.* **2014,** *114*, 9919-9986.

16. Liu, L.; Chen, X., Titanium dioxide nanomaterials: self-structural modifications. *Chem. Rev.* **2014,** *114*, 9890-9918.

17. Suchanek, W. L.; Riman, R. E., Hydrothermal Synthesis of Advanced Ceramic Powders. *Adv. Sci. Technol.* **2006,** *45*, 184-193.

18. Kobayashi, M.; Petrykin, V. V.; Kakihana, M.; Tomita, K.; Yoshimura, M., One-Step Synthesis of TiO2(B) Nanoparticles from a Water-Soluble Titanium Complex. *Chem. Mater.* **2007,** *19*, 5373-5376.

19. Lin, J.; Lin, Y.; Liu, P.; Meziani, M. J.; Allard, L. F.; Sun, Y.-P., Hot-Fluid Annealing for Crystalline Titanium Dioxide Nanoparticles in Stable Suspension. *J. Am. Chem. Soc.* **2002,** *124*, 11514-11518.

20. Cozzoli, P. D.; Kornowski, A.; Weller, H., Low-temperature synthesis of soluble and processable organic-capped anatase TiO$_2$ nanorods. *J. Am. Chem. Soc.* **2003,** *125*, 14539-14548.

21. Deng, Q.; Wei, M.; Ding, X.; Jiang, L.; Ye, B.; Wei, K., Brookite-type TiO$_2$ nanotubes. *Chem.Commun.* **2008**, 3657-3659.

22. Kasuga, T., Formation of titanium oxide nanotubes using chemical treatments and their characteristic properties. *Thin Solid Films* **2006,** *496*, 141-145.

23. Kasuga, T.; Hiramatsu, M.; Hoson, A.; Sekino, T.; Niihara, K., Formation of Titanium Oxide Nanotube. *Langmuir* **1998,** *14*, 3160-3163.

24. Kasuga, T.; Hiramatsu, M.; Hoson, A.; Sekino, T.; Niihara, K., Titania Nanotubes Prepared by Chemical Processing. *Adv. Mater.* **1999,** *11*, 1307-1311.

25. Nian, J.-N.; Teng, H., Hydrothermal Synthesis of Single-Crystalline Anatase TiO$_2$ Nanorods with Nanotubes as the Precursor. *J. Phys. Chem. B* **2006,** *110*, 4193-4198.

26. Joo, J.; Kwon, S. G.; Yu, T.; Cho, M.; Lee, J.; Yoon, J.; Hyeon, T., Large-scale synthesis of TiO$_2$ nanorods via nonhydrolytic sol-gel ester elimination reaction and their application to photocatalytic inactivation of E. coli. *J. Phys. Chem. B* **2005,** *109*, 15297-15302.

27. Seo, J. W.; Jun, Y. W.; Ko, S. J.; Cheon, J., In situ one-pot synthesis of 1-dimensional transition metal oxide nanocrystals. *J. Phys. Chem. B* **2005,** *109*, 5389-5391.

28. Wu, B.; Guo, C.; Zheng, N.; Xie, Z.; Stucky, G. D., Nonaqueous production of nanostructured anatase with high-energy facets. *J. Am. Chem. Soc.* **2008,** *130*, 17563-17567.

29. Dinh, C. T.; Nguyen, T. D.; Kleitz, F.; Do, T. O., Shape-controlled synthesis of highly crystalline titania nanocrystals. *ACS Nano* **2009,** *3*, 3737-3743.

30. Menzel, R.; Duerrbeck, A.; Liberti, E.; Yau, H. C.; McComb, D.; Shaffer, M. S. P., Determining the Morphology and Photocatalytic Activity of Two-Dimensional Anatase Nanoplatelets Using Reagent Stoichiometry. *Chem. Mater.* **2013,** *25*, 2137-2145.

31. Ding, K.; Miao, Z.; Liu, Z.; Zhang, Z.; Han, B.; An, G.; Miao, S.; Xie, Y., Facile synthesis of high quality TiO$_2$ nanocrystals in ionic liquid via a microwave-assisted process. *J. Am. Chem. Soc.* **2007,** *129*, 6362-6363.

32. Sugimoto, T.; Okada, K.; Itoh, H., Synthetic of Uniform Spindle-Type Titania Particles by the Gel–Sol Method. *J. Colloid Interface Sci.* **1997,** *193*, 140-143.

33. Sugimoto, T.; Zhou, X., Synthesis of Uniform Anatase TiO$_2$ Nanoparticles by the Gel–Sol Method: 2. Adsorption of OH$^-$ Ions to Ti(OH)$_4$ Gel and TiO$_2$ Particles. *J. Colloid Interface Sci.* **2002,** *252*, 347-353.

34. Sugimoto, T.; Zhou, X.; Muramatsu, A., Synthesis of uniform anatase TiO$_2$ nanoparticles by gel–sol method: 3. Formation process and size control. *J. Colloid Interface Sci.* **2003,** *259*, 43-52.

35. Sugimoto, T., Monodispersed Particles: Nucleation and Growth. In *Ency. Surf. Colloid Sci.*, CRC Press: 2015; pp 4776-4789.

36. Kanie, K.; Sugimoto, T., Shape control of anatase TiO$_2$ nanoparticles by amino acids in a gel-sol system. *Chem. Commun.* **2004**, 1584-1585.

37. Yang, H. G.; Sun, C. H.; Qiao, S. Z.; Zou, J.; Liu, G.; Smith, S. C.; Cheng, H. M.; Lu, G. Q., Anatase TiO$_2$ single crystals with a large percentage of reactive facets. *Nature* **2008,** *453*, 638.

38. Joo, J.; Chow, B. Y.; Prakash, M.; Boyden, E. S.; Jacobson, J. M., Face-selective electrostatic control of hydrothermal zinc oxide nanowire synthesis. *Nature Mater.* **2011,** *10*, 596.

39. Barnard, A. S.; Curtiss, L. A., Prediction of TiO$_2$ Nanoparticle Phase and Shape Transitions Controlled by Surface Chemistry. *Nano Lett.* **2005,** *5*, 1261-1266.

40. Lovette, M. A.; Browning, A. R.; Griffin, D. W.; Sizemore, J. P.; Snyder, R. C.; Doherty, M. F., Crystal Shape Engineering. *Ind. Eng. Chem. Res.* **2008,** *47*, 9812-9833.

41. Liu, G.; Yu, J. C.; Lu, G. Q.; Cheng, H.-M., Crystal facet engineering of semiconductor photocatalysts: motivations, advances and unique properties. *Chem. Commun.* **2011,** *47*, 6763-6783.

42. Jun, Y. W.; Casula, M. F.; Sim, J. H.; Kim, S. Y.; Cheon, J.; Alivisatos, A. P., Surfactant-assisted elimination of a high energy facet as a means of controlling the shapes of TiO$_2$ nanocrystals. *J. Am. Chem. Soc.* **2003,** *125*, 15981-15985.

43. Buonsanti, R.; Carlino, E.; Giannini, C.; Altamura, D.; De Marco, L.; Giannuzzi, R.; Manca, M.; Gigli, G.; Cozzoli, P. D., Hyperbranched Anatase TiO$_2$ Nanocrystals: Nonaqueous Synthesis, Growth Mechanism, and Exploitation in Dye-Sensitized Solar Cells. *J. Am. Chem. Soc.* **2011,** *133*, 19216-19239.

44. Bai, Q.; Lavenas, M.; Vauriot, L.; Le Tréquesser, Q.; Hao, J.; Weill, F.; Delville, J.-P.; Delville, M.-H., Hydrothermal Transformation of Titanate Scrolled Nanosheets to Anatase over a Wide pH Range and Contribution of Triethanolamine and Oleic Acid to Control the Morphology. *Inorg. Chem.* **2019,** *58*, 2588-2598.

45. Boyle, T. J.; Lambert, T. N.; Pratt, H. D.; Lu, P.; Griego, J. J. M.; Bush, N.; Chavez, C. A.; Welk, M., Morphological and phase dependence of nanotitania materials generated under extreme pH conditions for large scale production of TiO$_2$ nanowires (basic) and nanosquares or nanrods (acidic). *J.*

Mater. Sci. **2010,** *45*, 1744-1759.

46. Tran, T. H.; Nosaka, A. Y.; Nosaka, Y., Adsorption and Photocatalytic Decomposition of Amino Acids in TiO$_2$ Photocatalytic Systems. *J. Phys. Chem. B* **2006,** *110*, 25525-25531.

47. Bae, H. S.; Lee, M. K.; Kim, W. W.; Rhee, C. K., Dispersion properties of TiO$_2$ nano-powder synthesized by homogeneous precipitation process at low temperatures. *Colloids Surf., A* **2003,** *220*, 169-177.

48. Parks, G. A., The Isoelectric Points of Solid Oxides, Solid Hydroxides, and Aqueous Hydroxo Complex Systems. *Chem. Rev.* **1965,** *65*, 177-198.

49. Wu, D.; Liu, J.; Zhao, X.; Li, A.; Chen, Y.; Ming, N., Sequence of Events for the Formation of Titanate Nanotubes, Nanofibers, Nanowires, and Nanobelts. *Chem. Mater.* **2006,** *18*, 547-553.

50. Liu, Y.; Tang, A.; Zhang, Q.; Yin, Y., Seed-Mediated Growth of Anatase TiO$_2$ Nanocrystals with Core-Antenna Structures for Enhanced Photocatalytic Activity. *J. Am. Chem. Soc.* **2015,** *137*, 11327-11339.

References page 63

Chapter 3

Setup Configuration and Laser Control

Table of contents

In this chapter, we will describe three different setups built and used to perform the photochemical deposition of the metallic dots onto the semiconductor nanoparticles (NPs). The first one uses a UV laser with a beam waist focused inside a microchannel, later called microchannel setup, the second one uses the same UV laser with a waist large enough to correctly illuminate a 1 cm wide PMMA cuvette, later called "cuvette setup using UV laser" and finally a classical UV lamp setup where a PMMA cuvette is exposed to a collimated 1 cm wide UV beam produced by a high-pressure mercury lamp. The setups either use different light sources (UV laser or UV lamp of very close wavelengths) or variable reaction vessels (microchannel or UV cuvette). The photochemical deposition induced by focused lasers in the microchannel setup involves neither mask nor asymmetric environment: the experiment is carried out in volume (and not at the interface between two media, for instance). The method is contactless since it is based on the localized excitation of semiconductor nanoparticles in suspension for the generation of electron-hole pairs. Special care should nonetheless be taken to get accurate control of the UV laser beam size and power and on the microchannel inner surface modification. The results obtained from cuvette setups using either UV laser or UV lamp will be presented and discussed.

3.1 Microchannel setup for photodeposition

The microfluidic setup consists of building a dedicated microchannel and laser exposure system to perform the Janus synthesis in a continuous flow. Figure 3.1 shows a simplified scheme of this microchannel setup.

References page 96
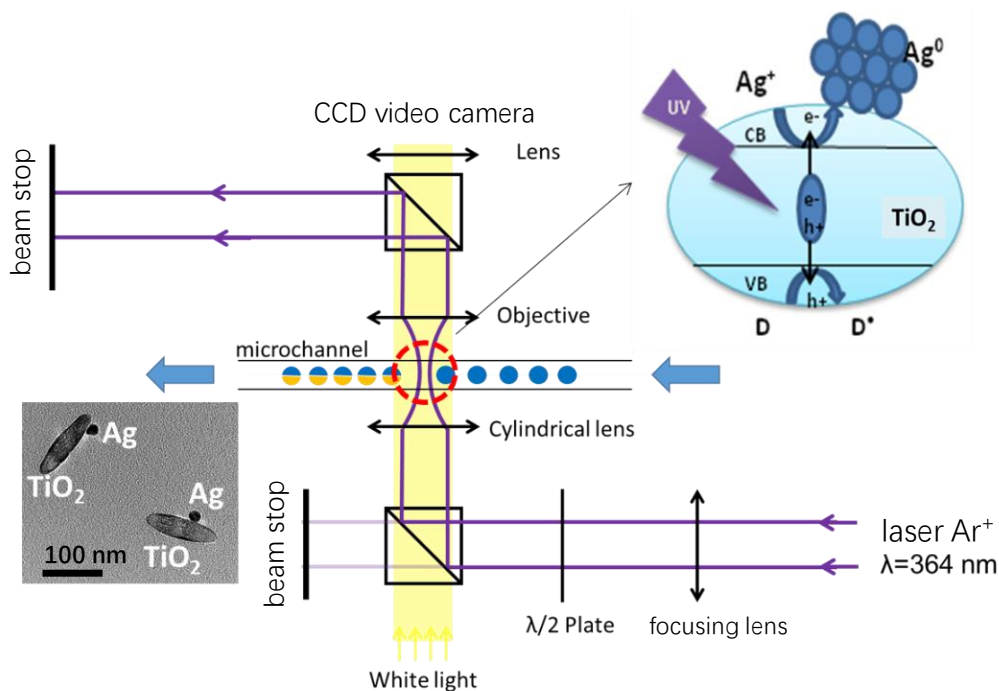
Figure 3.1 Simplified scheme of the microchannel setup.

The precursor solution is driven by a syringe pump into the microchannel. The UV laser goes through the microchannel, irradiates the mixture solution and excites the TiO_2 NPs. Electron-hole pairs are produced in the TiO_2 NPs; they can then recombine in bulk, be trapped in the bulk and surface defects or migrate to the surface and react at the interface with species in solution. The electrons can be used to reduce metal ions flowing in the TiO_2 suspension, and the holes can oxidize hole scavengers also in solution. The white light illumination and the CCD camera help to detect the laser beam position inside the microchannel and to observe the photochemical deposition on the nanoparticles in the microchannel. At high laser intensities, dissymmetric dimers are formed in the solution, with a single metal particle deposited onto the surface of each TiO_2 NP as illustrated in Figure 3.1.

3.1.1 Global view of the microfluidic setup

A detailed picture of the microchannel setup is shown in Figure 3.2a. Quantitative description is given in Figure 3.2b. As discussed in the following, these optical elements, optical distances and optical materials are chosen on the one hand to control the beam size and intensity inside

72

the microchannel and on the other hand to build dedicated microchannels free of metallic components.
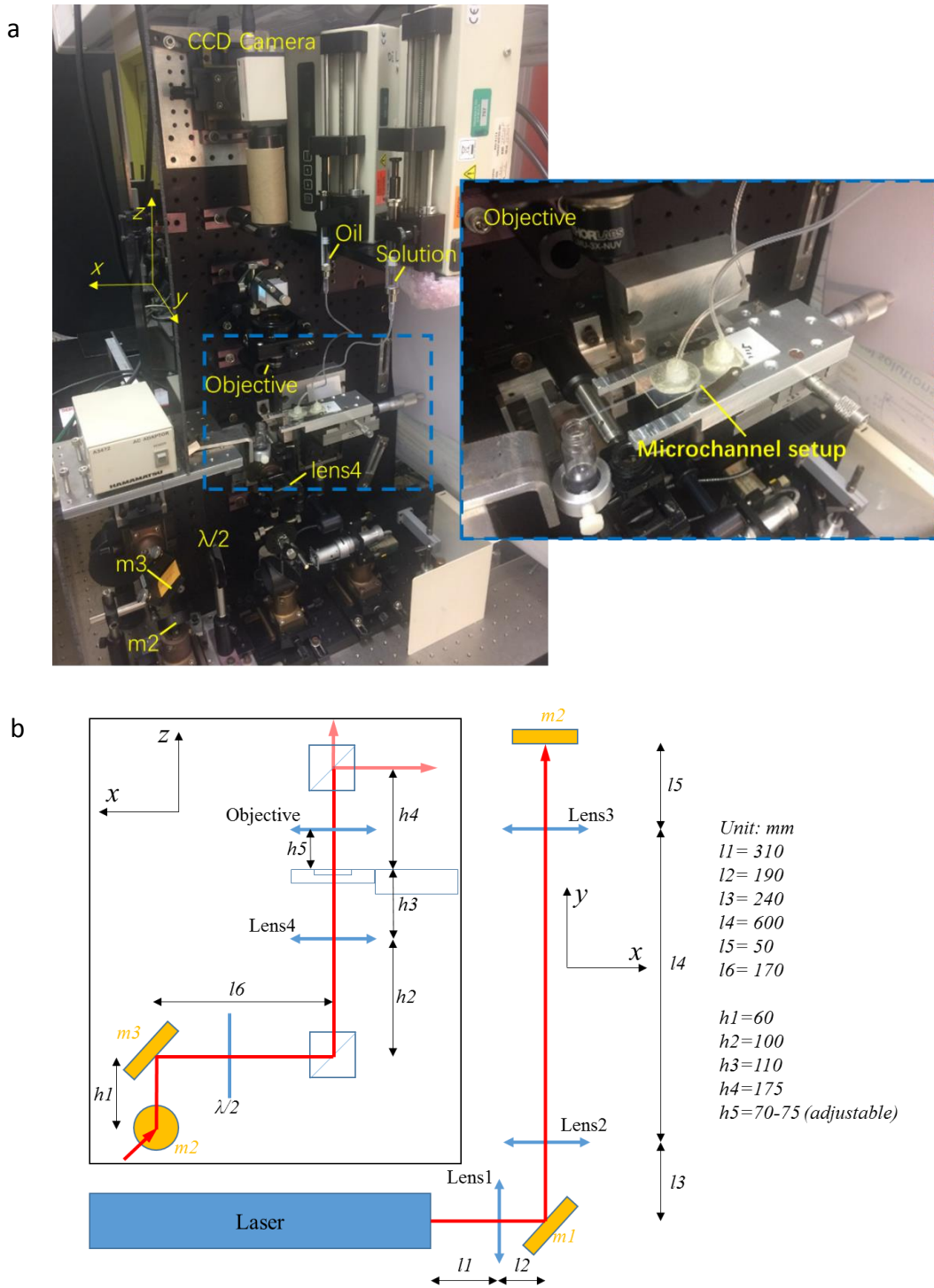
Figure 3.2 (a) Picture of the microchannel setup and (b)quantitative description.

73

3.1.1.1 Laser apparatus

Here we use a continuous Argon ion UV laser (Innova 306C, Coherent). The UV laser apparatus is shown in Figure 3.3.
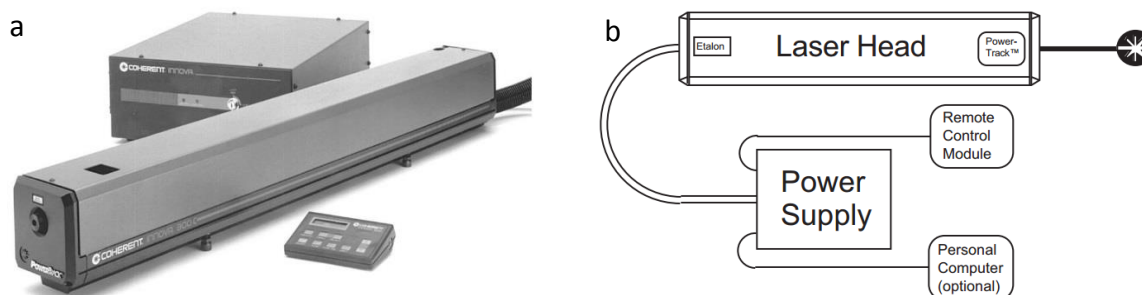
Figure 3.3 UV laser apparatus a) photo of the laser, b) schematic functional parts

The wavelength of the UV laser is 363.8 nm, used to excite TiO_2 anatase semiconductor, for which the band gap is around 3.2 eV (for bulk TiO_2)[1], corresponding to 380 nm. The nominal power given by the apparatus ranges from 5 to 200 mW, with a maximum current achievable of 50 A.

3.1.1.2 UV lens and positioning

Considering the distance from the laser head to the expected channel position, three UV lenses focus the laser beam, with minimum power losses, at the microchannel location with the desired size. All the information about the UV lens is listed in Table 3.1. The focal length f_i (I = 1, 2, 3) of Lens1, Lens2 and Lens3 are 300, 100 and 500 mm, respectively. Considering the beam size and divergence at the exit of the laser head, the distance between the laser head and the microchannel location on the one hand, and the chosen size of the microchannel, on the other hand, the goal is to produce a beam diameter that correctly fills the microchannel width, here around 500 μm. The system Lens2/lense3 is a magnification system (5X) that increases the beam waist created by Lens1 at a distance – f_2 from Lens2. Then Lens1 is chosen to create a first intermediate beam waist small enough to be increased by a factor of 5 at the right size in the microchannel.

	Lens1	Lens2	Lens3	Lens4
Series number	Thorlabs, LA4579-A-ML	Thorlabs, LA4380-A-ML	Thorlabs, LA4184-A-ML	\
Focal length	300 mm	100 mm	500 mm	125 mm
Antireflection coating range	350-700 nm	350-700 nm	350-700 nm	\
Lens shape	Plano/convex	Plano/convex	Plano/convex	Half cylindrical
Substrate materials	UV graded fused silica			\
Transmission	> 93%	> 93%	> 93%	93%

Table 3.1 UV lens parameters and objectives

Since the combination of lenses can be treated as a whole focusing system, the transmission of each lens is not measured experimentally. However, both the excellent transmission of uncoated fused silica (Lens4) and combined antireflection coating of Lens1-3 favour very good UV laser transmission through the optical path, and reduce energy loss (Figure 3.4).
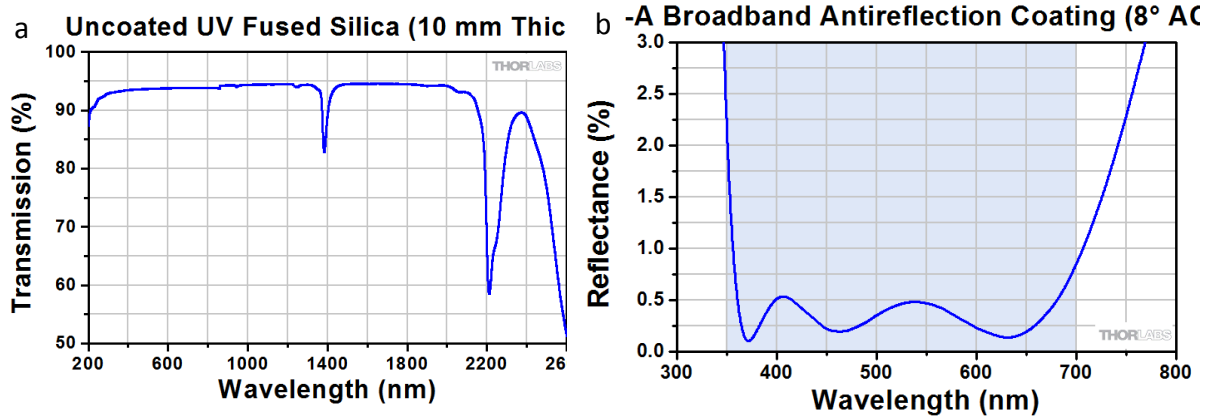
Figure 3.4 (a) Transmission curve for a 10 mm thick uncoated UV fused silica lens, as Lens4, when the incident light is normal to the surface. (b) The blue shaded region indicates the specified 350 - 700 nm wavelength range of antireflection coated lenses, as Lens1, Lens2 and Lens3. Data source: Thorlab corporation.

Ideally, a homogeneous intensity distribution with steep edges in the microchannel would be the best choice for photodeposition. Nonetheless, it is challenging to get such a homogeneously distributed photon intensity from a Gaussian laser (see Figure 3.5a) without losing a considerable amount of photons, which can be a severe drawback for the photochemical deposition yield.

75
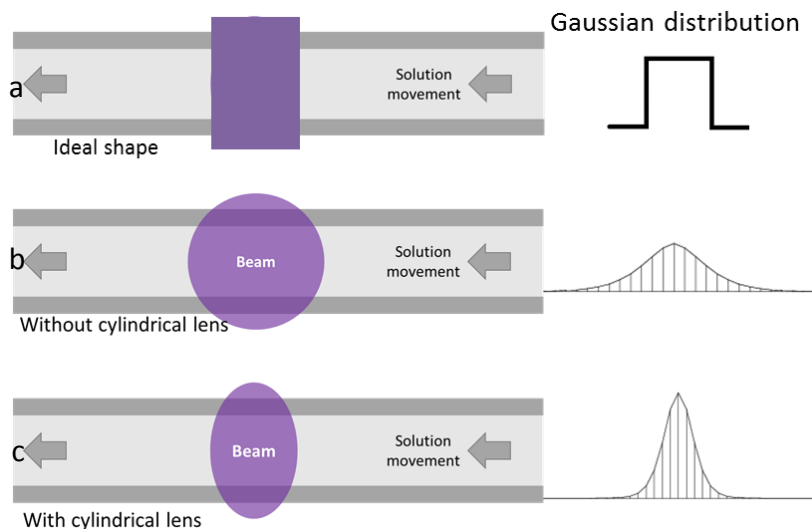
Figure 3.5 UV laser beam shape in a microchannel and the corresponding Gaussian distribution curve.

Consequently, we decide to keep the Gaussian distribution and use a cylindrical lens (f = 125 mm, lens4 in Figure 3.2) to create a sort of light bar passing through the microchannel and concentrate the photons. The beam cross-section varies from circular (Figure 3.5b) to elliptical (Figure 3.5c) when lens4 is added to the system, thus causing an even higher intensity in the beam area.

3.1.1.3 Imaging system

A CCD camera Hamamatsu C5405 is installed in order to check the laser location in the microchannel and, also to get some insights on the processing of the photochemical reaction. A Glan prism is used to remove UV light as much as possible and prevent potential damages to the camera. The laser location is easily observed from fluorescence at surfaces of the microchannel. The image of the microchannel is magnified by a UV objective (LMU-3X-NUV, Thorlabs), detected by the CCD camera, and finally recorded by a frame grabber (National Instrument, 1410 board and analyzed using a software, Visionstage (version 1.9fr, designed by Alliance vision) on a computer. The user interface of Visionstage is presented in Figure 3.6.
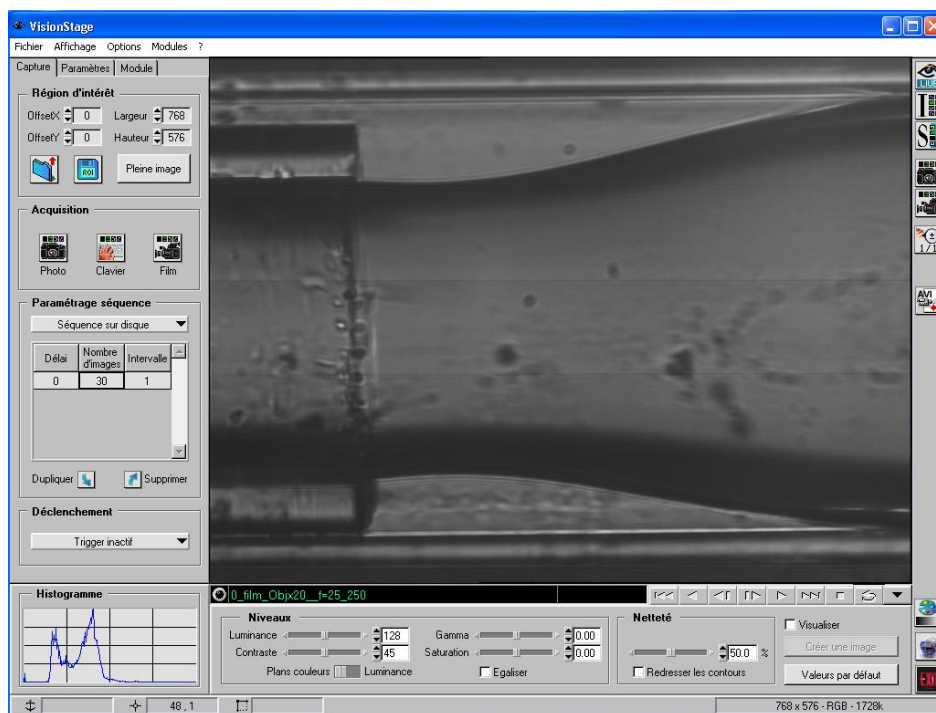
Figure 3.6 The user interface of Visionstage.

In the main window, a darkly shaded drop of solution is forming at the exit of the round channel located inside the square microchannel (see below for details on the microchannel fabrication). A real-time monitor can help us to calibrate and check the flow conditions, in the microchannel as a function of the flow rates imposed to the syringe pumps. The images recorded by the software can be merged and converted to a short video. So this simple software combined to the CCD camera is frequently used to check operating conditions and monitor the in situ photochemical processes inside the microchannel.

3.1.2 Single microchannel configuration

The first type of microchannel is a simple square glass capillary (from the Vitrocom company), with wall thickness of 120 μm and an internal 600x600 μm^2 area. Preliminary laser irradiation of flowing solutions in such a microchannel showed that photodeposition occurred on the TiO$_2$ NPs but also the internal surface of the channel, altering the beam transmission and then the photoproduction of Janus particles. We performed several experiments with this type of microchannel, and observed low reproducibility, which is likely

77

due to the photodeposition at the glass surface (Figure 3.7). This wall photodeposition could be attributed to the reduction of the Ag^+, which can interact, with the naturally negatively charged surface of the glass material.[2]
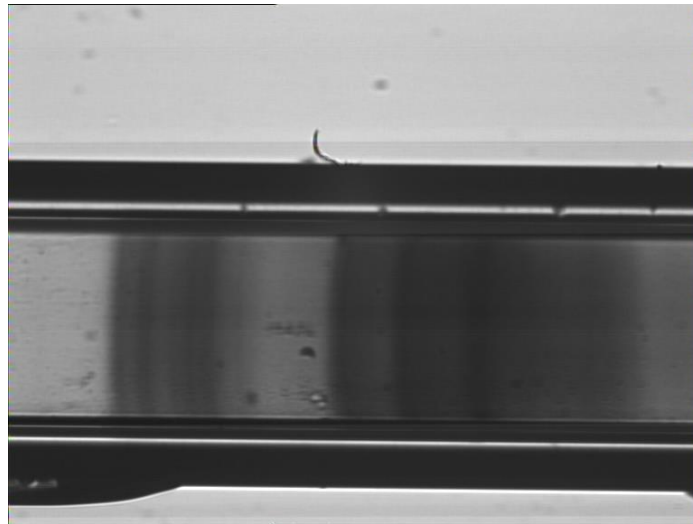
Figure 3.7 deposition on the inner surface of the glass channel.

We also tried another channel material, Purified Terephthalic Acid (PTA) tube (Diameter 1.5 mm) a hydrophobic material, in order to solve this problem of photodeposition on internal surfaces. However, the same issue still showed up around the laser crossing area. Glass and PTA, even though dielectric materials, may release electrons when activated by UV that can react with flowing metallic ions to produce metallic deposits on the surfaces at the beam location.

Transmission measurements of both glass and PTA channels were also performed. From Figure 3.8, the glass channel displays a much better transmission than the PFA channel, no matter filled with either water or TiO_2 solution. Glass channels were then chosen as the elementary bricks for future experiments.
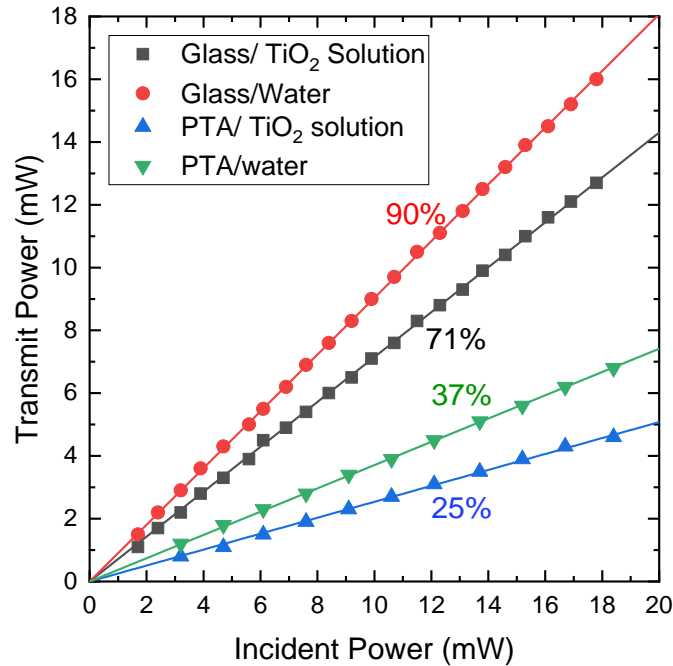
Figure 3.8 Beam power transmitted by the glass and PFA channels filled with water or TiO₂ solutions as a function of the incident power.

To solve this problem, in the following part, we first suggest a surface modification via a silanization process[3] to modify the surface properties of the glass channel and make it more hydrophobic; and then managed a two-fluid approach to avoid the deposition problem on the inner surface.

3.1.3 Double microchannel configuration

3.1.3.1 Silanization of the square glass channel

The aim of the silanization of the glass channel is to form a dense hydrophobic layer on the inner surface of the microchannel, in order to avoid any contact between the silica surface and the reactive solution during the photoexcitation process. The principle consists in using a functionalized alkoxysilane which will provide the targeted surface with the desired property. The mechanism of the surface modification is depicted in Figure 3.9.
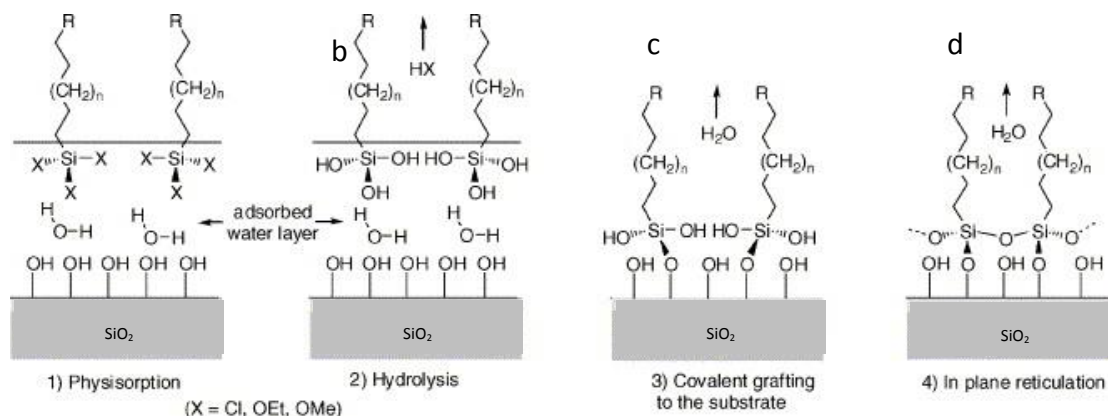
Figure 3.9 Scheme of the different steps involved in the mechanism of self-assembled-monolayer formation on a hydrated silica surface, adapted from ref.[3].

The surface modification takes place in four steps[3]. The first step is physisorption, in which the silane molecules get physisorbed at the hydrated silica surface. In the second step, the silane head-groups arriving close to the substrate hydrolyze—in the presence of the adsorbed water layer on the surface—into highly polar trihydroxysilane $Si(OH)_3$. These polar $Si(OH)_3$ groups react by condensation to form Si-O-Si covalent bonds not only with the hydroxyl groups on the SiO_2 surface (third step) but also with the remaining silanol functions of the neighbouring molecules. Self-assembly is driven by the lipophilic interactions between the linear alkane moieties. At longer times, the surface coverage eventually reaches the point where a well-ordered and compact monolayer is obtained (step four, Figure 3.9d).

The silanization process of the channels was performed using the following method. Firstly, the square glass channels were immersed in pure water in a plastic Falcone tube and were sonicated for 30 min. to remove impurities on the inner surface. Then the square channels were dried at 80 °C overnight. Secondly, the channels were pre-irradiated under UV light to form more OH groups on the inner surface for 2 min in a plasma cleaner and subsequently plunged into a chloroform solution containing 2 vol.% of octyltrichlorosilane. The tube containing the channels and the octyltrichlorosilane solution was sealed and rolled on a roller machine for 24h. The channels were eventually taken out and rinsed with chloroform three times to remove the remaining silane solution, and then dried at 80 °C in an oven. In the end, the glass capillaries are totally silanized, and in particular the inner surface. This induced hydrophobicity should help to prevent the photodeposition on the inner surface of the

80

microchannel. However, new experiments with simple silanized square channels showed that the silanization alone was not sufficient to do so. Therefore, we decided to use two-fluid flows in order to coat the glass surface with an inert liquid so as to remove this tedious difficulty.

3.1.3.2 Fabrication method

The need to create a thicker inert layer that prevents photodeposition on the glass surface led us to design a double microchannel system (Figure 3.10). The external square silanized one is used to flow an oil (here n-dodecane, transparent at the used UV wavelength, and considered as a good dielectric) with a non-ionic surfactant (here sorbitan oleate (SPAN80)). The internal one will flow the water solution containing the reactants. Indeed, as the oil is attracted by surfaces made hydrophobic by the silanization, it should tend to wrap a co-flowing aqueous solution and form large water-in-oil drops inside the microchannel, due to the Rayleigh instability of liquid threads.[4] As can be seen from Figure 3.10, a round channel (ID/OD, 400/550 μm) was embedded partially into the silanized square channel, from which the aqueous solution comes out.
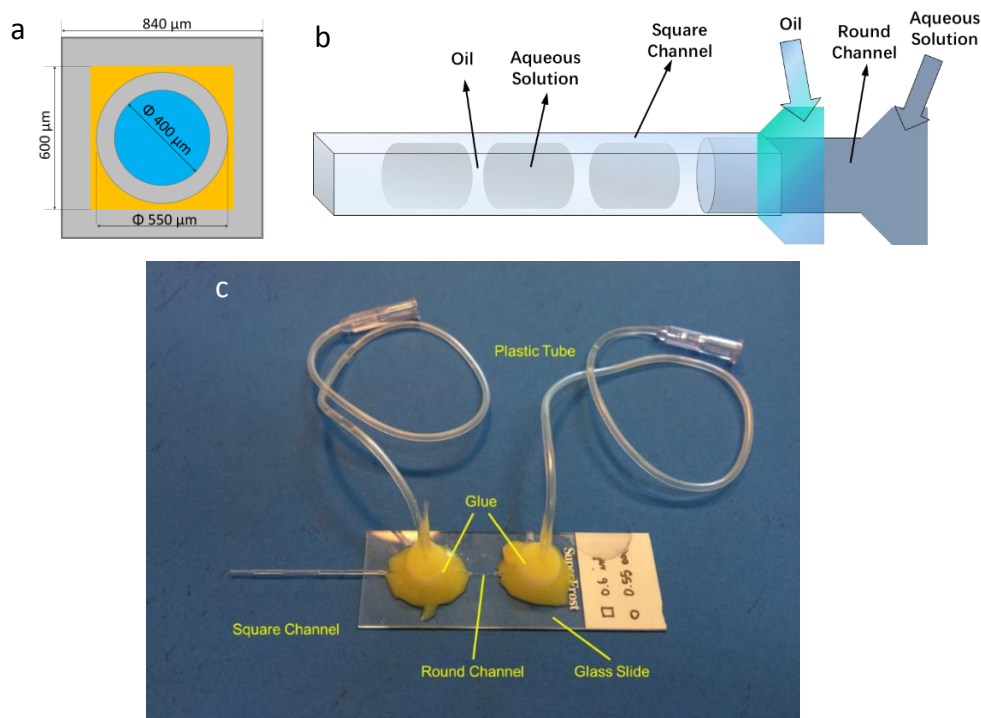
Figure 3.10 Scheme of the double microchannel system. Square cross-section (yellow part) indicates the oil flow, and interior circular cross-section (blue part) denotes the aqueous flow (top). Photograph of double microchannel setup (bottom).

The oil is injected through the four corners between the square and round channel. The two square and round channels were respectively connected with oil and aqueous solution reservoirs, by plastic tubes. The channels and the plastic tubes were both supported onto a glass slide. Syringe pumps drive the fluidic flow to proceed in the microchannel.

3.1.4 Fluid velocity vs. flow rate

Once the UV laser waist size is fixed, the exposure duration of the solution when passing the UV region can be determined by the velocity of the aqueous solution. Due to the uniform cross-section of the square channel, the velocity can be adjusted by the flow rate set on the syringe pumps.

The double microchannel system here contains one long square and one round microchannel, into which the oil and the aqueous solution were injected, respectively. The flow rate ratio between aqueous and oil part solutions was set as 4:1. That is, the volumetric ratio is also 4:1. At this ratio, the aqueous solution, wrapped by the oil part, form separated long drops inside the square channel. Thus, it provides us with an opportunity to observe the mean drop flow inside the square channel.

In order to measure the velocity of solution drop in the microchannel, we recorded images at three time points, where the length of drop A advances from l_1 to l_3 during the period from time t_1 to time t_3, as shown in Figure 3.11 on the CCD camera window. The velocity of drop A is then defined by $v = \dfrac{l_3 - l_1}{t_3 - t_1}$. For each velocity at a specific flow rate, at least four different drops were recorded and measured to obtain the average value.
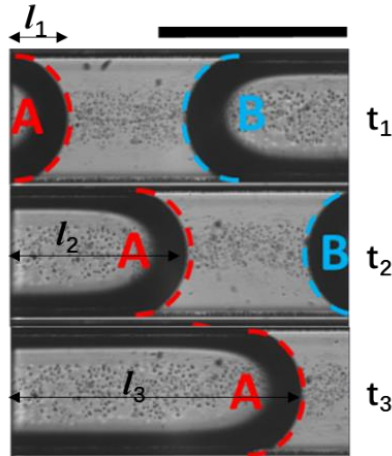
Figure 3.11 Flow evolution of water solution (drop A and B) in the microchannel at three-time points (t₁, t₂ and t₃, respectively). The length of drop A shown in the camera window was defined from the left side of the window to the forefront side of the drop and denoted as l₁, l₂ and l₃, respectively. The bar on top is 600 µm.

Figure 3.12 displays the velocity of a drop as a function of the applied water flow rate.
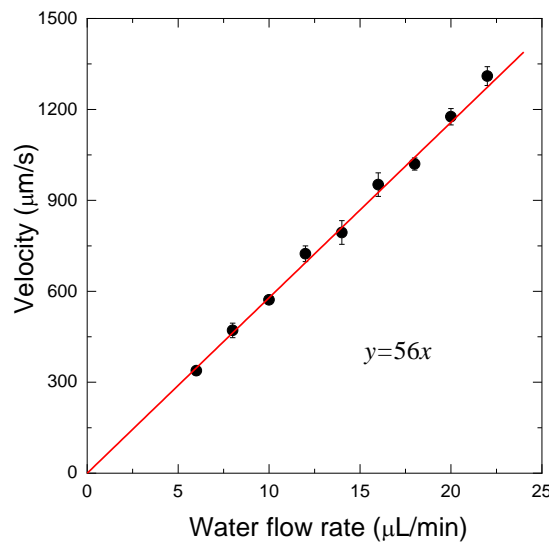
Figure 3.12 The velocity of drop vs applied water flow rate for a 4:1 imposed flow rate ratio.

The expected linear relationship between the velocity (in µm/s) and the imposed flow rate (in µL/min) follows $y = 56x$. Knowing the beam size inside the channel, this relation gives us the time spent in the UV exposed area by the flowing particles.

3.1.5 Laser size control

In practical terms, even with perfectly aberration-free lenses, a Gaussian beam cannot be focused to a geometric point. The position where the beam owns the smallest size along the

beam propagation direction is called beam waist (w_0). At the beam waist, the beam owns the most considerable photon intensity. In our setup, the beam waist produced by Lens1-3, is already adjusted at the channel position. Moreover in order to create a "light bar", just before arriving at microchannel setup, the UV laser is also focused in one direction by a well-positioned cylindrical lens Lens4 (focal length 125 mm) (Figure 3.13) to produce an elliptical beam whose waist in the two directions to the beam propagation are located at the channel position.
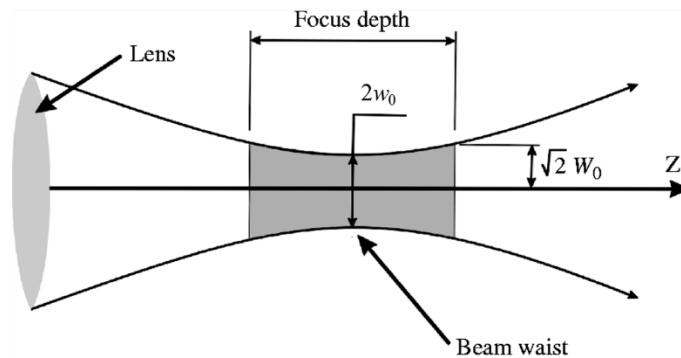
Figure 3.13 Schematics of a Gaussian beam with waist w_0 at the origin of the reference system (z = 0)
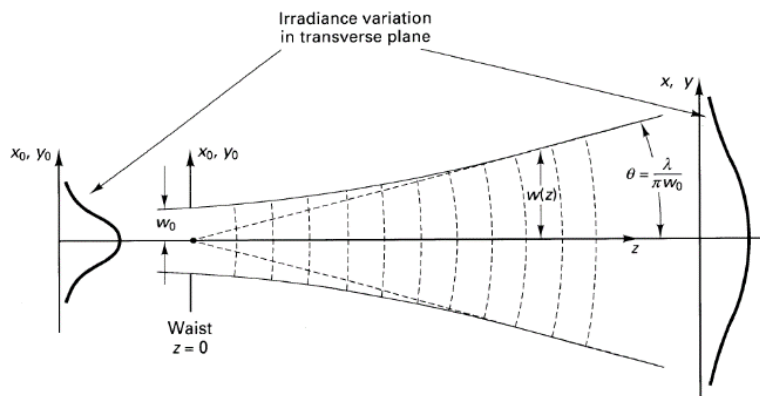
Figure 3.14 Gaussian beam propagation

As seen in Figure 3.14, along with the propagation direction *z*, the irradiance profile turns to broaden around *x,y* plane when increasing the distance to the beam waist. If we define the radius of the laser beam at position *z* as w_z. it follows equation behaviour given by:

$$w_z^2 = w_0^2 + (\frac{\lambda z}{\pi w_0})^2 \qquad \qquad \textit{Equation 3 1}$$

84

$$w_0^4 - w_z^2 w_0^2 + \left(\frac{\lambda z}{\pi}\right)^2 = 0 \qquad\qquad \textit{Equation 3 2}$$

Where λ is the optical wavelength in vacuum.

In order to carry out the size measurement of the two beam waists at the channel position, a power meter (Milles Griot brand) equipped with a spectral filter, is mounted at the place where the distance is z = 75 cm between the iris on the power meter and the beam waists position (see Figure 3.15).
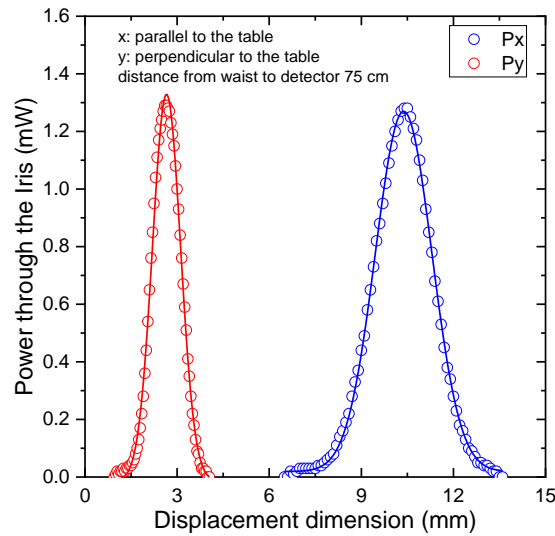
Figure 3.15 Measurement of the laser beam waists in the microchannel and the related fitting curves

The power meter was able to move parallel and perpendicular to the vertical table, in a step of 0.05 and 0.1 mm corresponding to x and y-axis, respectively. The measured data show a fitting to a Gaussian curve of the beam power at z = 75 cm. The fitting results indicate $w_{z,x}$ = 1.84 mm and $w_{z,y}$ = 0.91 mm.

According to $w_0^4 - w_z^2 w_0^2 + \left(\frac{\lambda z}{\pi}\right)^2 = 0$, with the values: λ = 363.8 nm, z = 75 cm, $w_{z,x}$ = 1.84 mm and $w_{z,y}$ = 0.91 mm, we find the waist sizes: $w_{0,x}$ = 215 µm, $w_{0,y}$ = 95 µm.

Finally, we determined that the UV beam waist size parallel to the table was 95 µm, and the beam waist perpendicular to the table was 215 µm. Perpendicularly to the flow direction, the beam size is 430 µm, very close to the internal size of the microchannel and then ensuring light exposure over the whole channel section. Moreover, following the flow direction, the

85

exposure length of the solution under UV laser is 190 µm (Figure 3.16), giving us the exposure

time if we know the flow velocity.
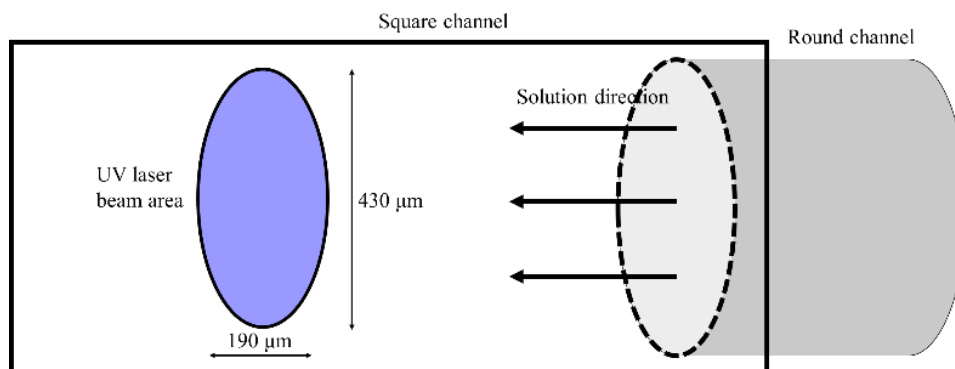
Figure 3.16 Scheme of actual UV beam exposure area in the microchannel system.

3.1.6 Laser power control

3.1.6.1 Half-wave plate angle

A half-wave plate turns the polarization state of the incident light wave travelling through it.

Thus, in addition to a first Glan prism, as illustrated on the optical setup, it can be used to

adjust the applied power in the channel. Figure 3.17 shows the laser power incident to the

microchannel versus the half-wave plate angle.
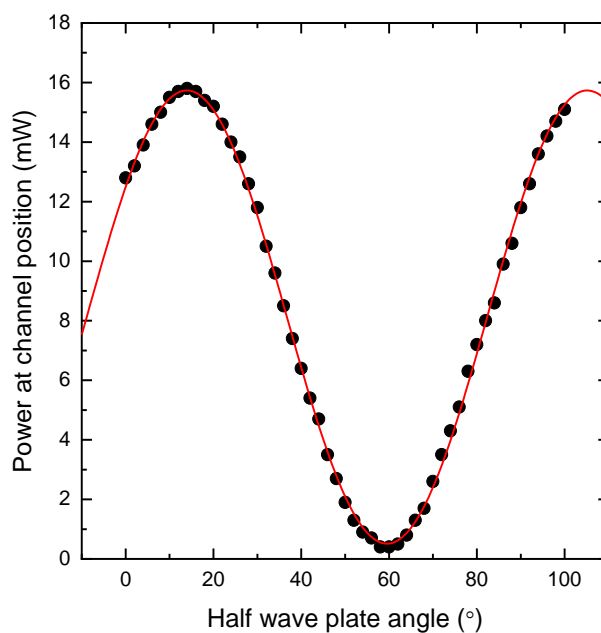
Figure 3.17 Incident power as a function of a half-wave plate angle.

86

From the result, we get:

$$P_{in} = 15.7 \cos[2(\theta - 14.6)]^2$$ *Equation 3.3*

under the condition: light control panel, 22 mW corresponding to 19.7 mW exit laser power.

3.1.6.2 Power in the microchannel

When the UV laser goes through the glass channel filled with a TiO_2 solution, the reflection of the glass and absorption/scattering effect of TiO_2 NPs causes losses of the UV laser power (Figure 3.18).
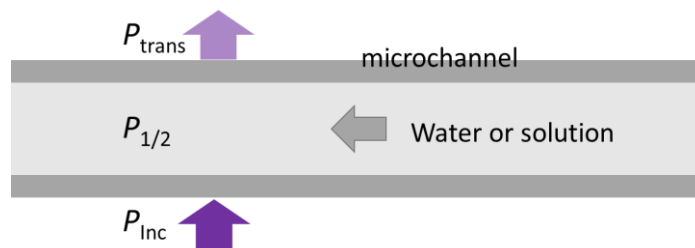
Figure 3.18 Diagram of a microchannel with the incident laser power, the transmitted power P_{trans}, and the power inside the microchannel $P_{1/2}$.

We get the relation between the power inside the microchannel $P_{1/2}$ and the incident power P_{Inc},

$$P_{1/2} = P_{inc} \sqrt{\frac{P_{trans}}{P_{inc}}} = \sqrt{0.71} P_{inc}$$ *Equation 3.4*

Figure 3.19 shows the linear relationship between exit power and panel power in light control mode,

$$P_{exit} = 0.951 P_{Panel}$$ *Equation 3.5*
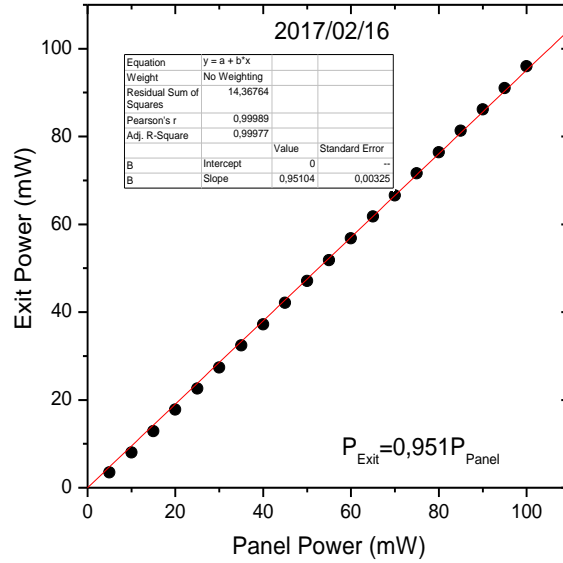
Figure 3.19 Exit power from the laser head as a function of the Panel Power.

Here follows the calculation of $P_{1/2}$ power depending on the panel power P_{panel} (in light control mode), when the microchannel is filled with TiO_2 solution.

$$P_{inc} = \frac{f(\theta)}{19.7} P_{exit} \qquad \text{Equation 3.6}$$

$$P_{1/2} = P_{inc} \sqrt{\frac{P_{trans}}{P_{inc}}} \quad \text{with} \quad P_{trans} = \sqrt{0.71} P_{inc}$$

Thus we get

$$P_{1/2} = \sqrt{0.71} \frac{f(\theta)}{19.7} 0.951 \, P_{Panel} = 0.64 \cos[2(\theta - 14.6)]^2 P_{Panel} \qquad \text{Equation 3.7}$$

For a fixed panel power, one can calculate the angle of the half-wave plate to obtain the expected power $P_{1/2}$ in the middle of the microchannel. Then, we perfectly characterized the properties of the UV laser beam, waists and power that goes through the microchannel for photodeposition experiments.

3.2 UV cuvette setup using large UV laser exposure

In this section, we discuss the other experimental setup used during the present work. While still keeping the UV laser as the light source, we use a UV cuvette instead of glass microchannel as a reaction vessel. The exposure area was designed to be around 1 cm in diameter to fill a 1

cm wide cuvette, while the microchannel setup owns an area in sub-millimeter scale; thus the intensities between these two setups largely differ for an identical laser power. Instead of the short exposure durations of the flowing solutions flow in the microchannel due to the small range of variation of the flow rate, the UV cuvette setup allows large duration experiments on demand. The much larger available solution volume in cuvette setup would also enable magnetic stirring inside the vessel, making sure that photochemical reactions are performed in well-controlled conditions. The UV cuvette setup is complementary to the microchannel one. For the same light energy deposited in the solution, in the microchannel configuration, this is the flux of photons that matters while in the cuvette setup it is more the time during which the photodeposition occurs.

3.2.1 Schematic picture of the UV cuvette setup

A schematic drawing and a photograph of the UV cuvette setup using the same UV laser are shown in Figure 3.20.
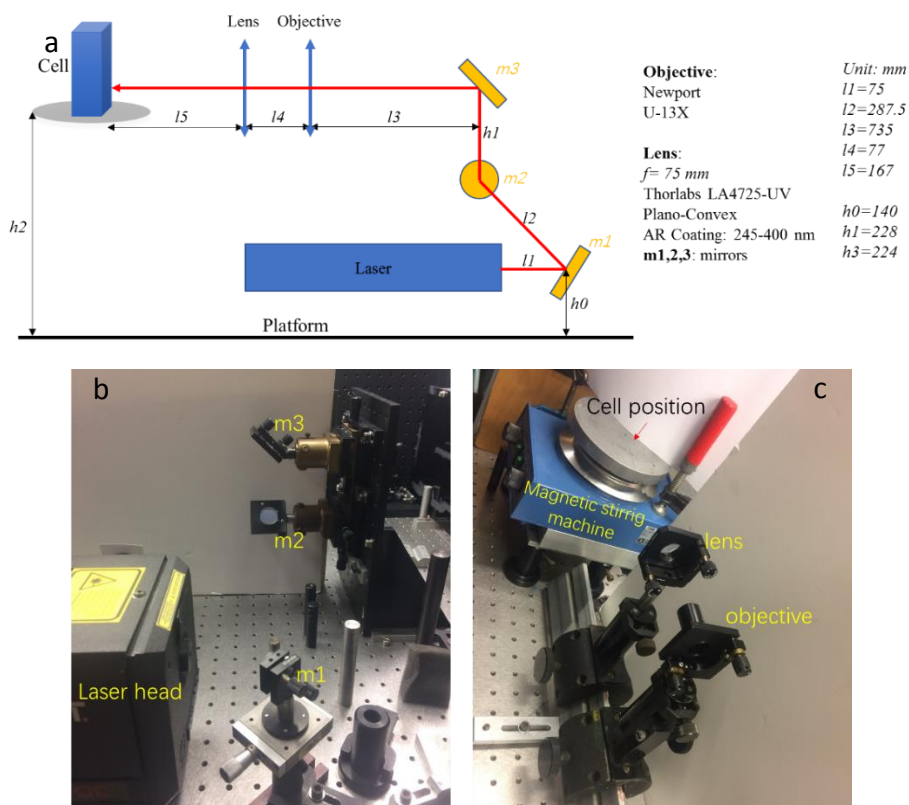
Figure 3.20 (a) Schematic drawing, and (b)(c)photograph of UV cuvette setup using UV laser.

89

After coming out from the laser head, the beam is reflected by one mirror and then elevated by two other mirrors at the same height of the reaction cuvette. The objective and the lens then enlarge and collimate the laser light onto the UV cuvette, leading a laser spot with 1 cm in diameter. The UV cuvette was placed on a magnetic stirring machine to continuously homogenize the particle solution and prevent sedimentation; the stirring speed was set at 300 rpm unless otherwise stated. All experiments made in the UV cuvette were performed under room temperature.

3.2.2 Transmission measurement of the UV cuvette

For the reaction vessels, we mainly use two types of the cuvette, PMMA (Brand, 7591-05) cuvette and Quartz cuvette (Hellma, 110-10-40), both with volume 10*10*40 mm^3, but always filled with 1 cm^3 solution corresponding to the area exposed to UV radiation.

In general, quartz cuvettes are thought to present better chemical stability and transmission, and PMMA cuvettes are frequently used for their disposable use. Transmission measurements in UV of both cuvettes were made in order to check out this issue (see Figure 3.21).
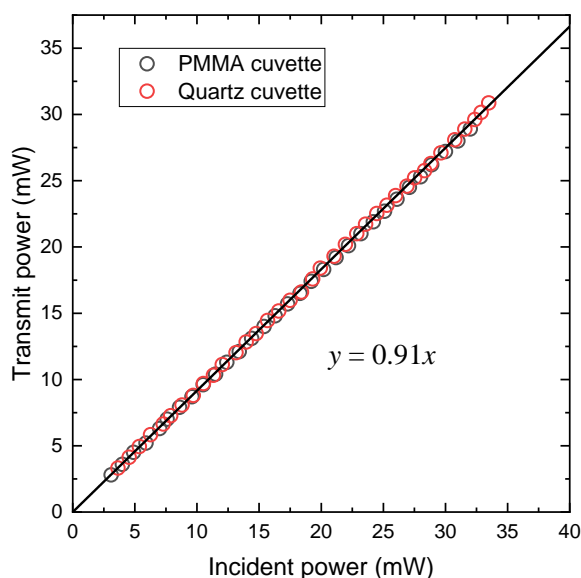
Figure 3.21 Transmission measurement of UV cuvettes fulfilled by pure water at the laser wavelength.

90

As shown from Figure 3.21, the PMMA cuvette shows a quite similar transmission as that of the Quartz cuvette, both displaying a good transmission quality (around 90%). The power inside the cuvette can be written as:

$$P_{1/2} = P_{inc}\sqrt{\frac{P_{trans}}{P_{inc}}} = \sqrt{0.91}P_{inc} = 0.95P_{inc}$$

Where P_{inc} is the incident power before arriving at the UV cuvette.

Since our reaction system mainly contains an aqueous solution or a mixture of water and alcohol the PMMA cuvette can be used without any problem. Therefore, most of our experiments using cuvette setup were performed in such disposable PMMA cuvettes for their good transmission and sake of simplicity.

3.2.3 Power in the UV cuvette vs Power on Panel

Before arriving at the UV cuvette, the UV laser is reflected by mirrors, and passes through the lens and the objective, so that the energy losses are inevitable. A clear linear relationship between the incident power and the panel power was obtained (Figure 3.22).
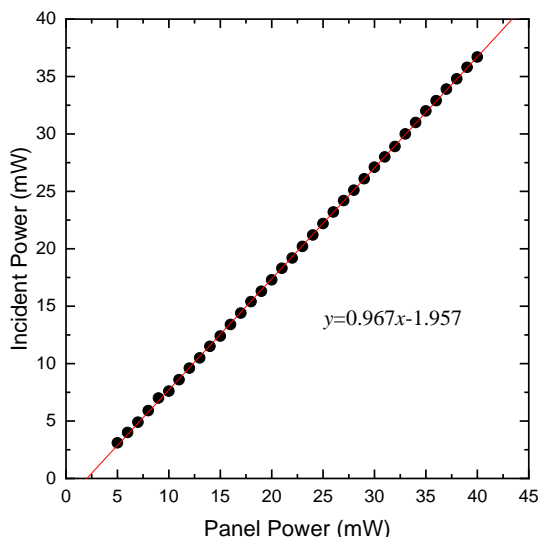
Figure 3.22 Incident Power as a function of panel power.

$$P_{inc} = 0.967P_{panel} - 1.957$$

Then

$$P_{1/2} = 0.95 P_{inc} = 0.95 \left(0.967 P_{panel} - 1.957 \right) = 0.92 P_{panel} - 1.86 \qquad \textit{Equation 3.10}$$

In this way, the applied power inside the cuvette can be adjusted by changing the panel power.

3.3 UV cuvette setup using a UV lamp

The previous two setups utilize a UV laser as the light source. In order to compare our results with already published data, we also exposed our samples to the UV wavelength of a high-pressure Hg lamp (365 nm, close to that of the laser). Most works about photodeposition use indeed a UV lamp (mostly Hg or Xe lamp) rather than a UV laser, for simplicity and convenience; note nonetheless that reachable photon fluxes are tremendously smaller than those obtained with a laser. It should also be noted that in many papers, the exact modus operandi is most of the time not specifically mentioned so that comparison from one paper to the other is often complicated and tedious.

3.3.1 Schematic picture of the UV cuvette setup using a UV lamp

The cuvette setup using a UV lamp is shown in Figure 3.23.
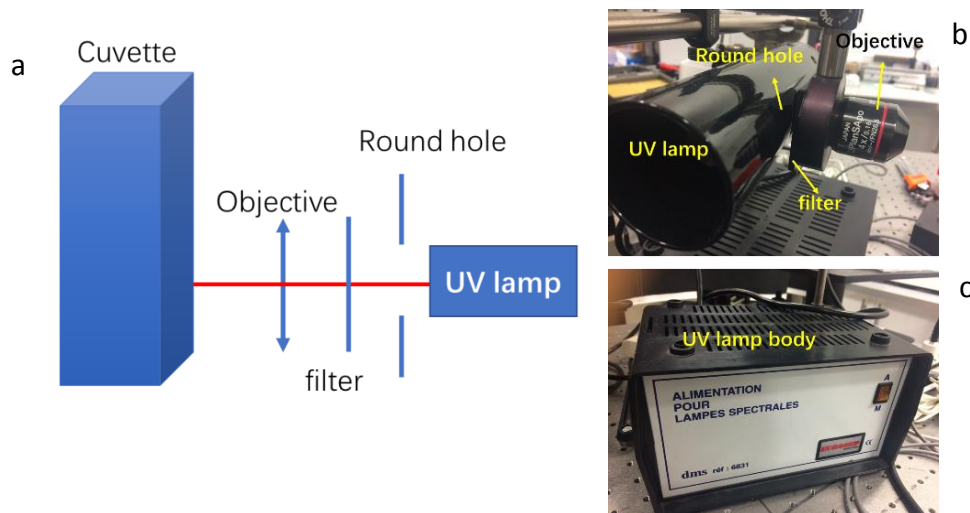
Figure 3.23 (a) Schematic drawing and (b,c)photographs of cuvette setup using a UV lamp.

The UV lamp was placed in a tube with a hole on one side. The UV light comes out from this round hole, passes through a filter and an objective precisely located to produce an exposure

92

area of a 1 cm diameter on the cuvette (Figure 3.23). The filter cuts those lights with wavelength shorter than 365 nm, but allow the visible light to pass. The distance from the round hole to the cuvette is approximately 5 cm put the value on the figure. The measured power inside the cuvette is 0.28 mW. Unfortunately, the power of the UV lamp is fixed so we can only perform experiments only at this power.

3.3.2 UV lamp and its wavelength distribution

The UV emission spectrum of the UV Hg lamp is shown in Figure 3.24.
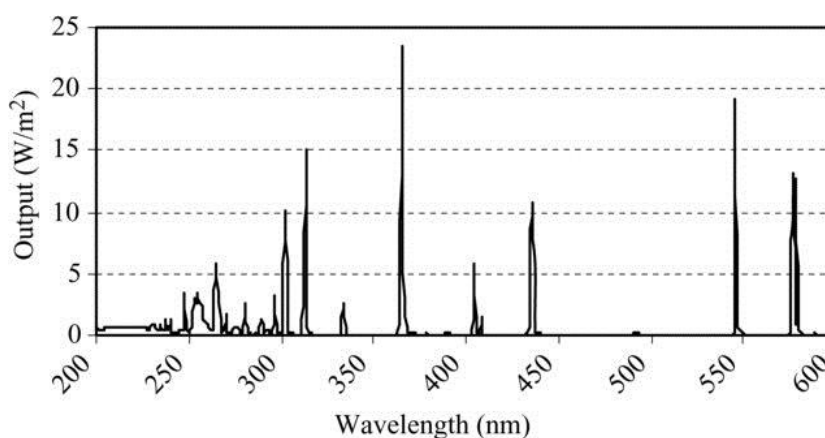
Figure 3.24 The UV emission spectrum of the medium-pressure Hg-lamp

Unlike the UV laser with a single wavelength of 363.8 nm, the Hg lamp emits multi-wavelength light, ranging from 250 to 580 nm, with the main peak at 365 nm. From the UV-vis spectrum of TiO_2 NPs, the shorter wavelengths (less than 365 nm) can photoactivate TiO_2 very efficiently. Even though the filter helps to block the shortest wavelengths, the visible light may affect the electron transfer behaviour, but for already formed Janus nanoparticles. For instance, Au-TiO_2 NPs can be affected by the 550 nm visible wavelength, because of the surface plasmon resonance band of gold nanoparticles. We can then say that the single wavelength-operating mode of a laser would favour us a better understanding of the light effect on the photodeposition process.

3.4 Power intensity and work duration comparison

Although the type and power of lamps used are usually mentioned in experimental procedures of photodeposition[5-10], the photon flux (in mW/cm^2) arriving at the semiconductor particles is not. This should be measured and provided, since the photon flux does primarily affect the rate of deposition and the resulting size of the deposited metallic nanoparticles. Reporting of the photon flux is also essential to allow comparison of studies aimed at determining the effects of process parameters on photodeposition rates.

For most of the papers[11-20] which mentioned the power intensity, the values vary from 1 to 5 mW/cm^2 (in our UV lamp setup, 0.28 mW/cm^2), and the exposure duration for the photodeposition process using a UV lamp takes hours, which may be a drawback for materials synthesis. Moreover, the photodeposition process using a UV lamp produces multi-nanoparticles deposition on each semiconductor nanoparticle, and most of the deposited particles are quite small (around 1-3 nm). In one single case, prolonging UV exposure seemed to increase the size of the deposited particles up to obtaining a single particle on each semiconductor[21], but this result is far from being well-established.

We also performed a few photodeposition experiments using the Hg UV lamp and found similar behaviours as those published in the literature. A mixture of AgNO$_3$ and TiO$_2$ in methanol/H$_2$O solution was irradiated under the UV lamp for 280 min. The TEM results (Figure 3.25) showed that dozens of Ag nanodots were deposited onto each TiO$_2$ surface.
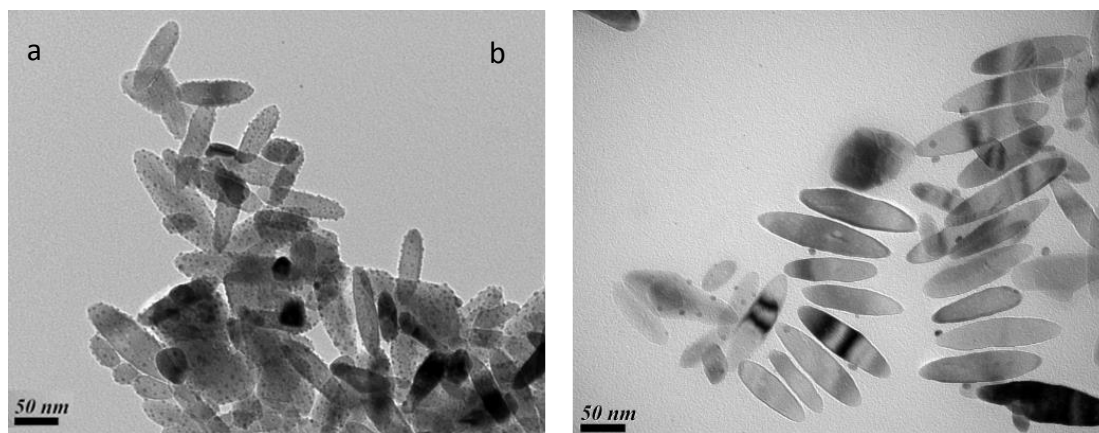
Figure 3.25 (a) Ag-TiO$_2$ NPs made in UV cuvette setup using UV lamp and (b) in a microchannel setup using UV laser. Intensity and exposure time are respectively 0.3 mW/cm^2 for 280 min. and 5000 mW/cm^2 for 0.2 s, while c[TiO$_2$] = 5.5 mM, c[AgNO$_3$] = 2 mM.

While using the high-intensity UV laser microchannel setup, we did obtain the Janus product with the deposition of a single metallic dot per TiO_2 NP, during a scale of milliseconds. The summary plot for the three approaches associated with the three setups concerning the power intensity and the work duration time is shown in Figure 3.26.
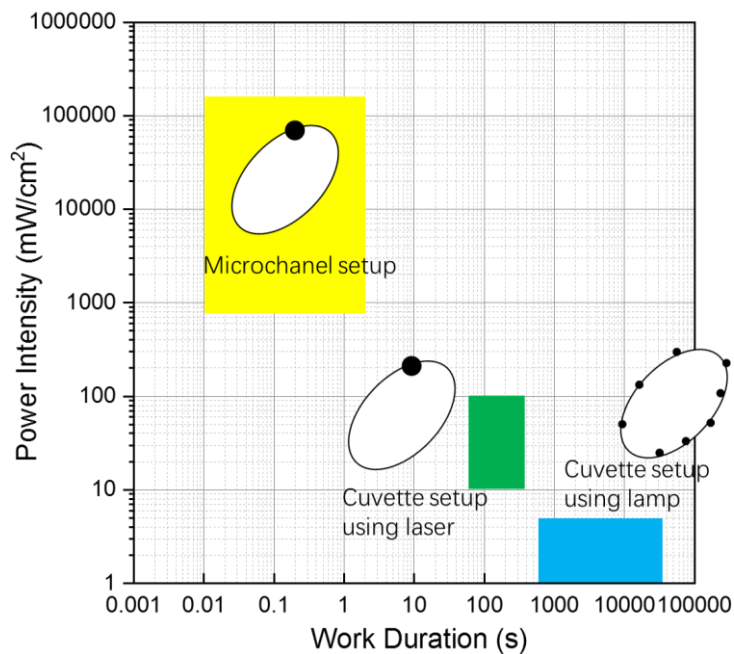
Figure 3.26 Three setups location concerning power intensity and work duration axes.

This diagram enlightens the novelty of our laser deposition approach compared to usual UV lamp experiments. Considering Figure 3.25, it appears that amplitude of the flux of photons matters more than the deposited energy in synthesizing nano-heterodimers, making laser focusing extremely appealing for photodeposition of single dots. The cuvette setup with laser also represents an intermediate situation that can help to understand the involved mechanisms (photon flux versus deposited energy).

95

3.5 Bibliography

1.   Grätzel, M., Photoelectrochemical cells. *Nature* **2001,** *414*, 338.

2.   Iler, R. K., *The colloid chemistry of silica and silicates*. LWW: 1955; Vol. 80.

3.   Aswal, D. K.; Lenfant, S.; Guerin, D.; Yakhmi, J. V.; Vuillaume, D., Self assembled monolayers on silicon for molecular electronics. *Anal. Chim. Acta* **2006,** *568*, 84-108.

4.   Papageorgiou, D. T., On the breakup of viscous liquid threads. *Physics of Fluids* **1995,** *7*, 1529-1544.

5.   Dunn, S.; Sharp, S.; Burgess, S., The photochemical growth of silver nanoparticles on semiconductor surfaces—initial nucleation stage. *Nanotechnology* **2009,** *20*, 115604.

6.   Dinh, C.-T.; Nguyen, T.-D.; Kleitz, F.; Do, T.-O., A New Route to Size and Population Control of Silver Clusters on Colloidal TiO$_2$ Nanocrystals. *ACS Appl. Mater. Interfaces* **2011,** *3*, 2228-2234.

7.   Takai, A.; Kamat, P. V., Capture, Store, and Discharge. Shuttling Photogenerated Electrons across TiO$_2$–Silver Interface. *ACS Nano* **2011,** *5*, 7369-7376.

8.   Yang, L.; Jiang, X.; Ruan, W.; Yang, J.; Zhao, B.; Xu, W.; Lombardi, J. R., Charge-Transfer-Induced Surface-Enhanced Raman Scattering on Ag–TiO$_2$ Nanocomposites. *J. Phys. Chem. C* **2009,** *113*, 16226-16231.

9.   Callegari, A.; Tonti, D.; Chergui, M., Photochemically Grown Silver Nanoparticles with Wavelength-Controlled Size and Shape. *Nano Lett.* **2003,** *3*, 1565-1568.

10.   Pacholski, C.; Kornowski, A.; Weller, H., Site-Specific Photodeposition of Silver on ZnO Nanorods. *Angew. Chem. Int. Ed.* **2004,** *116*, 4878-4881.

11.   Herrmann, J.-M.; Disdier, J.; Pichat, P., Photocatalytic deposition of silver on powder titania: Consequences for the recovery of silver. *J. Catal.* **1988,** *113*, 72-81.

12.   Jia, Z.; Ben Amar, M.; Brinza, O.; Astafiev, A.; Nadtochenko, V.; Evlyukhin, A. B.; Chichkov, B. N.; Duten, X.; Kanaev, A., Growth of Silver Nanoclusters on Monolayer Nanoparticulate Titanium-oxo-alkoxy Coatings. *J. Phys. Chem. C* **2012,** *116*, 17239-17247.

13.   Matsubara, K.; Tatsuma, T., Morphological Changes and Multicolor Photochromism of Ag Nanoparticles Deposited on Single-crystalline TiO$_2$ Surfaces. *Adv. Mater.* **2007,** *19*, 2802-2806.

14.   Sofianou, M.-V.; Boukos, N.; Vaimakis, T.; Trapalis, C., Decoration of TiO$_2$ anatase nanoplates with silver nanoparticles on the {101} crystal facets and their photocatalytic behaviour. *Appl. Catal., B* **2014,** *158-159*, 91-95.

15.   Piwoński, I.; Spilarewicz-Stanek, K.; Kisielewska, A.; Kądzioła, K.; Cichomski, M.; Ginter, J., Examination of Ostwald ripening in the photocatalytic growth of silver nanoparticles on titanium dioxide coatings. *Appl. Surf. Sci.* **2016,** *373*, 38-44.

16.   You, X.; Chen, F.; Zhang, J.; Anpo, M., A novel deposition precipitation method for preparation of Ag-loaded titanium dioxide. *Catal. Lett.* **2005,** *102*, 247-250.

17.   Naoi, K.; Ohko, Y.; Tatsuma, T., Switchable rewritability of Ag-TiO$_2$ nanocomposite films with multicolor photochromism. *Chem. Commun.* **2005**, 1288-1290.

18.   Naoi, K.; Ohko, Y.; Tatsuma, T., TiO$_2$ Films Loaded with Silver Nanoparticles: Control of Multicolor Photochromic Behavior. *J. Am. Chem. Soc.* **2004,** *126*, 3664-3668.

19.   Ohko, Y.; Tatsuma, T.; Fujii, T.; Naoi, K.; Niwa, C.; Kubota, Y.; Fujishima, A., Multicolour photochromism of TiO$_2$ films loaded with silver nanoparticles. *Nature Mater.* **2002,** *2*, 29-31.

20.   Tian, Y.; Tatsuma, T., Mechanisms and Applications of Plasmon-Induced Charge Separation at TiO$_2$

Films Loaded with Gold Nanoparticles. *J. Am. Chem. Soc.* **2005,** *127*, 7632-7637.

21. Lu, Q.; Lu, Z.; Lu, Y.; Lv, L.; Ning, Y.; Yu, H.; Hou, Y.; Yin, Y., Photocatalytic Synthesis and Photovoltaic Application of Ag-TiO$_2$ Nanorod Composites. *Nano Lett.* **2013,** *13*, 5698-5702.

Chapter 4

Photodeposition of silver nanodots on TiO$_2$ nanoparticles by UV laser

Table of contents

4.1 Introduction to photodeposition of Ag nanodots onto TiO$_2$ nanoparticles surface

Metallic silver decorated TiO$_2$ nanoparticles (NPs) are significant hybrid materials that have received extensive study over the past decades. Due to the special light-active features of the semiconductor TiO$_2$, surface plasmon resonance of Ag nanoparticles and also the combined metal-semiconductor structure, these heterostructured materials can be used in many fields, such as water splitting,[1, 2] pollution photodegradation,[3-6] sensors[7, 8] and photovoltaic cells.[9, 10] Many methods have been used to synthesize Ag decorated TiO$_2$ NPs, including chemical reduction,[11, 12] physical vapour deposition,[13, 14] impregnation-deposition[15, 16] and photodeposition[17-20], and so forth, among which the photodeposition method has been widely used for its simplicity, low energy cost and contactless approach. For more detailed references, the reader could refer to the following reviews.[21-23]

In 1982, Hiroshi et al. found that UV light at 365 nm could activate TiO$_2$ NPs to generate electrons which reduce Ag$^+$ ions on the TiO$_2$ surface.[24] Afterwards, Ohtani et al.[25] investigated the pH effect on the photocatalytic reaction rate of Ag metal production, showing that the reaction rate decreased with decreasing pH, but gave neither silver size nor morphology information. The pH effect was also studied by Zhang et al.,[26] who showed that Ag multi dots were deposited on each TiO$_2$ NP for a broad pH range (pH 3 ~ 12), proposing that Ag$_2$O forms at relatively high pH range (pH 11 ~ 12) and can act as an Ag^0 reservoir to keep local Ag$^+$ concentration extremely low on TiO$_2$ surface. The photodeposition of Ag onto either TiO$_2$ NPs or nanotubes was also probed, although the morphology of the final product is not well-established,[27] in terms of size distribution and Janus yield.

Deep UV laser (λ = 257 nm) was first introduced to deposit silver onto a Ti/TiO$_2$ film, and the silver deposits turned visibly larger and larger with increasing the laser exposure time.[28] Beyond the usually considered Ag precursors, silver nitrate (AgNO$_3$), silver acetate (AgOAc) were also tried as precursor using photodeposition method and succeeded in synthesizing Ag-P25 composites without external hole scavengers. Several researchers paid attention to the study of multicolour photochromic behaviours of Ag-TiO$_2$ film made by photodeposition method.[19, 29-31] As for the energy supply, most of the research concerning photodeposition of

Ag on TiO$_2$ were driven by a high-pressure Hg lamp as light source, which as mentioned in chapter 3 is limited in terms of photon flux. Furthermore, the information about the intensity applied to the mixture is often missing, while it is an essential parameter, as demonstrated in this thesis. Still, the reactions are mainly performed in fixed-volume vessels, usually magnetically stirred, with illumination time always of a few to dozens of hours. A new design of reaction vessel is thus highly in demand to improve the hybrid materials synthesis.

Moreover, few people investigated the pH effect on the growth and morphology evolution of silver particles on TiO$_2$ in order to clarify its role in photodeposition. Finally, as far as we know, a growth model to predict metal size evolution is still missing, while recent studies showed that control of the dot size is a key parameter for photocatalysis,[32-37]; modelling for given reaction conditions and optical excitation would also rise a predictive approach for the engineering of nano-heterodimers.

In this chapter, we use the setups designed in chapter 3 as powerful light sources to initiate the photodeposition process. We are able to study photodeposition under well-controlled conditions in terms of intensity or illumination time, owing to high intensity and the monochromic wavelength below the band gap of TiO$_2$. The microchannel setup is initially built to study the fluidic photoreaction that takes place inside a microchannel where the flowing mixture is actively irradiated by a focused UV laser. It will also be compared with the other two cuvette setups using either enlarged UV laser or high-pressure Hg lamp.

Characterization techniques, including X-ray photoelectron spectroscopy (XPS), UV-vis spectroscopy and High-Resolution Transmission Electron Microscope (HRTEM), confirmed the formation of metallic silver, the existence of Ag nanodots (Ag NDs) and good affinity bond between TiO$_2$ and Ag at the interface, respectively. The results also show that high-intensity UV laser exposure in a microchannel setup can help produce good quality hybrid Ag-TiO$_2$ heterodimers with a single dot on each TiO$_2$ and relatively high Janus yield, while cuvette setup using Hg lamp leads to multi silver dots on each TiO$_2$. The effects of the hole scavengers, the pH of the solution and the silver precursor are also investigated.

The data concerning the silver size obtained under different conditions are then plotted together and show a good fit to our proposed model (Appendix 2), indicating that engineering of nano-heterodimers by laser photodeposition should be foreseen.

4.2 Experimental methods

The reaction solution is prepared in the dark by mixing as-already made TiO_2 solution (in Chapter 2) and freshly made $AgNO_3$ solution together; then methanol is added to make a 50 vol. % methanol aqueous solution. The pH of the mixture solution is adjusted at pH 3 using nitric acid (pH = 1). The acidic solution helps to obtain a stable TiO_2 dispersion (isoelectric point of TiO_2: 6.1) and avoid precipitation of Ag_2O formed from the combination of Ag^+ ions with OH^- under basic conditions: *$2Ag^+ + 2OH^- \rightarrow Ag_2O\downarrow + H_2O$.*

In any circumstances, the final concentrations of TiO_2 and $AgNO_3$ in the solution going through the UV light are 5.5 mM and 2 mM (in atomic concentration), respectively. When sodium formate (HCOONa) is used as a hole scavenger instead of methanol, its concentration is also 2 mM.

For the TiO_2 substrate, we used mainly three shapes in this study, *i.e.,* polyhedrons, nanoplates and nanoneedles. Since the NPs do not have the same size, it should be mentioned that the molar concentration of 5.5 mM TiO_2 corresponds to a different concentration in nano-objects as mentioned below:

5.5 mM in atomic concentration correspond to 1×10^{-8} mol/L for polyhedrons in average size 33 nm; 2.3×10^{-8} mol/L for nanoplates in average size 30 nm (and thickness size 9 nm), and 4.2×10^{-9} mol/L for nanoneedles in average length 110 nm and width 28 nm.

4.2.1 Experimental methods in microchannel setup

The aqueous solution is then purged with Ar for at least 10 minutes to remove the dissolved oxygen in the solution before transfer to a glass syringe (5 mL, SGE). The oil part is loaded in another glass syringe (2.5 mL, SGE). Both syringes are connected to the microchannel setup and each pumped by a syringe pump (KD Scientific). All the process during the experiment avoids the use of metal part (such as metal syringe needle for instance) to avoid the possible Ag^+ ions reduction. The flow rates imposed to the aqueous solution and the oil part are typically set as 17.2 and 4.3 μL/min., respectively. In these conditions, the flow speed inside the microchannel is 960 μm/s. The photodeposition is performed at a laser power, right in the middle of the channel $P_{1/2}$ = 3.1 – 23.25 mW.

15 mM nonionic surfactant sorbitan mono-oleate SPAN 80 (Figure 4.1) is optionally added in the oil (n-dodecane for instance) to increase the wettability of the oil phase on glass and thus prevent photodeposition at the walls of the channel, and to transfer the nanoparticles from water into the organic phase by phase transfer, if necessary. This last option allows for avoiding the washing steps and for obtaining stable nanoparticles dispersion in nonpolar organic solvents (heptane, toluene).
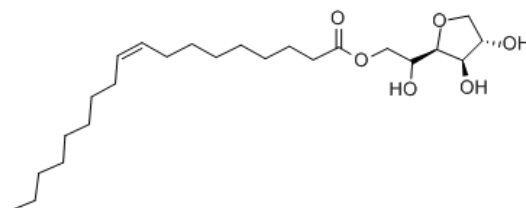
Figure 4.1 The nonionic surfactant sorbitan monooleate (SPAN80).

The product of the photodeposition gathered in a glass vial showed a brown colour in the aqueous part at the bottom, with a thin oil layer at the top. A rapid phase transfer occurred after gently shaking the vial for a few seconds. The brown colour moved to the upper oil part due to phase transfer with surfactant SPAN 80. The oil part containing Ag-TiO₂ is then diluted with 1 mL heptane.

The TEM grid preparation follows the procedures: the solution is sonicated for 10 min to disperse the nanoparticles, and then one drop is taken to be deposited on a TEM grid (carbon film face up). A few more heptane drops are added on the top and adsorbed through the carbon film to wash away the excessive surfactant. For the statistics of silver size, at least 200 Ag NDs were measured unless otherwise specified.

4.2.2 Experimental methods in cuvette setup

As in the previous case, the aqueous solution is purged with Ar for at least 10 min, to remove the dissolved oxygen in the solution before transfer to a cuvette. The laser exposure area is designed to be circular with a 1 cm diameter in order to fill a 1 cm wide square cuvette, so the volume of the solution is always kept to 1 cm^3 to be sure that the solution is exposed to the laser light. The cuvette is then capped under Ar, and the solution is continuously stirred at a speed of 300 rpm by a magnetic stirrer. The power and illumination time of the experiment

can be easily adjusted. All the experiments are performed at room temperature.

The TEM grid preparation is performed according to the following procedures: The solution is sonicated for 10 min to disperse the nanoparticles, and then one drop is deposited on a TEM grid (pre-activated by UV light, carbon film face up). A paper tissue can help absorb the liquid from the carbon film side from the back side of the grid, which allows only the liquid to pass through, and leaves the nanoparticles on the top side. Two or more nitric acid drops (at pH 3) are also deposited onside, to wash away the remaining unreacted metal salts if any on TiO_2 NPs.

4.3 Results and discussions

In this part, we first discuss the general characterization of the Ag-TiO₂ NPs produced in the microchannel setup, to confirm the existence of metallic silver photodeposition on TiO_2 surface and to verify the feasibility of synthesizing heterodimers using high-intensity UV laser. Due to optical absorption of TiO_2 at 364 nm, we show in Appendix 1 that the laser heating of the solution is negligible. The experimental data are also fitted to a growth model developed in Appendix 2. For the following sections, several parameters, including applied power, type of hole scavengers and pH values, are investigated to clarify their roles in the photodeposition process. We also discuss the comparison of product solutions synthesized in different setups, highlighting the importance of high-intensity microchannel setup for the production of heterodimers. The substrate morphology and the metal precursor effect will also be discussed.

4.3.1 General approach of photodeposition: towards Ag-TiO₂ nanoparticles

The general conditions, which will be fixed in the following are $c[Ag^+]$ = 2 mM, $c[TiO_2]$ = 5.5 mM; while the pH value, the type of hole scavenger, the laser power and the illumination time are the parameters which will be varied. We will not come back here on the control experiments, which were performed by Laetitia Vauriot during her PhD.[38] She conclusively showed that in these same conditions when she removed one of the reactants, she did not obtain the same results. The absence of a hole scavenger (MeOH) led to smaller silver dots and a much lower Janus yield, water becoming itself the hole scavenger, but a slow one.

$$h^+ + H_2O \longleftrightarrow H^+ + {}^{\bullet}OH$$
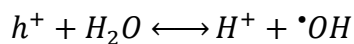
The absence of TiO$_2$ led to the formation of micrometer size of silver aggregates. This was likely due to interactions with the electrons generated at the surface of the glass wall.

In the following experiments, the aqueous solution and the oil are injected into the microchannel setup at a flow rate ratio of 4:1, thus resulting in 4 times longer length of the drop solution than the oil segment in the square channel. The UV irradiation causes an instantaneous colour change in the solution part from transparent to brownish while leaving the oil part transparent (Figure 4.2a).
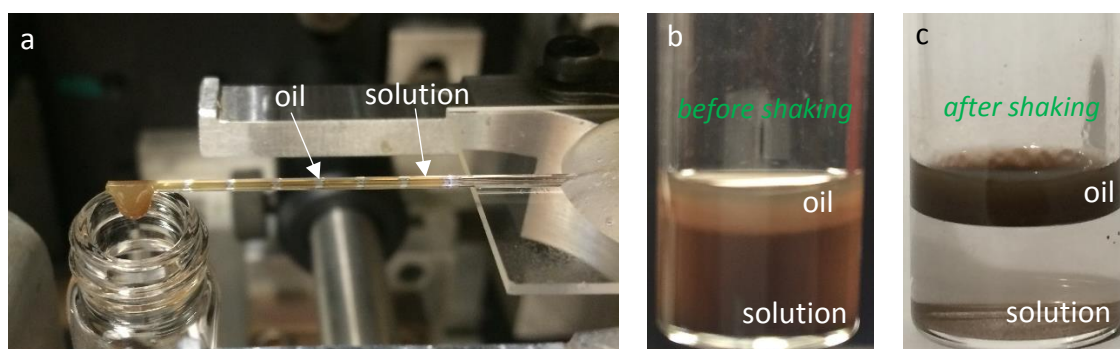
Figure 4.2 (a) Picture of an ongoing photodeposition reaction in a microchannel setup, (b) product solution containing oil and solution part before shaking, (c) product solution containing oil and solution part after shaking.

We can also observe this change with the CCD camera. This is illustrated in Figure 4.3 where a moving solution drop changes colour when crossing the UV exposed region. The product solution is gathered into a glass vial, where the two phases remain separated, showing two separated phases (see Figure 4.2b). A gentle shaking initiates a phase transfer process, where the nanoparticles in water solution are dragged into the oil part with the help of surfactant, SPAN 80 (phase transfer). The oil phase containing Ag NDs deposited on TiO$_2$ becomes brownish (Figure 4.2c), while leaving the aqueous solution clear and colourless, indicating the efficiency of the phase transfer process.
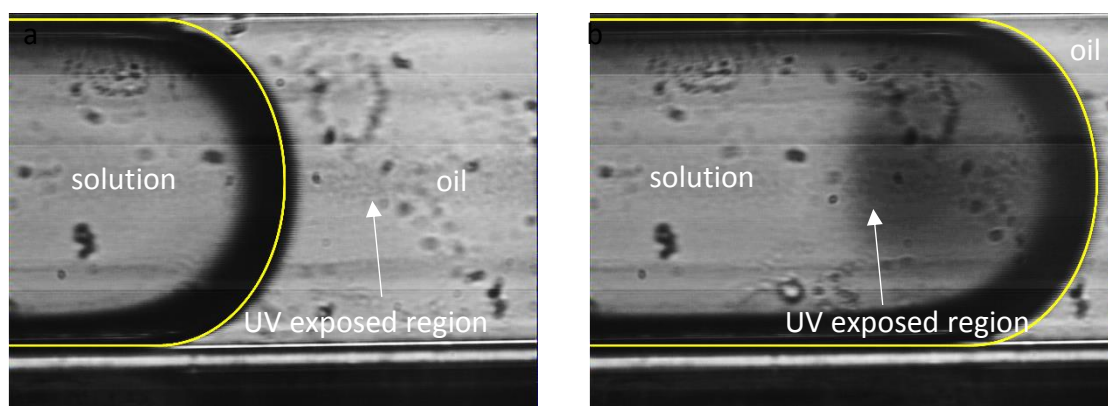
Figure 4.3 (a) A solution drop is flowing in the microchannel before crossing the UV exposed region. (b) The same solution drop in the microchannel when crossing the UV exposed region. The interface limit between the drop and the surrounding oil film is indicated by a yellow line. Note the darkness transition of the solution when crossing the UV exposed region (denoted by an arrow).

Three TiO$_2$ morphologies, *i.e.,* polyhedrons, nanoplates and nanoneedles, are involved in the photodeposition experiments, however, in this part, only the experiments using the TiO$_2$ polyhedrons will be fully characterized and discussed, by TEM, XPS, UV-vis. spectrum and HRTEM.

4.3.2 Characterization of Ag-TiO$_2$ (polyhedrons) synthesized in microchannel setup

The heterodimers were synthesized using the following experimental conditions: c[TiO$_2$] = 5.5 mM, c[Ag$^+$] = 2 mM, 50 vol. % methanol as hole scavenger, the power was set at 3.1 mW, the solution velocity in the microchannel setup at 960 µm/s,. The TEM images of the products based on photodeposition are shown in Figure 4.4.
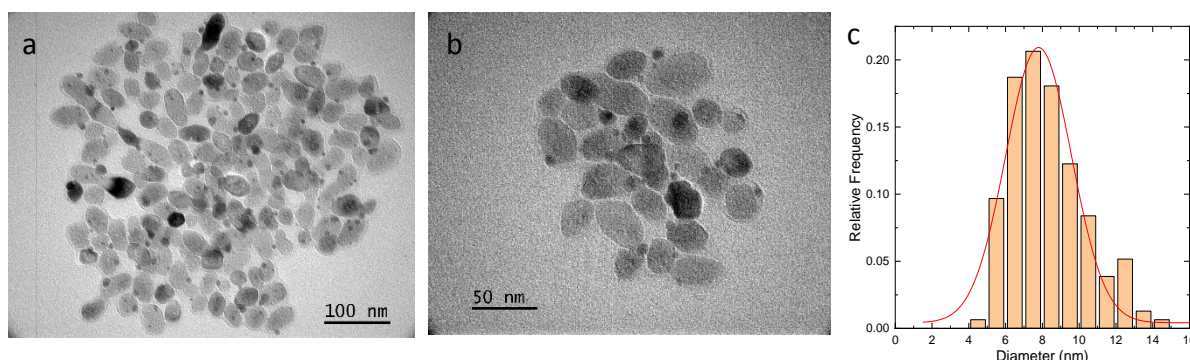
Figure 4.4 TEM images of Ag-TiO$_2$ NPs at (a) smaller and (b) larger magnification. (c) The silver size distribution histogram of the product Ag-TiO$_2$. The experimental conditions: c[TiO$_2$] = 5.5 mM, c[Ag$^+$] = 2 mM, pH 3, 50 vol. % methanol as hole scavenger, power 3.1 mW, velocity 960 µm/s, in microchannel setup

Both the smaller and larger magnification images confirm the formation of heterostructured Ag-TiO$_2$ NPs. Single Ag ND is deposited on the surface of TiO$_2$, with an average diameter of 7.8 nm (Figure 4.4c). The Janus yield production is about 85 %, by measuring at least 200 nanoparticles in the images. The yield was determined according to the following procedure: at least 10-15 TEM pictures at the same magnification were taken to provide both an accurate measurement and enough particles to measure at least 200 TiO$_2$ objects, from which were also counted the number of heterodimers. The yield was then estimated from the ratio of these two values.

The optical properties of the Ag-TiO$_2$ NPs are analyzed by UV-vis spectroscopy. As seen in Figure 4.5, The spectrum exhibits an absorption band with the maximum peak located at the wavelength of 410 nm, which corresponds to the specific absorption peak of Ag NDs due to the surface plasmon resonance (SPR) effect;[39] the band gap of TiO$_2$ is around 380 nm. This also confirms the presence of Ag NDs after the photodeposition process.
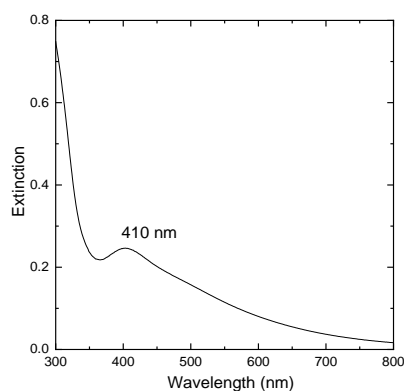
Figure 4.5 UV-vis spectrum of a solution of Ag-TiO₂ NPs formed in a microchannel, 50 vol. % methanol as hole scavenger, power 2.5 mW, velocity 960 μm/s.

XPS is an instrumental technique, which provides a sensitive measure of the chemical state in the near surface region of materials and is applied to study metal and metal oxide surface. The XPS analysis of the samples on Ag3d before and after etching is given as a representative illustration for all the obtained Ag-TiO$_2$ NPs (Figure 4.6). The observed binding energies (BE) are denoted beside the peak with Ti 2p as a reference (458.9 eV for Ti 2p$_{3/2}$ and 464.4 eV for Ti 2p$_{1/2}$).

The high-resolution Ag 3d XPS spectrum before the etching process (Figure 4.6a) shows the two distinct peaks at 367.9 and 373.8 eV. After 6 s etching process, the position of two peaks slightly was shifted by 0.2 eV, i.e., 367.7 and 373.6 eV. These two sets of peaks can be assigned to the Ag 3d$_{5/2}$ and Ag 3d$_{3/2}$ contributions, respectively. As compared to bulk metallic Ag (368.3

eV for Ag3d$_{5/2}$, and 374.3 eV for Ag3d$_{3/2}$), the peaks are slightly shifted to the lower binding energy. The electron transfer can explain this small shift from the TiO$_2$ to the Ag NDs.[40] These results confirm the formation of metallic silver during the photodeposition process.
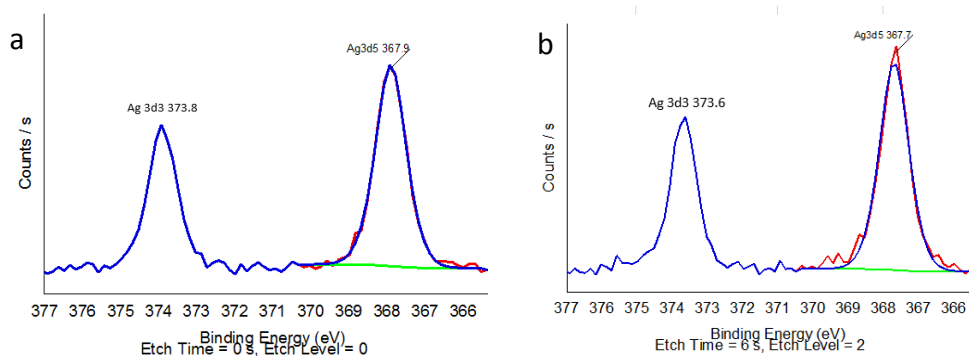
Figure 4.6 High-resolution spectra of Ag-TiO$_2$ NPs (a) before and (b) after 6 s etching.

The nature of the interface between the silver and the TiO$_2$ NP is further investigated by HRTEM (see Figure 4.7).
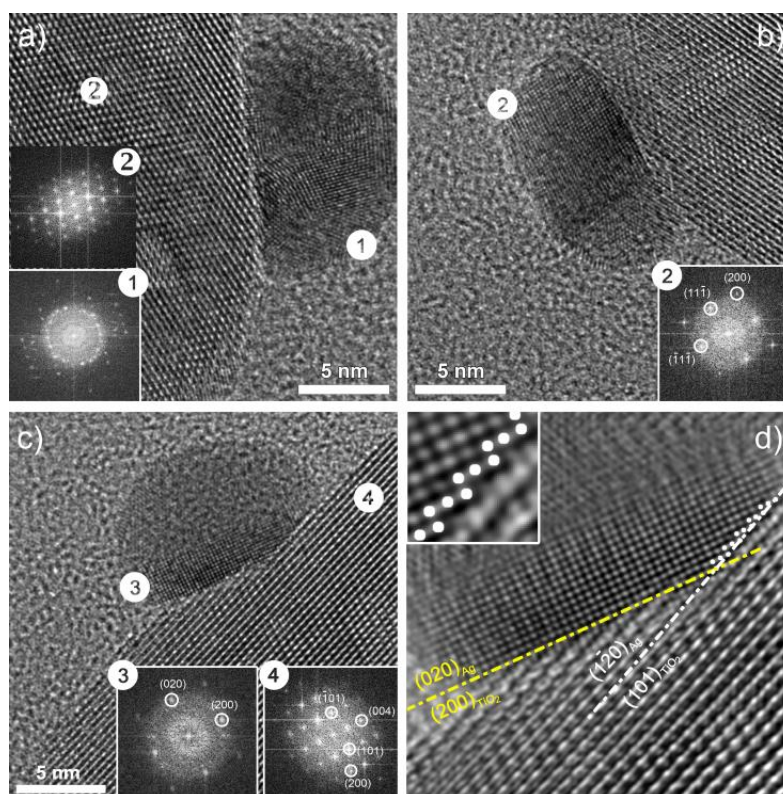
Figure 4.7 (a)(b)(c) HRTEM micrographs illustrating a variety of Ag-TiO$_2$ interfaces with corresponding digital diffractograms of labelled zones. (d) Higher magnification of image c is presented with zoom-in inset of (020), and (200) Ag stepped interface.

The TiO$_2$ NPs are single crystalline ones enclosed by (110) and (200) low index facets. These surfaces are mostly rough and made of terraces, valleys and steps. The Ag NDs are deposited

111

as nanosized clusters onto both (110) and (200) TiO₂ facets and on the three types of sites which involve flat terraces, as shown in Figure 4.7a, or convex or concave surfaces as in Figure 4.7b and c, respectively. One can also note in Figure 4.7d that for the same silver cluster, the interface with TiO₂ can be flat: $(020)_{Ag}$ parallel to $(200)_{TiO2}$; or stepped: $(101)_{TiO2}$ parallel to $(1\bar{2}0)_{Ag}$ mean plane with $(020)_{Ag}$ and $(200)_{Ag}$ steps. Such microstructural features seem to be induced by the TiO₂ particles surface defects in order to elastically reduce the interfacial strains and thus minimize the surface energy. The HRTEM results indicate the strong atomic structure of the interface between silver metal and semiconductors.

4.3.3 Hole scavenger effect on Ag photodeposition in the microchannel setup

Hole scavenger plays a vital role in the photodeposition process. If efficient enough, it consumes the holes generated in the TiO₂ by the UV irradiation and leaves much more free electrons to react at the interface with metal ions in solution by reducing the recombination of the electron-hole pairs. Several alcohols[41-43] (methanol, ethanol for instance), organic agent or salts[21] are often chosen as sacrificial reagents. As our reaction takes place in aqueous solution, the hole scavenger has to be miscible/dissolvable in water solution. In our study, methanol and HCOONa are chosen to play this role.

Methanol is frequently used in photodeposition experiments as a hole scavenger agent because it has a much higher reaction rate during photodeposition than other alcohols and its role as a hole scavenger in the presence of TiO₂ under UV activation is widely known.[44-50] Another hole scavenger, HCOONa, is also introduced in our investigations because the side product CO₂ is a gas which is easy to get rid of, and also to propose a comparison with methanol. The hole scavenging mechanism follows the equations depending on the hole scavenger.

$$TiO_2 \xrightarrow{h\nu} e_{CB}^- + h_{VB}^+$$
$$Ag^+ + e_{CB}^- \rightarrow Ag^0$$
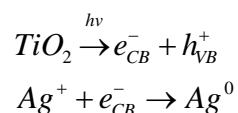
methanol hole scavenging:

$$CH_3OH + h_{VB}^+ \rightarrow CH_2OH\cdot + H^+ \rightarrow\rightarrow\rightarrow CO_2$$
$$Ag^+ + CH_2OH\cdot \rightarrow Ag^0 + CH_2O + H^+$$
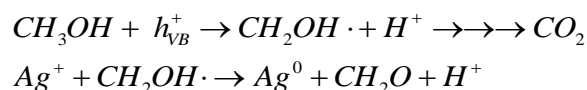
Formate hole scavenging:

$$HCOO^- + h_{VB}^+ \rightarrow H^+ + \cdot COO^-$$

$$\cdot COO^- + h_{VB}^+ \rightarrow CO_2$$

$$Ag^+ + \cdot COO^- \rightarrow Ag^0 + CO_2$$
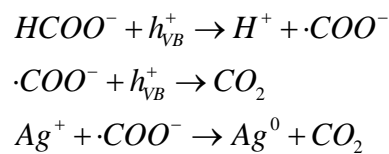
From these equations, we can see that methanol consumes the holes and produces formaldehyde or even CO$_2$ at the end, and formate leads to the production of carbon dioxide. Here we regard the formation of CH$_2$O as the primary reaction product, although researchers[48] claimed that other side products like methyl formate (HCOOCH$_3$) also formed in the reaction with methanol.

To check the role of the hole scavenger, we chose to keep all the parameters identical and as follows, TiO$_2$ polyhedrons as substrate, c[Ag$^+$] = 2 mM, c[TiO$_2$] = 5.5 mM, solution velocity v = 960 µm/s, and pH = 3. Two types of hole scavengers, $i.e.$, methanol (50 vol. %) and HCOONa (2 mM), will be introduced and discussed separately. The experimental data in terms of silver size as a function of different powers using either a) methanol or b) HCOONa will be shown and compared.

4.3.3.1 Role of HCOONa as a hole scavenger

The TEM results of Ag-TiO$_2$ NPs performed in the microchannel setup using HCOONa as a hole scavenger are shown in Figure 4.8. The mean size of TiO$_2$ is 33 nm, and Ag NDs are easily seen in darker contrast. According to Table 4.1, in the presence of formate, the Ag NDs continue to grow with the applied power in the microchannel from 3.1 to 23.25 mW.

Generally, a single Ag ND is found on each TiO$_2$ nanoparticle; bare TiO$_2$ NPs and TiO$_2$ deposited with Ag multidots are rarely seen.
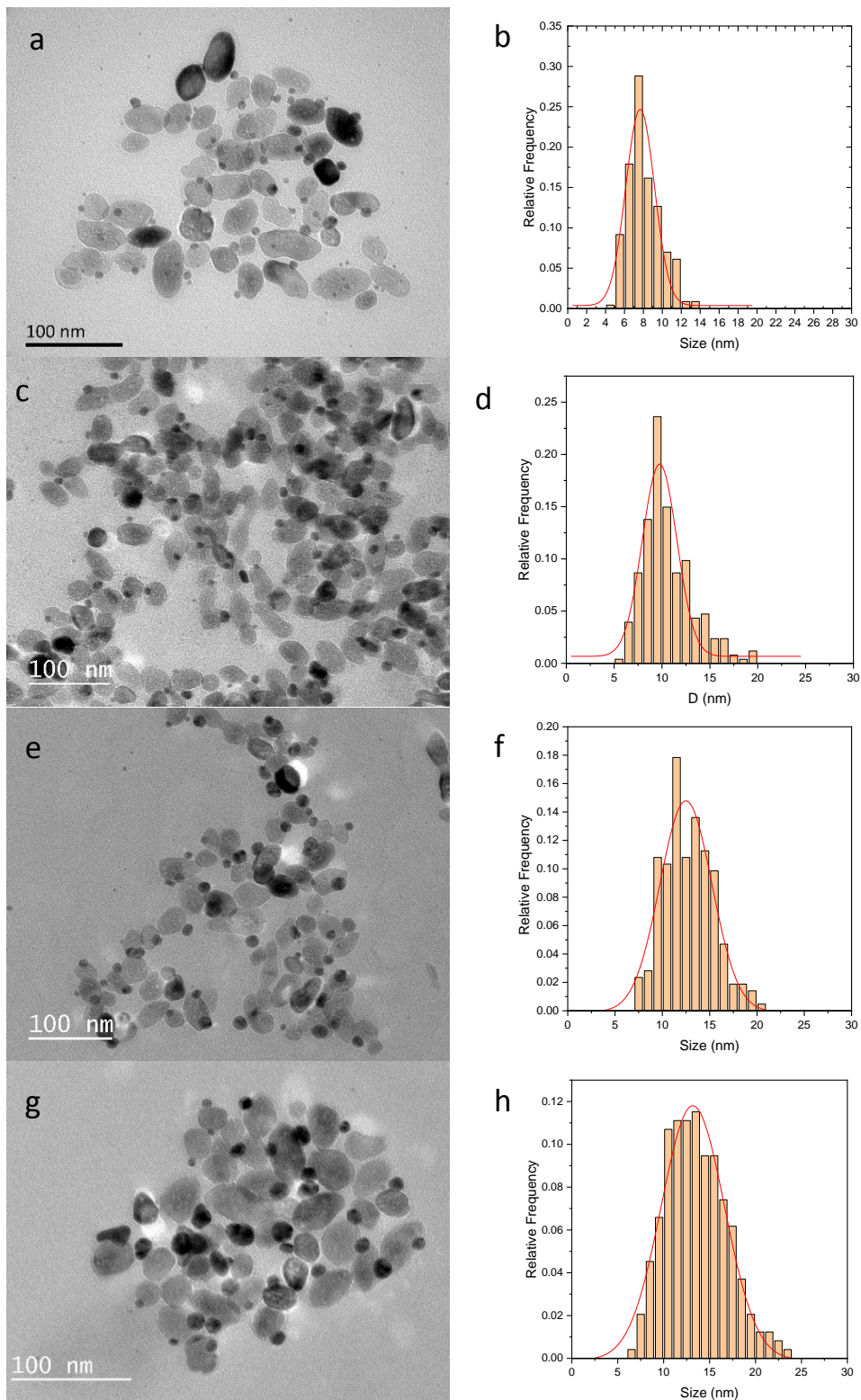
Figure 4.8 TEM images of Ag-TiO₂ NPs performed in a microchannel setup at powers of (a) 3.1 mW, (c) 7.75 mW, (e) 15.5 mW and (g) 23.25 mW, and their corresponding size histograms shown in (b), (d), (f), and (h) respectively. Experimental conditions are: illumination time 0.2s, 2 mM HCOONa as a hole scavenger, TiO₂ polyhedrons as substrate, mixture solution at pH 3.

114

Power (mW)	Ag diameter (nm)(SD) with HCOONa (2 mM)	Janus yield (%)	Ag diameter (nm)(SD) with methanol (50 vol. %)	Janus yield (%)
3.1	7.7(1.5)	86	7.8(1.8)	85
7.75	9.7(1.8)	90	9.8(2.4)*	multidots
15.5	12.5(2.8)	90	12(2.9)*	multidots
23.25	13(3.4)	88	13(3.4)*	multidots

*Table 4.1 Ag diameter values on TiO$_2$ polyhedrons at pH 3 under variable powers, using either methanol or HCOONa as a hole scavenger. * means that the value is the size of largest Ag NDs population on one TiO$_2$; for those owning one single large dot as well as several tiny dots, the yield is denoted as "multidots".*

UV-vis spectroscopy was performed and characterized in Figure 4.9.
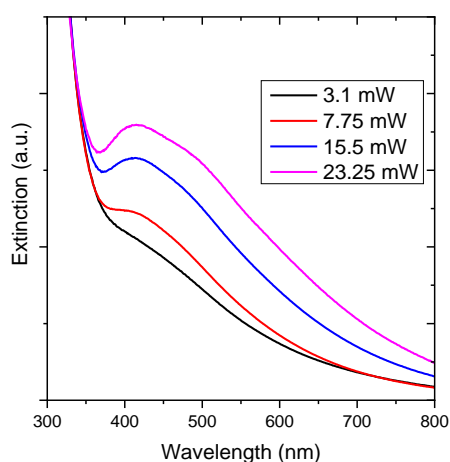
Figure 4.9 UV-vis spectra of sample solution made at four powers in a microchannel using HCOONa as hole scavenger.

A characteristic but broad band of Ag NDs corresponding to the surface plasmon band shown at 410 nm also appears[51] and becomes more and more evident when increasing the power, indicating the formation of Ag NDs in the photodeposition process. An extra contribution tends to grow at a wavelength larger than 410 nm when powers as high as 23.25 mW are used indicating an increase of silver size, which is consistent with the size distribution observed in the histogram in Figure 4.8.

4.3.3.2 Role of methanol as a hole scavenger

Interestingly, the photodeposition turned to be a bit different when we changed to another hole scavenger, methanol (Figure 4.10 and Table 4.2).

115
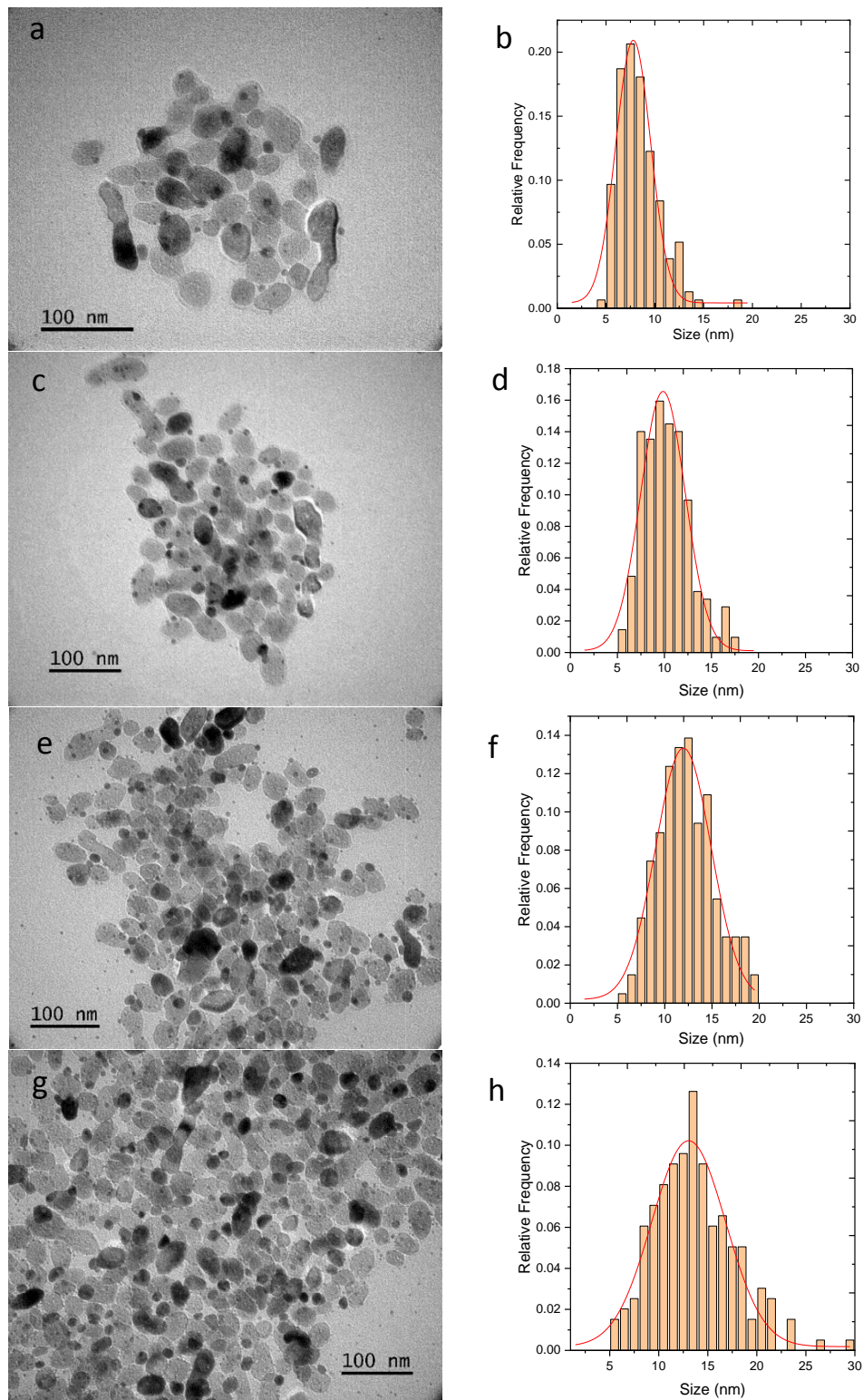
Figure 4.10 TEM images of Ag-TiO₂ NPs performed in microchannel at powers of (a) 3.1 mW, (c) 7.75 mW, (e) 15.5 mW and (g) 23.25 mW, and their corresponding size histograms (b) (d) (f) and (h) respectively. All these four samples with illumination time 0.2s, 50 vol. % methanol as a hole scavenger, TiO₂ polyhedrons as the substrate, mixture solution at pH 3. Note that the size of tiny dots (<4 nm) is not taken into account in the histogram.

Figure 4.10 illustrates the variation of the size of the silver particles successfully deposited onto the TiO$_2$ NPs, which is quantified in Table 4.1 and Figure 4.11. The diameter of the Ag NDs increases with increasing applied power in the microchannel and follows the same trend as experiments performed with formate as a hole scavenger. However, the difference between the two hole scavengers comes from the silver particle distributions. Besides the large silver particle, in the case of methanol, other much smaller Ag NDs appear on each TiO$_2$ nanoparticle, with a size ranging from 2 to 4 nm, which leads to a bi-modal distribution of silver particles. The number of small silver dots increases when increasing the applied power. An option to control this aspect as shown later on in chapter 5 on the photodeposition of gold NDs, is to decrease the methanol content in the water solution; indeed a 50 vol. % ratio provides a really large excess of hole scavenger (6×10^4) as compared to the metal source.
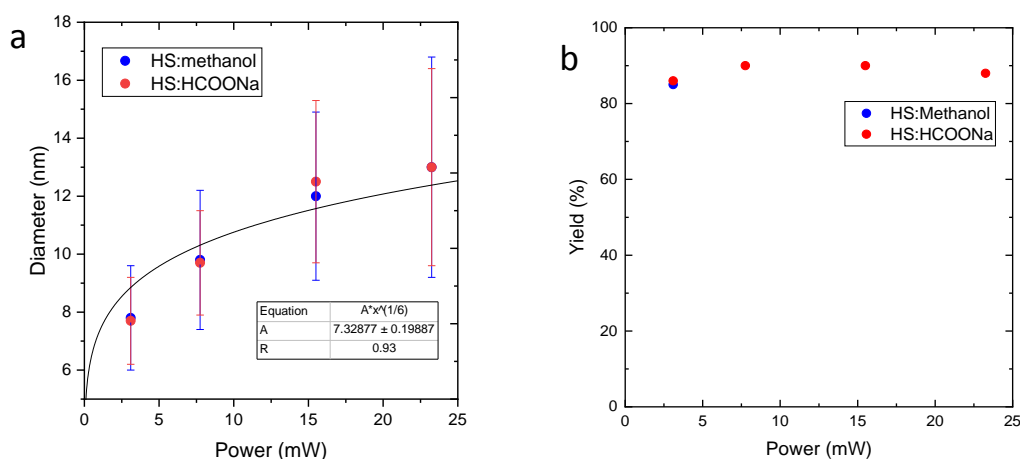
Figure 4.11 Ag diameter as a function of applied power in a microchannel setup, using either methanol or HCOONa as hole scavenger, at pH 3. A power-law fit is also plotted. Note that only the growth of the largest silver dots is shown in the case of co-existence of small dots (<3 nm) and larger ones.

UV-vis spectroscopy was performed and characterized in Figure 4.12. A characteristic peak of Ag NDs shown at 410 nm appears and becomes more and more evident when increasing the power, indicating the formation of Ag NDs in the photodeposition process.[51]

117
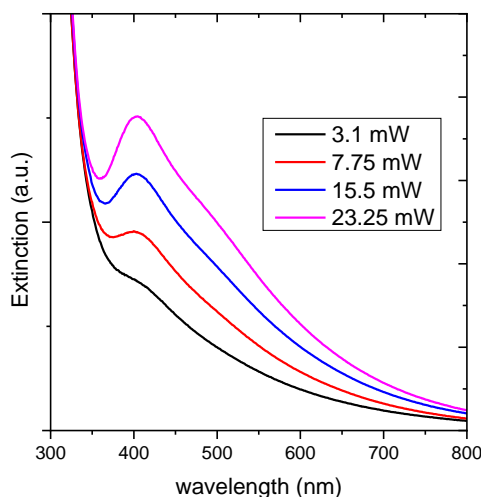
Figure 4.12 UV-vis spectra of sample solutions made at four powers in a microchannel using methanol as a hole scavenger.

To conclude, nearly all the TiO₂ NPs were decorated with Ag NDs, using either methanol or HCOONa as a hole scavenger, leading to at least around 80 % Janus yield for both cases of scavenging. It appears that an equivalent amount of silver nitrate and HCOONa in the precursor solution is the most reliable choice for a single dot deposition with a high yield. Since the by-product is easier to eliminate when using HCOONa as a hole scavenger, we did not try to focus on the best conditions to eliminate the germination of the tiny dots in the presence of methanol.

4.3.4 pH effect on Ag photodeposition in the microchannel setup

In this part, we would like to discuss the pH effect on the photodeposition process of Ag on TiO₂ NPs. People found that pH value plays a significant role in determining the morphology and composition of metal on the semiconductor.[52-54] Here, we investigated the pH effect on the photodeposition of silver on TiO₂. The chosen pH values were lower than 5, in order to stay in the domain of colloidal stability of TiO₂ and to avoid the precipitation of silver oxide at higher pH values as observed experimentally. Two kinds of TiO₂ shape, polyhedrons and nanoneedles, were selected to test the effect of the pH.

4.3.4.1 pH effect on photodeposition of Ag on TiO₂ polyhedrons

We first performed the silver photodeposition experiment on TiO₂ polyhedrons at different

118

pH values, using methanol as the hole scavenger. Figure 4.13 showed the TEM images of the resulting Ag-TiO$_2$ NPs performed at four pH values, *i.e.,* 3, 3.9, 4.3 and 4.7, with power 3.1 mW and illumination time 0.2 s, performed in the microchannel setup.

Figure 4.13. TEM images of Ag-TiO$_2$ NPs performed at different pH values (a) pH 3, (c) pH 3.9 and (e) pH 4.3, and their corresponding size histograms (b) (d) and (f), respectively.

As we can see, the number of silver dots on each TiO$_2$ nanoparticle differs from one pH value to the other. At the lowest value, pH 3, merely one silver dot is deposited on each TiO$_2$ nanoparticle (Figure 4.13a), whereas it tends to increase with the pH (Figure 4.13e), indicating the role of the pH value on the number of potential deposition sites (increasing OH groups at

119

the surface). There is a dual population for the pH values at 3.9 and 4.3 (Figure 4.13c and e). The surface charge of TiO_2 being less positive with increasing pH values allows better accessibility of the Ag^+ cations to the interface, which can be reduced by the photogenerated electrons.[26, 55]

These experiments were repeated with different powers, and we listed all the size data in Table 4.2 and drew a graph of the largest silver size as a function of the applied power for three pH values in Figure 4.14.

Power(mW)	Ag diameter (nm)(SD) at pH 3.0	Ag diameter (nm)(SD) at pH 3.9	Ag diameter (nm)(SD) at pH 4.7
3.1	7.8(1.8)	7.6(1.7)*	6.6(1.6)*
7.75	9.8(2.4)*	10(2.7)*	8.4(1.8)*
15.5	12(2.9)*	11.5(2.6)*	9.8(2.3)*
23.25	13(3.8)*	13.3(2.4)*	10.9(2.3)*

Table 4.2 Ag diameter at three different pH values under variable powers. Ag NDs are photodeposited onto TiO₂ polyhedrons. "" means that the value is the size of the largest Ag ND on one TiO₂.*
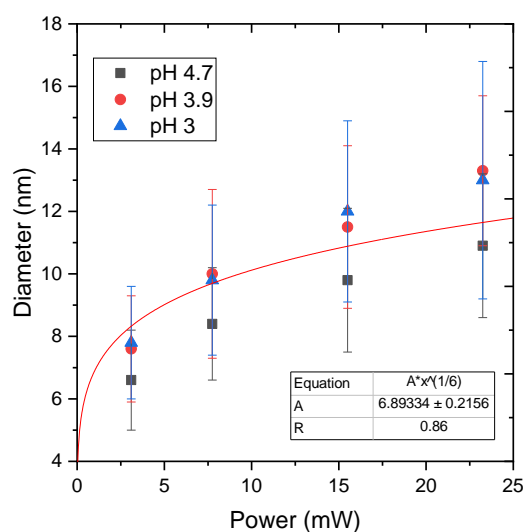
Figure 4.14 Ag diameter as a function of the applied power in the microchannel at different pH values, other conditions are kept the same: illumination time 0.2 s, 50 vol. % methanol as a hole scavenger, TiO₂ polyhedrons as substrate. A power-law fit was also plotted.

The silver diameter variation with the power follows the same trend whatever the pH, and tends to increase with increasing power (see §4.3.9 for the model). The main difference consists in the formation of tiny dots even at higher powers. The size of tiny dots reaches 3 - 4 nm in diameter.

4.3.4.2 pH effect on photodeposition of Ag on TiO₂ nanoneedles.

In this section, we continue to investigate the pH effect on the photodeposition of silver on another substrate, TiO₂ nanoneedles. The length and width of these nanoneedles are around 110 and 28 nm, respectively, with an aspect ratio of approximately 4:1. The larger size of TiO_2 possibly means a decrease of electric field gradient induced by nanodot growth, compared to the case of 30 nm TiO₂ nanoparticle, thus potentially giving rise to the nucleation of two or more isolated metal deposits on each substrate. Figure 4.15 shows the TEM results of Ag-TiO₂ nanoneedles made at various pH values.
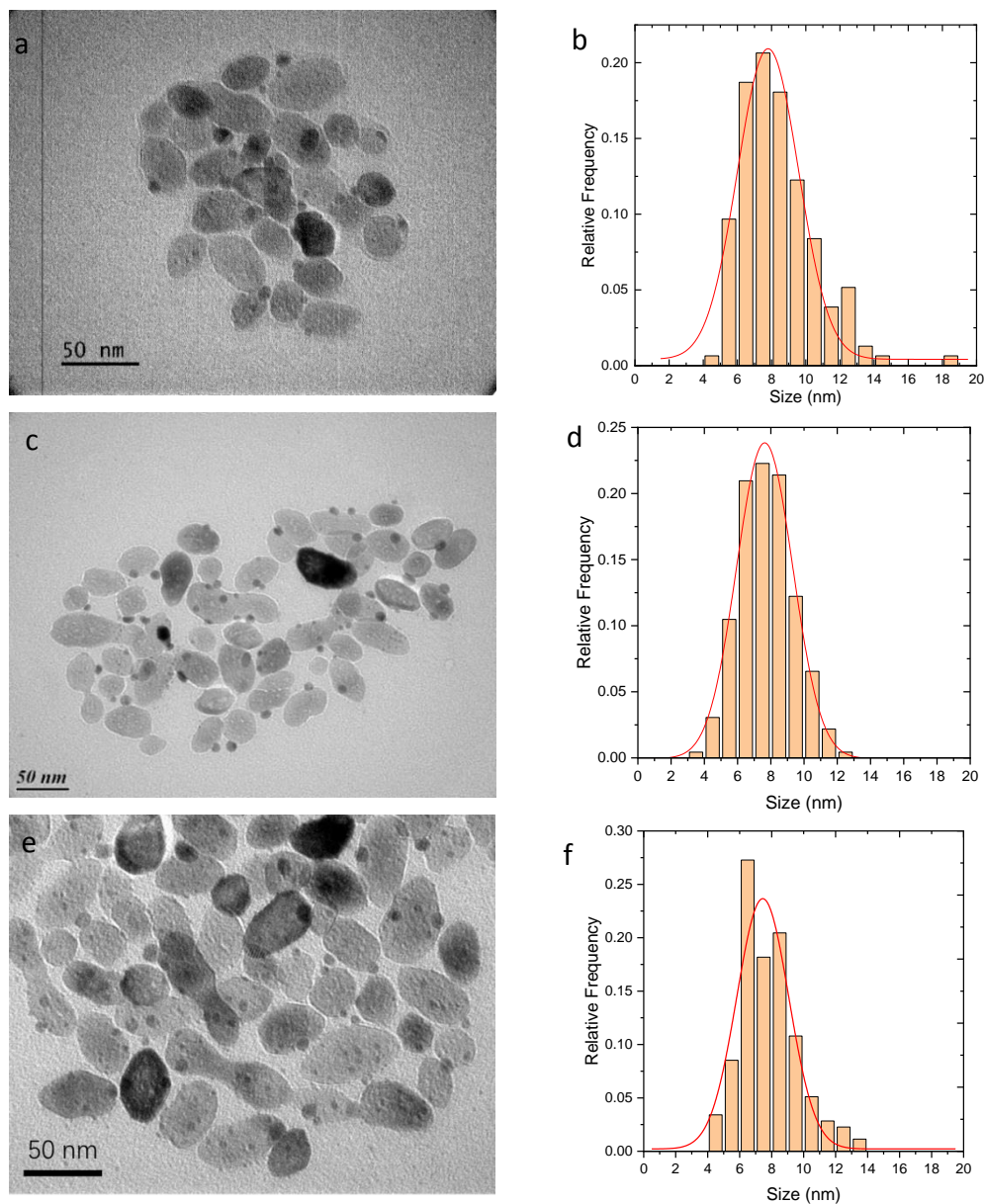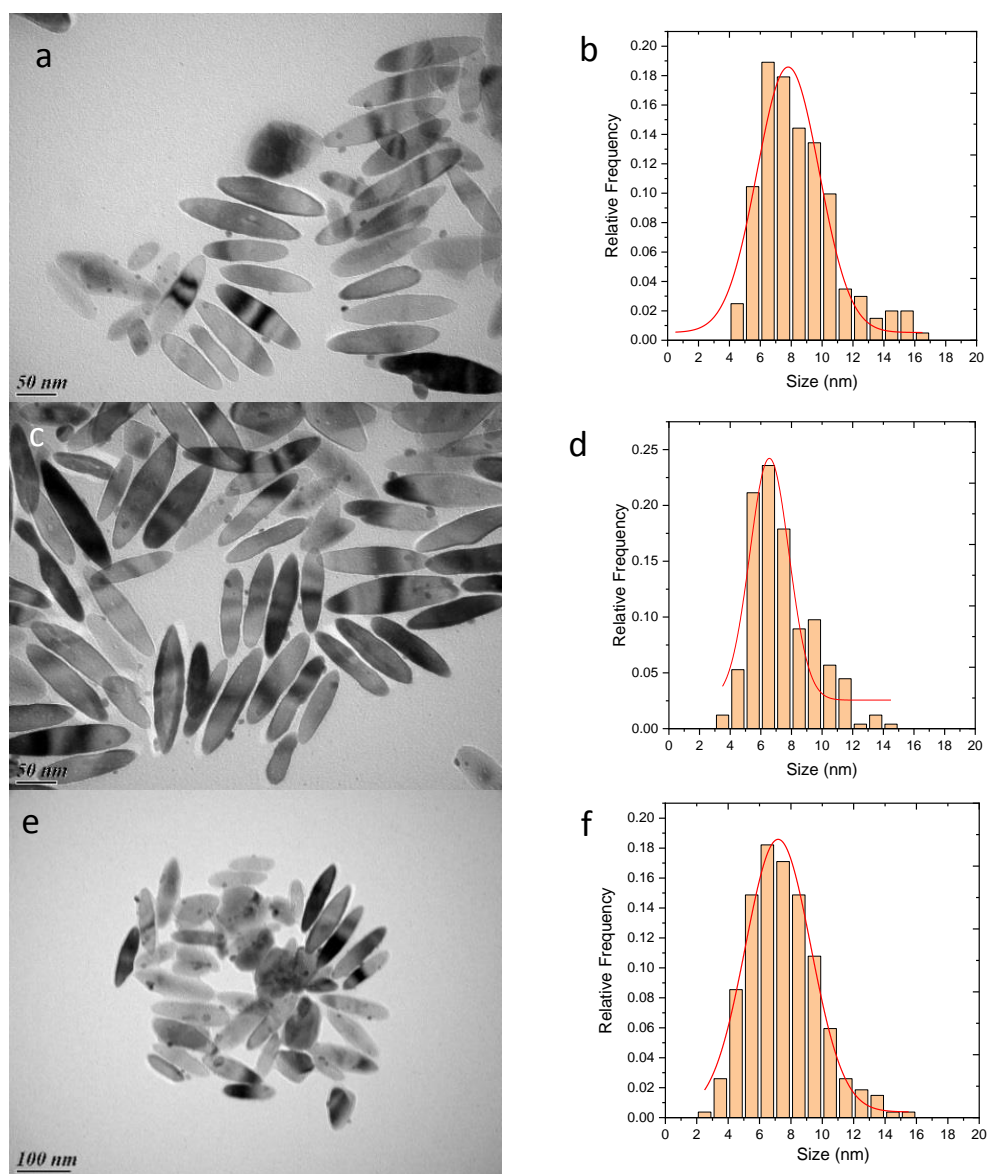

Figure 4.15 TEM images of Ag-TiO₂ NPs performed at different pH values, (a) pH 3, (c) pH 3.7 and (e) pH 4.5, and their corresponding size histograms (b) (d) and (f), respectively. Other conditions are kept the same: all in a microchannel, power 3.1 mW with illumination time 0.2 s, hole scavenger using 50 vol. % methanol, nanoneedle shape TiO₂.

It is believed that the high intensity produced by the focused UV laser still facilitates the formation of a single Ag ND and its growth proceeds according to the continuous Ag^+ reduction at the TiO₂ surface. The size values of Ag ND are listed in Table 4.3 and illustrated in Figure 4.16.

Power(mW)	Ag diameter (nm)(SD) at pH 3.7	Ag diameter (nm)(SD) at pH 4.5	Ag diameter (nm)(SD) at pH 5.0
3.1	6.6(1.3)*	7.2(2.1)*	6.4(1.3)*
7.75	11.7(3)*	11(3.7)*	10.6(3)*
15.5	13.2(3.6)*	12.8(3.3)*	12.8(4.1)*

Table 4.3 Ag diameter values at three different pH values under variable powers. Ag NDs are photodeposited onto nanoneedle shape TiO₂. "" means that the value is the size of the largest Ag NDs on one TiO₂.*
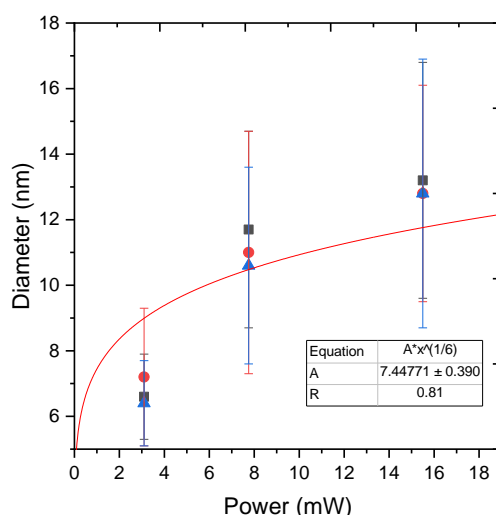
Figure 4.16 Ag diameter as a function of power at three different pH values. Nanoneedle shape TiO₂, hole scavenger using 50 vol. % methanol, an exposure illumination time of 0.2 s. A power-law fit was also plotted.

In this case, we also observed a size increase with increasing the applied power. The difference is much smaller than in the case of TiO₂ polyhedrons, possibly due to the larger size of the TiO₂ nanoneedles.

In conclusion, we have performed photodeposition of silver on TiO₂ using UV laser in a microchannel setup, succeeding in illustrating the weak role of pH on the nanodot diameter within the chosen pH range and a slight influence on the number of Ag NDs on TiO₂. Larger pH values may indeed favour interaction of the TiO₂ surface with cationic Ag^+ and induce an additional "secondary" nucleation with multidots on the TiO₂ surface. For our following experiments, to get Janus-like nanoparticles consisting in single Ag ND on the TiO₂ surface, we will keep the pH at a low value, like pH 3, unless stated elsewhere.

4.3.5 Comparison between the three setups on Ag photodeposition

In this part, we are about to discuss the effect of experimental setups on the photodeposition process. As mentioned in chapter 3, instead of commonly used Hg or Xe high-pressure UV lamps, we built a so-called "cuvette setup" also using a UV laser as the light source. For the microchannel and cuvette setups both using UV laser, the intensities can nonetheless differ by two orders of magnitude, owing to the large difference in the exposure area.

To compare the three setups, we chose the following conditions: an overall 1 mL solution, TiO$_2$ nanoneedles as a substrate, 50 vol. % methanol as a hole scavenger, $c[Ag^+]$ = 2 mM, $c[TiO_2]$ = 5.5 mM and pH 3, while we vary the illumination time and intensity in order to get the same order of energy per unit volume. The results are listed in Figure 4.17.

	TEM images	Histogram	Power (mW)	time (s)	Intensity (mW/cm^2)	Energy density (J/cm^3)	size (SD) (nm)	Janus yield (%)
a			3.1	0.2	4800	9	7.8(2)	47
b			13.88	480	18	7	16.8(4.8)	27
c			0.28	16800	0.4	5	3.5(1)	/
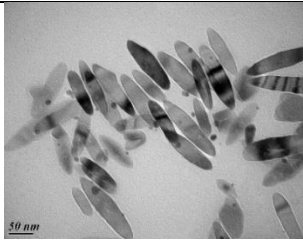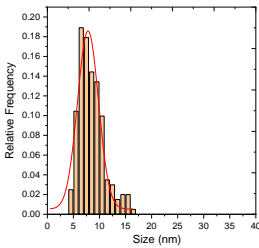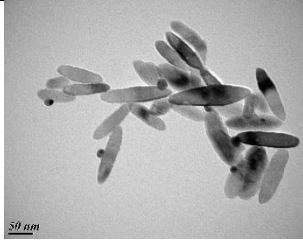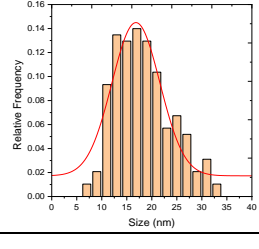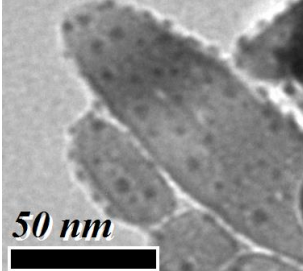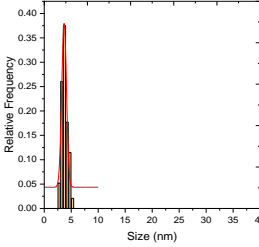
Figure 4.17 TEM images of Ag-TiO$_2$ NPs performed in (a) microchannel setup, (b) cuvette using UV laser and (c) cuvette setup using a mercury lamp. The size histogram, power, illumination time, intensity, energy density, size value and Janus yield are shown along with the TEM image in the same line. "/" indicates data are not available.

As shown in Figure 4.17a and b, both TEM samples give rise to a single Ag ND on each TiO$_2$ nanoneedle, but the average size of the Ag NDs obtained from the microchannel, and cuvette setup using UV laser differed a lot in mean size (respectively diameters of 7.8 and 17.6 nm), and polydispersity, the microchannel experiment offering the smallest one. The Janus yield in the microchannel setup (47 %) is almost two times that obtained with the cuvette setup (27 %). The flux of photons seems much more important than the deposited energy to produce well-calibrated Janus particles.

Since most researchers working on photodeposition customarily used a high-pressure Hg lamp as light source, we also implemented a UV lamp setup to reproduce photodeposition experiments. Here the intensity we had is only 0.4 mW/cm^2, which is 50 times less than that reached in the cuvette setup using UV laser. Once again we kept the same order of magnitude in deposited energy. We found many tiny Ag NDs distributed all over the TiO$_2$ surface, with a size of 3 ~ 4 nm (Figure 4.17c). The presence of tiny dots was in line with the results of other researchers in their experiments using a Hg lamp.[39, 56, 57]

Consequently, though we do our best to keep the energy density at the same level, these different results indicate that the magnitude of the intensity is likely at the origin of the induced photodeposited pattern and possibly explains all these different silver dot depositions.

4.3.6 Experiments performed in cuvette setup

We then focused on the silver photodeposition experiments performed with the cuvette setup using UV laser, to study the effect of illumination time on the photodeposition process.

In these experiments, methanol was used as a hole scavenger, TiO$_2$ nanoneedles as substrate, c[TiO$_2$] = 5.5 mM, c[Ag$^+$] = 2 mM. The representative TEM images of Ag-TiO$_2$ NPs with illumination times of 60, 240 and 1710 s are shown in Figure 4.18. All these photodeposition experiments show a single Ag ND deposited on the surface of TiO$_2$ and no multidots.
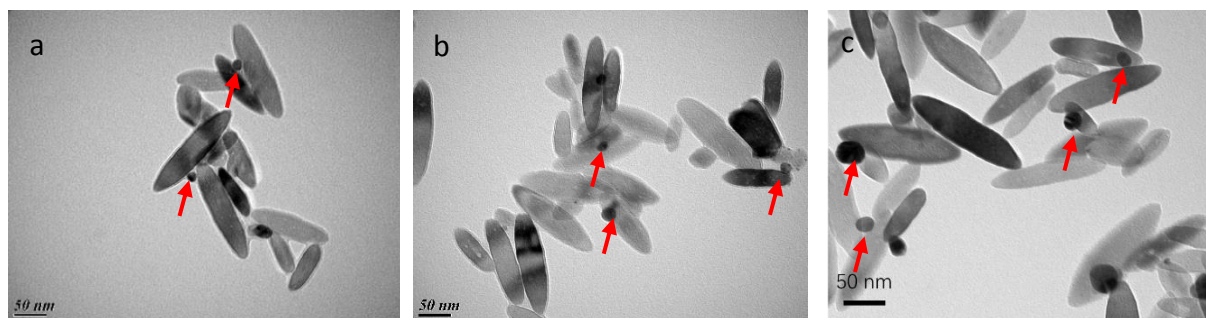
Figure 4.18 TEM images of Ag-TiO₂ made in cuvette setup using UV laser at power 13.88 mW, with illumination time of (a) 60 s, (b) 240 s and (c) 1710 s, respectively. The Ag NDs are denoted by red arrows.

The Ag diameter variation, as well as the Janus yield with the illumination time, are shown in Figure 4.19 and Table 4.4.

Power(mW)	Illumination time (s)	Ag diameter (nm)(SD)	Janus yield (%)
13.88	30	/	/
13.88	60	17.6(4.8)	23
13.88	120	22(4)	27
13.88	240	17(5.6)	28
13.88	342	16.3(3)	35
13.88	480	16.8(4.8)	27
13.88	855	20(5)	26
13.88	960	16.9(5.6)	30
13.88	1710	21(6)	21

*Table 4.4 Ag diameters and Janus yields as a function of illumination time at 13.88 mW. *: Janus not detectable on a TEM grid."/" denotes no Janus detection on the grid.*
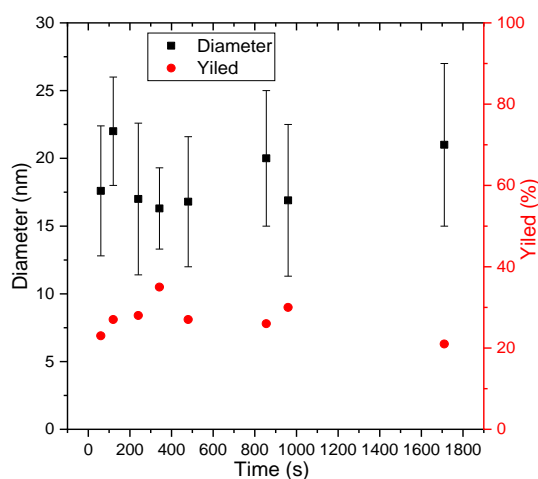
Figure 4.19 Ag diameter and Janus yield as a function of the illumination time at an applied power of 13.88 mW.

Figure 4.19 shows the silver size and Janus yield when experiments are performed in the cuvette setup using UV laser, as a function of the applied illumination time, by fixing the power at 13.88 mW. In the case of the cuvette setup, the exposure always corresponds to the cuvette size, *i.e.*, 1 cm². According to Table 4.4, the Ag dots were detectable only after illumination times as long as 60 s. All the attempts made at shorter illumination times led to unsuccessful observations on TEM grids despite our repeated efforts. The observable sizes otherwise vary from 18 nm to 21 nm with no apparent growth trend. It then seems that beyond 60 s, the growth process has already reached saturation. It can also be seen that whatever the long illumination time, it is still hard to get appreciable Janus yield in the cuvette setup.[58] This is probably due to the fact that, other than the Ag-TiO₂ heterodimers, we could also detect some micro-sized larger silver particles in some places on the TEM grid (Figure 4.20a). This phenomenon was even more frequent when the illumination time lasted longer.

The TEM samples made in the microchannel setup (Figure 4.20b) are much cleaner, and there are scarcely micro-size silver particles detected. The presence of micro-size Ag particles suggests a large consumption of the silver ions and prevents further growth of the silver dots even after a long UV irradiation time; silver ions may also be trapped by other radicals or species present in the medium.[59]
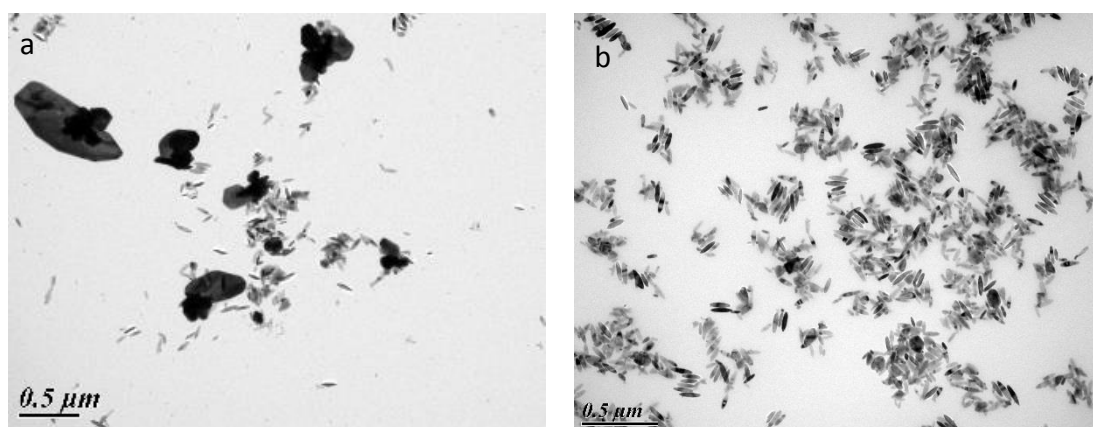
Figure 4.20 (a) TEM image of micro-sized silver particles at specific places on the TEM grid of a sample performed in cuvette setup using UV laser, at a power of 13.88 mW for 960 s. (b) A TEM image of a sample grid made in microchannel setup at 3.1 mW for 0.2 s.

In short, working with such a small power, or let us say low intensity in the cuvette setup case, seems to be hard to control the variation of the Ag NDs size as well as the Janus yield. A higher intensity in a microchannel setup with short time illumination leads to much cleaner TEM grids with very few micro-size Ag particles in product solution, which makes it an advantage for

microchannel setup as compared to the cuvette one using relatively low intensity but longer illumination time.

4.3.7 TiO₂ morphology effect on Ag photodeposition

Another parameter which may play a key role in applications in photocatalysis is the morphology of the TiO₂ NPs since depending on the morphology we get access to specific facets of the crystal structure and then specific redox properties. We will then discuss in the following the role of the TiO₂ morphology on the photodeposition process. Many researchers paid much more attention to the metal size or weight loading ratio[37, 60-62] on the semiconductor, but few of them discuss the preferred deposition site for the metal-TiO₂.[63, 64] In this case, we compare the TiO₂ polyhedrons, nanoneedles and nanoplates, which are made under conditions specified in chapter 2. The other parameters are kept identical, including Ag⁺ ions and TiO₂ molar concentrations, using 50 vol. % methanol as hole scavenger, pH 3, experiments made in the cuvette setup using UV laser. The TEM results are shown in Figure 4.21.
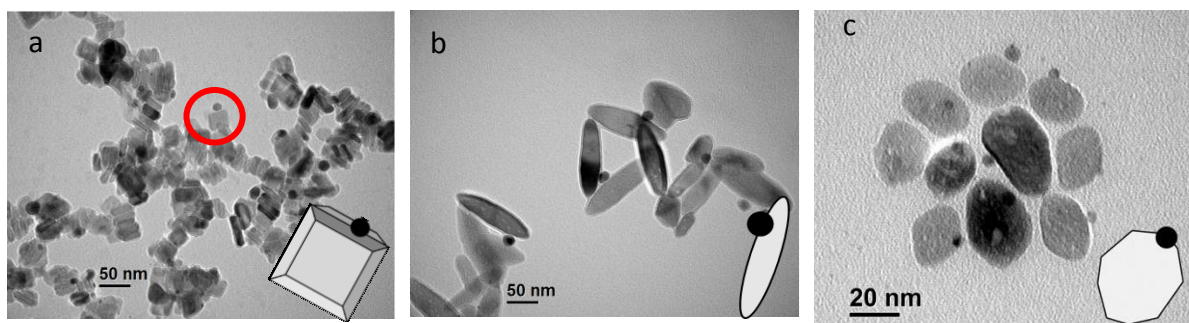
Figure 4.21 TEM images of Ag-TiO₂ NPs using variable TiO₂ shapes: (a) nanoplates, 8.1 mW for 480 s, (b) nanoneedles, 13.88 mW for 342 s and (c) polyhedrons, 50.8 mW for 240 s. Insets located at the right-bottom corner of each figure present the Ag preferred site on TiO₂ surface.

As illustrated in Figure 4.21, one single Ag ND per TiO₂ is observed, and the preferred deposition sites depend on the substrate morphology. For TiO₂ nanoplates (Figure 4.21a), Ag NDs tend to deposit on the edge of the plate,[65] corresponding to crystal facet of (101) which is the most stable surface presenting 50 % 6-fold coordinated Ti (Ti6c) and 50 % Ti5c atoms and already recognized to provide reductive sites which do not directly assist the oxidative processes.[58] For TiO₂ nanoneedles (Figure 4.21b), the preferred site of nucleation is mainly

<div align="center">127</div>

located close to the rod tip, where steps between the different planes become to be preponderant leading to the much sharper part of the nanoobject. In the case of TiO$_2$ polyhedrons (Figure 4.21c), the most stable facet is the (101). As a consequence, the facet (101) also becomes the preferred site of the silver deposit, as already shown in paragraph 4.3.2.

In conclusion, the morphology of TiO$_2$ plays a role in the photodeposition process, leading to silver deposition on preferential sites, considering minimization of surface energy and also atomic matching at the interface between TiO$_2$ and Ag ND.

4.3.8 Metal precursor effect on Ag photodeposition

The last parameter to test is the chemical nature of the silver precursor. Beyond the common and widely used AgNO$_3$ in most silver-concerned photodeposition research, another silver precursor that we decided to use is silver acetate (AgOAc).

 a) Presence of a hole scavenger

The photodeposition experiments using a AgOAc precursor solution were performed in the microchannel setup, with HCOONa as hole scavenger, at pH 3, with TiO$_2$ polyhedrons as the substrate. Figure 4.22 shows the TEM images of the resulting Ag-TiO$_2$ NPs obtained at powers varying between 3.1 and 23.25 mW.

All the powers lead to Janus-like structures, *i.e.*, a single Ag ND is deposited on each TiO$_2$ polyhedrons. A comparison between AgNO$_3$ and AgOAc is listed in Table 4.5 and Figure 4.23 shown below.
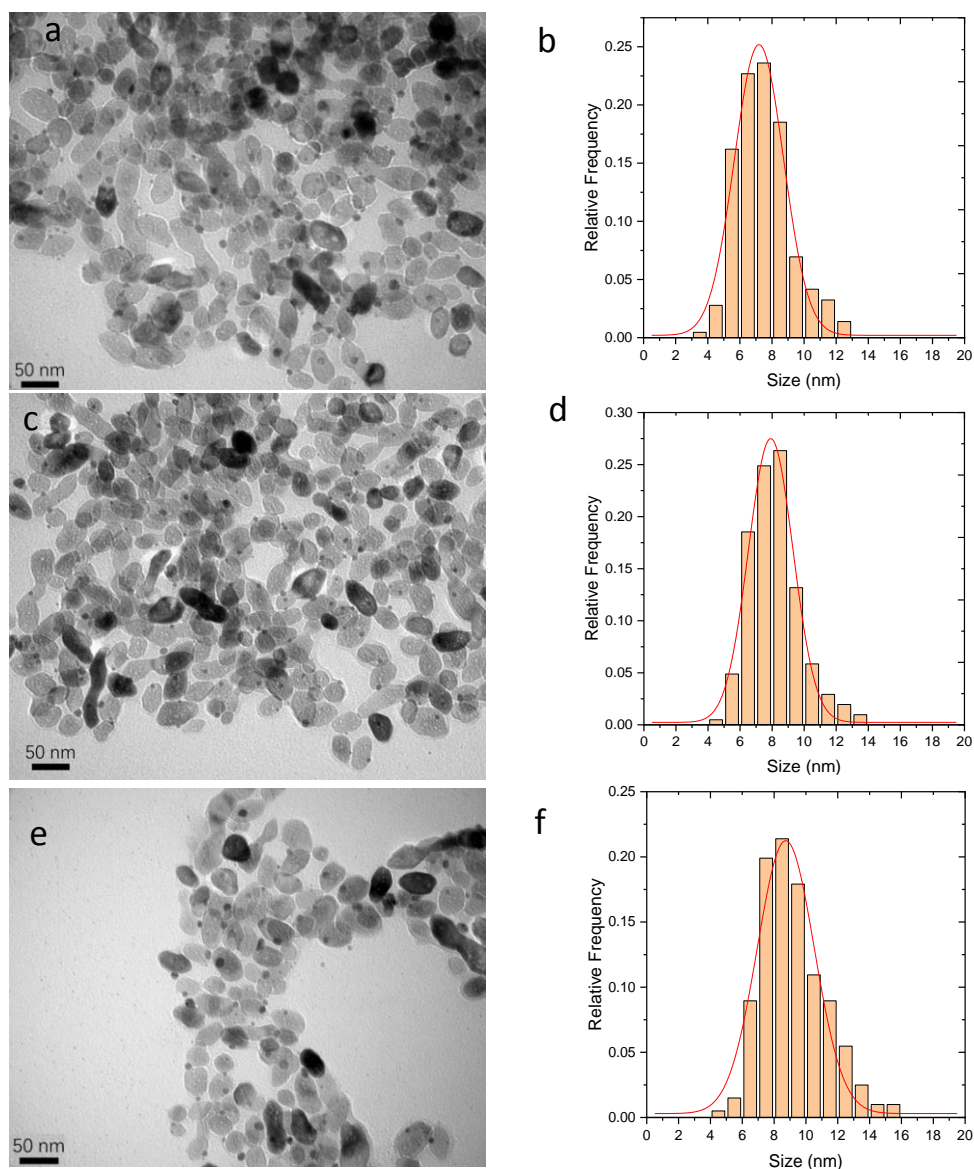
Figure 4.22 TEM images of Ag-TiO₂ NPs performed in a microchannel using AgOAc as metal salt precursor, HCOONa as hole scavenger, at powers of (a) 3.1 mW, (c) 7.75 mW and (e) 15.5 mW, and their corresponding size distributions (b), (d) and (f), respectively.

Power (mW)	Ag diameter (SD) (nm) AgNO₃	Janus yield %	Ag diameter(SD) (nm) AgOAc	Janus yield %
3.1	7.7(1.5)	86	7.2(1.5)	80
7.75	9.7(1.8)	90	7.9(1.4)	82
15.5	12.5(2.8)	90	8.7(1.8)	85
23.25	13(3.4)	88	9.1(2)	85

Table 4.5 Comparison table of the size vs applied power using two different silver precursors, AgNO₃ and AgOAc, both use HCOONa as a hole scavenger. SD means deviation values.
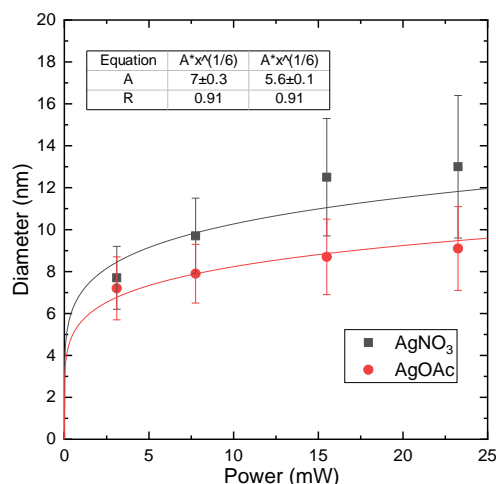
Figure 4.23 (a) Ag diameter as a function of applied power using either AgNO$_3$ or AgOAc as a metal salt precursor, with a fitting curve for each precursor in the function of D = A*P$^{1/6}$.

The Janus yield of the Ag-TiO$_2$ product is high, up to at least 80 % for the tested powers (Table 4.5). The silver size goes from 7.2 to 9.1 nm when increasing the power from 3.1 to 23.25 mW. Figure 4.23 clearly shows that the magnitude "A" of size growth is smaller when AgOAc replaces silver precursor AgNO$_3$. The silver size fits well the function D = A*P$^{1/6}$, justifying the validity of the prediction model (see § 4.3.9). Using the same method as in Figure 4.28, we obtained an atomic reaction rate of AgOAc around 0.31×10^9 M^{-1}s^{-1}, which is four times smaller than the value found for AgNO$_3$ (1.36×10^9 M^{-1}s^{-1}).

b)   Absence of a hole scavenger

The acetate ions in AgOAc solution itself can act as well as a hole scavenger. In this way, we could assume that no external hole scavenger should be added to the reaction system. That is why experiments without any external hole scavenger were performed in both microchannel and cuvette setups using UV laser, while the other conditions were kept identical, (c[AgOAc] = 2 mM, c[TiO$_2$] = 5.5 mM). The TEM results are shown below in Figure 4.24.
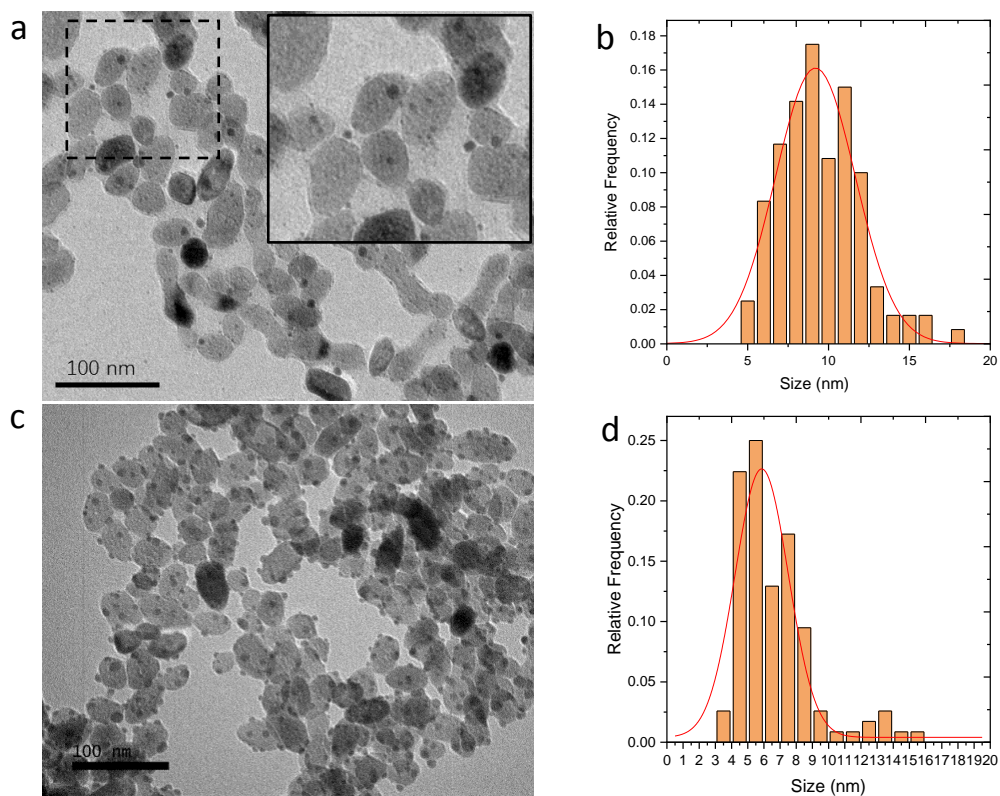
Figure 4.24 TEM images of Ag-TiO₂ using AgOAc as metal salt precursor made in (a) microchannel setup, 15.5 mW for 0.2 s and (c) cuvette setup using UV laser, 13.88 mW, 240 s. (b), (d) are their corresponding size distribution, respectively. Note that an enlarged inset is shown on the right top of (a).

As shown in Figure 4.24a, as opposed to Figure 4.24c, beside the large Ag ND we always more or less observed the presence of several tinier NDs. The larger Ag NDs have an average size of 9.2 nm (Figure 4.24b), while the tiny dots are around 1 - 3 nm size. This result is not yet clearly understood and still needs further work to be fully clarified.

For comparison, in the cuvette setup (Figure 4.24c), we observe the formation of several Ag NDs of the same size on each TiO₂, with a similar diameter of 5.9 nm (Figure 4.24d). The large intensity difference between the two setups may justify the number of Ag NDs on TiO₂, that is, higher intensity facilitates the single silver dot deposition on TiO₂.

4.3.9 Modelling fit of silver size data

Over the past decade, the variation of the size growth of the Ag NDs on the TiO₂ NPs has been studied as a function of many parameters (physical ones, chemical ones as well as human ones).[38, 66] There was then a real need to find a model which would optimize and provide a general trend for all these data. The detailed part of this model is given in Appendix 2, and

131

here, we will only briefly summarize the spirit of this growth prediction model.

The main stages to describe the growth law of Ag ND, will be set according to the different parameters involved in the photodeposition process. The sketch is the following:

(a) Electron-hole pairs are produced in the bulk and at the surface of the TiO$_2$ particle when TiO$_2$ is excited by the light within its band gap.

(b) The fate of electrons is either to recombine with holes, or to be trapped on defects, or to reduce Ag$^+$ ions at the surface of TiO$_2$; correspondingly, the holes may recombine with electrons, or may be trapped on defects or may oxidize species on the surface of TiO$_2$.

(c) Reduction of Ag$^+$ ions produces Ag^0 atoms. Beyond a certain amount of Ag^0 atoms, an Ag ND is nucleated at the surface of TiO$_2$. The Ag ND grows as a function of (i) the production of electrons related to the laser absorption and intensity, (ii) the Ag$^+$ ions concentration and (iii) the illumination time.

Two growth mechanisms may be possible, *i.e.,* (i) growth under a flux of metal atoms and (ii) growth by diffusion of metal atoms at the surface of TiO$_2$. The measured growth laws based on experimental data should allow the differentiation between the two mechanisms. We show in Appendix 2 that the growth of Ag ND is compatible with growth under a flux of metal atoms, considering time variation and scaling.

Two sections will be involved in the deduction of the growth model. The first stage consists in setting the different equations to determine the Ag^0 atoms concentration at the surface of TiO$_2$, by determinating the electron production due to light absorption. In a second step, the Ag^0 atoms concentration is used to predict the growth of an Ag ND deposited onto the surface of TiO$_2$.

4.3.9.1 Ag size as a function of Ag$^+$ ions concentration, solution velocity in previous works

According to the model presented in Appendix 2, in the high laser field case, late-stage growth regime of Ag ND should follow Equation 4.1:

$$D^3(T \gg 1) - D_0^3 \approx (8\frac{3\Omega^2}{\kappa}\frac{k_{HS}^{'}}{k_r})[\sqrt{\frac{k_r k_{Ag}^{'} g}{k_{HS}^{'}}} \cdot t] \sim \sqrt{g}\sqrt{k_{Ag}^{'}}t \qquad \textit{Equation 4.1}$$

132

Where k_r is the recombination rate, $k'_A = k_A[Ag^+]$ is the effective rate for the production of Ag^0, $k'_{HS} = k_{HS}[HS]$ is the rate of hole scavenging, g is the electron source term proportional to the absorption coefficient of TiO$_2$ and the beam intensity, Ω and κ are respectively a characteristic volume factor and a dimensionless factor related to the contact angle of the silver dot on the TiO$_2$ surface.

According to the prediction shown above, the silver dot diameter ($D = 2R$) should behave as $P^{1/6}$ in power, $[Ag^+]^{1/6}$ in concentration, and $t^{1/3}$ in illumination time.

To illustrate the validity of this model, previous experimental data in terms of silver size are gathered on a single graph shown below (Figure 4.25) as well as mine in the case of the power variation (Figure 4.27), both corresponding to the high field regime. All the data in Figure 4.25 are obtained under fixed conditions c[TiO$_2$] = 5.5 mM, pH at 3.5, in a microchannel setup and variable parameters (the illumination time is defined as $t = 2w_0/v$, where w_0 is the waist of the laser beam and v is the flow velocity in the microchannel).
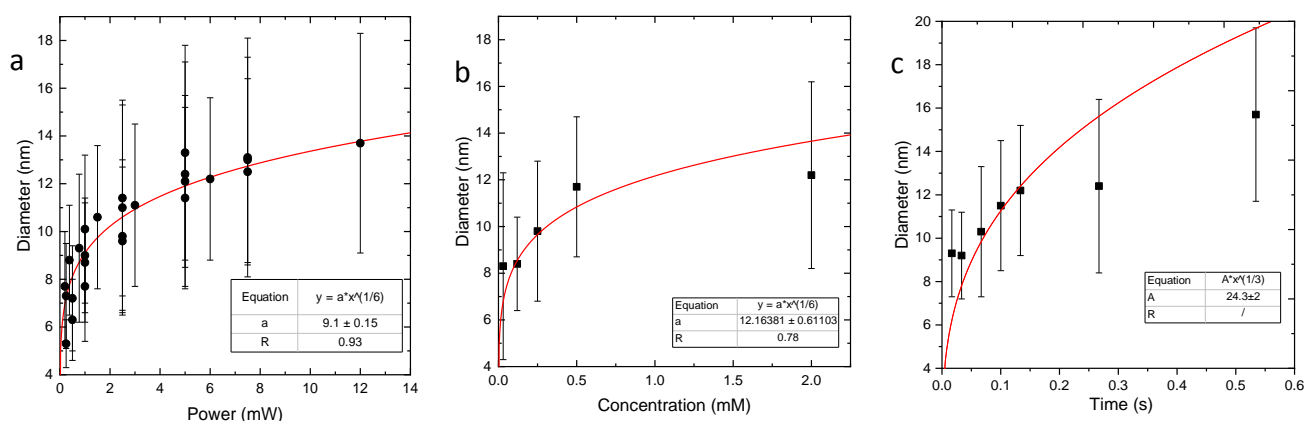
Figure 4.25 Data from previous works. (a) silver diameter as a function of power at a constant concentration, and velocity, c[Ag$^+$] = 2 mM, and illumination time 0.13 s (b) silver diameter as a function of Ag$^+$ concentration in bulk at 6 mW and illumination time 0.13 s, (c) silver diameter as a function of illumination time (varying from flow velocity) at c[Ag$^+$] = 2 mM, power 6 mW.

In Figure 4.25a, the variation of the Ag size is plotted as a function of the power; the data on this graph are obtained in conditions: c[Ag$^+$] = 2 mM in bulk, illumination time 0.13 s, with either methanol or HCOONa as a hole scavenger, dodecane as the oil with or without SPAN 80. These data seem to follow a single trend. When they are all fitted together with a power-law $D = A*P^{1/6}$, the correlation coefficient between the silver size and the power is as high as 0.93, indicating a good fit with the prediction in power. The fit also shows that critical radii (of diameter D$_0$) are extremely small and can be neglected.

References page 138

In Figure 4.25b, the data are obtained with the following conditions: illumination time 0.13 s, methanol as a hole scavenger, dodecane with 15 mM SPAN 80. The variation in the Ag$^+$ ions concentration results in a variation of the silver size. When the data are fitted with a function $D = A*c^{1/6}$, the correlation coefficient between the silver size and the concentration is 0.78, still an acceptable value. In Figure 4.25c, the data are obtained with the following conditions: c[TiO$_2$] = 5.5 mM, power 6 mW. When the data are fitted in the function of $D = A*t^{1/3}$, the fitting seems to be acceptable only during the first 100 ms. In the present work, using the same microchannel setup, we also succeed in reproducing the same trend (Figure 4.26). The conditions we use here are: c[Ag$^+$] = 2mM in bulk, c[TiO$_2$] = 5.5 mM, pH 3, illumination time 0.2 s, experiments performed in microchannel setup, dodecane with 15 mM SPAN 80.

As shown in Figure 4.26, the power variation leads to a silver size growth evolution which follows the same trend and type of law as P$^{1/6}$, with a correlation coefficient of 0.93, indicating a good fit of the experimental data with the model.
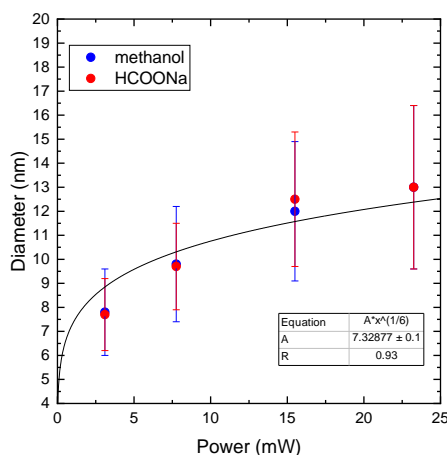
Figure 4.26 Data from the present work, silver diameter as a function of the power, at pH 3, using HCOONa and methanol as a hole scavenger, illumination time 0.2 s. A power law was also plotted.

4.3.9.2 Ag size as a function of power in present work at high field regime

More variable parameters are also investigated to broaden the research area, including pH values, and TiO$_2$ morphologies. All these effects on the silver growth will be fully discussed in the following parts. A fitting curve of the corresponding data is shown in Figure 4.27.
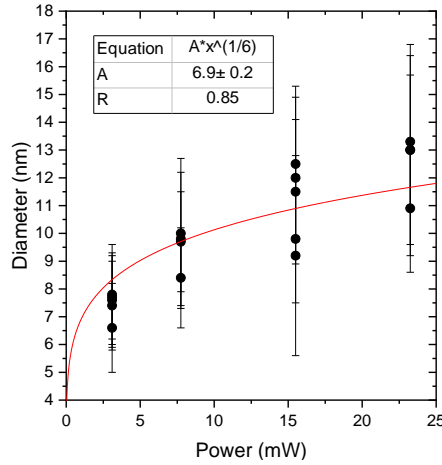
Figure 4.27 Silver diameter as a function of the power (conditions at c[Ag⁺] = 2 mM, c[TiO₂] = 5.5 mM, velocity 960 µm/s in the microchannel setup). TiO₂ morphologies (polyhedrons, nanoneedles and nanoplates), pH values and hole scavengers are additional variables which are detailed in the following sections. A power law for all data was also plotted.

Although these parameters may cause variations in the mean size distribution, the silver size still behaves as $P^{1/6}$ in power.

4.3.9.3 Modelling and fit of all the silver size data

In order to better understand the modelling, we made some transformation of Equation 4.1, as shown below in Equation 4.2:

$$D^3(T \gg 1) - D_0^3 \approx (8\frac{3\Omega^2}{\kappa}\frac{k_{HS}^{'}}{k_r})\frac{t}{\tau}$$

Equation 4.2

where t is the illumination time, $\tau = \left(\sqrt{\frac{k_r k_{Ag}^{'} g}{k_{HS}^{'}}}\right)^{-1} \sim \left([Ag^+]_{ads} \cdot P\right)^{-1}$ is a characteristic time for

the growth, which is related to the Ag⁺ ions concentration at the interface and the power. However, as we do not know accurately the production rate k_{Ag} of Ag atom, we assume a

theoretical slope $8\frac{3\Omega^2}{\kappa}\frac{k_{HS}^{'}}{k_r} = 1.94 \times 10^{-3} nm^3$ from data extracted in the literature (see

Appendix 2 for evaluations), and we artificially extract $\sqrt{k_{Ag}}$ from $\frac{t}{\tau}$ by plotting the cube

diameter as a function of $\frac{t}{\tau} / \sqrt{k_{Ag}}$. All the data fitted together on a single graph gives a linear

fit as shown in Figure 4.28a.
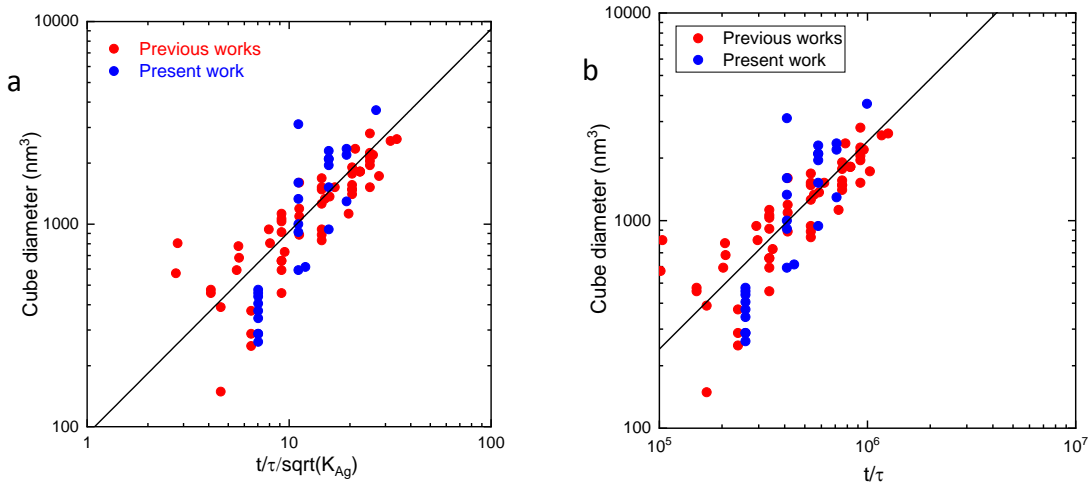
Figure 4.28 (a) Cube diameter as a function of t/τ/sqrt(K_Ag), (b) Cube diameter as a function of t/τ with a known value K_Ag.

Since this slope is equal to $1.94 \times 10^{-3} nm^3 \cdot \sqrt{k_{Ag}}$, we finally find $k_{Ag} = 1.36 \times 10^9 M^{-1} s^{-1}$, which is smaller than the data given in the literature. The growth law with this value $k_{Ag} = 1.36 \times 10^9 M^{-1} s^{-1}$ is then represented in Figure 4.28b.

We also represent the plot of diameter instead of cube diameter (volume), as a function of t/τ. As shown in Figure 4.29b, the data from the present work in blue, overlap perfectly with those from previous works, showing, by the way, the reproducibility of this photodeposition method. Beyond consistency, the global fit of all the data set indicates that our model well predicts the photodeposition of Ag NDs growth on the TiO₂ surface.
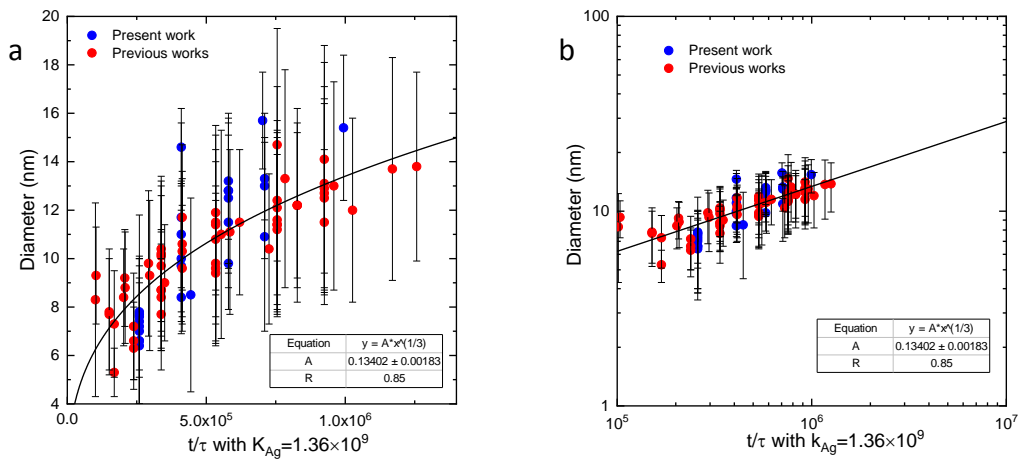
Figure 4.29 Diameter as a function of t/τ with a known value of k_Ag, in either (a) linear or (b) logarithm coordinates.

136

4.4 Conclusions

In this chapter, we performed the photodeposition of silver on TiO$_2$ in the microchannel setup. Techniques including TEM, XPS and UV-vis spectroscopy have confirmed the existence of metallic Ag NDs deposited on the TiO$_2$ surface and the formation of heterodimer structures with single Ag ND on each TiO$_2$.

The growth model successfully predicted the silver size variation in the photodeposition process. The silver size behaves as $P^{1/6}$ in power, $[Ag^+]_{ads}^{1/6}$ in concentration, and $t^{1/3}$ in time. The silver reduction rate in the photodeposition process is also deduced, and it is in the same order of the reported values.

We have also studied the effects of other parameters on the photodeposition process. Two kinds of hole scavengers, methanol and HCOONa, have been investigated and found to lead to a high ratio of silver deposits on TiO$_2$ surface. HCOONa offers much better yields in heterodimers, while using methanol may lead to multi Ag NDs onside. Several pH values, within a range from pH 3 to 5, were varied to investigate the role of the pH value in the photodeposition process. We found that lower pH facilitates the synthesis of heterodimers, while relatively high pH environments induce multi dots nucleation on the TiO$_2$ surface. Beyond experiments performed with the microchannel setup, the photodeposition was also investigated in a cuvette setup, illuminated by either the same UV laser or a high-pressure UV lamp. Cuvette experiments using the UV laser showed either single nanoparticle or multi nanoparticles deposition on TiO$_2$ surface depending on experimental conditions, while the UV lamp experiments lead systematically to the nucleation of tiny dots with a diameter smaller than 3 nm. Finally, depending on the nature of the metal precursor, silver acetate induces a much smaller size range as compared to the usually considered AgNO$_3$, it is suggested that the smaller value of K_{Ag} for AgOAc induces the smaller silver size.

4.5 Bibliography

1.   Melvin, A. A.; Illath, K.; Das, T.; Raja, T.; Bhattacharyya, S.; Gopinath, C. S., M-Au/TiO$_2$ (M=Ag, Pd, and Pt) nanophotocatalyst for overall solar water splitting: role of interfaces. *Nanoscale* **2015,** *7*, 13477-13488.

2.   Shang, M.; Hou, H.; Gao, F.; Wang, L.; Yang, W., Mesoporous Ag@TiO$_2$ nanofibers and their photocatalytic activity for hydrogen evolution. *RSC Adv.* **2017,** *7*, 30051-30059.

3.   Leong, K. H.; Gan, B. L.; Ibrahim, S.; Saravanan, P., Synthesis of surface plasmon resonance (SPR) triggered Ag/TiO$_2$ photocatalyst for degradation of endocrine disturbing compounds. *Appl. Surf. Sci.* **2014,** *319*, 128-135.

4.   Devadi, M. A. H.; Krishna, M.; Murthy, H. N. N.; Sathyanarayana, B. S., Statistical Optimization for Photocatalytic Degradation of Methylene Blue by Ag-TiO$_2$ Nanoparticles. *Procedia Mater. Sci.* **2014,** *5*, 612-621.

5.   Zhang, H.; Liang, C.; Liu, J.; Tian, Z.; Wang, G.; Cai, W., Defect-Mediated Formation of Ag Cluster-Doped TiO$_2$ Nanoparticles for Efficient Photodegradation of Pentachlorophenol. *Langmuir* **2012,** *28*, 3938-3944.

6.   Whang, T.-J.; Huang, H.-Y.; Hsieh, M.-T.; Chen, J.-J., Laser-Induced Silver Nanoparticles on Titanium Oxide for Photocatalytic Degradation of Methylene Blue. *Int. J. Mol. Sci.* **2009,** *10*, 4707-4718.

7.   Lin, C.-Y.; Lai, Y.-H.; Balamurugan, A.; Vittal, R.; Lin, C.-W.; Ho, K.-C., Electrode modified with a composite film of ZnO nanorods and Ag nanoparticles as a sensor for hydrogen peroxide. *Talanta* **2010,** *82*, 340-347.

8.   Bai, J.; Zhou, B., Titanium dioxide nanomaterials for sensor applications. *Chem. Rev.* **2014,** *114*, 10131-10176.

9.   Lu, Q.; Lu, Z.; Lu, Y.; Lv, L.; Ning, Y.; Yu, H.; Hou, Y.; Yin, Y., Photocatalytic Synthesis and Photovoltaic Application of Ag-TiO$_2$ Nanorod Composites. *Nano Lett.* **2013,** *13*, 5698-5702.

10.   Clavero, C., Plasmon-induced hot-electron generation at nanoparticle/metal-oxide interfaces for photovoltaic and photocatalytic devices. *Nature Photonics* **2014,** *8*, 95.

11.   Coto, M.; Divitini, G.; Dey, A.; Krishnamurthy, S.; Ullah, N.; Ducati, C.; Kumar, R. V., Tuning the properties of a black TiO$_2$-Ag visible light photocatalyst produced by a rapid one-pot chemical reduction. *Mater. Today Chem.* **2017,** *4*, 142-149.

12.   Kim, K. D.; Han, D. N.; Lee, J. B.; Kim, H. T., Formation and characterization of Ag-deposited TiO$_2$ nanoparticles by chemical reduction method. *Scr. Mater.* **2006,** *54*, 143-146.

13.   Kusdianto, K.; Jiang, D.; Kubo, M.; Shimada, M., Effect of annealing temperature on the photocatalytic activity of Ag-TiO$_2$ nanocomposite films by one-step gas-phase deposition. *Mater. Res. Bull.* **2018,** *97*, 497-505.

14.   Ozimek, M.; Palewicz, M.; Hreniak, A., Optical properties of TiO$_2$ nanopowder doped by silver (copper) during synthesis or PVD method. *Acta Phys. Pol. A* **2016,** *129*, 1214-1219.

15.   Mohamed, R. M.; Shironita, S.; Mori, K.; Yamashita, H., Effect of metal deposition on the photocatalytic activity of titania-silica for the removal of 2-propanol diluted in water. *Res. Chem. Intermed.* **2009,** *35*, 305-312.

16.   Li, J.; Xu, J.; Dai, W. L.; Fan, K., Dependence of Ag deposition methods on the photocatalytic activity and surface state of TiO$_2$ with twistlike helix structure. *J. Phys. Chem. C* **2009,** *113*, 8343-8349.

17.   Espino-Estévez, M. R.; Fernández-Rodríguez, C.; González-Díaz, O. M.; Araña, J.; Espinós, J. P.; Ortega-Méndez, J. A.; Doña-Rodríguez, J. M., Effect of TiO$_2$-Pd and TiO$_2$-Ag on the photocatalytic oxidation of diclofenac, isoproturon and phenol. *Chem. Eng. J.* **2016,** *298*, 82-95.

18.   Diak, M.; Grabowska, E.; Zaleska, A., Synthesis, characterization and photocatalytic activity of noble metal-modified TiO$_2$ nanosheets with exposed {001} facets. *Appl. Surf. Sci.* **2015,** *347*, 275-285.

19.   Naoi, K.; Ohko, Y.; Tatsuma, T., TiO$_2$ Films Loaded with Silver Nanoparticles: Control of Multicolor Photochromic Behavior. *J. Am. Chem. Soc.* **2004,** *126*, 3664-3668.

20. Mohamed, H. H.; Dillert, R.; Bahnemann, D. W., Growth and Reactivity of Silver Nanoparticles on the Surface of TiO$_2$: A Stopped-Flow Study. *J. Phys. Chem. C* **2011,** *115*, 12163-12172.

21. Wenderich, K.; Mul, G., Methods, Mechanism, and Applications of Photodeposition in Photocatalysis: A Review. *Chem. Rev.* **2016,** *116*, 14587-14619.

22. Lee, Y.; Kim, E.; Park, Y.; Kim, J.; Ryu, W.; Rho, J.; Kim, K., Photodeposited metal-semiconductor nanocomposites and their applications. *J. Materiomics* **2018,** *4*, 83-94.

23. Tada, H.; Fujishima, M.; Kobayashi, H., Photodeposition of metal sulfide quantum dots on titanium(iv) dioxide and the applications to solar energy conversion. *Chem. Soc. Rev.* **2011,** *40*, 4232-4243.

24. Hada, H.; Yonezawa, Y.; Saikawa, M., Photoreduction of Silver Ion in a Titanium Dioxide Suspension. *Bull. Chem. Soc. Jpn.* **1982,** *55*, 2010-2014.

25. Ohtani, B.; Kakimoto, M.; Miyadzu, H.; Nishimoto, S.; Kagiya, T., Effect of surface-adsorbed 2-propanol on the photocatalytic reduction of silver and/or nitrate ions in acidic titania suspension. *J. Phys. Chem.* **1988,** *92*, 5773-5777.

26. Zhang, F.; Guan, N.; Li, Y.; Zhang, X.; Chen, J.; Zeng, H., Control of Morphology of Silver Clusters Coated on Titanium Dioxide during Photocatalysis. *Langmuir* **2003,** *19*, 8230-8234.

27. Guin, D.; Manorama, S. V.; Latha, J. N. L.; Singh, S., Photoreduction of Silver on Bare and Colloidal TiO$_2$ Nanoparticles/Nanotubes: Synthesis, Characterization, and Tested for Antibacterial Outcome. *J. Phys. Chem. C* **2007,** *111*, 13393-13397.

28. Bade, K.; Karstens, O.; Michaelis, A.; Schultze, J. W., Localization of electrode reactions by a focused laser beam. *Faraday Discuss.* **1992,** *94*, 45-62.

29. Matsubara, K.; Tatsuma, T., Morphological Changes and Multicolor Photochromism of Ag Nanoparticles Deposited on Single-crystalline TiO$_2$ Surfaces. *Adv. Mater.* **2007,** *19*, 2802-2806.

30. Naoi, K.; Ohko, Y.; Tatsuma, T., Switchable rewritability of Ag-TiO$_2$ nanocomposite films with multicolor photochromism. *Chem. Commun.* **2005**, 1288-1290.

31. Kawahara, K.; Suzuki, K.; Ohko, Y.; Tatsuma, T., Electron transport in silver-semiconductor nanocomposite films exhibiting multicolor photochromism. *Phys. Chem. Chem. Phys.* **2005,** *7*, 3851-3855.

32. Dinh, C. T.; Nguyen, T. D.; Kleitz, F.; Do, T. O., Shape-controlled synthesis of highly crystalline titania nanocrystals. *ACS Nano* **2009,** *3*, 3737-3743.

33. Barbé, C. J.; Arendse, F.; Comte, P.; Jirousek, M.; Lenzmann, F.; Shklover, V.; Grätzel, M., Nanocrystalline Titanium Oxide Electrodes for Photovoltaic Applications. *J. Am. Ceram. Soc* **2005,** *80*, 3157-3171.

34. O'Regan, B.; Grätzel, M., A low-cost, high-efficiency solar cell based on dye-sensitized colloidal TiO$_2$ films. *Nature* **1991,** *353*, 737-740.

35. Chen, X.; Mao, S. S., Titanium dioxide nanomaterials: synthesis, properties, modifications, and applications. *Chem. Rev.* **2007,** *107*, 2891-2959.

36. Rozhkova, E. A.; Ulasov, I.; Lai, B.; Dimitrijevic, N. M.; Lesniak, M. S.; Rajh, T., A High-Performance Nanobio Photocatalyst for Targeted Brain Cancer Therapy. *Nano Lett.* **2009,** *9*, 3337-3342.

37. Bo, Z.; Eaton, T. R.; Gallagher, J. R.; Canlas, C. P.; Miller, J. T.; Notestein, J. M., Size-Selective Synthesis and Stabilization of Small Silver Nanoparticles on TiO$_2$ Partially Masked by SiO$_2$. *Chem. Mater.* **2015,** *27*, 1269-1277.

38. Vauriot, L. Synthèse microfluidique de nanomatériaux multifonctionnels par laser. 2012.

39. Dinh, C.-T.; Nguyen, T.-D.; Kleitz, F.; Do, T.-O., A New Route to Size and Population Control of Silver Clusters on Colloidal TiO$_2$ Nanocrystals. *ACS Appl. Mater. Interfaces* **2011,** *3*, 2228-2234.

40. Su, C.; Liu, L.; Zhang, M.; Zhang, Y.; Shao, C., Fabrication of Ag/TiO$_2$ nanoheterostructures with visible light photocatalytic function via a solvothermal approach. *Cryst. Eng. Comm.* **2012,** *14*, 3989-3999.

41. Kenens, B.; Chamtouri, M.; Aubert, R.; Miyakawa, K.; Hayasaka, Y.; Naiki, H.; Watanabe, H.; Inose, T.; Fujita, Y.; Lu, G.; Masuhara, A.; Uji-i, H., Solvent-induced improvement of Au photo-deposition and resulting photo-catalytic efficiency of Au/TiO$_2$. *RSC Adv.* **2016,** *6*, 97464-97468.

42.   Jiang, Z.; Zhang, Z.; Shangguan, W.; Isaacs, M. A.; Durndell, L. J.; Parlett, C. M. A.; Lee, A. F., Photodeposition as a facile route to tunable Pt photocatalysts for hydrogen production: on the role of methanol. *Catal. Sci. Technol.* **2016,** *6*, 81-88.

43.   López, C. R.; Melián, E. P.; Ortega Méndez, J. A.; Santiago, D. E.; Doña Rodríguez, J. M.; González Díaz, O., Comparative study of alcohols as sacrificial agents in H$_2$ production by heterogeneous photocatalysis using Pt/TiO$_2$ catalysts. *J. Photochem. Photobiol., A* **2015,** *312*, 45-54.

44.   Ismail, A. A.; Al-Sayari, S. A.; Bahnemann, D. W., Photodeposition of precious metals onto mesoporous TiO$_2$ nanocrystals with enhanced their photocatalytic activity for methanol oxidation. *Catal. Today* **2013,** *209*, 2-7.

45.   Liu, S.; Liu, A. A.; Wen, B.; Zhang, R.; Zhou, C.; Liu, L. M.; Ren, Z., Coverage Dependence of Methanol Dissociation on TiO$_2$ (110). *J. Phys. Chem. Lett.* **2015**, 3327-3334.

46.   Phillips, K. R.; Jensen, S. C.; Baron, M.; Li, S. C.; Friend, C. M., Sequential photo-oxidation of methanol to methyl formate on TiO$_2$ (110). *J. Am. Chem. Soc.* **2013,** *135*, 574-577.

47.   Shen, M.; Henderson, M. A., Identification of the Active Species in Photochemical Hole Scavenging Reactions of Methanol on TiO$_2$. *J. Phys. Chem. Lett.* **2011,** *2*, 2707-2710.

48.   Xu, C.; Yang, W.; Guo, Q.; Dai, D.; Chen, M.; Yang, X., Molecular hydrogen formation from photocatalysis of methanol on anatase-TiO$_2$ (101). *J. Am. Chem. Soc.* **2014,** *136*, 602-605.

49.   Wenderich, K.; Han, K.; Mul, G., The Effect of Methanol on the Photodeposition of Pt Nanoparticles on Tungsten Oxide. *Part. Part. Syst. Char.* **2018,** *35*, 1700250.

50.   Zhang, J.; Nosaka, Y., Photocatalytic oxidation mechanism of methanol and the other reactants in irradiated TiO$_2$ aqueous suspension investigated by OH radical detection. *Appl. Catal. B* **2015,** *166-167*, 32-36.

51.   Takai, A.; Kamat, P. V., Capture, Store, and Discharge. Shuttling Photogenerated Electrons across TiO$_2$–Silver Interface. *ACS Nano* **2011,** *5*, 7369-7376.

52.   Sano, T.; Negishi, N.; Mas, D.; Takeuchi, K., Photocatalytic Decomposition of N$_2$O on Highly Dispersed Ag$^+$ Ions on TiO$_2$ Prepared by Photodeposition. *J. Catal.* **2000,** *194*, 71-79.

53.   Guo, Y.; Siretanu, I.; Zhang, Y.; Mei, B.; Li, X.; Mugele, F.; Huang, H.; Mul, G., pH-Dependence in facet-selective photo-deposition of metals and metal oxides on semiconductor particles. *J. Mater. Chem. A* **2018,** *6*, 7500-7508.

54.   Zhang, F.; Chen, J.; Zhang, X.; Gao, W.; Jin, R.; Guan, N.; Li, Y., Synthesis of Titania-Supported Platinum Catalyst: The Effect of pH on Morphology Control and Valence State during Photodeposition. *Langmuir* **2004,** *20*, 9329-9334.

55.   Zhang, F.; Jin, R.; Chen, J.; Shao, C.; Gao, W.; Li, L.; Guan, N., High photocatalytic activity and selectivity for nitrogen in nitrate reduction on Ag/TiO$_2$ catalyst with fine silver clusters. *J. Catal.* **2005,** *232*, 424-431.

56.   Ko, S.; Banerjee, C. K.; Sankar, J., Photochemical synthesis and photocatalytic activity in simulated solar light of nanosized Ag doped TiO$_2$ nanoparticle composite. *Composites Part B* **2011,** *42*, 579-583.

57.   Sclafani, A.; Mozzanega, M.-N.; Pichat, P., Effect of silver deposits on the photocatalytic activity of titanium dioxide samples for the dehydrogenation or oxidation of 2-propanol. *J. Photochem. Photobiol., A* **1991,** *59*, 181-189.

58.   D'Arienzo, M.; Carbajo, J.; Bahamonde, A.; Crippa, M.; Polizzi, S.; Scotti, R.; Wahba, L.; Morazzoni, F., Photogenerated Defects in Shape-Controlled TiO2 Anatase Nanocrystals: A Probe To Evaluate the Role of Crystal Facets in Photocatalytic Processes. *J. Am. Chem. Soc.* **2011,** *133*, 17652-17661.

59.   Hu, S.; Qiao, P.; Fu, Y.; Li, F.; Xiao, X.; Zhao, C.; Feng, Q.; Jiang, B., In-situ Platinum Plasmon Resonance Effect Prompt Titanium Dioxide Nanocube Photocatalytic Hydrogen Evolution. *Chemistry – An Asian Journal* **2019,** *14*, 592-596.

60.   Shoaib, A.; Ji, M.; Qian, H.; Liu, J.; Xu, M.; Zhang, J., Noble metal nanoclusters and their in situ calcination to nanocrystals: Precise control of their size and interface with TiO$_2$ nanosheets and their versatile catalysis applications. *Nano Res.* **2016,** *9*, 1763-1774.

61.   Park, H.-H.; Zhang, X.; Lee, K. W.; Sohn, A.; Kim, D.-W.; Kim, J.; Song, J.-W.; Choi, Y. S.; Lee, H. K.; Jung, S. H.; Lee, I.-G.; Cho, Y.-D.; Shin, H.-B.; Sung, H. K.; Park, K. H.; Kang, H. K.; Park, W.-K.; Park, H.-

H., Selective photochemical synthesis of Ag nanoparticles on position-controlled ZnO nanorods for the enhancement of yellow-green light emission. *Nanoscale* **2015,** *7*, 20717-20724.

62.   Bansal, A.; Madhavi, S.; Tan, T. T. Y.; Lim, T. M., Effect of silver on the photocatalytic degradation of humic acid. *Catal. Today* **2008,** *131*, 250-254.

63.   D'Arienzo, M.; Carbajo, J.; Bahamonde, A.; Crippa, M.; Polizzi, S.; Scotti, R.; Wahba, L.; Morazzoni, F., Photogenerated Defects in Shape-Controlled TiO₂ Anatase Nanocrystals: A Probe To Evaluate the Role of Crystal Facets in Photocatalytic Processes. *J. Am. Chem. Soc.* **2011,** *133*, 17652-17661.

64.   Sofianou, M.-V.; Boukos, N.; Vaimakis, T.; Trapalis, C., Decoration of TiO₂ anatase nanoplates with silver nanoparticles on the {101} crystal facets and their photocatalytic behaviour. *Appl. Catal., B* **2014,** *158-159*, 91-95.

65.   Liu, G.; Yang, H. G.; Pan, J.; Yang, Y. Q.; Lu, G. Q.; Cheng, H. M., Titanium dioxide crystals with tailored facets. *Chem. Rev.* **2014,** *114*, 9559-9612.

66.   Shupyke, I., Unpublished work.

Chapter 5

Photodeposition of Gold, Palladium and Platinum nanodots on TiO$_2$ by UV laser

Table of contents

5.1 Photodeposition of Au nanodots onto the surface of TiO_2 nanoparticles

5.1.1 Introduction to photodeposition of Au nanodots onto the surface of TiO_2 nanoparticles

In the periodic table of elements, the element gold is just below silver in group 11. The properties of gold are thus similar to that of silver in many aspects including the crystal structure, atomic structure and existence of a surface plasmon resonance effect in the visible light range. Herein, apart from silver, we then choose to test this method for the deposition of gold on the surface of the TiO_2 semiconductor. The photodeposition of Au nanodots (Au NDs) on the surface of TiO_2 is indeed another important research topic. It was performed back to 1995 by Bamwenda et al.[1] using TiO_2 powder in aqueous suspensions containing $HAuCl_4$.

In general, people use gold chloride complexes as the metal precursors for the photodeposition of gold. Gartner et al.[2] synthesized Au NDs on TiO_2 commercial product using three different Au metal salts, i.e., $NaAuCl_4$, $AuCl_3$, $[Au(PPh_3)]Cl$ and $AuCl$, and found that $NaAuCl_4$ and $AuCl_3$ as precursors gave the best activity towards hydrogen generation from water/methanol (1/1vol.) mixture. They found that the evolved gas during the photodeposition process consisted mainly of H_2; CO and CO_2 were only detected in trace amounts. In addition, formic acid was detected via high-performance liquid chromatography (HPLC), and the qualitative product concentrations were formic acid > CO_2 > CO. They established an order in terms of efficiency between hole scavengers: (Methanol > isopropanol > glycerine > glucose). Sangeetha et al.[3] also made a comparison between $HAuCl_4$ and $AuCl_3$, and found no significant difference in metal loading.

Kenens et al.[4] investigated the effect of hole scavengers on the photodeposition of Au on TiO_2 and found that ethylene glycol showed better efficiency than ethanol for hole consumption, making it an efficient hole scavenger. It was demonstrated that Au NDs made by

photodeposition using ethanol were large (50-100 nm for 0.4 wt.% $HAuCl_4$) and aggregated, while those using ethylene glycol were small (5-15 nm for 0.4 wt.%) and abundant.[4]

It is also believed that the size control of Au NDs is vital in photocatalytic reactions.[5, 6] Wang et al.[5] found that the size of Au NDs could be easily regulated by changing the concentration of gold precursor from 0.05 to 0.25 mM or the Au loading in the range of 0.3 to 1.5 wt.% using photodeposition method. Deepagan et al.[7] indicated that the size of Au NDs could be adjusted by varying the irradiation time when illuminated with a 256 nm UV light. An exposure time as short as 3 min resulted in the formation of unimodal small Au NDs (< 2 nm) on the surface of TiO₂. An exposure time of 10 min irradiation led to the formation of large Au NDs (> 5 nm) with the coexistence of smaller ones. Prolonged exposure over 12 h resulted in the growth of large Au NDs with complete disappearance of small ones. Therefore, by controlling the exposure time, the author obtained three representative composites of TiO₂ nanoparticle with small, bimodal, and large Au NDs .[7]

Nonetheless, most of the works concerning gold photodeposition at the surface of TiO₂ always found the presence of gold multidots more or less homogeneously distributed on each TiO₂ particle, no matter the gold content loading or the kind of TiO₂ or its morphology.[8-11]

In this part, we continue to implement our UV laser exposition as a powerful light source to initiate the photodeposition of a single gold ND per TiO₂ particle. The effect of the laser power and the illumination time in both the microchannel and the cuvette setups on the Au size distribution and Janus yield are investigated. The fit of the data of Au size variation is also made to verify the validity of the model proposed for Ag photodeposition.

5.1.2 Experimental methods

5.1.2.1 Experimental methods in microchannel setup

The semiconductor supports to be used are the TiO₂ polyhedrons all along with this chapter. The reaction solution is prepared by mixing an already made TiO₂-water solution and freshly prepared $KAuCl_4$ under Ar, to make the final concentration c[TiO₂] = 5.5 mM and c[$KAuCl_4$] =

0.1 - 1 mM. Then the oxygen-free hole scavenger methanol is added to get the final solution (50 vol. %). The pH of the mixture is adjusted at pH 3 using nitric acid (pH = 1). The acidic solution helps to obtain a good TiO_2 dispersion because pH 3 is below the isoelectric point of TiO_2 (pH 6.1).

As in the case of silver deposition within the microchannel reactor, the product in the aqueous solution and the dodecane containing 15 mM SPAN 80 are collected in a glass vial and then gently shaken to initiate a phase transfer process, during which the Au-TiO_2 NPs are transferred to the oil part. The oil part containing Au-TiO_2 is then diluted by the addition of 1 mL heptane. To make a TEM grid, the solution is sonicated for 10 min to disperse the NPs, and then one drop is cast on a TEM grid (carbon film face up). A few more heptane drops are continuously cast on top of the grid, to wash away the remaining excessive surfactant. For the statistics of Au size, at least 200 Au NDs were measured unless otherwise specified.

5.1.2.2 Experimental methods in cuvette setup

As in the previous case, the aqueous solution is purged with Ar gas for at least 10 min, to remove the dissolved oxygen in the solution before transfer to a cuvette. The laser exposure area is designed to be circular of 1 cm in diameter in order to fill a 1 cm wide square cuvette, so the volume of the solution is always kept to 1 cm³ to be sure that the solution is exposed to laser light. The cuvette is capped, and the solution is continuously stirred at a speed of 300 rpm by a magnetic stirrer. The power and illumination time of the experiment can be easily adjusted. All experiments are performed at room temperature.

The TEM grid preparation is performed according to the following procedures: The solution is sonicated for 10 min to disperse the nanoparticles, and then one drop is cast on a TEM grid (previously activated by UV light, carbon film face up). A paper tissue can help absorb the liquid from the carbon film side to the back side of the grid, which only allows the liquid to pass through and leaves the nanoparticles on the top side. Two or more nitric acid drops (at pH 3) are also cast to clean the sample particles.

5.1.3 Results and discussions

In this part, we first discuss the general characterization of the Au-TiO$_2$ NPs produced in the microchannel setup, to confirm the existence of metallic Au photodeposition on TiO$_2$ surface and to verify the feasibility of synthesizing heterodimers using a high-intensity UV laser. The experimental data are also fitted according to the growth model developed in Appendix 2. The effect of laser power, precursor concentration and illumination time on the photodeposition process are investigated in detail.

5.1.3.1 Characterization of Au-TiO$_2$

Examples of the TEM results of the Au-TiO$_2$ NPs obtained by photodeposition in the double microchannel setup are shown in Figure 5.1.
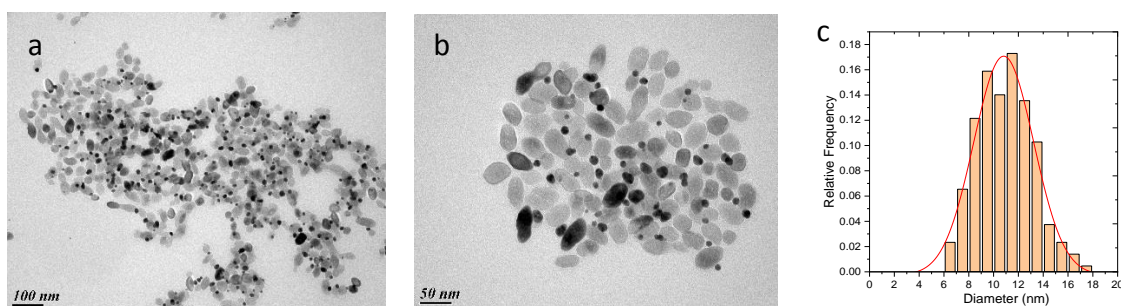
Figure 5.1 (a) (b) TEM images of Au-TiO$_2$ NPs and (c) the corresponding size distribution. Experimental conditions are: TiO$_2$ polyhedrons as substrate, c[TiO$_2$] = 5.5 mM, c[Au^{3+}] = 0.5 mM, 50 vol. % methanol as a hole scavenger, power 23.25 mW, illumination time 0.2 s, 15 mM SPAN 80 in dodecane, made in microchannel setup.

Both the smaller and larger magnification images confirm the formation of heterostructured Au-TiO$_2$ NPs. A single Au ND is deposited on the surface of TiO$_2$, with an average diameter of 10.8 (±2.4) nm in the present conditions (Figure 5.1c). The yield of heterodimers production is about 58 %, by measuring at least 200 Au NDs in the images.

Typical HRTEM images sitting at the interface between Au deposit NDs and their TiO$_2$ substrate are shown in Figure 5.2.

References pages 198
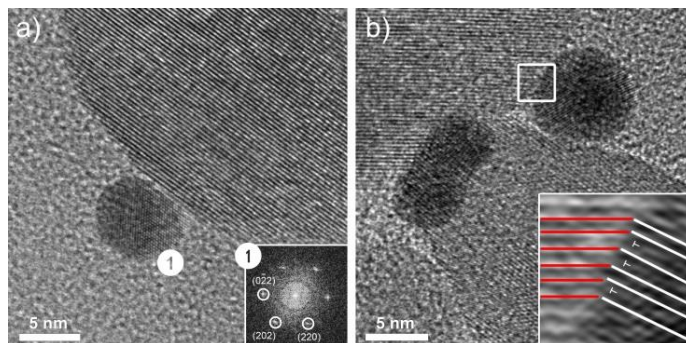
Figure 5.2 HRTEM micrographs of Au-TiO₂ interfaces and the corresponding digital diffractogram of the labelled zone. Dislocation network zoom-in is presented on the inset of figure b (noted as ⊥).

When the gold NP is small enough, it is a monocrystal as in Figure 5.2a. As a soft material to accommodate and compensate for the $\Delta a/a$ interface lattice mismatch with the oxide particles, it tends to induce the formation of a dislocation network. It is represented by the additional reticular half-planes shown on the inset of Figure 5.2b. A dislocation can be seen every 2 or 3 lattice planes, which is in good agreement with the evaluated misfit value of about 39 %.[12]

The XPS analysis of the samples carried out in the Au 4f region is given as a representative illustration for all the obtained Au-TiO₂ NPs (Figure 5.3). The fit of the XPS spectra clearly shows peaks centered at 83.5 and 87.2 eV before etching process which are characteristics of the metallic Au^0 formed during photodeposition,[13] without any gold oxide (Au^{3+} expected at 86.3 and 89.6 eV)[14] on TiO₂ surface. After 6 s etching, no variation of the peak position was observed (Figure 5.3b), combined with the spectra under even longer etching time up to 16 s as shown in Figure 5.4, it confirmed that the deposited gold was effectively in metallic form.
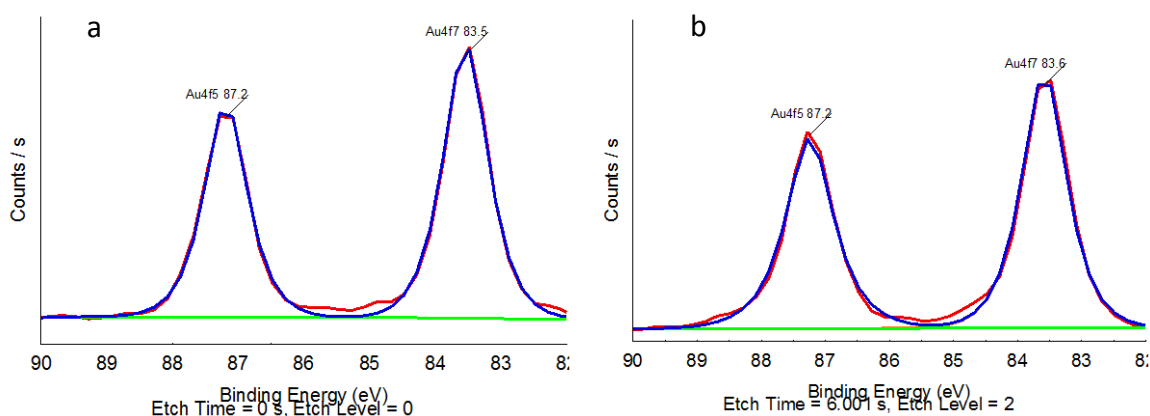
Figure 5.3 Fit of high-resolution XPS spectra of Au-TiO₂ in the Au 4f region (a) before nand (b) after 6 s etching time.
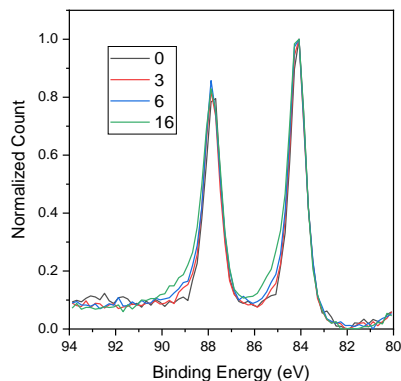
Figure 5.4 XPS spectra of Au-TiO₂ under etching conditions at t = 0, 3, 6, and 16 s.

The optical properties of the Au-TiO₂ NPs were analyzed by UV-vis absorption spectroscopy (Figure 5.5).
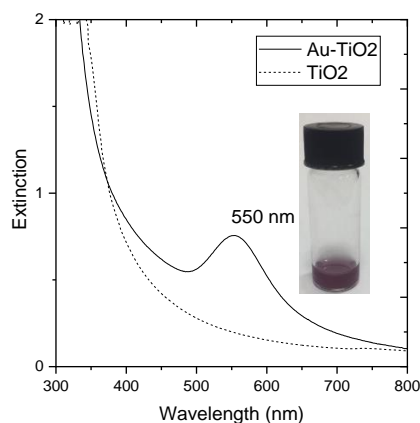
Figure 5.5 UV-vis spectrum of only TiO₂ solution (dash line) and a solution of Au-TiO₂ NPs formed in a cuvette setup (solid line), inset shows the Au-TiO₂ solution showing purple color. Experimental conditions are: power 13.88 mW, illumination time 4 min, c[TiO₂] = 5.5 mM, c[Au³⁺] = 0.5 mM, pH = 3, 50 vol. % methanol as a hole scavenger.

The spectrum exhibits an absorption band with a maximum peak located at the wavelength of 550 nm, which corresponds to the specific extinction peak of Au NDs due to the surface plasmon resonance (SPR) effect;[4, 15, 16] the band gap of TiO₂ is around 380 nm. This confirms the presence of Au NDs after the photodeposition process.

5.1.3.2 Au-TiO₂ nanoparticles made in the microchannel setup

(a) Power effect

The first parameter to test is the effect of power on the photodeposition process of Au on TiO₂.

Here, using the microchannel setup, we fix the illumination time at 0.2 s and vary the applied power: (a) 7.75 mW, (b) 15.5 mW and (c) 23.25 mW. The TEM results of Au-TiO$_2$ NPs obtained using these 3 powers are shown in Figure 5.6 and Table 5.1.
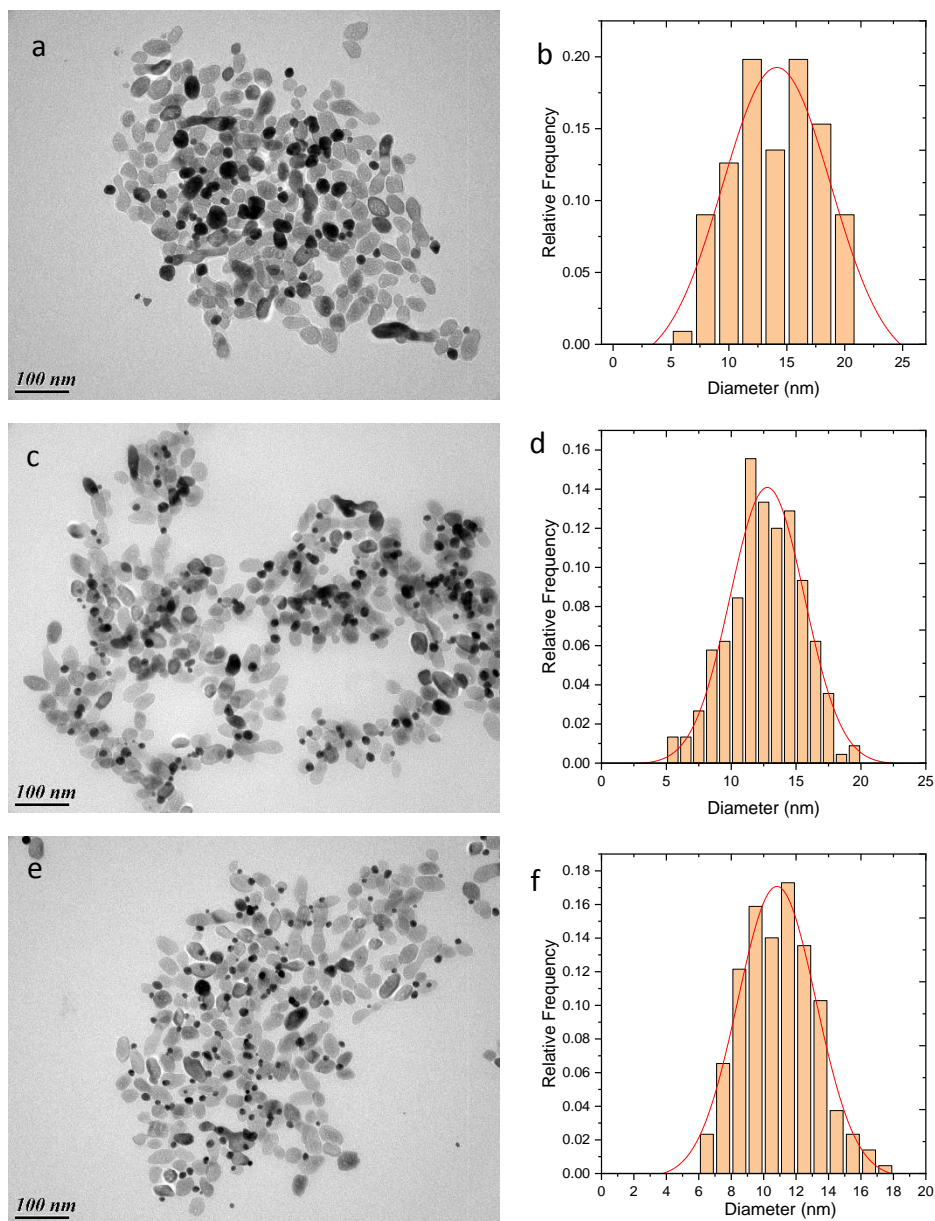
Figure 5.6 TEM image of Au-TiO$_2$ NPs made in microchannel setup at power (a) 7.75 mW, (c) 15.5 mW, and (e) 23.25 mW, and their corresponding size distributions in (b), (d) and (f). Experimental conditions are: illumination time 0.2 s, c[Au^{3+}] = 0.5 mM, c[TiO$_2$] = 5.5 mM, 50 vol.% methanol as a hole scavenger, 15 mM SPAN 80 in dodecane, TiO$_2$ polyhedrons as substrate.

The size distribution becomes narrow with increasing power. Besides the three powers we applied, we also experimented a smaller one, 3.1 mW. However, no Au NDs were found in this case. We suggest that for the gold photodeposition, a threshold power is needed to

References pages 198

significantly initiate the photoreduction process.

As we can see in Figure 5.7, the size of the Au NDs tends to decrease with the applied power, while the Janus yield increases. The trend of size and Janus yield could be explained by the competition between the effect of nucleation on the surface defects, and the effect of intensity applied on the TiO₂ for nucleation sites. A huge amount of electrons on the surface of TiO₂, due to the excitation of high-intensity (here larger power) laser, favors the nucleation of metal dots anywhere on TiO₂ surface rather than staying on the surface defects, thus leading to a higher Janus yield but a generally smaller size due to fixed amount of gold precursor.

Power (mW)	Illumination time (s)	Au diameter (SD) (nm)	Janus yield
3.1	0.2	/	/
7.75	0.2	14.1(4.9)	27 %
15.5	0.2	12.8(2.9)	36 %
23.25	0.2	10.8(2.4)	58 %

Table 5.1 Data of Au size and Janus yield of Au-TiO₂ NPs made in a double microchannel setup at various powers. Experimental conditions are:, c[Au³⁺]= 0.5 mM, c[TiO₂] = 5.5 mM, 50 vol.% methanol as a hole scavenger, 15 mM SPAN 80 in dodecane, TiO₂ polyhedrons as substrate.
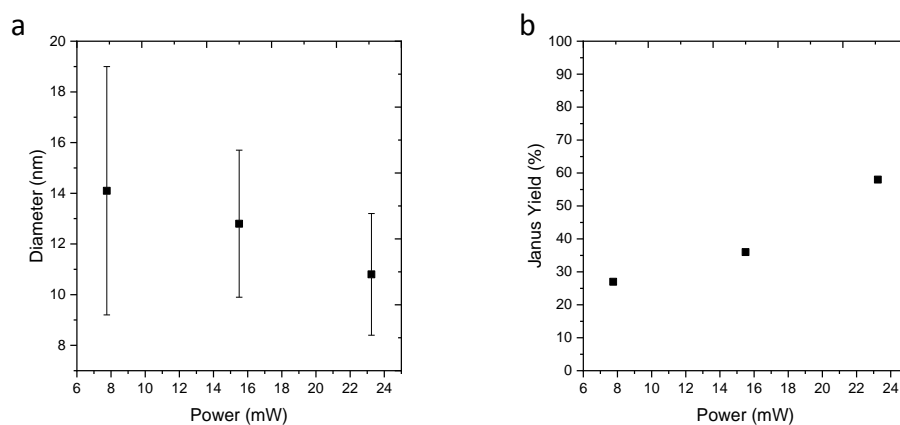
Figure 5.7 (a) Au size and (b) Janus yield of Au-TiO₂ NPs made in microchannel setup at various powers. Experimental conditions are: illumination time 0.2 s, c[Au³⁺] = 0.5 mM, c[TiO₂] = 5.5 mM, 50 vol.% methanol as a hole scavenger, 15 mM SPAN 80 in dodecane, TiO₂ polyhedrons as substrate.

(b) Effect of the gold precursor concentration

In this section, we fix the power at 46.3 mW and illumination time at 0.2 s. In this case, the

154

applied intensity and energy are fixed. We then vary the concentration of the gold precursor to test its role in the photodeposition process. The TEM results of Au-TiO$_2$ NPs are shown in Figure 5.8 and Table 5.2.
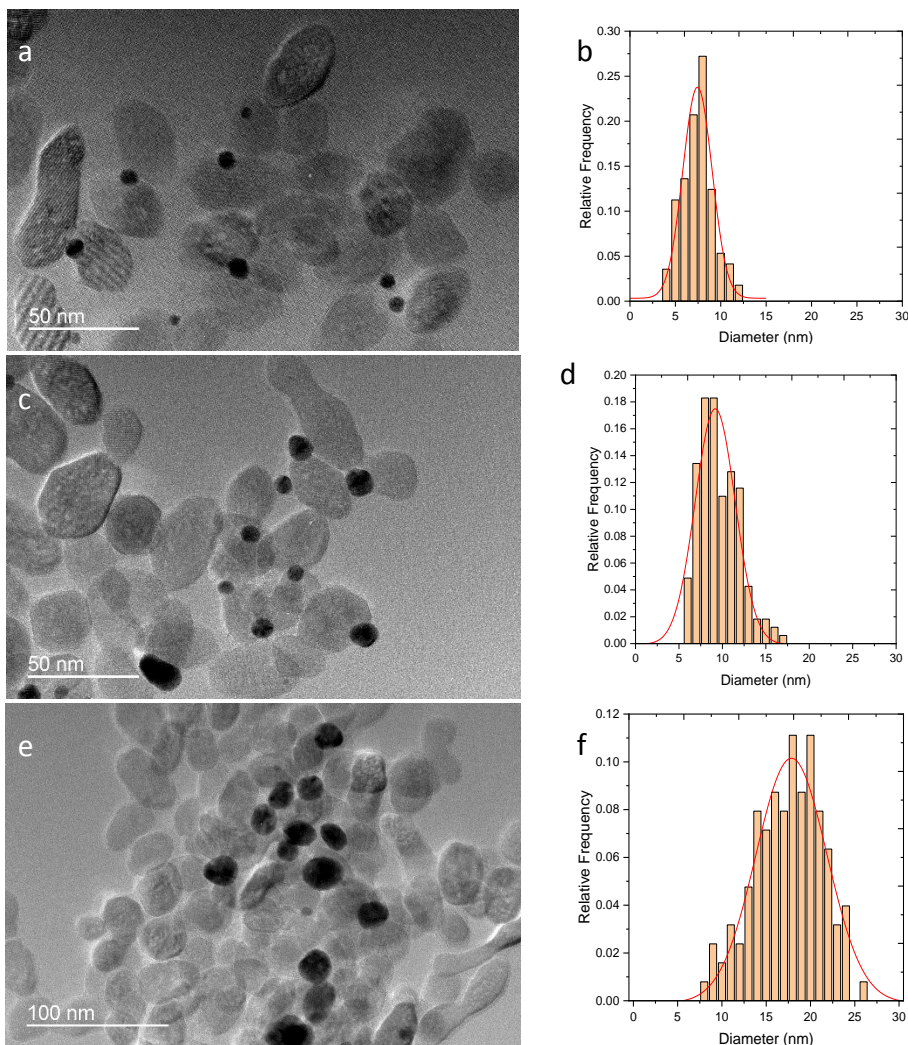
Figure 5.8 TEM images of Au-TiO$_2$ made in microchannel setup at various KAuCl$_4$ concentrations (a) 0.1 mM (c) 0.5 mM and (e) 1 mM, their corresponding size distributions are shown in (b), (d) and (f).Experimental conditions are: Power 46.3 mW, illumination time 0.2 s, c[TiO$_2$] = 5.5 mM, 50 vol.% methanol as a hole scavenger, TiO$_2$ polyhedrons as substrate.

It can be seen that, with the Au^{3+} concentration, the Au size becomes larger, so does the size distribution (Table 5.2). The Au size obtained is always smaller than the theoretical ones (see Appendix 3, A3.1), assuming that all the precursor was reduced and the Janus yield of Au-TiO$_2$ was 100 %. The Janus yield nonetheless shows a stable trend, with a narrow range from 40-50 % (Figure 5.9). This is a general trend whatever the power, as already shown earlier in the

group.[17]

Power (mW)	Time (s)	c[Au³⁺] (mM)	Au diameter (SD) (nm)	Estimated size (nm)	Janus yield
46.3	0.2	0.1	7.4(1.6)	8.7	35 %
46.3	0.2	0.5	9.2(2.3)	14.8	50 %
46.3	0.2	1	17.8(4)	18.7	37 %
46.3	0.2	2	17.9(3.2)	23.6	45 %

Table 5.2 Data of Au size made in microchannel setup at various KAuCl₄ concentrations. Experimental conditions are: Power 46.3 mW, illumination time 0.2 s, c[TiO₂] = 5.5 mM, 50 vol.% methanol as a hole scavenger, TiO₂ polyhedrons as substrate.
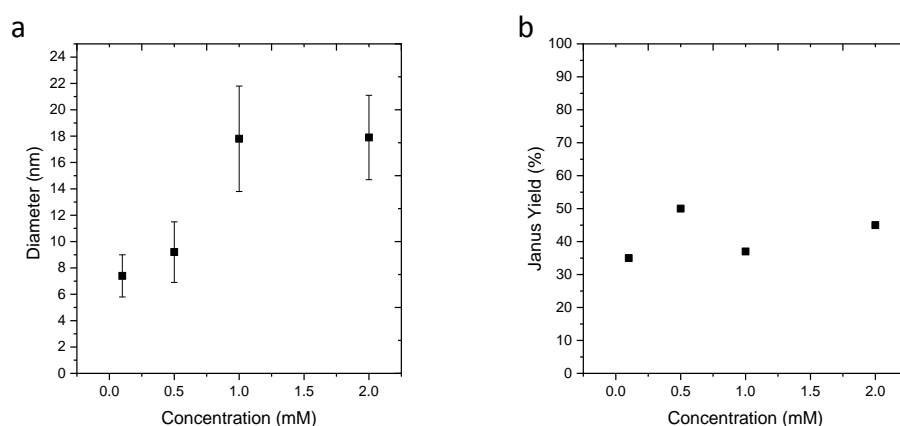
Figure 5.9 (a) Au size and (b) Janus yield of Au-TiO₂ NPs made in a single microchannel setup using various KAuCl₄ concentrations. Experimental conditions are: Power 46.3 mW, illumination time 0.2 s, c[TiO₂] = 5.5 mM, 50 vol.% methanol as a hole scavenger, no dodecane was used, TiO₂ polyhedrons as substrate.

In short conclusion, we discussed the effect of power and concentration on the photodeposition process of gold on TiO₂, which related to the two important parameters regarding the prediction model. High intensity facilitates a high nucleation rate of gold on the surface of TiO₂, leading to a high Janus yield and a relatively smaller size. A high concentration of gold precursor resulted in a larger gold size given the same power and exposure time.

5.1.3.3 Au-TiO₂ nanoparticles made in the cuvette setup

As for the photodeposition of silver nanodots, we also used the cuvette setup to perform the experiments the UV laser. The effect of three parameters, including the amount of hole scavenger, power and illumination time, will be discussed.

The hole scavenger chosen for these experiments is methanol and the first parameter we test here is its amount with regard to the gold precursor. Here we choose three different volumetric ratios of methanol, i.e., 2.5 %, 50 % and 75 % while the other parameters are kept the same. The TEM results of Au-TiO₂ NPs using these different ratios of methanol are shown in Figure 5.10 and Table 5.3.
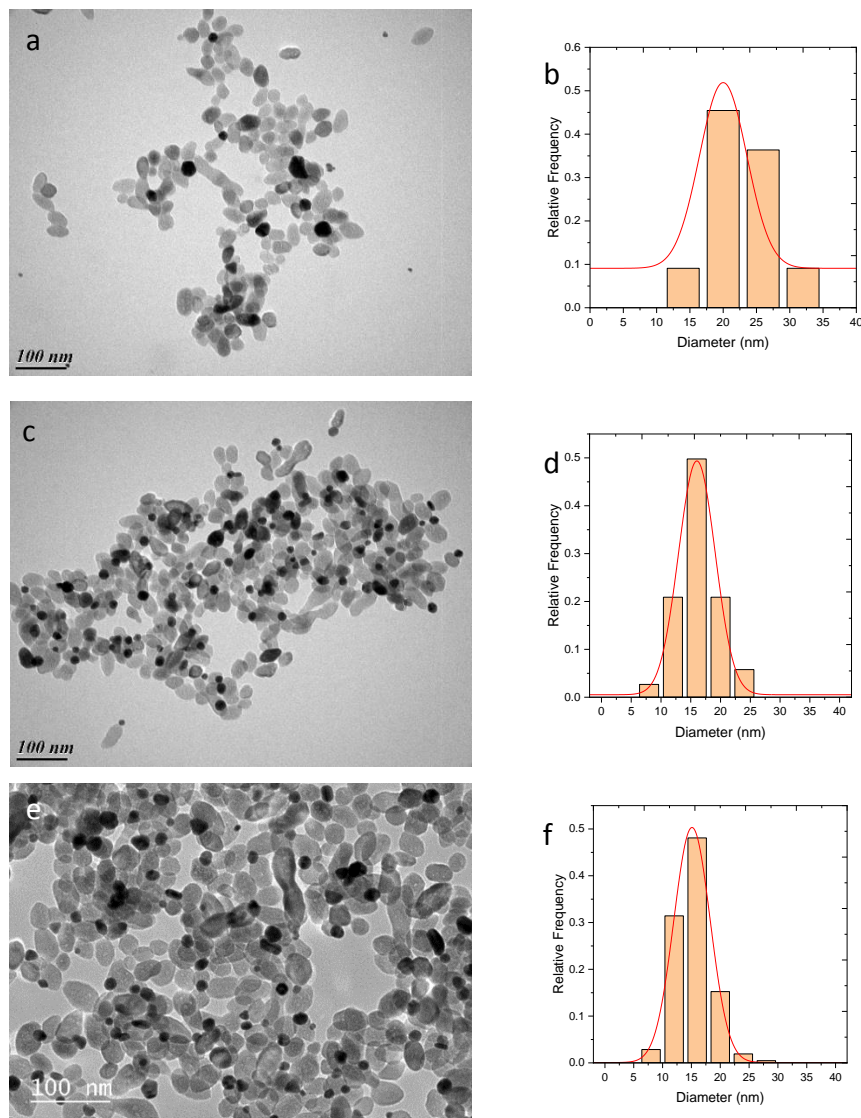
Figure 5.10 TEM images of Au-TiO₂ NPs made in cuvette setup at various volumeric ratio of methanol (a) 2.5 vol.%, (c) 50 vol.% and (e) 75 vol.% and their corresponding size distribution in (b), (d) and (f), respectively. Experimental conditions are: power 50.8 mW, illumination time 4 min, c[Au³⁺] = 0.5 mM, c[TiO₂] = 5.5 mM, TiO₂ polyhedrons as substrate.

ratio of methanol	Au diameter (SD) (nm)	Janus yield
2.5 %	22 (5)	< 10 %
50 %	15.9 (2.8)	45 %
75 %	15.4 (2.8)	39 %

Table 5.3 Data of Au size and Janus yield of Au-TiO₂ NPs made in cuvette setup at various volumetric ratio of methanol (a) 2.5 vol.%, (c) 50 vol.% and (e) 75 vol.% and their corresponding size distribution in (b), (d) and (f), respectively. Experimental conditions are: power 50.8 mW, illumination time 4 min, c[Au³⁺] = 0.5 mM, c[TiO₂] = 5.5 mM, TiO₂ polyhedrons as substrate.

It is observed that at the lowest ratio of 2.5 % methanol, the Au size tends to be much larger with a much lower Janus yield. At relatively high ratio (50 % or 75 %), the Au size turns smaller with a much larger Janus yield around 40 %. In fact, the lowest ratio of methanol still represents a large molar excess (2500 times) as compared to the Au³⁺ precursor. The low yield may be explained by the respective dilution of the reactants and the slow diffusion of methanol to the TiO₂ surface as compared to the reactions taking place at the NP under illumination. This is illustrated with a higher ratio of methanol, leading to a higher yield of Janus particles. According to Figure 5.11, the volumetric ratio of 50 % seems to result in the best yield with invariable size. Thus we keep this ratio for the following cuvette experiments.

Figure 5.11 (a) Au size and (b) Janus yield of Au-TiO₂ NPs made in the cuvette setup using various volume ratios of methanol. Experimental conditions are: power 50.8 mW, illumination time 4 min, c[Au³⁺] = 0.5 mM, c[TiO₂] = 5.5 mM, TiO₂ polyhedrons as substrate.

(b) Power effect

The effect of power was then investigated. Here we fix the illumination time at 4 min and vary the applied laser power to see its influence on both the size and the Janus yield. The TEM results of Au-TiO_2 as a function of the different applied powers are illustrated in Figure 5.12 and Table 5.4.
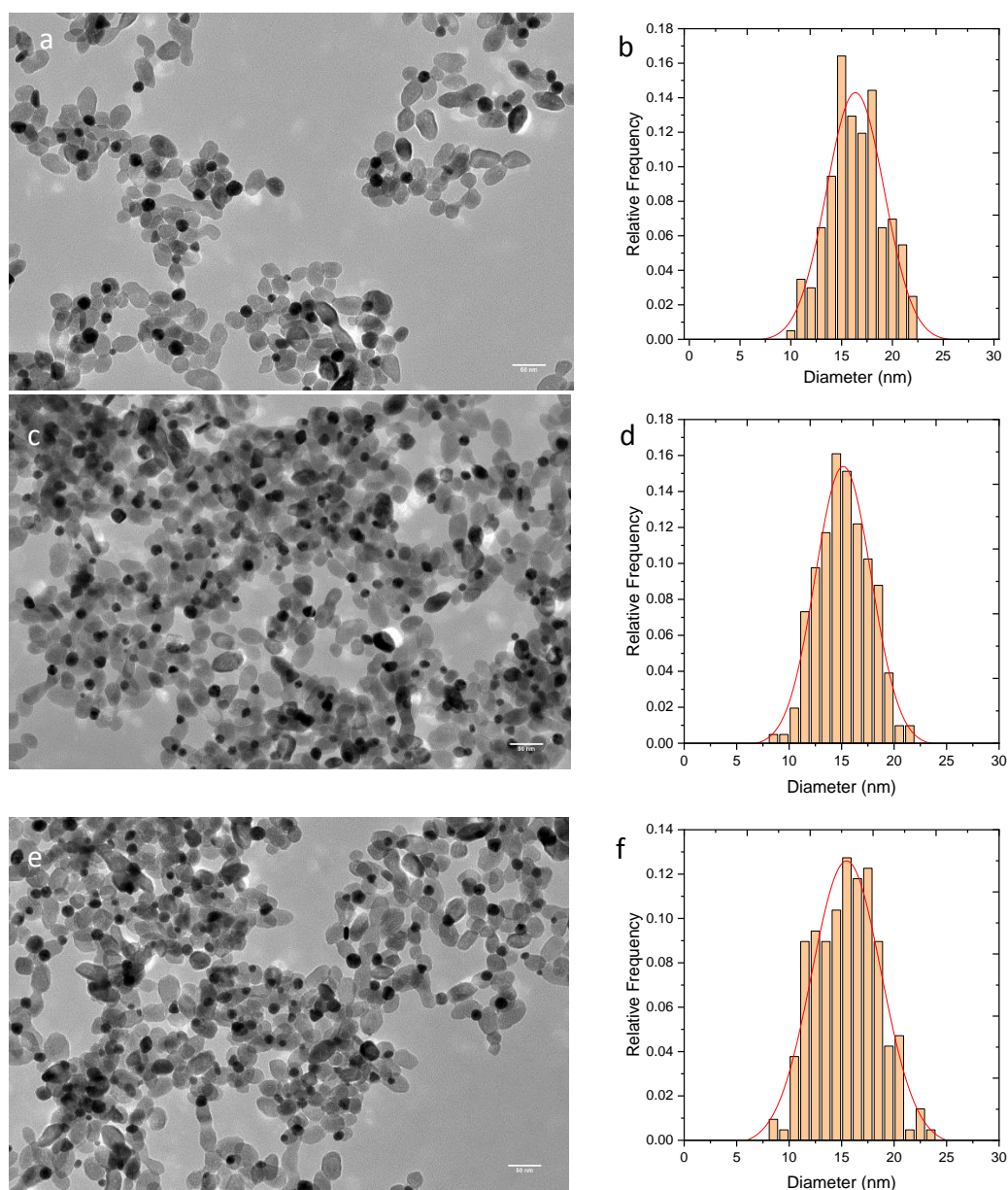
Figure 5.12 TEM images of Au-TiO₂ NPs made in cuvette setup for 4 min illumination at various powers, (a) 6.94 mW, (c) 28.05 mW and (e) 112 mW, and their corresponding size distributions in (b), (d) and (f). Experimental conditions are: c[Au³⁺] = 0.5 mM, c[TiO₂] = 5.5 mM, 50 vol.% methanol as a hole scavenger, TiO₂ polyhedrons as substrate.

(b) Power effect

159

Power (mW)	Illumination time (s)	Au diameter (SD) (nm)	Janus yield
6.94	240	16.4(2.8)	30 %
13.88	240	15.5(3.4)	35 %
28.05	240	15.2(2.7)	41 %
50.8	240	15.9 (3.4)	46 %
56.1	240	14.4(2.8)	49 %
112	240	15.5(3.3)	46 %

Table 5.4 Data of Au size and Janus yield of Au-TiO$_2$ NPs made in the cuvette setup at various powers. Experimental conditions are: c[Au^{3+}] = 0.5 mM, c[TiO$_2$] = 5.5 mM, 50 vol.% methanol as a hole scavenger, TiO$_2$ polyhedrons as substrate.

It can be seen from the TEM images that Au-TiO$_2$ heterodimers with only one Au ND on each TiO$_2$ nanoparticle are successfully synthesized in the cuvette setup. The Au size slightly decreased with the applied power, but the Janus yield increases when increasing the power suggesting an increase of the nucleation probability with increasing Laser power.

The UV-vis spectra of the Au-TiO$_2$ heterodimers are illustrated in Figure 5.14. The extinction peak exhibits a blue shift from 580 to 550 nm for powers increasing from 6.94 to 13.88 mW. The highest power also led to higher peak intensity, meaning that a larger amount of Au NDs is formed in the same volume solution.
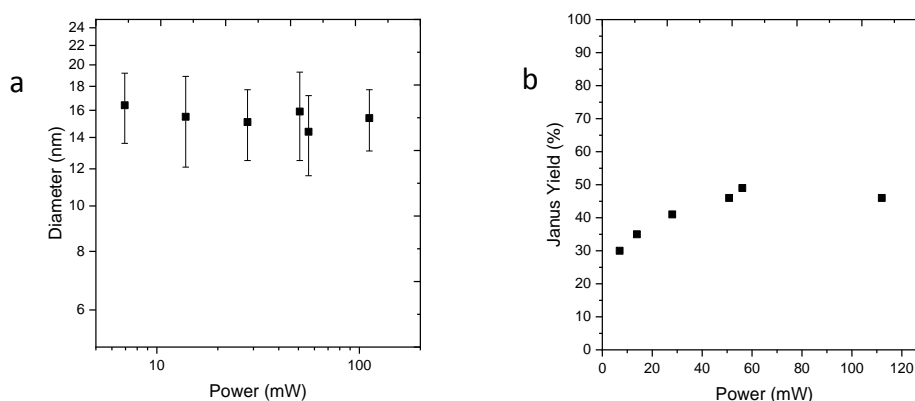
Figure 5.13 (a) Au size and (b) Janus yield of Au-TiO$_2$ NPs made in cuvette setup at various powers. Experimental conditions are: c[Au^{3+}] = 0.5 mM, c[TiO$_2$] = 5.5 mM, 50 vol.% methanol as a hole scavenger, TiO$_2$ polyhedrons as substrate.
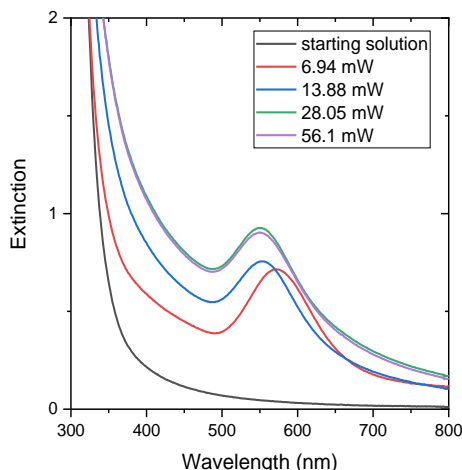
Figure 5.14 UV-vis spectra of Au-TiO₂ NPs solution made in cuvette setup using various powers. Experimental conditions are: c[Au³⁺] = 0.5 mM, c[TiO₂] = 5.5 mM, 50 vol.% methanol as a hole scavenger, TiO₂ polyhedrons as substrate.

(c) Illumination time effect

Here we turn to the effect of illumination time on the photodeposition process of Au onto the TiO₂ surface. In this section, we vary the illumination time inside the cuvette setup while the applied power was fixed at 13.88 mW. The TEM results of Au-TiO₂ NPs from 60 to 960 s are shown in Figure 5.15 and Table 5.5.

Based on these data, it looks like the Au size and the Janus yield seem to increase and reach a plateau for a 240 s and longer illumination time (Figure 5.16). The unchanged size and Janus yield are probably due to the complete consumption of the gold ions in the reaction solution. The Au size obtained (15.9 nm) at 960 s is rather close to the estimated theoretical value (18.7 nm) assuming that a gold hemisphere was obtained and all the gold ions were reduced with a Janus yield of 50 % (see calculations in Appendix 3, A3.1)
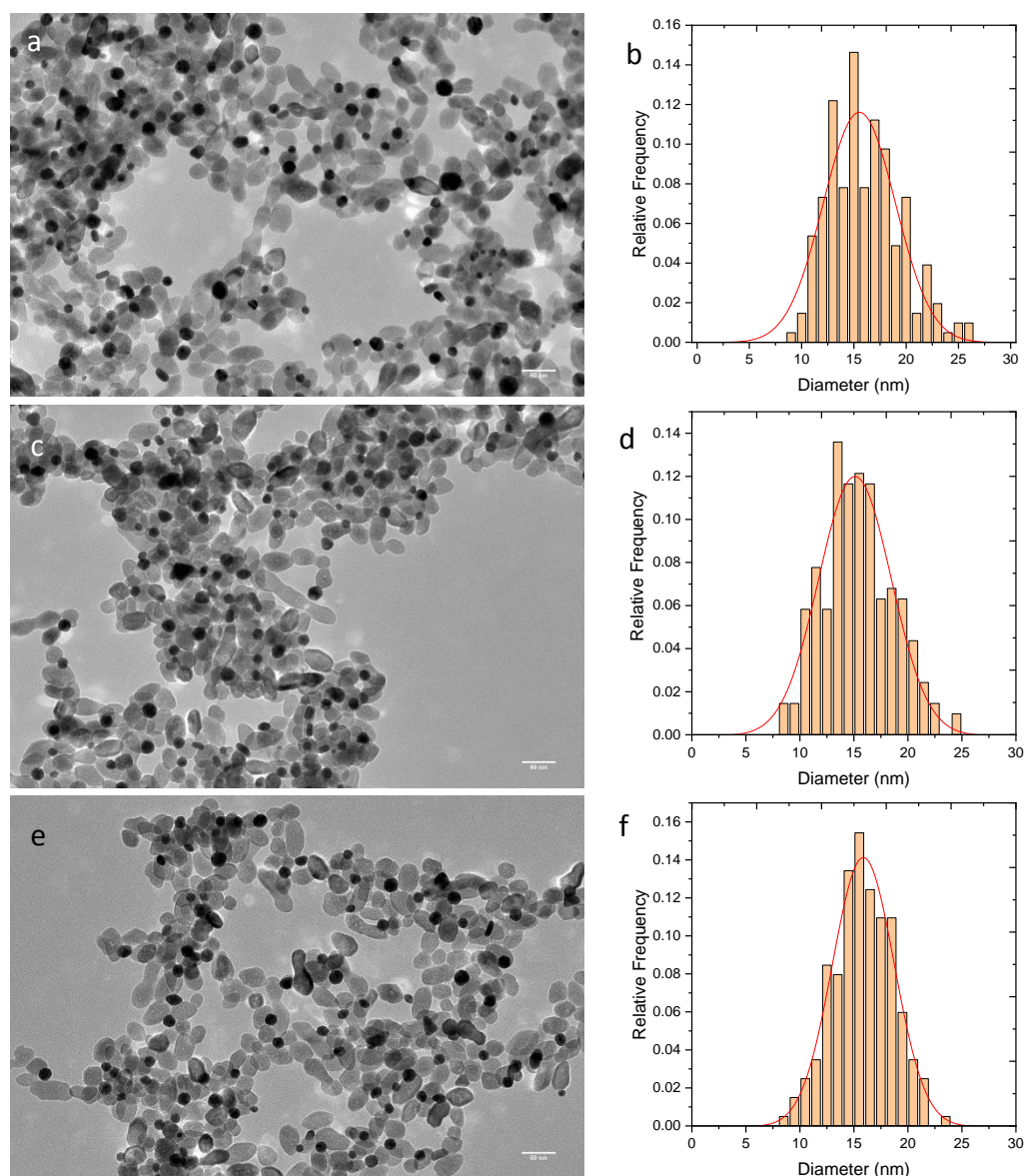
Figure 5.15 TEM images of Au-TiO₂ NPs made in cuvette setup at 13.88 mW for various illumination time, (a) 240 s, (c) 480 s, (e) 960 s and their corresponding size distribution in (b), (d) and (f), respectively. Experimental conditions are: c[Au³⁺] = 0.5 mM, c[TiO₂] = 5.5 mM, 50 vol.% methanol as a hole scavenger, TiO₂ polyhedrons as substrate.

Power (mW)	Illumination time (s)	Au diameter (SD) (nm)	Janus yield
13.88	60	/	/
13.88	120	8.9(3.4)	10 %
13.88	240	15.5(3.4)	35 %
13.88	480	15.1(3.4)	40 %
13.88	960	15.9(2.9)	35 %

Table 5.5 Data of Au size and Janus yield of Au-TiO₂ NPs made in cuvette setup at various illumination time. Experimental conditions are: c[Au³⁺] = 0.5 mM, c[TiO₂] = 5.5 mM, 50 vol.% methanol as a hole scavenger, TiO₂ polyhedrons as substrate./ means that the Au NDs were not detected on the grid.
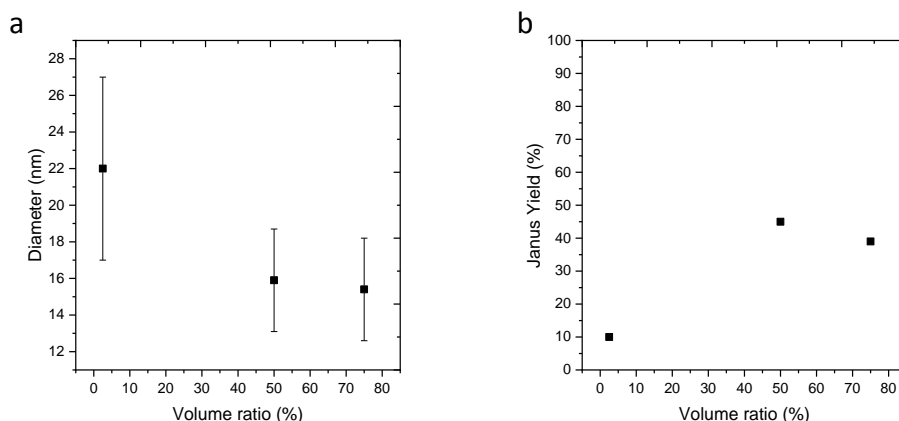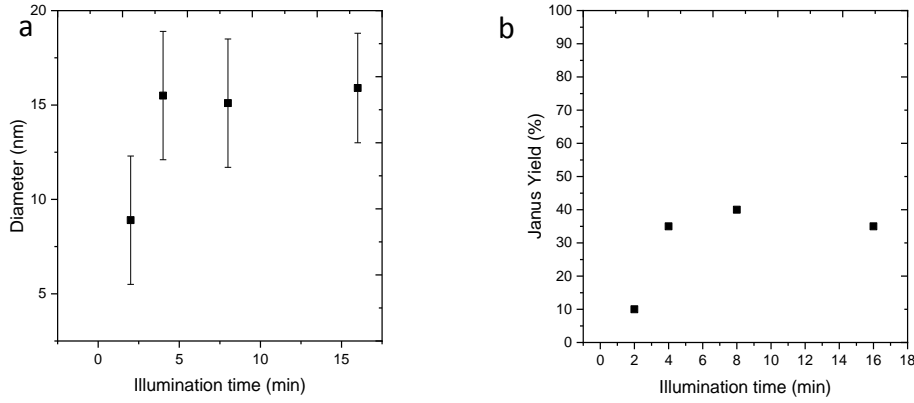
Figure 5.16 (a) Au size and (b) Janus yield of Au-TiO₂ NPs made in cuvette setup at various illumination time. Experimental conditions are: c[Au³⁺] = 0.5 mM, c[TiO₂] = 5.5 mM, 50 vol.% methanol as a hole scavenger, TiO₂ polyhedrons as substrate.

In short conclusion, we discussed in this section of the effect of the amount of methanol, power and illumination time on the photodeposition of Au on TiO₂ in the cuvette setup. Large applied powers do not vary much about the gold size but increase the Janus yield. There exists an incubation time to trigger the Au photodeposition on TiO₂ (at least > 60 s), while the gold size tends to quickly reach a stable stage after only 5 min.

5.1.3.4 Modelling fit of gold size data

As we mentioned above, we have obtained data of gold size in microchannel setup under different conditions like laser power, illumination time and precursor concentration. We then tried to model the nucleation growth of the gold NDs using the model developed in Appendix 2. According to this model, the late growth stage in the high field case regime of Au ND should respect the following equation:

$$R^3\left(t \gg\right) = \frac{3\Omega^2}{\kappa}\left[Au\right](t) = \frac{3\Omega^2}{\kappa}k'_{Au}\left(\frac{gk'_{HS}}{k_r k'_{Au}}\right)^{\frac{3}{4}} t = \frac{3\Omega^2}{\kappa}\frac{k'_{HS}}{k_r}\left(\frac{k_r k'_{Au} g^3}{k'_{HS}}\right)^{1/4} t \sim g^{\frac{3}{4}}k'_{Au}^{\frac{1}{4}} t \qquad \begin{array}{c}Equation\\5.1\end{array}$$

Where k_r is the recombination rate, $k'_{Au} = k_{Au}[Au^{3+}]_{ads}$ is the effective rate for the production of Au^0, $k'_{HS} = k_{HS}[HS]_{ads}$ is the rate of hole scavenging, g is the electron source term proportional to the absorption coefficient of TiO₂ and the beam intensity, Ω and κ are respectively a characteristic volume factor and a dimensionless factor related to the contact angle of the Au

dot on the TiO₂ surface.

After we did the fitting process to Figure 5.17, we found the correlation coefficients for the Au size versus expected power law with power (or time) to be 0.4 (or 0.34), indicating a reasonable fit agreement with the prediction model.
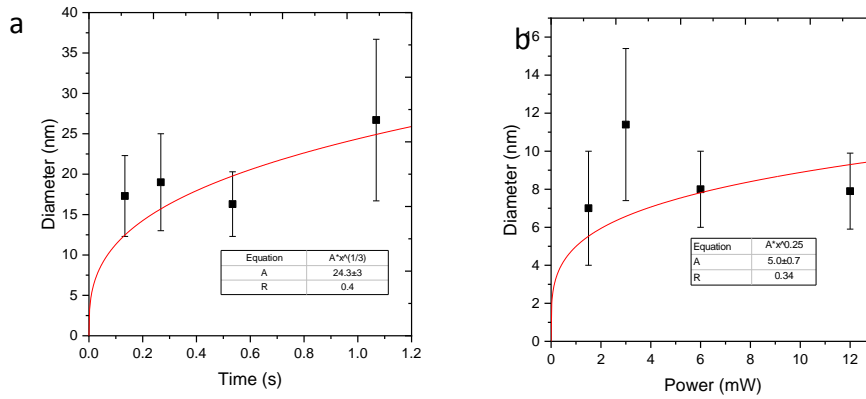
Figure 5.17 (a) Au diameter as a function of illumination time, (b) Au diameter as applied power.

In order to better understand the modelling, we re-wrote Equation 5.1, as shown below:

$$D^3(T >> 1) - D_0^3 \approx (8 \frac{3\Omega^2}{\kappa} \frac{k'_{HS}}{k_r}) \frac{t}{\tau}$$ *Equation 5.2*

where t is the illumination time and $\tau = \left(\frac{k_r k'_{Au} g^3}{k'_{HS}} \right)^{-\frac{1}{4}}$ is a characteristic time for the growth,

which is related to the Au³⁺ ions concentration and power.

However, as we do not know accurately the production rate k_{Au} of Au atom, we assume a

theoretical slope $8 \frac{3\Omega^2}{\kappa} \frac{k'_{HS}}{k_r} = 2.37 \times 10^{-3} nm^3$ (see Appendix 2 for evaluations), and we

artificially extract $(k_{Au})^{1/4}$ from $\frac{t}{\tau}$ by plotting the cube diameter as a function of

$\frac{t}{\tau} / (k_{Au})^{1/4}$.

All the data, including previous sets obtained by previous collaborators,[17] fitted together on a single graph, give a linear trend in Figure 5.18a.
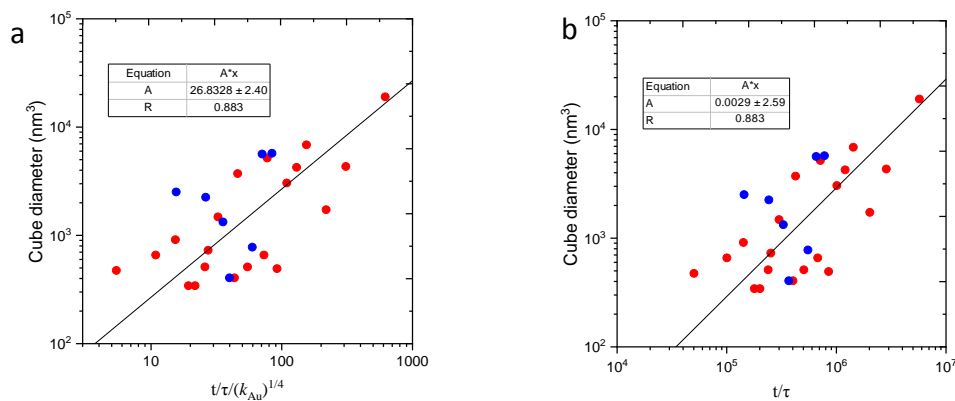
Figure 5.18 (a) Cube diameter as a function of t/τ/(k_Au)^{1/4}, (b) Cube diameter as a function of t/τ with a known value k_Au.

Although our experiments mainly showed a tendency to saturation in the growth process with the presence of a plateau at the largest powers, most of the experiments performed previously were set up with parameters (power, and illumination time) which allowed access to a large range of the gold size (7-27nm). This overall set of data showed, on the contrary, a reasonable growth rate with time, with nonetheless a much higher variability than that observed for silver and a tendency to lower yields. The variability in dot diameters is likely due to the requirement of three electrons for the full reduction of a gold ion the involvement of Au(I) intermediate species, and therefore, mechanisms which are statistically much more complex than for silver ions that just need one electron.

In the present investigation, our goal was to focus on this yield, instead of the growth, and try to increase it by drastically varying some parameters. We reasonably succeeded, but the price seems to be that the growth is disturbed in an uncontrolled way when shifting conditions from a sort of main mean set. Back to Figure 5.18a, since the slope should be equal to $2.37 \times 10^{-3} nm^3 \cdot (k_{Au})^{1/4}$, we finally find $k_{Au} = 7.28 \times 10^{15} M^{-3} s^{-1}$. The growth law with this value is then represented in Figure 5.18b. Note that the production rate of Au atom is not reported in the literature as far as acknowledged. Consequently, just looking at the growth without paying attention to the yield, it seems that the growth model still catches the main observations and could be used to predict size for a given set of parameters.

5.1.4 Conclusions

In this section, we performed experiments on the photodeposition of Au NDs on TiO$_2$ in the microchannel and the cuvette setup. Techniques including TEM, HRTEM, XPS and UV-vis spectroscopy have confirmed the existence of metallic-Au NDs deposited on the TiO$_2$ surface and the formation of heterodimer structures with single Au ND on each TiO$_2$ NP. The effect of the power, the gold precursor concentration and the illumination time on the photodeposition process were discussed. The gold size data were fitted to verify the rightness of the model, which can reasonably predict the size growth in a general trend. The production rate of Au atom is also deduced for the first time.

References pages 198

5.2 Photodeposition of Pd nanodots onto the surface of TiO$_2$ nanoparticles

5.2.1 Introduction to photodeposition of Pd nanodots onto the surface of TiO$_2$ nanoparticles

The elements of group 10 in the element periodic table, i.e. platinum group, including palladium and platinum, will be the subject of the following part. The photodeposition of Pd nanodots (Pd NDs) on the surface of TiO$_2$ is indeed another important research topic. In 1975, Kelly investigated the nucleation reaction of Pd by photodeposition when TiO$_2$ films were in contact with palladium ions and exposed to UV light.[18] Polycrystalline metallic Pd particles were found on the TiO$_2$ films.

The effect of hole scavenger on the Pd photodeposition was also studied. Very recently, Jones et al.[19] found that the size of Pd NDs differed when using methanol or triethanolamine (TEOA) as hole scavengers, owing to their difference in the electronic structure and basic character. The photodeposition using methanol gave Pd size in 2-3 nm range, while that of TEOA led to a Pd size of 4-7 nm, with a difference of two times. Dadsetan et al.[20] made a detailed work on the effect of organic alcohols on palladium photodeposition. They tested four kinds of alcohol, i.e., methanol, ethanol, ethylene glycol, and 1-propanol, and found that methanol resulted in the highest photodeposition rate. They suggested that the alcohols with lowest carbon numbers and molar weights did lead to a higher reduction rate of Pd on TiO$_2$.

Several palladium precursors, including palladium chloride (PdCl$_2$), palladium nitrate (Pd(NO$_3$)$_2$) and disodium tetrachloropalladate (Na$_2$PdCl$_4$), have been reported to be used as the metal precursor for the photodeposition of palladium.[21-27] PdCl$_2$ is the most commonly used palladium precursor for photodeposition experiments.[23-27] Note that when using PdCl$_2$ as the precursor, a certain amount of concentrated hydrochloric acid is necessary to allow a better solubility of the PdCl$_2$. In Fan's study[23], PdCl$_2$ was used to load Pd NDs on TiO$_2$ and they found tiny metallic ones (1-2 nm) well distributed on the surface of TiO$_2$. Also, Espino et al.[21]

References pages 198

found a similar size distribution (1-3 nm) when using $Pd(NO_3)_2$ as Pd metal salt while Leong obtained much larger palladium sizes of 17-29 nm on TiO_2 using Na_2PdCl_4 as the precursor.[28] In these papers, the nominal metal loading was the same (1 wt.% Pd-TiO_2), however, we observe a large difference in the size of the photodeposited NDs; a conclusion on the effect of the Pd precursor is then difficult to draw probably because the other applied conditions (including light intensity, illumination time, solvent, hole scavenger, etc.) in these studies were also different.

Unlike the studies reviewed above, which all used a cuvette or flask as a reactor, Dadsetan et al.[27] built in 2017 a channel type quartz reactor (see Figure 5.19) to improve the loading amount of the metals. The reactant solution in this system can repeatedly react in the quartz tube by UV irradiation. However, the Pd NDs synthesized with this setup showed large size distribution of the NDs on the surface of TiO_2; besides large Pd particles with 8 nm in size, several smaller dots of 2.5 nm were also observed.
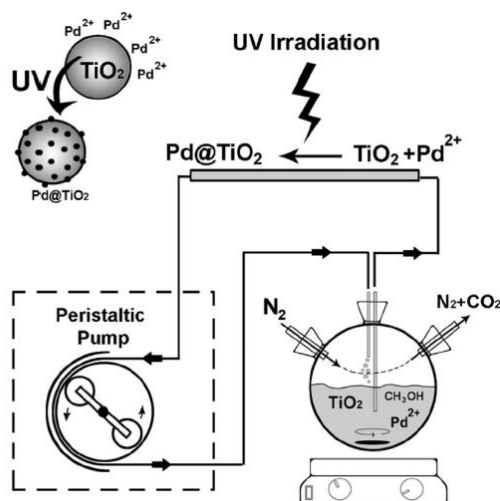
Figure 5.19 Apparatus for photodeposition of Pd NDs on TiO₂ (P25) by circulation through a quartz tube reactor.[27]

Strictly speaking, few people investigated the growth and morphology evolution of Pd particles on TiO_2 under a confined intensity and illumination time. Furthermore, modelling of the growth is also missing while recent studies[29, 30] showed that the control of the dot size is an important parameter for photocatalysis; modelling for given reaction conditions and optical excitation would also rise a predictive approach for the engineering of nano-heterodimers.

References pages 198

In this chapter, we implement the UV laser exposition as a powerful light source to initiate the photodeposition of Pd NDs on TiO$_2$. Thanks to its monochromic excitation below the band gap of TiO$_2$ and the high intensity, the study of the photochemical reaction will be performed under well-controlled conditions in terms of intensity or illumination time, to investigate the growth of heterodimers based on palladium.

The use of two metal precursors, Na$_2$PdCl$_4$ and palladium acetate (Pd(OAc)$_2$) will be analyzed. The effect of hole scavengers including methanol, HCOONa, or just water will also be discussed. Modelling of the data will also be performed.

5.2.2 Experimental methods

The experimental procedures for the Pd photodeposition performed in a microchannel or cuvette setup are the same as those for Au photodeposition in part 5.1.2, except that the hole scavenger used are now methanol, HCOONa and water itself, and the metal precursors used are sodium tetrachloropalladate(II) (Na$_2$PdCl$_4$) or palladium acetate (Pd(OAc)$_2$), one may refer to the previous part for more details.

The semiconductor supports to be used are TiO$_2$ polyhedrons all along with this chapter. The reaction solution is prepared by mixing an already made TiO$_2$ water solution and freshly prepared under Ar, sodium tetrachloropalladate(II) (Na$_2$PdCl$_4$) or palladium acetate (Pd(OAc)$_2$), then the oxygen-free hole scavenger (either methanol or sodium formate solution or just water itself) is added to make the initial aqueous solution. The pH of the mixture is adjusted at pH 3 using nitric acid (pH = 1) in order to obtain an excellent TiO$_2$ dispersion. Unless otherwise specified, the final concentrations of TiO$_2$ and Na$_2$PdCl$_4$ in solution were generally 5.5 mM and 1 mM (atomic concentration), respectively.

5.2.3 Results and discussions

In this part, we first discuss the general characterization of the Pd-TiO$_2$, to confirm the existence of metallic Pd photodeposition on TiO$_2$ surface and to verify the feasibility and the reproducibility of synthesizing heterodimers using either microchannel or cuvette setup. For

References pages 198

the following sections, several parameters, including metal precursor, hole scavengers and applied power, are investigated to clarify their roles in the photodeposition process. The experimental data are also fitted according to the growth model developed in Appendix 2.

5.2.3.1 Characterization of Pd-TiO₂

The resulting nanoobjects were analyzed by TEM after each experiment. The TEM results of one sample are shown in Figure 5.20 and confirm the formation of heterostructured Pd-TiO₂ NPs. A single Pd ND is deposited on the surface of TiO₂ polyhedrons, with an average diameter of 6.1 nm in the present conditions using Na_2PdCl_4 as a precursor (Figure 5.20c). The yield of heterodimers production is about 85 %, by measuring at least 200 NPs in the images.
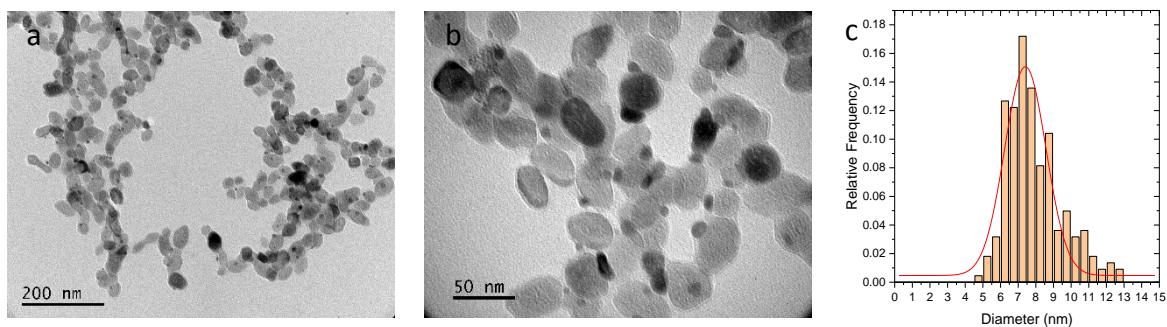
Figure 5.20 TEM image of Pd-TiO₂ NPs at (a) smaller and (b) larger magnification. (c) The corresponding Pd size distribution histogram. Experimental conditions are: Na_2PdCl_4 as metal precursor, c[TiO₂] = 5.5 mM, c[Pd²⁺] = 1 mM, without external hole scavenger, power 23.25 mW, illumination time 0.2 s, 15 mM SPAN 80 in dodecane, made in microchannel setup.

The XPS analysis of the samples carried out in the Pd 3d region is given as a representative illustration for all the obtained Pd-TiO₂ NPs (Figure 5.21).
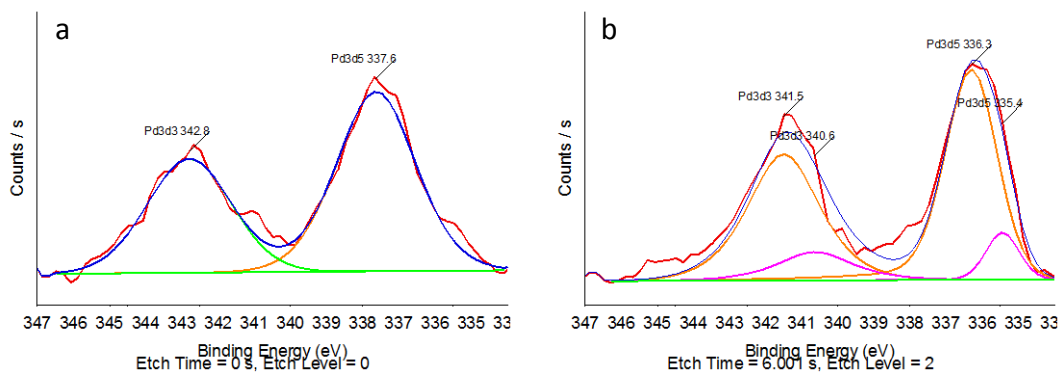
Figure 5.21 Fit of high-resolution XPS spectra in the Pd 3d region (a) before and (b) after 6 s etching time.

The fit of the XPS spectra before etching process (Figure 5.21a) clearly shows peaks with one contribution centered at 342.8 and 337.6 eV, which represents the Pd (II) due to the Pd oxide layer[31, 32] while after etching two doublets are detected, one stays at 341.5 and 336.3 eV, which represents that the Pd oxide layer still present; the other at 340.6 and 335.4 eV, which is characteristic of the metallic Pd^0.[33-35] With increasing the etching time (results not shown), the peaks of metallic Pd^0 became much more dominant, indicating the removal of the oxide layer during the etching process.

5.2.3.2 Pd-TiO$_2$ nanoparticles made in microchannel setup

(a) Precursor effect on Pd photodeposition on TiO$_2$ surface

The first parameter to test is the chemical nature of the palladium precursor and its influence on the photodeposition process. Two types of Pd precursor are investigated, Na$_2$PdCl$_4$ and Pd(OAc)$_2$. It has to be noted that Pd(OAc)$_2$ can only be dissolved in the organic solvent,[36] here we used 13.3 vol.% acetone to help dissolve this precursor, meanwhile keeping the precursor miscible in the aqueous part.

The photodeposition experiments using these precursor solutions were performed in the microchannel setup, both at a concentration of 2 mM, with 50 vol.% methanol as hole scavenger, at pH 3, with TiO$_2$ polyhedrons as the substrate. Figure 5.22 shows the TEM images of the resulting Pd-TiO$_2$ NPs obtained using the two types of precursors.

References pages 198
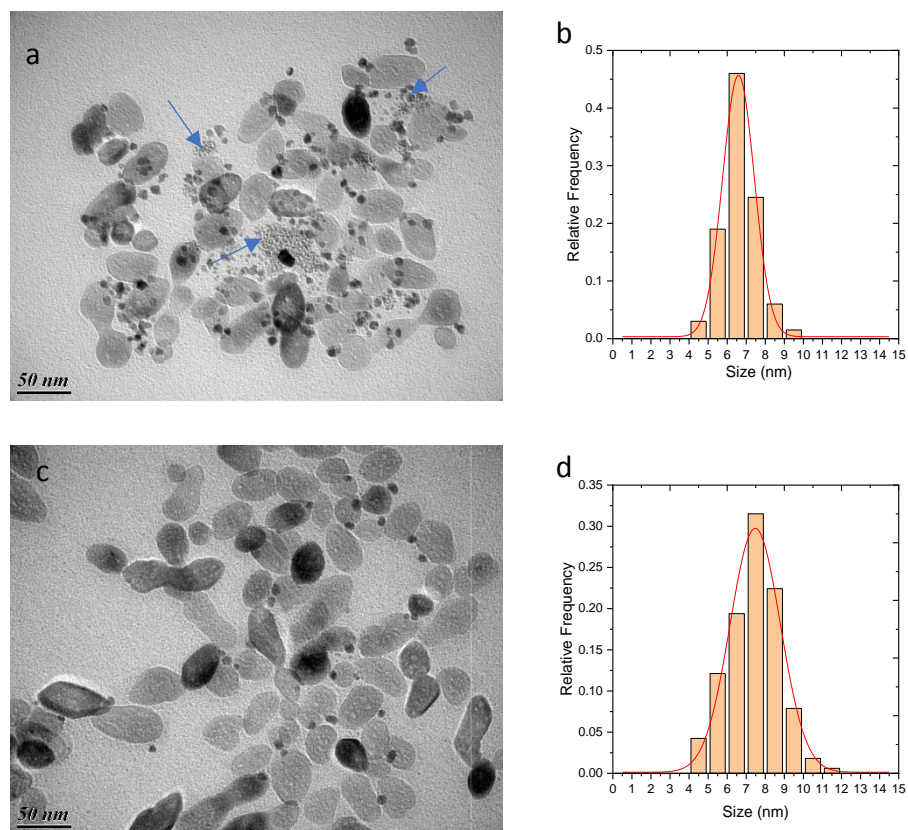
Figure 5.22 TEM images of Pd-TiO₂ using precursor (a) Na₂PdCl₄, (c) Pd(OAc)₂. and their corresponding size distribution in (b) and (d), respectively. Experimental conditions are: concentration 2 mM, power 3.1 mW in microchannel setup, illumination time 0.2 s, 15 mM SPAN 80 in dodecane, c[TiO₂] = 5.5 mM, pH 3, TiO₂ polyhedrons as substrate.

Both precursors lead to Pd NDs deposition on the TiO₂ surface. Nonetheless, from Na₂PdCl₄, we frequently observed as pointed by the blue arrows on Figure 5.22a, the presence of insoluble starting material on the TEM grid (presence of chloride confirmed by EDX experiments). A comparison in terms of Pd size between Na₂PdCl₄ and Pd(OAc)₂ is listed in Table 5.6 and shown in Figure 5.23 below.

Power (mW)	Na₂PdCl₄		Pd(OAc)₂	
	Diameter (SD) (nm)	Janus yield	Diameter (SD) (nm)	Janus yield
3.1	6.6(0.8)	multidots	7.5(1.3)	23 %
7.75	5.8(1)	multidots	7.2(1.2)	20 %
15.5	7.3(2.1)	multidots	7.6(1.1)	17 %
23.25	6.1(1)	multidots	7.9(1.1)	24 %

Table 5.6 Data of Pd size and Janus yield of Pd-TiO₂ NPs using Na₂PdCl₄ or Pd(OAc)₂. Other conditions are kept identical, including: concentration 2 mM, power 3.1 mW in microchannel setup, illumination time 0.2 s, 15 mM SPAN 80 in dodecane, c[TiO₂] = 5.5 mM, pH 3, TiO₂ polyhedrons as substrate.

172
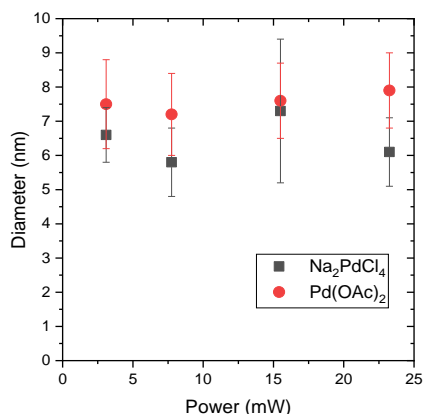
Figure 5.23 Pd size as a function of power for Na$_2$PdCl$_4$ and Pd(OAc)$_2$. Experimental conditions are: power 3.1 mW in microchannel setup, illumination time 0.2 s, 15 mM SPAN 80 in dodecane, c[TiO$_2$] = 5.5 mM, pH 3, TiO$_2$ polyhedrons as substrate.

In these conditions, and in both cases, the palladium is co-localized with the TiO$_2$ particles. The clear difference lies in the number of Pd NDs deposited on each TiO$_2$, that is, Na$_2$PdCl$_4$ leads to several Pd NDs per TiO$_2$ with a mean size of 6.6 nm while Pd(OAc)$_2$ leads to single Pd ND per TiO$_2$ with a size around 7.5 nm. The Janus yield obtained using Pd(OAc)$_2$ is below 25 %, which is not good merit for the efficiency of the metal loading. However, it is hard to draw any conclusions comparing these two precursors since they are dissolved in different mixture systems. Na$_2$PdCl$_4$ can be more easily dissolved in the mixture of methanol/H$_2$O system even if not totally, while Pd(OAc)$_2$ cannot without the presence of acetone (or other organic agents miscible with water). The addition of acetone may cause more variables to the photodeposition process, which drove us to use the water-soluble precursor Na$_2$PdCl$_4$.

In the following section, we also test the photodeposition of Pd using Na$_2$PdCl$_4$ without any external hole scavenger (methanol), show it is possible making the photodeposition process simpler and that additionally, we can produce nano heterodimers. Therefore, for our photodeposition experiments, we will keep using Na$_2$PdCl$_4$ as the metal precursor unless stated elsewhere.

173

(b) Hole scavenger effect on Pd photodeposition in microchannel setup

Like what we have discussed about Ag photodeposition in Chapter 4, the nature of the hole scavenger should also play a key role in the photodeposition process of Pd on TiO_2. If efficiently enough, it consumes the holes generated in the TiO_2 by the UV irradiation and leaves much more free electrons to react at the interface with the metal ions in solution by reducing the recombination of the electron-hole pairs. Alcohol including methanol[20] and isopropanol[23] or organic agent TEOA[19] have been used as hole scavengers for Pd photodeposition. In our study, we kept the same two hole scavengers as for silver photodeposition: methanol and HCOONa. Since, as opposed to the photodeposition of gold or silver, people already showed that H_2O could be itself an efficient hole scavenger for the Pd(II)–chloride complexes,[24] which means that no external hole scavenger like alcohols needs be considered for the reduction, we also performed Pd photodeposition experiments in pure water.

To check the role of the hole scavenger, we chose to keep all the parameters identical and as follows, TiO_2 polyhedrons as substrate, $c[Pd^{2+}] = 1$ mM, $c[TiO_2] = 5.5$ mM, solution velocity $v = 960$ μm/s (illumination time 0.2 s), and pH = 3. Three types of hole scavengers, *i.e.*, methanol (50 vol.%) and HCOONa (2 mM) and H_2O itself, will be evaluated.

The TEM results of Pd-TiO_2 NDs performed in the microchannel setup using HCOONa, methanol and H_2O as a hole scavenger are shown in Figure 5.24. Pd NDs were successfully deposited onto the TiO_2 polyhedrons, which is quantified in Table 5.7 and Figure 5.25. Interestingly, we find that a single Pd ND was successfully deposited on TiO_2 polyhedrons only when H_2O itself was used as a hole scavenger, while both methanol and HCOONa are found to lead to multiple Pd NDs loading on TiO_2 surface even for the lowest power. These two hole scavengers will then be disregarded, and we will focus on the role of water as a hole scavenger.

References pages 198
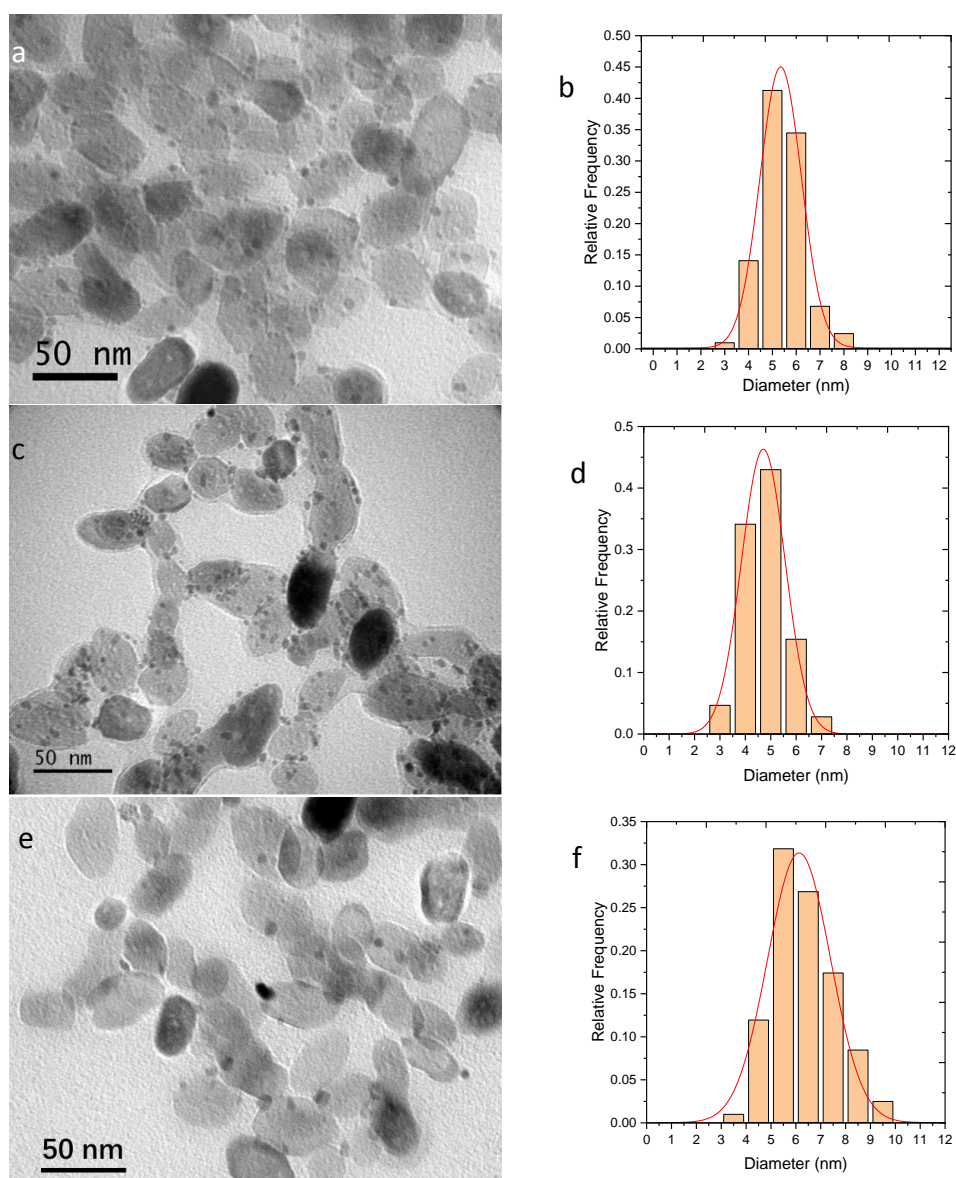
Figure 5.24 TEM image of Pd-TiO₂ NPs using (a) HCOONa, (c) methanol and (e) H₂O as hole scavengers, and their corresponding size distribution in (b), (d) and (f). Experimental conditions are: c[Na₂PdCl₄] = 1 mM, c[TiO₂] = 5.5 mM, pH 3, 15 mM SPAN 80 in dodecane, power 7.75 mW, illumination time 0.2 s, TiO₂ polyhedrons as substrate.

The only additional thing which can be said is that the diameter of the Pd NDs seems to increase with increasing applied power in the microchannel and follows the same trend for all these three hole scavengers. However, the difference between the hole scavengers comes from the Pd particle distributions. The mean size of Pd NDs obtained using H_2O is larger than those obtained using methanol or HCOONa. Kriek suggested that in the absence of an added hole scavenger, the Pd(II) complex can be reduced.[24] The Pd(II) complex-formation of the $[PdCl_n(H_2O)_{4-n}]^{n-4}$ (n = 0–4) system is pH dependent, and the complex form $PdCl_2(H_2O)_2$ at near

175

pH 3 is evident to exhibit the largest photoreduction rate.[24] The addition of external hole

scavengers (methanol or HCOONa) provides a strong enhancement of the photodeposition

process as stated by Dadsetan et al. generating swifter nucleation and the presence of

multidots.[20] These authors showed among others that comparing a series of alcohols there

was a strong dependence of the hole scavenging rate on the mobility and diffusivity of the

hole scavenger.

| Power (mW) | Hole scavenger type | | | | | |
| | H$_2$O itself | | 2 mM HCOONa | | 50 vol.%Methanol | |
	Pd size (SD) (nm)	Janus yield	Pd size (SD) (nm)	Janus yield	Pd size (SD) (nm)	Janus yield
3.1	5.4(1)	84 %	4.5(1)	multidots	4(1)	multidots
7.75	6.1(1.3)	85 %	5.4(1)	multidots	4.7(1)	multidots
15.5	7.2(1.5)	90 %	5.6(1.2)	multidots	5.2(1)	multidots
23.25	7.1(1.3)	90 %	5.8(1)	multidots	5.2(1)	multidots

Table 5.7 Data of Pd size made by photodeposition on TiO$_2$ surface using three hole scavengers. other conditions are kept identical: c[PdCl$_4^{2-}$] = 1 mM, c[TiO$_2$] = 5.5 mM, pH 3, 15 mM SPAN 80 in dodecane, illumination time 0.2 s, TiO$_2$ polyhedrons as substrate.
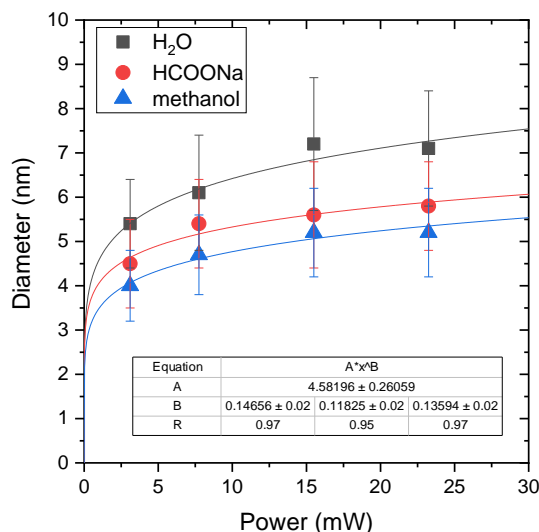
Figure 5.25 Pd size as a function of laser power in the microchannel setup, using three hole scavengers. Experimental conditions are: c[PdCl$_4^{2-}$] = 1 mM, c[TiO$_2$] = 5.5 mM, pH 3, 15 mM SPAN 80 in dodecane, illumination time 0.2 s, TiO$_2$ polyhedrons as substrate. A power law fit was performed for each set of data.

Surprisingly, a power law fit of the growth of the palladium dots for the three hole scavenging

processes, while very similar, shows a growth exponent 0.12 - 0.14 significantly smaller than

the 1/3 expected from our model; this important aspect will be investigated below in detail.

To conclude, the photodeposition experiments of Pd on TiO$_2$ surface have been successfully performed, using either methanol, HCOONa or H$_2$O as hole scavengers, leading to relatively high photodeposition rates for all products. It appears that the direct irradiation of the Pd salt solution containing TiO$_2$ NDs without any external hole scavengers is the most reliable as well as compulsory choice to obtain a single dot deposition with a high yield and to synthesize heterodimers based on palladium.

(c) Power effect on the Pd photodeposition in microchannel setup

Here we turn to study the effect of the power on the photodeposition of Pd on TiO$_2$. Since the exposure area is unchanged in the microchannel setup, the intensity is proportional to the power applied to the reaction solutions. To check the effect of the power, we chose to keep all the other parameters identical and as follows, TiO$_2$ polyhedrons as substrate, c[Na$_2$PdCl$_4$] = 1 mM, c[TiO$_2$] = 5.5 mM, illumination time 0.2 s, pH = 3, no external hole scavenger and 15 mM SPAN 80 in dodecane for the phase transfer. Several representative TEM images made at various powers are shown in Figure 5.26.

According to Table 5.8, the size of the Pd NDs increases very regularly with the applied power in the microchannel from 0.5 to 94.4 mW; as shown in Figure 5.27. A power law fit gives an exponent 0.11, which is still much smaller than that expected from the model (1/3). The Janus yield showed slight increase all over the power range. It is worth mentioning that the largest Pd size we obtained is still smaller than the estimated value (17.8 nm), assuming all the precursor is reduced and Janus yield is 100 %, as discussed in Appendix 3, A3.1.
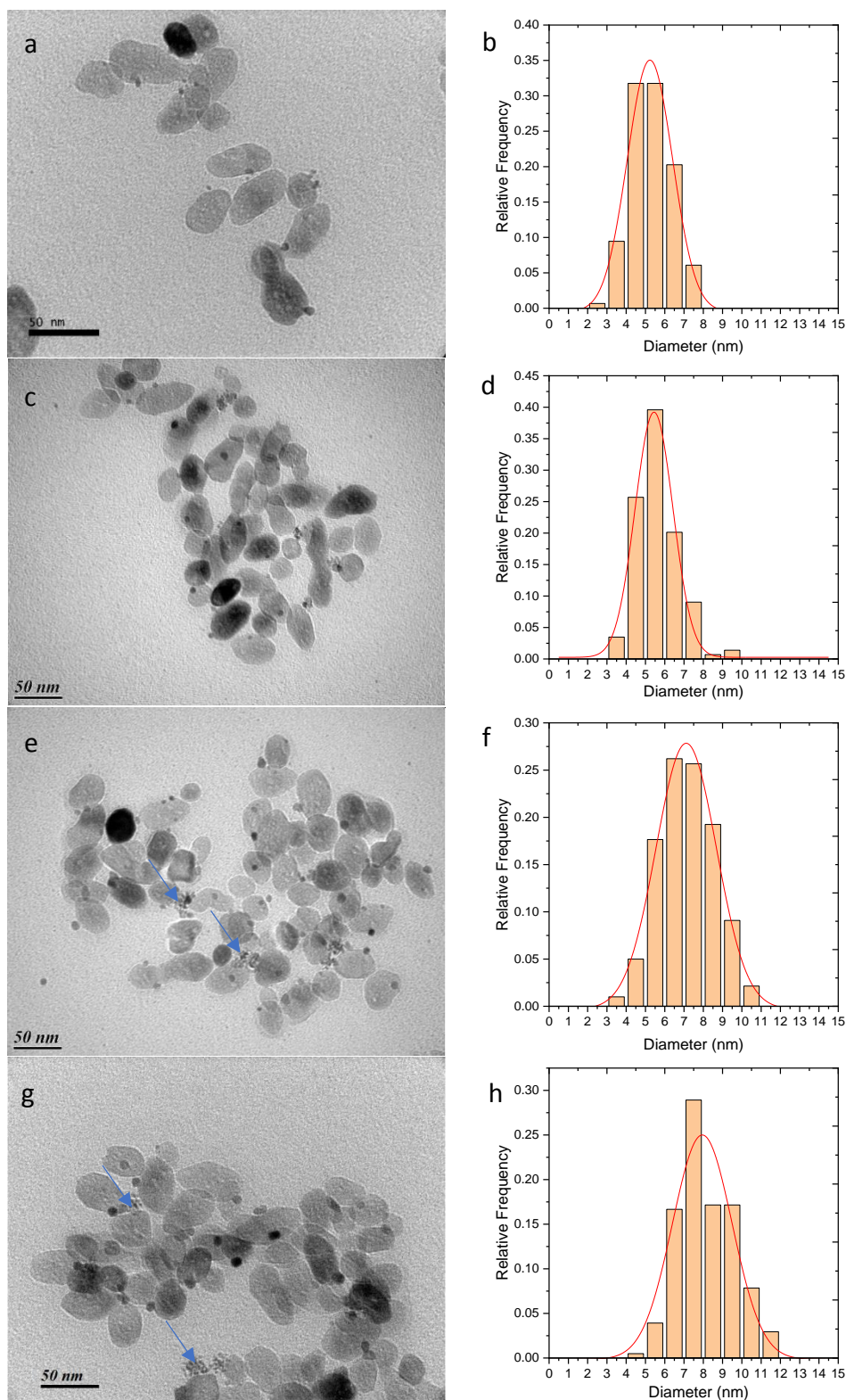
Figure 5.26 TEM images of Pd-TiO$_2$ NPs made at various powers (a) 0.5, (c) 3.1, (e) 15.5 and (g) 46.3 mW in microchannel setup, and their corresponding size distributions in (b), (d), (f) and (h), respectively. Experimental conditions are: c[PdCl$_4^{2-}$] = 1 mM, c[TiO$_2$] = 5.5 mM, pH 3, 15 mM SPAN 80 in dodecane, illumination time 0.2 s, TiO$_2$ polyhedrons as substrate.

Power (mW)	Pd size (SD) (nm)	Janus yield
0.5	5.2(1.2)	82 %
1	5.4(1)	86 %
2	5.9(1.1)	86 %
3.1	5.4(1)	84 %
7.75	6.1(1.3)	85 %
15.5	7.2(1.5)	90 %
23.25	7.1(1.3)	90 %
46.3	7.9(1.5)	89 %
94.4	9.2(1.6)	90 %

Table 5.8 Data of Pd size and Janus yield obtained at various powers. other conditions are kept identical: c[PdCl$_4$$^{2-}$] = 1 mM, c[TiO$_2$] = 5.5 mM, pH 3, 15 mM SPAN 80 in dodecane, illumination time 0.2 s, TiO$_2$ polyhedrons as substrate.

Figure 5.27 Pd size as well as Janus yield as a function of power in microchannel setup. Experimental conditions are: c[Na$_2$PdCl$_4$] = 1 mM, c[TiO$_2$] = 5.5 mM, pH 3, 15 mM SPAN 80 in dodecane, illumination time 0.2 s, TiO$_2$ polyhedrons as substrate. A power law fit was performed on the set of data.

5.2.3.3 Pd-TiO$_2$ nanoparticles made in cuvette setup

We then focused on the Pd photodeposition experiments performed with the cuvette setup using UV laser, to study the effect of the laser power, illumination time and hole scavengers on the photodeposition process. In these experiments, TiO$_2$ polyhedrons were used as substrates, c[PdCl$_4$$^{2-}$] = 1 mM, c[TiO$_2$] = 5.5 mM.
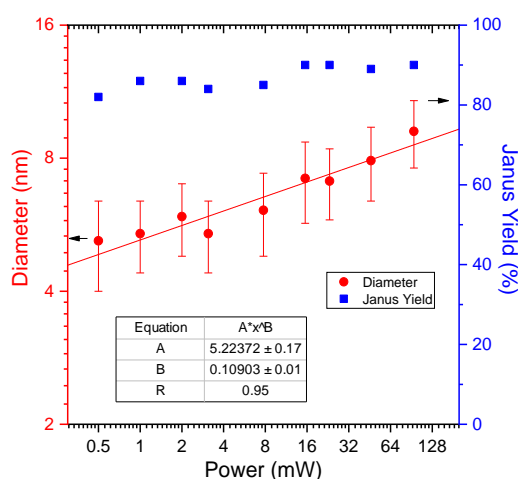
179

(a) Power effect

The effect of laser power was firstly investigated. Here we fixed the illumination time at 8 min and varied the laser power applied into the cuvette. The TEM results of Pd-TiO₂ with various applied powers are illustrated in Figure 5.28.
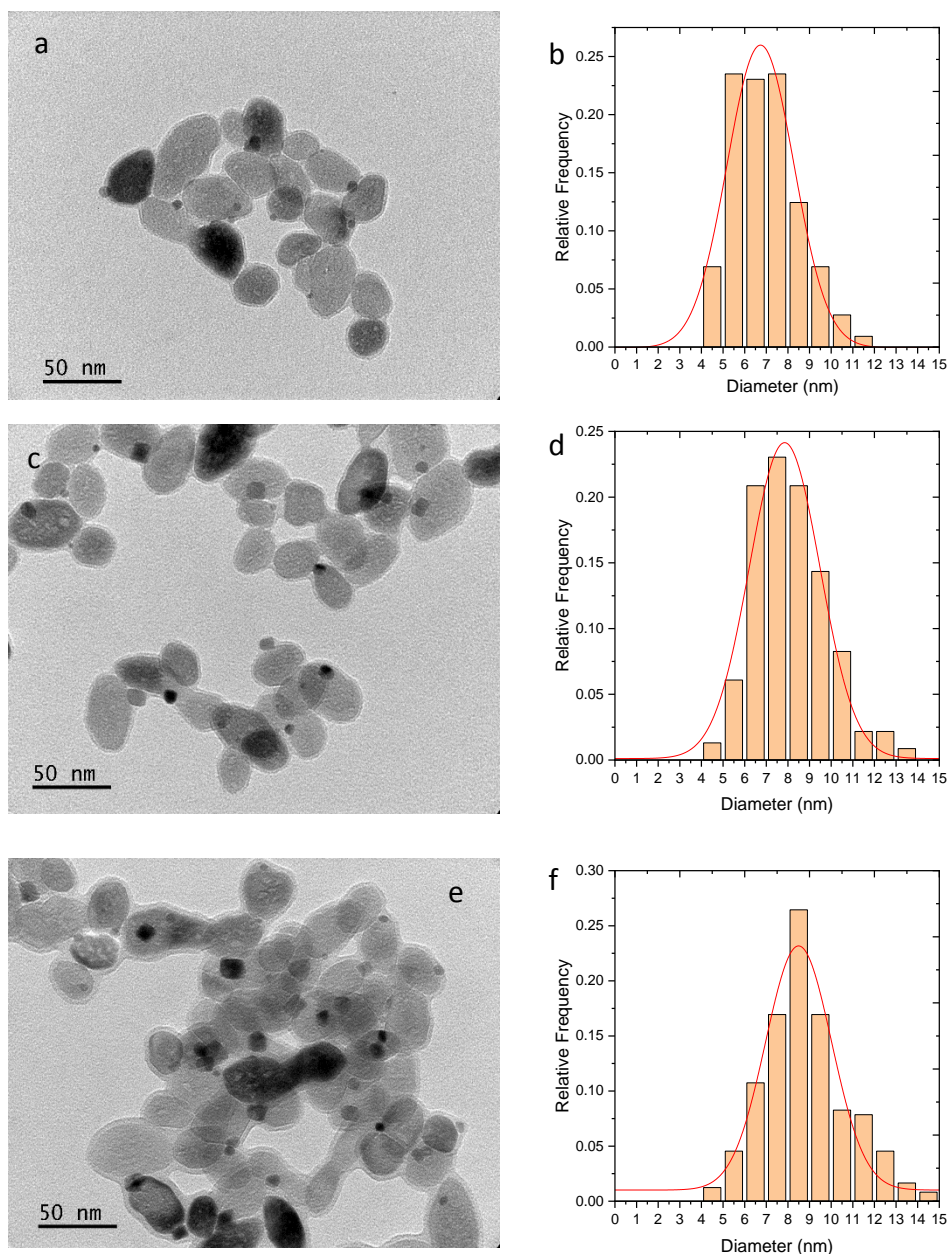
Figure 5.28 TEM images of Pd-TiO₂ NPs made in cuvette setup for 8 min illumination at various powers, (a) 6.94 mW, (c) 28.05 mW and (e) 56.1 mW, and their corresponding size distributions in (b), (d) and (f). Experimental conditions are: c[PdCl₄²⁻] = 1 mM, c[TiO₂] = 5.5 mM, no external hole scavenger, TiO₂ polyhedrons as substrate.

180

The Pd diameter variation, as well as the Janus yield with the applied power, are shown in Table 5.9 and Figure 5.29. The size of the Pd NDs also increases regularly, still with an exponent smaller than that expected for the photodeposition of M^{2+}, as well as the corresponding Janus yield with the power. Both the largest Pd size and the highest Janus yield are obtained at the applied power 112 mW. However, compared to the results obtained in the microchannel setup, the cuvette setup results in much lower Janus yield for any applied power.

Power (mW)	Illumination time (s)	Pd Size (SD) (nm)	Janus yield
6.94	480	6.7(1.5)	44 %
13.88	480	7.1(2)	56 %
28.05	480	7.8(1.6)	67 %
56.1	480	8.5(1.6)	73 %
112	480	9.1(2.4)	79 %

Table 5.9 Data of Pd size and Janus yield made in the cuvette setup at various powers. Other conditions are kept the same, including illumination time 8 min, c[PdCl₄²⁻] = 1 mM, c[TiO₂] = 5.5 mM, no external hole scavenger, TiO₂ polyhedrons as substrate.
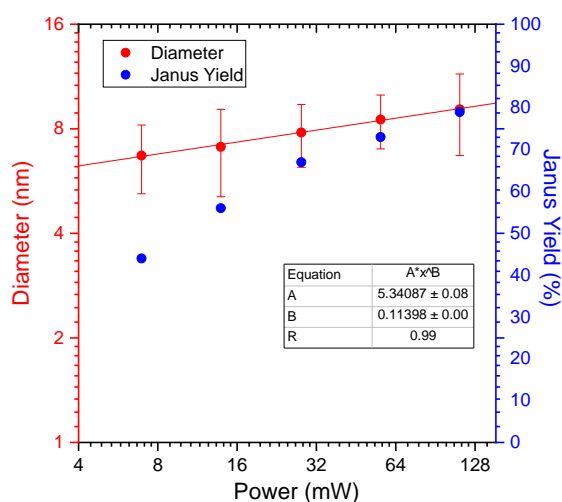
Figure 5.29 Pd size and Janus yield as a function of the laser power in the cuvette setup. Experimental conditions are: illumination time 8 min, c[PdCl₄²⁻] = 1 mM, c[TiO₂] = 5.5 mM, no external hole scavenger, TiO₂ polyhedrons as substrate. A power law fit was performed on the set of data.

    (b) Illumination time effect

The effect of illumination time was then investigated. Here we fixed the applied power at 13.88 mW and varied the illumination time. The TEM results of Pd-TiO₂ with various illumination

times are illustrated in Figure 5.30.
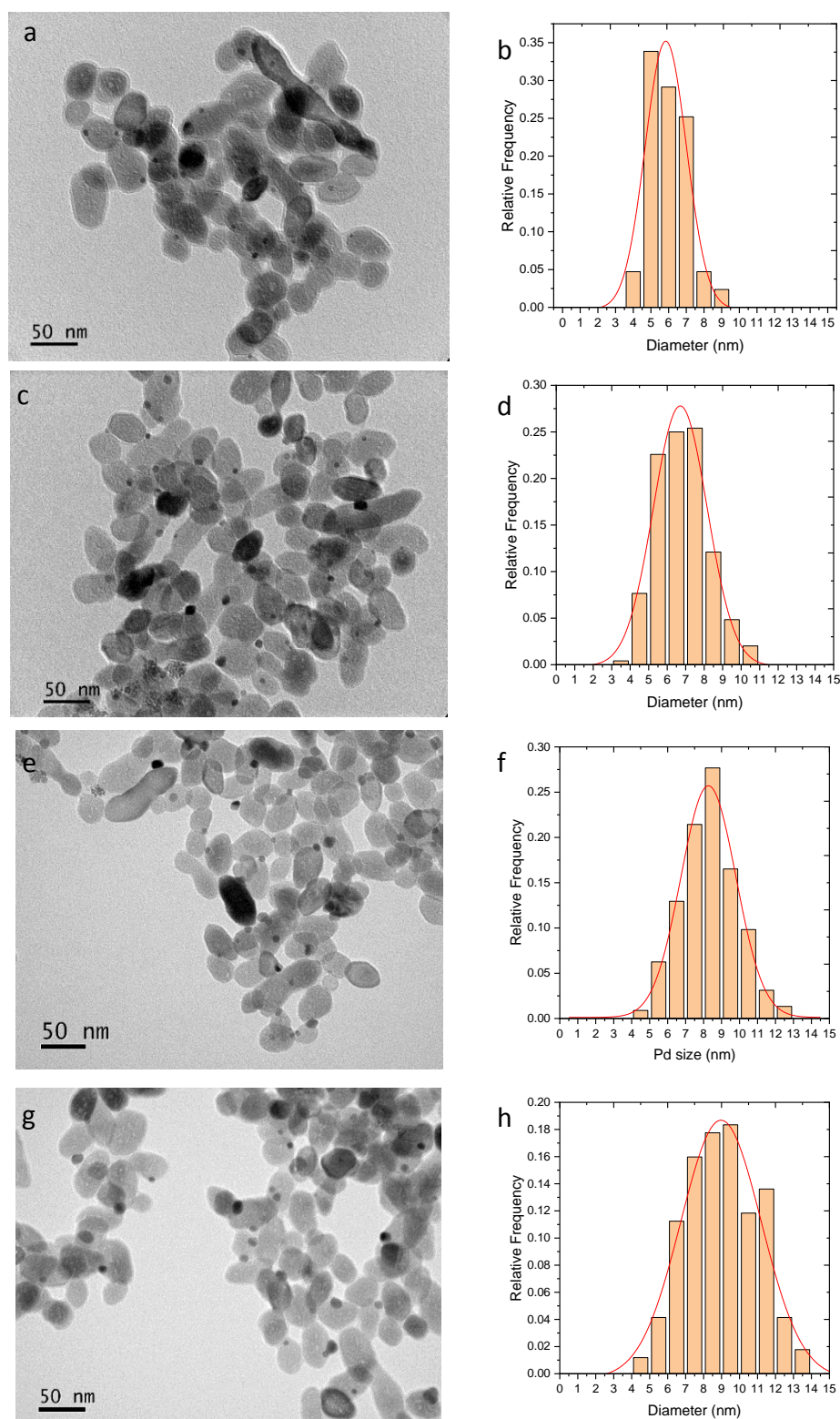
Figure 5.30 TEM images of Pd-TiO$_2$ NPs made in cuvette setup at 13.88 mW for various illumination time, (a) 60 s, (c) 240 s, (e) 600 s and (g) 1200 s, and their corresponding size distribution in (b), (d), (f) and (h), respectively. Experimental conditions are: c[PdCl$_4^{2-}$] = 1 mM, c[TiO$_2$] = 5.5 mM, no external hole scavenger, TiO$_2$ polyhedrons as substrate.

The Pd diameter variation, as well as the Janus yield with various illumination time, are shown in Table 5.10 and Figure 5.31.

Power (mW)	illumination time (s)	Pd diameter (SD) (nm)	Janus yield
13.88	60	5.7(1)	33%
13.88	120	6.1(1.2)	33 %
13.88	240	6.7(1.5)	47 %
13.88	480	7.1(2)	56 %
13.88	600	8.3(1.5)	42 %
13.88	960	7.8(2)	48 %
13.88	1200	9(2.2)	53 %
13.88	2000	10.7(2.4)	54 %
13.88	3000	11.9(3)	64 %
13.88	5300	11.6(2.4)	67 %
13.88	7000	11(2.2)	67 %
13.88	10000	11(3.1)	68 %

Table 5.10 Pd size and Janus yield of Pd-TiO$_2$ NPs made in a cuvette at 13.88 mW for various illumination time. Other conditions are kept identical, including: c[PdCl$_4^{2-}$] = 1 mM, c[TiO$_2$] = 5.5 mM, no external hole scavenger, TiO$_2$ polyhedrons as substrate.

Once again both the size of the Pd NDs and the corresponding Janus yield increase regularly with illumination time, with a sort of saturation or plateau for the longer duration. The largest Pd size (11.9 nm) we obtained is still smaller than our estimated value of 17.8 nm, assuming all Pd ions are reduced and Janus yield is 100 %.
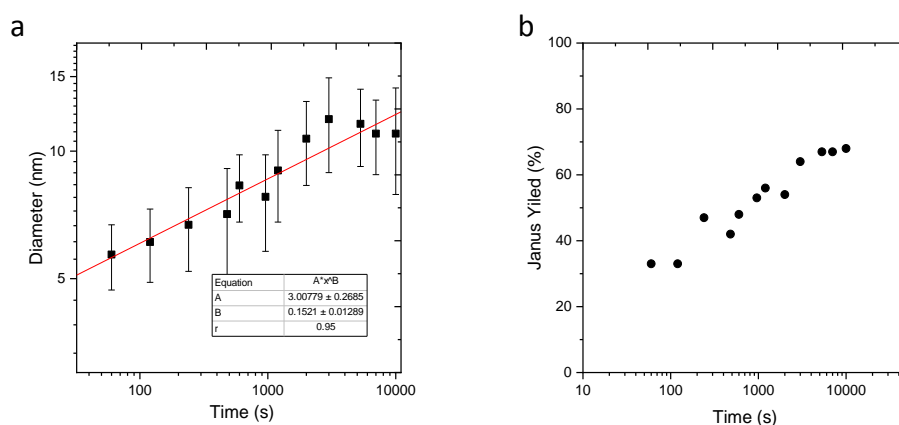
Figure 5.31 (a) Pd size and (b) Janus yield of Pd-TiO$_2$ NPs as a function of illumination time, A power law fit was performed on the set of data. Experimental conditions are: c[PdCl$_4^{2-}$] = 1 mM, c[TiO$_2$] = 5.5 mM, no external hole scavenger, TiO$_2$ polyhedrons as substrate.

References pages 198

(c) Hole scavenger effect

The last parameter to test is the effect of hole scavengers on photodeposition experiments made in cuvette setup. Similar to what we did in microchannel setup, to check the role of the hole scavenger, we chose to keep all the parameters identical and as follows, TiO_2 polyhedrons as substrate, $c[Pd^{2+}]$ = 1 mM, $c[TiO_2]$ = 5.5 mM, pH = 3, power 13.88 mW and illumination time 10 min. The role of three types of hole scavengers, *i.e.*, methanol (50 vol.%) and HCOONa (2 mM) and H_2O itself, are analyzed.

The TEM results of Pd-TiO_2 NDs performed in the cuvette setup using HCOONa, methanol and H_2O as a hole scavenger are shown in Figure 5.32.
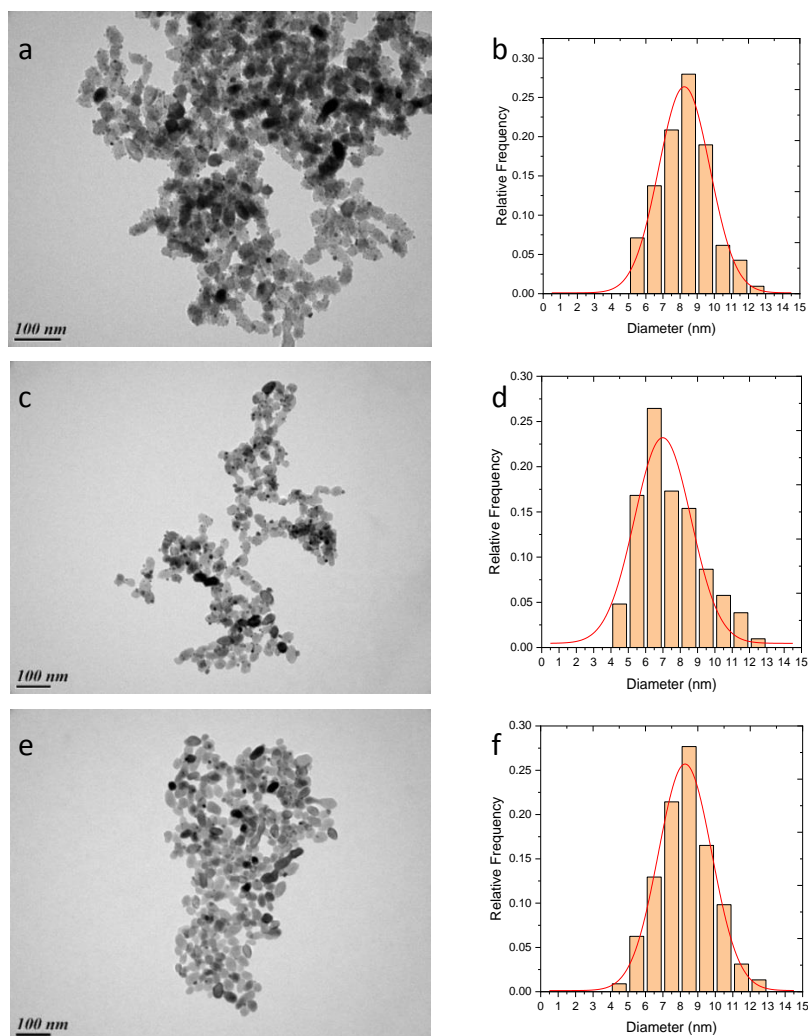
Figure 5.32 TEM image of Pd-TiO₂ NPs made in cuvette setup using (a) HCOONa, (c) methanol and (e) H₂O as hole scavengers, and their corresponding size distribution in (b), (d) and (f). Experimental conditions are: c[Na₂PdCl₄]= 1 mM, c[TiO₂] = 5.5 mM, pH 3, power 13.88 mW, illumination time 10 min, TiO₂ polyhedrons as substrate.

Interestingly, we find that a single Pd ND was successfully deposited on TiO₂ NDs only when H₂O itself was used as a hole scavenger, while both methanol and HCOONa are found to lead to multiple Pd NDs loading on TiO₂ surface even for the lowest power. These findings obtained in cuvette setup are similar to the experiments made performed in the microchannel setup in terms of deposits number on each TiO₂, even though the intensities of the two setups differ from 100 to 1000 times.

5.2.3.4 Modelling fit of palladium size data

Over the past decades, the variation of the size growth of the Pd NDs on the TiO₂ NDs has been studied as a function of many parameters.[21, 23, 25-27, 37-42] There was then a real need to find a model which would optimize and provide a general trend for all these data.

According to the model presented in Appendix 2, in the high and low field cases, the late growth stage regime of Pd ND should respect the following Equation 5.3 and Equation 5.4, respectively:

$$R^3(t>>) = \frac{3\Omega^2}{\kappa}[Pd](t) = \frac{3\Omega^2}{\kappa}k'_{Pd}\left(\frac{gk'_{HS}}{k_r k'_{pd}}\right)^{\frac{2}{3}}t = \frac{3\Omega^2}{\kappa}\frac{k'_{HS}}{k_r}\left(\frac{k_r k'_{pd}g^2}{k'_{HS}}\right)^{1/3}t \sim g^{\frac{2}{3}}k'_{Pd}{}^{\frac{1}{3}}t \qquad \textit{Equation 5.3}$$

$$R^3(t>>) = \frac{3\Omega^2}{\kappa}[M](t) = \frac{3\Omega^2}{\kappa}gt \qquad \textit{Equation 5.4}$$

Where k_r is the recombination rate, $k'_{Pd} = k_{Pd}[Pd^{2+}]$ is the effective rate for the production of Pd⁰, $k'_{HS} = k_{HS}[HS]$ is the rate of hole scavenging, g is the electron source term proportional to the absorption coefficient of TiO₂ and the beam intensity, Ω and κ are respectively a characteristic volume factor and a dimensionless factor related to the contact angle of a Pd dot on the TiO₂ surface.

According to the prediction shown above, the Pd ND diameter (D = 2R) should behave at a fixed time as $P^{2/9}$ for the high field regime and $P^{1/3}$ in power for the low field regime, respectively; and $t^{1/3}$ in illumination time for either high or low field regime.

Figure 5.33 shows the size dependence of these Pd NDs synthesized in the microchannel setup with power and time (conditions given in above section 5.2.3.2).
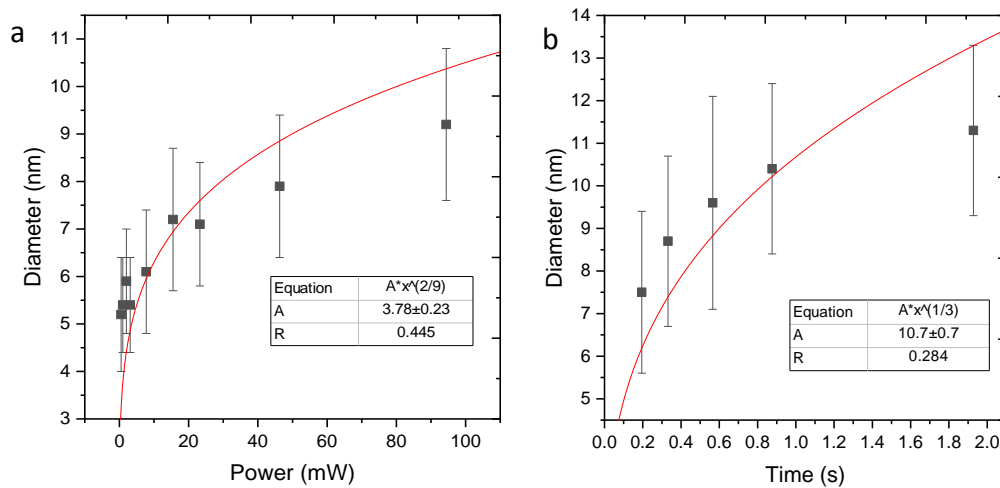
Figure 5.33 (a) Pd diameter as a function of power. (b) Pd diameter as a function of time made in microchannel setup.

When the data are fitted with a function $D = A*P^{2/9}$ in Figure 5.33a, and fitted with a function $D = A*t^{1/3}$ in Figure 5.33b, the correlation coefficient between the Pd size and the expected power law in power (or in time) is 0.445 (or 0.284), indicating a very poor agreement with the prediction; pure power law fits give respectively $D = A*P^{0.11}$ and $D = A*t^{0.18}$ (with respective correlations R = 0.91 and R = 0.98), i.e., half the expected exponent.

Figure 5.34 shows the size of Pd NDs synthesized with the cuvette setup when plotted as a function of power and time (conditions given in section 5.2.3.3 above).
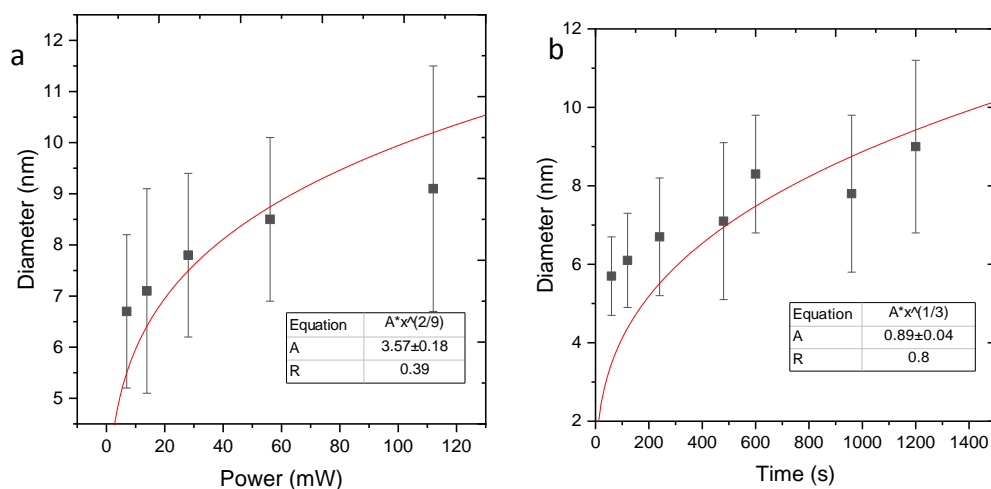
Figure 5.34 (a) Pd diameter as a function of power. (b) Pd diameter as a function of time made in cuvette setup.

After we did the same fitting process to Figure 5.34a and b, and we found the correlation

References pages 198

coefficients for the Pd size versus expected power law with power (or time) to be 0.39 (or 0.8), indicating again a very poor fit agreement with the prediction; pure power law fits give respectively $D = A*P^{0.11}$ and $D = A*t^{0.18}$ (with respective correlations R = 0.99 and R = 0.96), i.e. half the expected exponents again. What is remarkable is the robustness of these power law exponents whatever the setup used. Moreover, to probe this reliability we plotted in Figure 5.32 the whole set of data, from the cuvette and microchannel setups, as a function of the rescaled time expected for both the high and the low field regimes on a single curve. They stay separated with the high field scaling indicating that data do not belong to this regime. Conversely, they all collapse perfectly on the behaviour $D = A*(gt)^{0.13}$ (correlation R = 0.94) over five decades in rescaled time using the low field scaling, showing meantime surprising robustness and a global power law exponent 1/3 of the expected value.
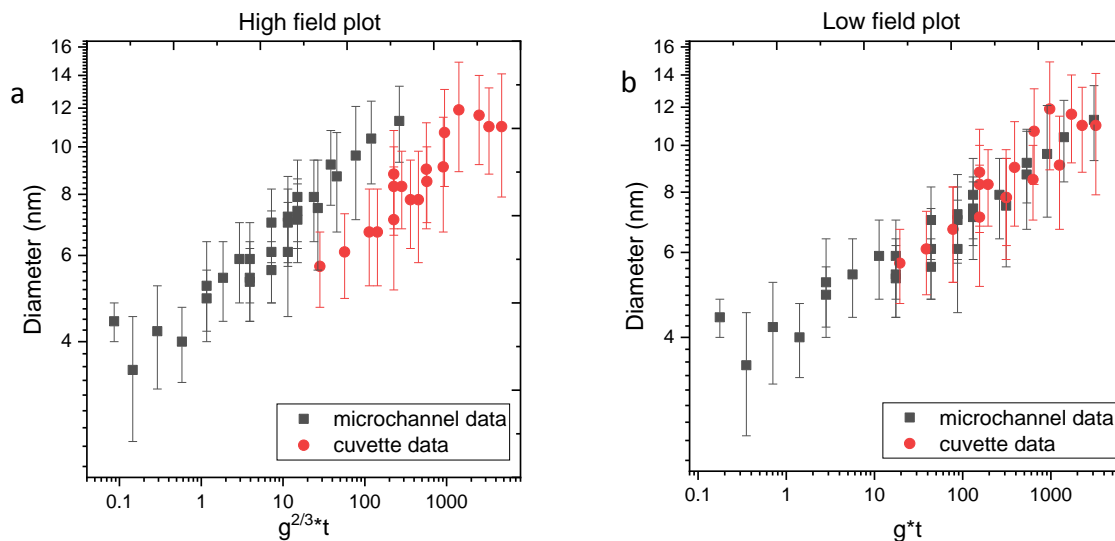
Figure 5.35 Pd diameter made in both microchannel and cuvette setups plotted at (a) high field and (b) low field.

Nonetheless, the conclusion is that the growth of palladium dot on TiO₂, even if very stable, definitely does not follow, at least for this precursor, the predictions of the growth model. A possible explanation relies on the complicated nature of the precursor itself. Indeed, palladium(II) is known to form stable complexes with chloride. The complexation equilibria of Na_2PdCl_4 in water is strongly pH[43]. and pCl [24] dependent leading to the formation of the different forms of the palladium chloride aqua complexes, $[PdCl_n(H_2O)_{4-n}]^{2-n}$ (n = 0–4).

Cruywagen [43] established, for example, the distribution of the Pd(II)–chloride complexes as a function of pCl based on the formation constants of the complexation reactions (Figure 5.36) and the photoreduction trends using water as a hole scavenger.
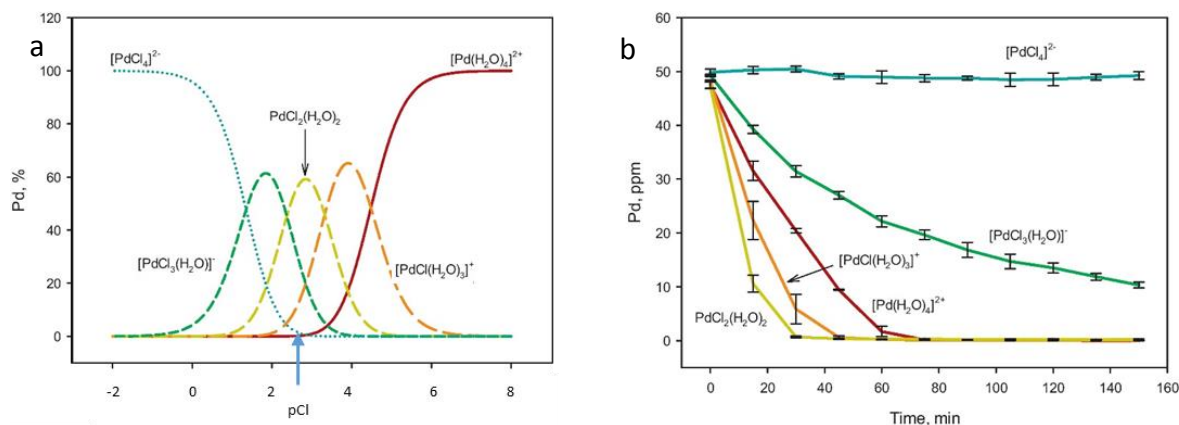
Figure 5.36 (a) Distribution of [PdCl$_n$(H$_2$O)$_{4-n}$]$^{2-n}$ species as a function of pCl, (b) Photocatalytic reduction trends of the [PdCl$_n$(H$_2$O)$_{4-n}$]$^{2-n}$-system (n = 0–4) in the absence of an external hole scavenger. The associated legends indicate the Pd(II)-complexes present in greater abundance at a specific chloride concentration at 25 °C.[24]

In our case, with a Pd(II) concentration of 1 mM, we can assume a maximum concentration of chloride of 4 mM in solutions and a pCl of 2.4. If we assume this value, 3 palladium precursors may as well be supposed in solution PdCl$_n$(H$_2$O)$_{4-n}$]$^{2-n}$ with n= 1,2 and 3 (blue arrow in Figure 5.22a).

5.2.4 Conclusions

In this section, we investigated the photodeposition of palladium on TiO_2 with both the microchannel and the cuvette setups. Techniques including TEM and XPS have confirmed the existence of metallic-Pd NDs deposited on the TiO_2 surface and the formation of heterodimer structures with single Pd ND on each TiO_2.

Metal precursor effects were investigated with both $Pd(OAc)_2$ and Na_2PdCl_4. It was found that $Pd(OAc)_2$ could lead to single Pd ND on TiO_2 but it needs the addition of organic agent like acetone to be well dissolved in aqueous solution. The water-soluble Na_2PdCl_4 was then considered as a better choice as a metal precursor for Pd photodeposition.

We have also studied the effects of other parameters on the photodeposition process. Two types of hole scavengers, methanol and HCOONa, were investigated and their use showed constantly the formation of multi Pd NDs on TiO_2 surface. Conversely, photodeposition experiments without any external hole scavengers resulted in the formation of nano heterodimers with single Pd ND on each TiO_2 with relatively high Janus yield.

Beyond experiments performed with the microchannel setup, photodeposition was also investigated in a cuvette setup illuminated by a UV laser. Cuvette experiments using the UV laser also led to single Pd ND deposition on TiO_2 surface, with growth law very similar to that obtained with the microchannel setup in the absence of external hole scavenger.

However, our growth model poorly predicts the palladium size variation in the photodeposition process and actually we do not have any quantitative insight that can definitively explain this clear disagreement since experiments show a single behaviour for more than five decades in reduced time.

5.3 Photodeposition of Pt nanodots onto the surface of TiO$_2$ nanoparticles

5.3.1 Introduction to photodeposition of Pt nanodots onto the surface of TiO$_2$ nanoparticles

Photodeposition of Pt nanodots (Pt NDs) on the surface of TiO$_2$ is an important technique to synthesize Pt-TiO$_2$ NPs, as such heterostructures are widely used for alcohol oxidation[44-46], hydrogen generation[47, 48] and water splitting.[49, 50] In 1985, Curran et al.[51] firstly confirmed the existence of Pt NDs distributed on the surface of TiO$_2$ P25 when the mixture solution of H$_2$PtCl$_6$ and TiO$_2$ particles were irradiated by UV light.

The significance of the presence of a hole scavenger in the photodeposition process of Pt on anatase was demonstrated by Sungbom et al.[52] The authors showed that the presence or absence of a combination of CH$_3$COOH and CH$_3$COONa largely affected the obtained oxidation state of Pt, as analyzed by X-ray photoelectron spectroscopy (XPS). The authors found that Pt^{II} and Pt^{IV} formed, rather than Pt^0, at low concentrations of CH$_3$COOH–CH$_3$COONa, while a higher concentration of CH$_3$COOH–CH$_3$COONa resulted in a high concentration of Pt^0. This suggested that the extent of reduction of the Pt precursor is largely dependent on the rate of hole scavenging, which is typically higher in the conversion of an organic molecule as compared to the oxidation of water. Interestingly, when photocatalytic methanol decomposition was performed with as-obtained Pt-loaded TiO$_2$, oxidized platinum was readily reduced to metallic Pt^0 in situ. Illumination in methanol-containing solutions is thus expected to be very effective in reducing platinum oxides to Pt.

The high effectiveness of methanol to obtain fully reduced Pt was confirmed by Lee and Choi,[53] who used Degussa P25 as a TiO$_2$ photocatalyst. They employed methanol at high and low concentrations. Complete reduction to Pt^0 particles was achieved at high concentration, whereas Pt^{II} remained dominant at relatively low methanol concentration. Methanol radicals, formed by oxidation of methanol by holes, were proposed to contribute to the reduction of Pt.

A comparison of hole scavengers in determining Pt particle size and dispersion was reported by Nakamatsu et al.[54] The Pt–Pt particle nearest-neighbour distance as a function of the hole scavenger used is illustrated in Figure 5.37a. In agreement with Lee and Choi,[53] the authors propose a model where the radicals of the organic compounds used (methanol, ethanol, 2-propanol, and acetic acid), provide electrons for the reduction of adsorbed Pt species at the semiconductor surface. Nakamatsu et al.[54] also observed that the use of radicals with a relatively high reduction potential results in a large Pt–Pt particle distance (Figure 5.37b).
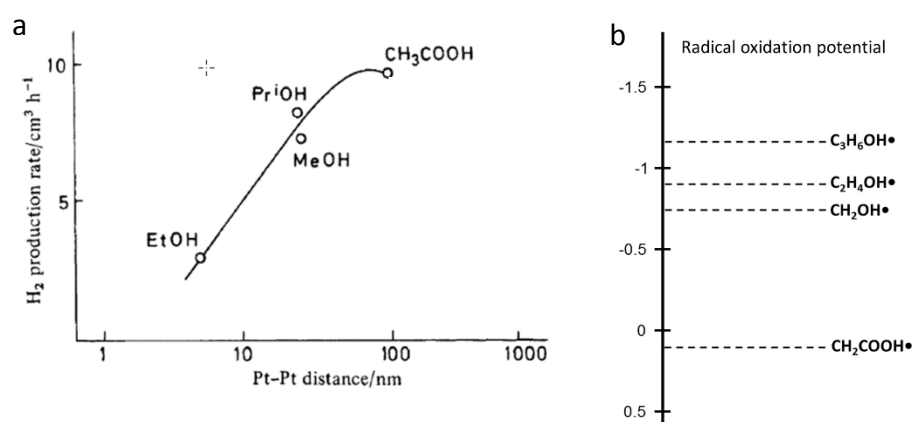
Figure 5.37 (a) Effect of hole scavengers used on Pt–Pt particle distance on P25 TiO$_2$, and the resulting hydrogen production rate of the photocatalysts in reforming of ethanol. Circles indicate the hole scavengers used in the photodeposition procedure and serve as data points for this graph. (b) Radical oxidation potentials in volts vs NHE.[54, 55]

The trend proposed in Figure 5.37 indicates that a high reduction potential of in situ formed organic radicals favours the nucleation of small Pt particles, rather than the stimulation of the growth of existing particles. The relatively large Pt particle size of the catalysts prepared with 2-propanol is explained by its high concentration (50 vol. %) used, as compared to the other hole scavengers, even though the radical has the highest oxidation potential. This is in agreement with the data of Lee and Choi,[53] who observed significantly larger Pt particles when high concentrations of CH$_3$OH were used. Further investigations are recommended to substantiate the conclusions of the work by Nakamatsu et al.[54] on the effect of the hole scavenging on Pt-Pt distance and dispersion.

For the effect of other parameters on the Pt photodeposition process, one may refer to the

excellent review paper by Wenderich [56] for more information.

5.3.2 Experimental methods

The experimental procedures for the Pt photodeposition performed in the microchannel or cuvette setups are the same as those for Au photodeposition in part 5.1.2, except that the metal precursor used is now hexachloroplatinic acid (H$_2$PtCl$_6$). One may refer to the previous part for more details.

5.3.3 Results and discussions

The Pt-TiO$_2$ NPs made in the microchannel setup are firstly investigated. The TEM result of Pt-TiO$_2$ NPs is shown in Figure 5.38.
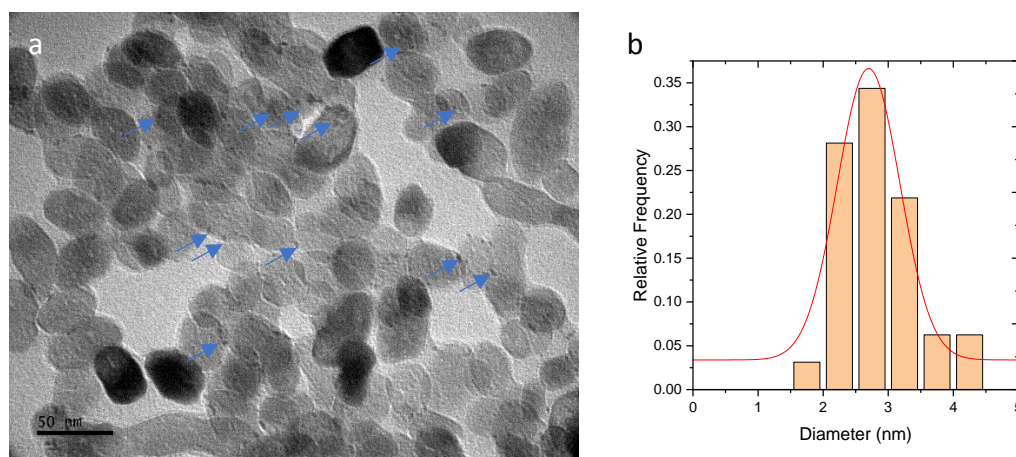
Figure 5.38 (a) TEM image of Pt-TiO$_2$ NPs made in microchannel setup and (b) its size distribution. Experimental conditions are: power 15.5 mW, illumination time 0.2 s, pH = 3, c[H$_2$PtCl$_6$]= 2 mM, c[TiO$_2$] = 5.5 mM, 50 vol. % methanol as hole scavenger, TiO$_2$ polyhedrons as substrate.

It can be seen that the Pt NDs are deposited on the surface of TiO$_2$, denoted by the blue arrows, are extremely small compared to the other deposited metals in the same conditions. Moreover, the yield of Pt-decorated nanoparticles is far below 10 %, probably due to the quite short illumination time 0.2 s when four electrons are required to reduce the platinum ions. The mean size of Pt ND is around 2.7 (1) nm, which is coherent with the reported values of Pt NDs

synthesized by photodeposition methods using a UV lamp.[57]

Then we turned to synthesize Pt photodeposition using the cuvette setup. We first analyzed the effect of the hole scavengers on the morphology of the Pt NDs. In these experiments, we fixed the power at 50.8 mW and illumination time for 8 min, and use H_2O, HCOONa and methanol as hole scavengers. The HRTEM images of strawberry-like Pt-TiO₂ products are shown in Figure 5.39.
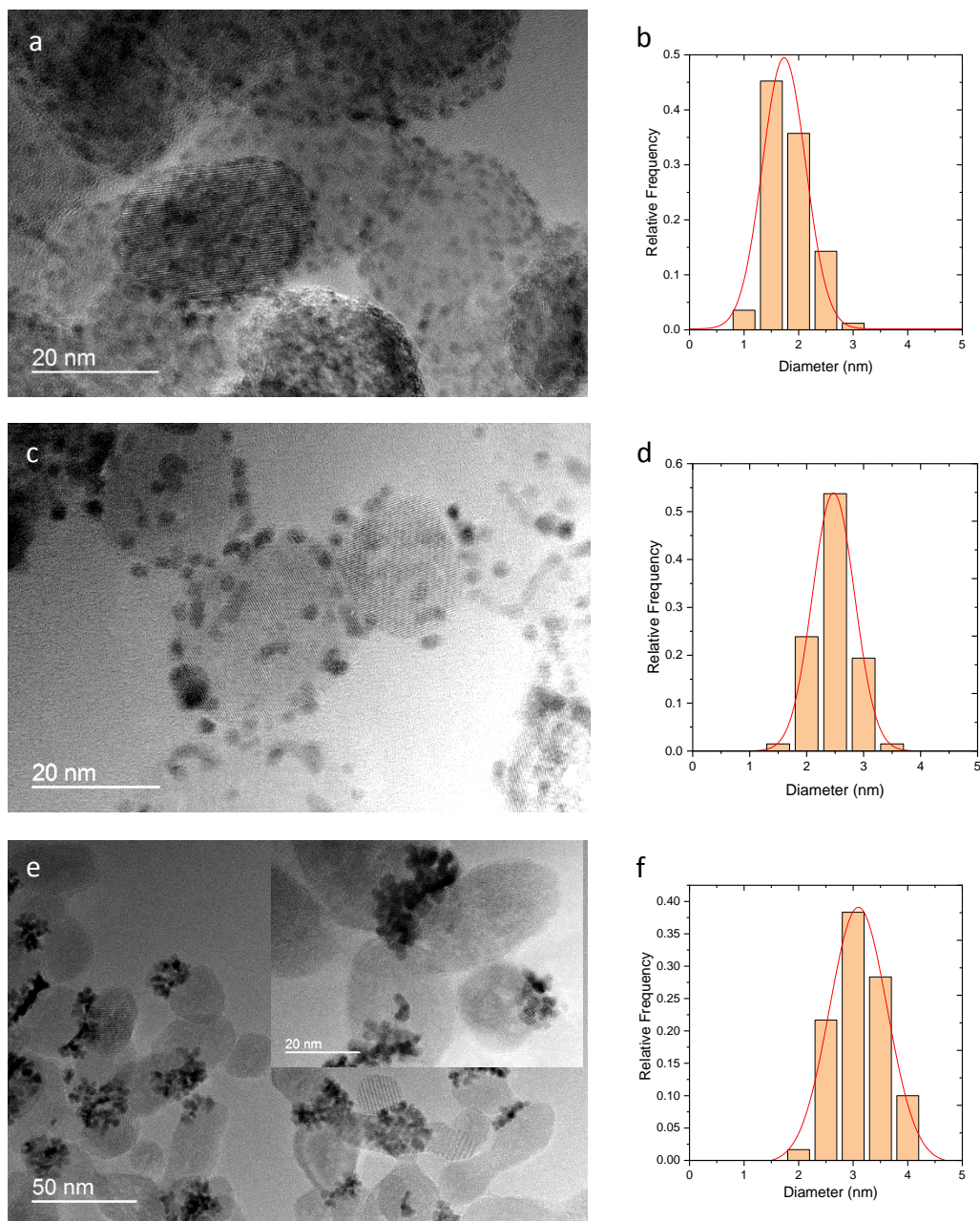
Figure 5.39 HRTEM images of Pt-TiO₂ NPs made in cuvette setup using different hole scavengers (a) H₂O, (c) HCOONa and (e) methanol, and their corresponding size distributions in (b), (d) and (f). Experimental conditions: Power 50.8 mW, illumination time 8 min, c[H₂PtCl₆] = 0.5 mM, c[TiO₂] = 5.5 mM, pH = 3, TiO₂ polyhedrons as substrate.

193

It can be seen that all the TiO$_2$ NPs are decorated with photodeposited Pt NDs, while the size and the morphology of the Pt NDs are different. The product using H$_2$O as hole scavenger exhibits the smallest Pt size (mean value 1.7 nm), with Pt NDs densely and uniformly distributed on the surface of TiO$_2$, while the one using HCOONa lead to a larger Pt size of 2.5 nm, with a looser distribution (much larger distance between the NDs). The use of methanol as hole scavenger results instead in aggregates of small Pt NDs (mean size 3.1 nm) and these aggregates tend to stay on one side of the TiO$_2$, thus forming Janus-like nanoparticles. If we assume such nanoparticles as heterodimers, the Janus yield is high at 75 %. The aggregation phenomenon was also observed in Wenderich's work,[58] in which they used methanol as hole scavenger but on WO$_3$ support. The aggregates can be explained by the highly reducing methoxy radicals coming from the holes oxidation product.[58]

The XPS analysis carried out in the Pt 4f region is given as a representative illustration for all the obtained Pt-TiO$_2$ NPs using H$_2$O as a hole scavenger (Figure 5.40). The observed binding energies (BE) are denoted beside the peak with Ti 2p as a reference (458.9 ± 0.2 eV for Ti 2p$_{3/2}$ and 464.4 ± 0.2 eV for Ti 2p$_{1/2}$).
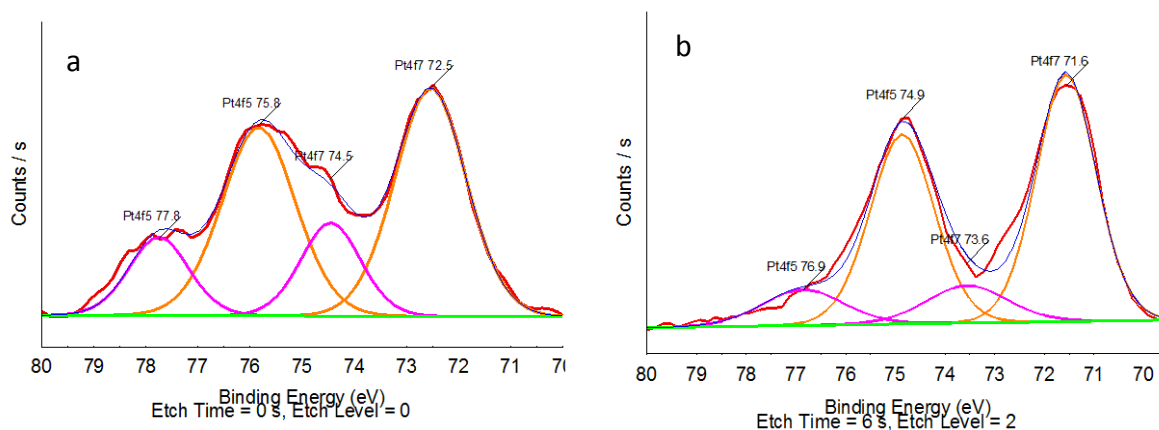
Figure 5.40 Fit of high-resolution XPS spectra of Pt-TiO₂ in the Pt 4f region (a) before and (b) after 6 s etching time.

For the sake of clarity, we shall focus on the Pt4f$_{7/2}$ of each of the two doublets. The fit of the 71-79 eV region requires the contribution of two oxidation states of platinum, one located at 74.5 eV for the oxidized contribution and the other at 72.5 eV for the more reduced form of platinum. As illustrated in Figure 5.40b after 6 s etching, the ratio between these two contributions is increased confirming the reduction of this contribution by the Ar$^+$ beam on

the surface of the Pt NPs. There is also a 1 eV shift which is then stabilized at 71.6 ± 0.2 eV as illustrated in Figure 5.41. These values are positively shifted with regards to classical values found in the literature[59-63], they are in the same range as those reported by Vovk,[64] who showed in a nice work that the size of Pt particles decreases and the Pt 4f core level peak in XPS spectra are connected; then smaller the size the higher binding energy,[65] confirming the small size we observed by HRTEM.
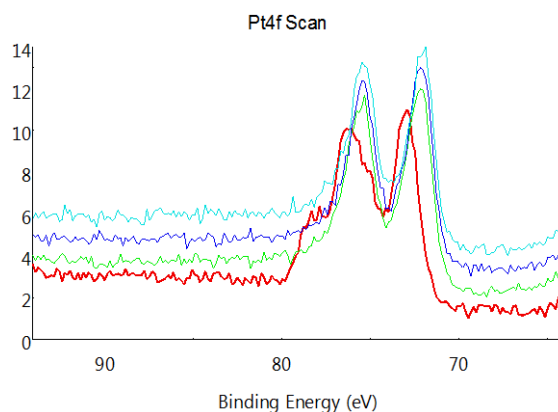
Figure 5.41 XPS spectra of Pt-TiO₂ under etching conditions at t = 0, 3, 6, and 16 s (increase upward).

The Pt size range is relatively small as compared to that of the Au or Ag NDs made by the same photodeposition method. We noted the same tendency in the literature,[49, 66, 67,68, 69] with a size range of 2-6 nm, some remaining even at the atomic scale.[70]. This prevented us for the moment from using the Pt size data to fit them with our growth model. Still, more experiments in the future concerning other parameters (like pH, and power effect) should be done to fulfil the whole story of the Pt photodeposition even if our experiments show for the first time how photodeposition can produce Janus-like nanoparticles with TiO₂ and platinum.

5.3.4 Conclusions

In this section, we performed the photodeposition of Pt on TiO$_2$ in microchannel and cuvette setup. We systematically found that Pt NDs were successfully deposited on the surface of TiO$_2$. The illumination time is too short to obtain heterodimers in the microchannel setup. We have found the photodeposition of Pt NDs takes place in the cuvette setup and gives rise to a variety of nanostructures. The morphology of the Pt NDs distributed on the surface of TiO$_2$ is dependent on the type of hole scavenger used. Specifically, the use of methanol favours the aggregation of small Pt NDs, thus forming a Janus-like NPs with relatively large clusters on one side of the TiO$_2$. While water and formate allowed to control the final size of the Pt NDs deposited on the overall surface of the semiconductor. The lack of data and the small size range of Pt NPs prevented us from fitting the available data with our model.

References pages 198

5.4 Conclusions of Chapter 5

In this chapter, we have moved to other metal precursors M^{n+} (n= 2, 3, 4) and performed the photodeposition of gold, palladium and platinum on the surface of TiO_2 using both the microchannel and the cuvette setups. In all cases, metal nanodots were successfully deposited on the surface of TiO_2.

Growth law fits were also performed to verify the validity of the proposed model developed in Appendix 2. In the case of gold, the fit can be used to reasonably predict the growth process, although it is not that good as compared to the case of Ag. It was suggested that the release of chloride ions, which can be used as a hole scavenger, could play a role in the reaction[22], even if this assumption seems to be efficient only in the presence of another efficient hole scavenger as methanol or sodium formate. The pH range also allows the co-existence of three different complexes of Au^{3+} in solution, which probably react with different rates in the medium leading to an overall more complex system. In the case of Pd, the growth process cannot be predicted by the proposed model. Some extra work with other chloride-free palladium precursors should be performed and may help contribute to the understanding of the actual mystery. In the case of Pt, the fit was not performed due to the observed small size range 2-6 nm, and the number of electrons required for a full reduction. Nonetheless, we succeeded in synthesizing nano-heterodimers with silver, gold, palladium and platinum on TiO_2 (Figure 5.42), showing that laser deposition seems to be much more efficient than of the usual UV lamp photodeposition, as the flux of photons matters much more than the deposited energy. Some more work is needed to better understand the case of platinum deposition.
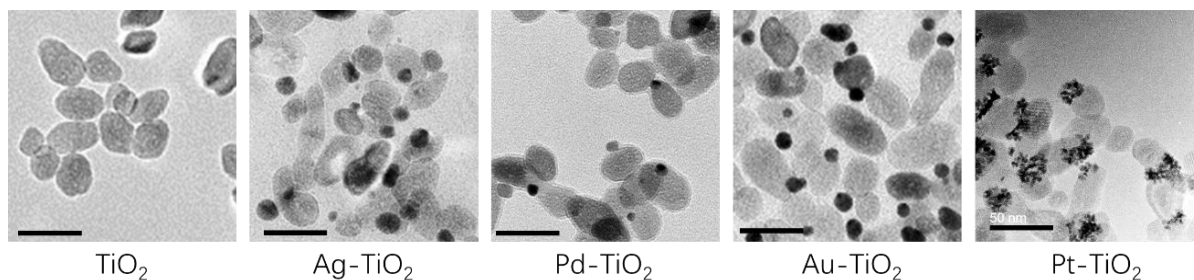
Figure 5.42 Evolution from TiO₂ to metal-TiO₂ NPs. The bar in each owns the same scale.

5.5 Bibliography

1.   Bamwenda, G. R.; Tsubota, S.; Nakamura, T.; Haruta, M., Photoassisted hydrogen production from a water-ethanol solution: a comparison of activities of Au-TiO₂ and Pt-TiO₂. *J. Photochem. Photobiol., A* **1995,** *89*, 177-189.

2.   Gärtner, F.; Losse, S.; Boddien, A.; Pohl, M.-M.; Denurra, S.; Junge, H.; Beller, M., Hydrogen Evolution from Water/Alcohol Mixtures: Effective In Situ Generation of an Active Au/TiO₂ catalyst. *Chem. Sus. Chem* **2012,** *5*, 530-533.

3.   Sangeetha, P.; Chang, L.-H.; Chen, Y.-W., Preferential Oxidation of CO in H₂ Stream on Au/TiO₂ Catalysts: Effect of Preparation Method. *Ind. Eng. Chem. Res.* **2009,** *48*, 5666-5670.

4.   Kenens, B.; Chamtouri, M.; Aubert, R.; Miyakawa, K.; Hayasaka, Y.; Naiki, H.; Watanabe, H.; Inose, T.; Fujita, Y.; Lu, G.; Masuhara, A.; Uji-i, H., Solvent-induced improvement of Au photo-deposition and resulting photo-catalytic efficiency of Au/TiO₂. *RSC Adv.* **2016,** *6*, 97464-97468.

5.   Wang, D.; Bi, Q.; Yin, G.; Wang, P.; Huang, F.; Xie, X.; Jiang, M., Photochemical Preparation of Anatase Titania Supported Gold Catalyst for Ethanol Synthesis from CO₂ Hydrogenation. *Catal. Lett.* **2018,** *148*, 11-22.

6.   Wei, Z.; Rosa, L.; Wang, K.; Endo, M.; Juodkazis, S.; Ohtani, B.; Kowalska, E., Size-controlled gold nanoparticles on octahedral anatase particles as efficient plasmonic photocatalyst. *Appl. Catal., B* **2017,** *206*, 393-405.

7.   Deepagan, V. G.; You, D. G.; Um, W.; Ko, H.; Kwon, S.; Choi, K. Y.; Yi, G.-R.; Lee, J. Y.; Lee, D. S.; Kim, K.; Kwon, I. C.; Park, J. H., Long-Circulating Au-TiO₂ Nanocomposite as a Sonosensitizer for ROS-Mediated Eradication of Cancer. *Nano Lett.* **2016,** *16*, 6257-6264.

8.   Yan, J.; Wu, G.; Guan, N.; Li, L., Synergetic promotion of the photocatalytic activity of TiO₂ by gold deposition under UV-visible light irradiation. *Chem. Commun.* **2013,** *49*, 11767-11769.

9.   Sato, Y.; Naya, S. I.; Tada, H., A new bimetallic plasmonic photocatalyst consisting of gold(core)-copper(shell) nanoparticle and titanium(IV) oxide support. *APL Mater.* **2015,** *3*, 104502.

10. Dobosz, A.; Sobczyński, A., Water detoxification: Photocatalytic decomposition of phenol on Au/TiO₂. *Monatsh. Chem.* **2001,** *132*, 1037-1045.

11. Tong, R.; Liu, C.; Xu, Z.; Kuang, Q.; Xie, Z.; Zheng, L., Efficiently Enhancing Visible Light Photocatalytic Activity of Faceted TiO₂ Nanocrystals by Synergistic Effects of Core-Shell Structured Au@CdS Nanoparticles and Their Selective Deposition. *ACS Appl. Mater. Interfaces* **2016,** *8*, 21326-21333.

12. Majimel, J.; Lamirand-Majimel, M.; Moog, I.; Feral-Martin, C.; Tréguer-Delapierre, M., Size-Dependent Stability of Supported Gold Nanostructures onto Ceria: an HRTEM Study. *J. Phys. Chem. C* **2009,** *113*, 9275-9283.

13. Moulder, J. F.; Stickle, W. F.; Sobol, P. E. B., K. E, *Handbook of X-ray photoelectron spectrscopy*. Physical Electronics:Chanhassen: 1995.

14. Epling, W. S.; Hoflund, G. B.; Weaver, J. F.; Tsubota, S.; Haruta, M., Surface Characterization Study of Au/α-Fe₂O₃ and Au/Co₃O₄ Low-Temperature CO Oxidation Catalysts. *J. Phys. Chem. C* **1996,** *100*, 9929-9934.

15. Hidalgo, M. C.; Murcia, J. J.; Navío, J. A.; Colón, G., Photodeposition of gold on titanium dioxide for photocatalytic phenol oxidation. *Appl. Catal., A* **2011,** *397*, 112-120.

16. Hidalgo, M. C.; Maicu, M.; Navío, J. A.; Colón, G., Effect of Sulfate Pretreatment on Gold-Modified TiO₂ for Photocatalytic Applications. *J. Phys. Chem. C* **2009,** *113*, 12840-12847.

17. Vauriot, L. Synthèse microfluidique de nanomatériaux multifonctionnels par laser. 2012.

18. Kelly, J. J.; Vondeling, J. K., The Nucleation Reaction on Photosensitive TiO₂ Films. *J. Electrochem. Soc.* **1975,** *122*, 1103-1107.

19. Jones, W.; Martin, D. J.; Caravaca, A.; Beale, A. M.; Bowker, M.; Maschmeyer, T.; Hartley, G.; Masters, A., A comparison of photocatalytic reforming reactions of methanol and triethanolamine with Pd supported on titania and graphitic carbon nitride. *Appl. Catal., B* **2019,** *240*, 373-379.

20. Dadsetan, S.; Baghshahi, S.; Hadavi, S. M. M., Photodeposition of Pd nanoparticles on TiO₂ using sacrificial organic alcohols. *J. Aust. Ceram. Soc.* **2018,** *54*, 383-388.

21. Espino-Estévez, M. R.; Fernández-Rodríguez, C.; González-Díaz, O. M.; Araña, J.; Espinós, J. P.; Ortega-Méndez, J. A.; Doña-Rodríguez, J. M., Effect of TiO₂-Pd and TiO₂-Ag on the photocatalytic oxidation of diclofenac, isoproturon and phenol. *Chem. Eng. J.* **2016,** *298*, 82-95.

22. Hippargi, G.; Mangrulkar, P.; Chilkalwar, A.; Labhsetwar, N.; Rayalu, S., Chloride ion: A promising hole scavenger for photocatalytic hydrogen generation. *Int. J. Hydrogen Energy* **2018,** *43*, 6815-6823.

23. Fan, Q.; He, S.; Hao, L.; Liu, X.; Zhu, Y.; Xu, S.; Zhang, F., Photodeposited Pd Nanoparticles with Disordered Structure for Phenylacetylene Semihydrogenation. *Sci. Rep.* **2017,** *7*, 42172.

24. Kriek, R. J.; Mahlamvana, F., Dependency on chloride concentration and 'in-sphere' oxidation of H₂O for the effective TiO₂-photocatalysed electron transfer from H₂O to $[PdCl_n(H_2O)_{4-n}]^{2-n}$ (n=0–4) in the absence of an added sacrificial reducing agent. *Appl. Catal., A* **2012,** *423-424*, 28-33.

25. Camposeco, R.; Castillo, S.; Mejía-Centeno, I.; Navarrete, J.; Marín, J., Characterization of physicochemical properties of Pd/TiO₂ nanostructured catalysts prepared by the photodeposition method. *Mater. Charact.* **2014,** *95*, 201-210.

26. Diak, M.; Grabowska, E.; Zaleska, A., Synthesis, characterization and photocatalytic activity of noble metal-modified TiO₂ nanosheets with exposed {001} facets. *Appl. Surf. Sci.* **2015,** *347*, 275-285.

27. Dadsetan, S.; Baghshahi, S.; Farshidfar, F.; Hadavi, S. M. M., Photodeposition of Pd nanoparticles on TiO₂ utilizing a channel type quartz reactor. *Ceram. Int.* **2017,** *43*, 9322-9326.

28. Leong, K. H.; Chu, H. Y.; Ibrahim, S.; Saravanan, P., Palladium nanoparticles anchored to anatase TiO₂ for enhanced surface plasmon resonance-stimulated, visible-light-driven photocatalytic activity. *Beilstein J. Nanotechnol.* **2015,** *6*, 428-437.

29. Oros-Ruiz, S.; Pedraza-Avella, J. A.; Guzmán, C.; Quintana, M.; Moctezuma, E.; del Angel, G.; Gómez, R.; Pérez, E., Effect of Gold Particle Size and Deposition Method on the Photodegradation of 4-Chlorophenol by Au/TiO₂. *Top. Catal.* **2011,** *54*, 519-526.

30. Nakibli, Y.; Mazal, Y.; Dubi, Y.; Wachtler, M.; Amirav, L., Size Matters: Cocatalyst Size Effect on Charge Transfer and Photocatalytic Activity. *Nano Lett.* **2018,** *18*, 357-364.

31. Maicu, M.; Hidalgo, M. C.; Colón, G.; Navío, J. A., Comparative study of the photodeposition of Pt, Au and Pd on pre-sulphated TiO₂ for the photocatalytic decomposition of phenol. *J. Photochem. Photobiol., A* **2011,** *217*, 275-283.

32. Kabcum, S.; Channei, D.; Tuantranont, A.; Wisitsoraat, A.; Liewhiran, C.; Phanichphant, S., Ultra-responsive hydrogen gas sensors based on PdO nanoparticle-decorated WO₃ nanorods synthesized by precipitation and impregnation methods. *Sens. Actuator B-Chem* **2016,** *226*, 76-89.

33. Venezia, A. M.; Rossi, A.; Duca, D.; Martorana, A.; Deganello, G., Particle size and metal-support interaction effects in pumice supported palladium catalysts. *Appl. Catal. A* **1995,** *125*, 113-128.

34. Han, C.; Yang, M.-Q.; Zhang, N.; Xu, Y.-J., Enhancing the visible light photocatalytic performance of ternary CdS–(graphene–Pd) nanocomposites via a facile interfacial mediator and co-catalyst strategy. *J. Mater. Chem. A* **2014,** *2*, 19156-19166.

35. Konda, S. K.; Chen, A., One-step synthesis of Pd and reduced graphene oxide nanocomposites for enhanced hydrogen sorption and storage. *Electrochem. Commun.* **2015,** *60*, 148-152.

36. Cátia, O.; Ruiz, A. J.; Lionel, S.; Didier, A., "Click" Dendrimers: Synthesis, Redox Sensing of Pd(OAc)₂, and Remarkable Catalytic Hydrogenation Activity of Precise Pd Nanoparticles Stabilized by 1,2,3-Triazole-Containing Dendrimers. *Chem. Eur. J.* **2008,** *14*, 50-64.

37. Wang, J.; Rao, P.; An, W.; Xu, J.; Men, Y., Boosting photocatalytic activity of Pd decorated TiO₂ nanocrystal with exposed (001) facets for selective alcohol oxidations. *Appl. Catal., B* **2016,** *195*, 141-148.

38. Fernández, A.; González-Elipe, A. R., "In situ" XPS study of the photoassisted reduction of noble-metal cations on TiO₂. *Appl. Surf. Sci.* **1993,** *69*, 285-289.

39. Zhang, H.; Jin, M.; Xiong, Y.; Lim, B.; Xia, Y., Shape-Controlled Synthesis of Pd Nanocrystals and Their Catalytic Applications. *Acc. Chem. Res.* **2013,** *46*, 1783-1794.

40. Kettemann, F.; Wuithschick, M.; Caputo, G.; Kraehnert, R.; Pinna, N.; Rademann, K.; Polte, J., Reliable palladium nanoparticle syntheses in aqueous solution: the importance of understanding precursor chemistry and growth mechanism. *Cryst. Eng. Comm.* **2015,** *17*, 1865-1870.

41. Zhang, F.; Chen, J.; Zhang, X.; Gao, W.; Jin, R.; Guan, N., Simple and low-cost preparation method for highly dispersed Pd/TiO₂ catalysts. *Catal. Today* **2004,** *93-95*, 645-650.

42. Borgarello, E.; Serpone, N.; Emo, G.; Harris, R.; Pelizzetti, E.; Minero, C., Light-induced reduction of rhodium(III) and palladium(II) on titanium dioxide dispersions and the selective photochemical separation and recovery of gold(III), platinum(IV), and rhodium(III) in chloride media. *Inorg. Chem.* **1986,** *25*, 4499-4503.

43. Cruywagen, J. J.; Kriek, R. J., Complexation of palladium(II) with chloride and hydroxide. *J. Coord. Chem.* **2007,** *60*, 439-447.

44. Beltram, A.; Romero-Ocaña, I.; Josè Delgado Jaen, J.; Montini, T.; Fornasiero, P., Photocatalytic valorization of ethanol and glycerol over TiO₂ polymorphs for sustainable hydrogen production. *Appl. Catal., A* **2016,** *518*, 167-175.

45. Murcia, J. J.; Hidalgo, M. C.; Navío, J. A.; Vaiano, V.; Ciambelli, P.; Sannino, D., Ethanol partial photoxidation on Pt/TiO₂ catalysts as green route for acetaldehyde synthesis. *Catal. Today* **2012,** *196*, 101-109.

46. Kennedy, J. C.; Datye, A. K., Photothermal Heterogeneous Oxidation of Ethanol over Pt/TiO₂. *J. Catal.* **1998,** *179*, 375-389.

47. Truong, Q.; Hoa, H.; Le, T., Pt nanoparticles loaded titanium picolinate framework for photocatalytic hydrogen generation. *Catal. Commun.* **2015,** *59*, 55-60.

48. Chowdhury, P.; Malekshoar, G.; Ray, M. B.; Zhu, J.; Ray, A. K., Sacrificial Hydrogen Generation from Formaldehyde with Pt/TiO₂ Photocatalyst in Solar Radiation. *Ind. Eng. Chem. Res.* **2013,** *52*, 5023-5029.

49. Fang, W.; Qin, Z.; Liu, J.; Wei, Z.; Jiang, Z.; Shangguan, W., Photo-switchable pure water splitting under visible light over nano-Pt@P25 by recycling scattered photons. *Appl. Catal., B* **2018,** *236*, 140-146.

50. Yu, J.; Qi, L.; Jaroniec, M., Hydrogen Production by Photocatalytic Water Splitting over Pt/TiO₂ Nanosheets with Exposed (001) Facets. *J. Phys. Chem. C* **2010,** *114*, 13118-13125.

References pages 198

51. Curran, J. S.; Domenech, J.; Jaffrezic-Renault, N.; Philippe, R., Kinetics and mechanism of platinum deposition by photoelectrolysis in illuminated suspensions of semiconducting titanium dioxide. *J. Phys. Chem.* **1985,** *89*, 957-963.

52. Choi, S.; Maki, K.; Kazunori, T., XPS Studies of the Platinum Species Photodeposited on Titania from Aqueous Chloroplatinic Acid. *Bull. Chem. Soc. Jpn.* **1984,** *57*, 871-872.

53. Lee, J.; Choi, W., Photocatalytic Reactivity of Surface Platinized TiO₂: Substrate Specificity and the Effect of Pt Oxidation State. *J. Phys. Chem. B* **2005,** *109*, 7399-7406.

54. Nakamatsu, H.; Kawai, T.; Koreeda, A.; Kawai, S., Electron-microscopic observation of photodeposited Pt on TiO₂ particles in relation to photocatalytic activity. *J. Chem. Soc., Faraday Trans.* **1986,** *82*, 527-531.

55. Haynes, W. M.; Lide, D. R.; Bruno, T. J., *CRC handbook of chemistry and physics a ready-reference book of chemical and physical data*. 2016.

56. Wenderich, K.; Mul, G., Methods, Mechanism, and Applications of Photodeposition in Photocatalysis: A Review. *Chem. Rev.* **2016,** *116*, 14587-14619.

57. Murcia, J. J.; Navío, J. A.; Hidalgo, M. C., Insights towards the influence of Pt features on the photocatalytic activity improvement of TiO₂ by platinisation. *Appl. Catal. B* **2012,** *126*, 76-85.

58. Wenderich, K.; Han, K.; Mul, G., The Effect of Methanol on the Photodeposition of Pt Nanoparticles on Tungsten Oxide. *Part. Part. Syst. Char.* **2018,** *35*, 1700250.

59. Yang, J. C.; Kim, Y. C.; Shul, Y. G.; Shin, C. H.; Lee, T. K., Characterization of photoreduced Pt-TiO₂ and decomposition of dichloroacetic acid over photoreduced Pt-TiO₂ catalysts. *Appl. Surf. Sci.* **1997,** *121-122*, 525-529.

60. Tada, H.; Suzuki, F.; Ito, S.; Akita, T.; Tanaka, K.; Kawahara, T.; Kobayashi, H., Au-Core/Pt-Shell Bimetallic Cluster-Loaded TiO₂. 1. Adsorption of Organosulfur Compound. *J. Phys. Chem. B* **2002,** *106*, 8714-8720.

61. Iliev, V.; Tomova, D.; Bilyarska, L.; Eliyas, A.; Petrov, L., Photocatalytic properties of TiO₂ modified with platinum and silver nanoparticles in the degradation of oxalic acid in aqueous solution. *Appl. Catal. B* **2006,** *63*, 266-271.

62. Kozlova, E. A.; Lyubina, T. P.; Nasalevich, M. A.; Vorontsov, A. V.; Miller, A. V.; Kaichev, V. V.; Parmon, V. N., Influence of the method of platinum deposition on activity and stability of Pt/TiO₂ photocatalysts in the photocatalytic oxidation of dimethyl methylphosphonate. *Catal. Communi.* **2011,** *12*, 597-601.

63. Hou, W.; Dong, X.; Li, Y.; Zhang, H.; Xu, L.; Tian, Y.; Jiao, A.; Chen, M., Ultraviolet laser beam-assisted one-step synthesis of clean PtPd nanoarchitectures with excellent electrocatalytic properties for direct methanol fuel cells. *Mater. Chem. Phys.* **2019,** *221*, 409-418.

64. Vovk, E. I.; Kalinkin, A. V.; Smirnov, M. Y.; Klembovskii, I. O.; Bukhtiyarov, V. I., XPS Study of Stability and Reactivity of Oxidized Pt Nanoparticles Supported on TiO₂. *J. Phys. Chem. C* **2017,** *121*, 17297-17304.

65. Smirnov, M. Y.; Kalinkin, A. V.; Bukhtiyarov, V. I., X-ray photoelectron spectroscopic study of the interaction of supported metal catalysts with NOₓ. *J. Struct. Chem.* **2007,** *48*, 1053-1060.

66. Yu, L.; Shao, Y.; Li, D., Direct combination of hydrogen evolution from water and methane conversion in a photocatalytic system over Pt/TiO₂. *Appl. Catal., B* **2017,** *204*, 216-223.

67. Melián, P. E.; López, C. R.; Santiago, D. E.; Quesada-Cabrera, R.; Méndez, J. A.; Rodríguez, J. M.; Díaz, G. O., Study of the photocatalytic activity of Pt-modified commercial TiO₂ for hydrogen production in the presence of common organic sacrificial agents. *Appl. Catal., A* **2016,** *518*, 189-197.

68.   Xing, J.; Li, Y.; Jiang, H.; Wang, Y.; Yang, H., The size and valence state effect of Pt on photocatalytic H$_2$ evolution over platinized TiO$_2$ photocatalyst. *Int. J. Hydrogen Energy* **2014,** *39*, 1237-1242.

69.   Qamar, M.; Ganguli, A. K., Self-assembling behaviour of Pt nanoparticles onto surface of TiO$_2$ and their resulting photocatalytic activity. *Bull. Mater. Sci.* **2013,** *36*, 945-951.

70.   Sui, Y.; Liu, S.; Li, T.; Liu, Q.; Jiang, T.; Guo, Y.; Luo, J.-L., Atomically dispersed Pt on specific TiO$_2$ facets for photocatalytic H$_2$ evolution. *J. Catal.* **2017,** *353*, 250-255.

References pages 198

Chapter 6

Photodeposition of core-shell structured bimetallic nanodots on TiO$_2$ nanoparticles by UV laser

Table of contents

6.1 Introduction to photodeposition of bimetallic nanodots onto TiO₂ nanoparticles surface

Beside the monometallic nanoparticles (MNPs) that we have discussed in the previous chapters (Chapter 4 and Chapter 5), bimetallic nanoparticles (BNPs), composed of two different metal elements, have also attracted much attention from both scientific and technological viewpoints, due to potential unique electronic, optical, catalytic or photocatalytic properties that are absent in the coincident MNPs. The BNPs are expected to exhibit not only the combination of the properties of two individual metals but also new properties due to a synergy between the two metals.[1]

Photodeposition method is one of the widely used methods to prepare noble metal catalysts supported on semiconductors. The TiO₂-based MNPs have been successfully synthesized using photodeposition method, as shown in the previous chapters and also in other works.[2] However, only a few studies were reported for the preparation of supported bimetallic catalyst.[3-8] Significantly, the properties of the MNPs could be further improved by decorating with another metal to form bimetallic systems. Mostly the metal Au works as a size of the stable support due to its high reduction potential, so as to receive the decorations from other metals. In the following, we mainly introduce several works concerning BNPs synthesis using photodeposition method in terms of Au@M (M=Ag, Pd and Pt, etc.) structures.

Patra et al.[3] demonstrated that the Au@Ag core-shell structured nanoparticles (NPs) on TiO₂ support ((Au@Ag)-TiO₂)) could be synthesized by a sequential two-step photodeposition method. Firstly, the Au-TiO₂ NPs was prepared by photodeposition method, and the Ag⁺ ions were then photoreduced on the Au NPs in the same manner. The authors showed that their attempts to increase the density of nanometal clusters did not work out, they rather increased the size of the already formed particle . It was found that, compared to pure Au-TiO₂ NPs, the composite (Au@Ag)-TiO₂ doubled the solar water splitting activity with increasing light-absorption capacity, while the electronic structure of heterojunction between Au and TiO₂ remained unchanged.

In 2016, Ren et al.[9] synthesized PdAu alloyed NPs on TiO₂ nanowires using a one-step photodeposition method. The advantage of this method is that the Pd/Au atomic ratio in alloyed NPs could be adjusted by just changing the Pd²⁺/Au³⁺ratio in the precursor solution.

207

According to the HRTEM, the lattice fringe of metal NPs is 0.23 nm, which lies between the (111) lattice spacing of Pd (0.22 nm) and that of Au (0.24 nm). The fairly uniform elemental distribution of both Au and Pd in the whole particles also indicates the formation of the alloyed structure, rather than a core-shell structure.

Tanaka et al.[10] applied a two-step photodeposition method using a Hg lamp to synthesize a core (Au)-shell (Pd) structured NPs on TiO₂ surface (Figure 6.1). By controlling the weight ratio of Pd, the author succeeded in obtaining a varying thickness of Pd shell on the Au core. The author suggested that the thickness control of the Pd shell was very important for both a satisfactory cocatalyst effect and absorption due to SPR of Au NPs.[10] Using the same two-step photodeposition method, Jones et al.[11] confirmed the formation of core-shell structured Au@Pd NPs on TiO₂, with the controlled deposition of one and two monolayers (ML) equivalent of Pd onto Au NPs. The author indicated that no evidence of isolated Pd or Au NPs were found on the surface of TiO₂.[11]
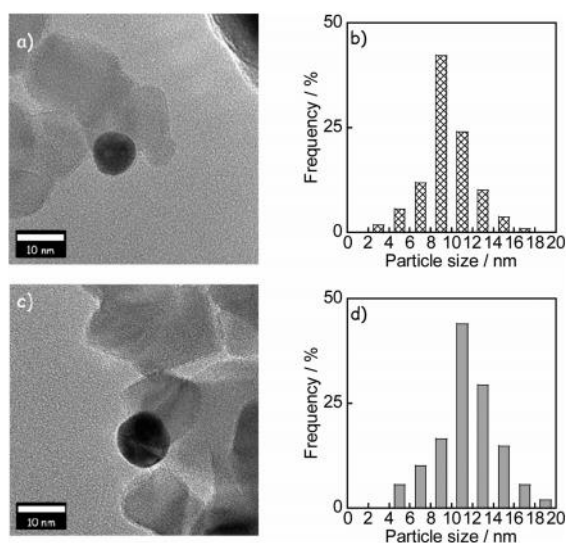
Figure 6.1 TEM images and size distributions of (a, b) Au-TiO₂ and (c, d) (Au@Pd)-TiO₂. [10]

Au-core@Pt-shell bimetallic clusters have been loaded on the surface of TiO₂ in a highly dispersed state by a two-step deposition method consisting of the Au impregnation-deposition and the subsequent Pt photodeposition.[8] It was found that the mean size of the metal particle increases after the Pt photodeposition, whereas it was apparent that the number density of metal particles hardly changed, which suggested that Pt deposits were mainly on the Au sites of Au-TiO₂ NPs.

In addition to Au acting as the core, the other noble metals, for instance, Pt, could also work

as a core site. Han et al.[7] reported a stable Pt–Ag alloy supported on TiO_2. It was confirmed that the photodeposition process led to the site-specific deposition of metallic Ag domain on Pt particles. In this regard, the site-specific deposition of metallic Ag domain on the surface of Pt particles.

Here in this chapter, a two-step photodeposition method will be introduced to synthesize Au-M (M = Ag, Au, Pd and Pt) core-shell NPs on the surface of TiO_2. Different from the normally used UV lamp as light source, we will choose UV laser (364.8 nm) to initiate the photodeposition process in a cuvette setup. In principle, metallic Au must first be deposited on the surface of TiO_2, followed by photodeposition of the other metal on Au-TiO_2 in the second step. Because the formed Au particles serve as a sink of photoinduced electrons due to its high work function, metal ions M^{n+} (n = 1, 2, 3, 4) are reduced and deposited on the Au particle surface in the second photodeposition process, forming core-shell structured BNPs (Au@M) on TiO_2.

6.2 Experimental methods

The photodeposition of core-shell type bimetallic nanoparticles (BNPs) is performed in the cuvette setup using a two-step deposition method. The semiconductor supports are TiO$_2$ polyhedrons all along this chapter, and the core in the core-shell structured part is Au, thanks to high reduction potential. The reaction solution is prepared by mixing an already made TiO$_2$ aqueous solution and freshly prepared KAuCl$_4$ under Ar, then the oxygen-free hole scavenger methanol (50 vol. %) is added to the aqueous solution with a pH adjusted at 3 using nitric acid (pH=1). The solution is continuously stirred at a speed of 300 rpm by a magnetic stirrer in a sealed cuvette capped by rubber septum. All the experiments are performed at room temperature. The applied power and illumination time are respectively 50.8 mW and 4 min. The previous work in Chapter 5 has confirmed that all the gold precursor is completely consumed during this exposure process. Then, a given amount of the other metal precursor (final concentration of 0.5 mM AgNO$_3$, 0.5 mM KAuCl$_4$, 0.5 mM Na$_2$PdCl$_4$ and 0.2 mM H$_2$PtCl$_6$ in the final mixture solution) is added into the solution for the second photodeposition. The power and illumination time are applied at 50.8 mW and 4 min, the same as for the gold photodeposition process.

The TEM grid preparation is performed according to the following procedures: The solution is sonicated for 10 min to disperse the nanoparticles, and then one drop is cast on a TEM grid (pre-activated by UV light, carbon film face up). A paper tissue can help absorb the liquid from the carbon film side to the back side of the grid, which allows only the liquid to pass through and leaves the nanoparticles on the top side. Two or more nitric acid drops (at pH 3) are also cast, to wash away the remaining unreacted metal salts if any. The TEM samples are immediately prepared after both the first and the second photodeposition processes.

6.3 Results and discussions

6.3.1 Photodeposition of Au on Au-TiO₂

In the first part, we used this method to regrow some gold on the pre-existing gold nanodots of the Au-TiO₂ NPs. Au@Au-TiO₂ NPs were then synthesized using the two-step photodeposition method. The Janus yield of Au-TiO₂ NPs shown in Figure 6.2 based on the counting of at least 300 NPs remained nearly unchanged, from initial 49 % to 47%, which suggests that in the second step all the Au^{3+} ions are prone to be reduced on the existing Au site of the TiO₂, rather than on the pure surface of TiO₂.

Assuming the lately added gold precursor is completely consumed and reduced on the existing Au cores in the second step, and thus the eventual Au deposits form a hemisphere shape at the interface of TiO₂, after adding more gold precursor (0.5 µmol KAuCl₄) into the existing Au-TiO₂ NPs (with mean size of 15.5 (2.8) nm and in number of 3×10^{12} in 1 mL solution) in the second photodeposition step, we expect to obtain the metal size of 21.7 if c[Au^{3+}]=0.5 mM (see calculation procedure in Appendix 3, A3.2).
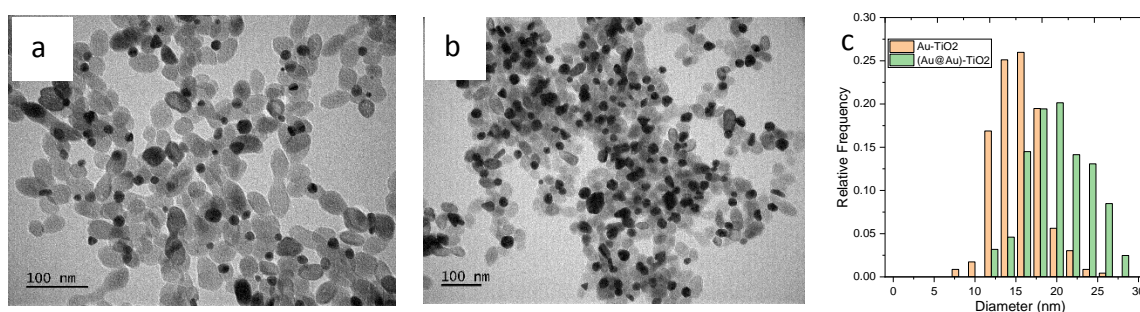
Figure 6.2 TEM images of Au-TiO₂ after (a) the first and (b) the second photodeposition process, and (c) their respective size distributions.

After the second photodeposition process, we finally obtained the Au-TiO₂ NPs with mean Au size of 19.8 (4.1) nm (Figure 6.2b), which is smaller than what we expect (21.7 nm). No more particles are observed below 10 nm size. The increase of standard deviation value may imply the difference of electron trapping ability among Au NPs of variable size made in the first photodeposition step.

6.3.2 Photodeposition of Ag on Au-TiO₂

Then we turn to deposit other metals, for instance, Ag, on the Au-TiO₂ nanoparticles. The TEM images of Au-TiO₂ is shown in Figure 6.4. The mean size of Au is 15.9 (3.4) nm, which is quite close to what we got in the case of Au@Au-TiO₂ (15.8 (1.9) nm), showing the good reproducibility. The Janus yield of Au-TiO₂ NPs is around 46 %.

In the second step, we add the silver precursor (0.5 µmol AgNO₃) into the existing Au-TiO₂ NPs (with mean size of 15.9 nm and in number of 3×10^{12} in 1 mL solution), we expect to get a metal size of 21.9 nm for the Au@Ag NPs, assuming that the Ag⁺ ions are completely reduced on the existing Au cores and thus forming a hemisphere shape at the surface (see Appendix 3, A3.2).

As shown in Figure 6.3b and c, after Ag⁺ ions are photoreduced on the Au-TiO₂ NPs, the mean size of metal NPs increase to 18.2 (3.4) nm, which is far smaller than our expected size. The Janus yield slightly increased after the second photodeposition (from 46 % to 53 %). The average shell thickness was calculated to be 1.2 nm (=(18.2 – 15.9)/2).
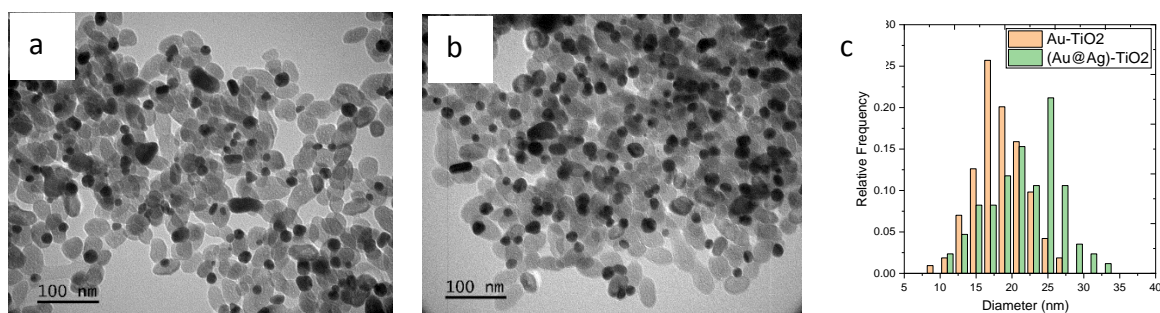
Figure 6.3 TEM images of (a) Au-TiO₂ and (b) (Au@Ag)-TiO₂, and (c) their metal size distributions.

More insight into the morphology of metal particles in the BNPs could be gained by EDS line-scanning and elemental mapping analysis (see Figure 6.4).
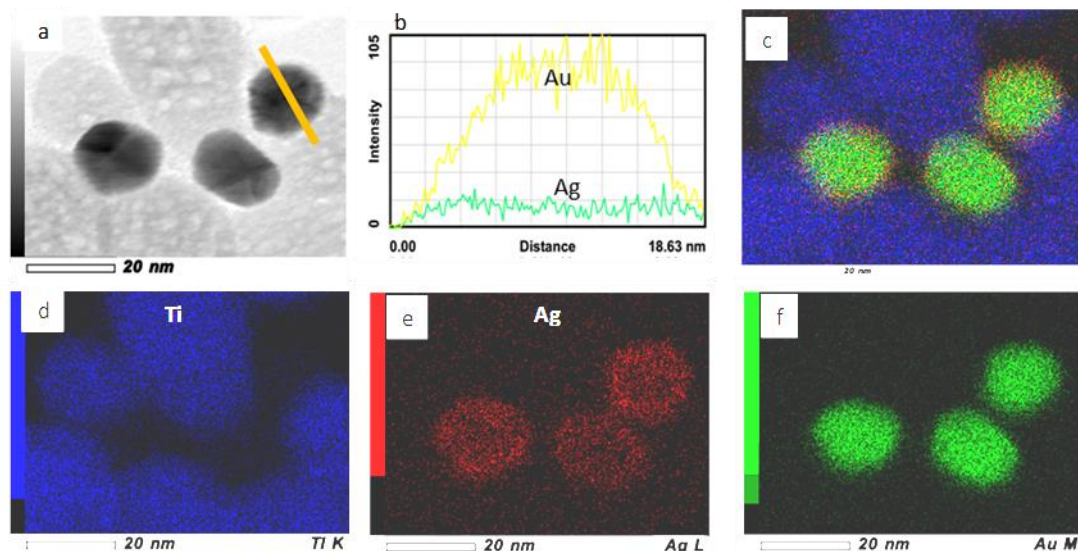
Figure 6.4 (a) STEM image of (Au@Ag)-TiO₂, (b) line-scan distribution profile and (c)-(f) the representative EDS mapping images.

Figure 6.4a shows three representative metal nanoparticles deposited on the surface of TiO₂. The line scans results (Figure 6.4b) illustrate that the intensity contribution of Au increases from the edge to the center of the metal particle, whereas Ag distribution keeps almost constant from the edge to the center of the selected particle, confirming a core-shell structure of the Au@Ag particle with Au as the core and Ag as the shell. Similar conclusions were also obtained from the elemental mapping of Au and Ag on the metal particle, and the results are compared in Figure 6.4c-f. The clear spatial correlation between Ag (red) and Au (green) signals revealed that Ag atoms are in close contact with Au particles. Additionally, the elemental map of Au had a higher atomic density in the center region (Figure 6.4f), while the elemental map of Ag exhibited a slightly larger distribution area with a sparse center and dense edges (see Figure 6.4e), again confirming the formation of an Au@Ag particle on TiO₂.

6.3.3 Photodeposition of Pd on Au-TiO₂

We then now discuss the photodeposition of Pd on Au-TiO₂ nanoparticles. TEM images of Au-TiO₂ made in the first photodeposition process are shown in Figure 6.5a. The mean size of the Au NPs is around 15.9 nm, and the Janus yield of Au-TiO₂ is 49%.

In the second photodeposition, we add Pd precursor (0.5 μmol Na₂PdCl₄) into the existing Au-TiO₂ NPs (with mean size of 15.9 (1.9) nm and in number of 3×10^{12} in 1 mL solution), expecting

to get a metal size of 21.3 nm for the Au@Pd NPs, assuming that the Pd^{2+} ions are completely reduced on the existing Au cores and thus forming a hemisphere shape at the surface (according to Appendix 3, A3.2).
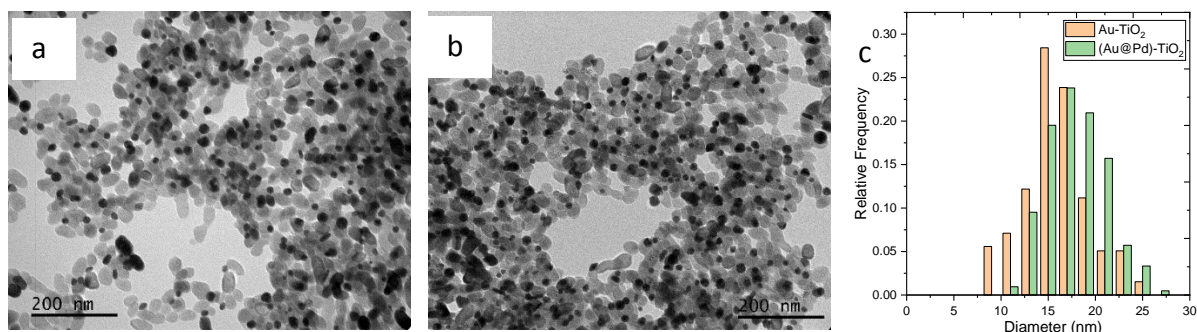
Figure 6.5 TEM image of (a) Au-TiO$_2$ and (c) (Au@Pd)-TiO$_2$, and (c) their metal size distributions respectively.

After the second deposition process, the Janus yield of metal-TiO$_2$ NPs has slightly increased from 49 % to 53 %, indicating that most of Pd are reduced onto the Au part on the surface of TiO$_2$ (Figure 6.5b). The mean size of the metal particle after second deposition is 17.6 (3.5) nm, which is slightly smaller than the expected value (21.3 nm). We attributed the difference to the formation of larger Pd aggregates which consumed much of the Pd precursor. The average shell thickness was calculated to be 0.9 nm ((17.6-15.9)/2).

We also performed the line-scanning and EDS elemental mapping analysis on the (Au@Pd)-TiO$_2$ NPs (Figure 6.6).
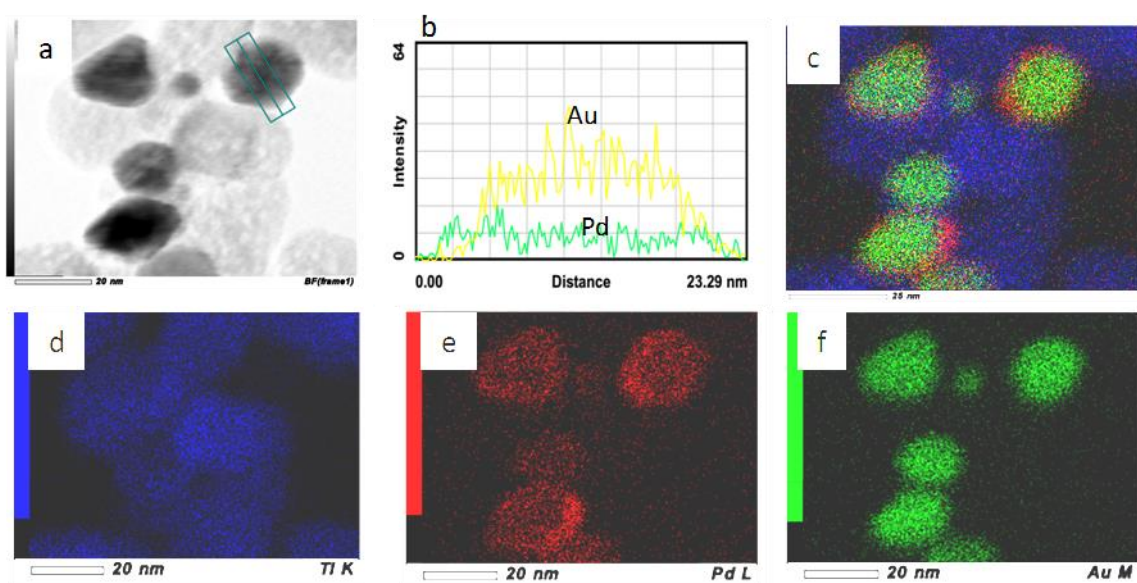
Figure 6.6 (a) STEM image of (Au@Pd)-TiO$_2$, (b) line-scan distribution profile and (c)-(f) the representative EDS mapping images.

Figure 6.6a shows three relative large and one small metal nanoparticles deposited on the

surface of TiO$_2$. The line scans results (Figure 6.6b) show that the intensity contribution of Au increases from the edge to the center of the metal particle, whereas Pd distribution follows an up-down trend from the edge to the center of the selected particle, this is in line with the results of the elemental mapping, showing that the center region reveals a high atomic density of Au (Figure 6.6f) and sparse density of Pd, while Pd owns dense edges in the map (Figure 6.6e). All the data above have confirmed a core-shell structure of the Pd-Au particle with Au as the core and Pd as the shell. Note that in certain edges of Pd (Figure 6.6c and e), some are brighter than others, exhibiting non-uniform distribution around the Au core. When there is a large lattice mismatch (> 3 %), the second material will exhibit anisotropic growth on a seed particle to produce multicomponent heterojunctions.[12] The nonuniform distribution of Pd element may be due to the larger mismatch (4.5 %) of lattice constants between Au (a = 4.07) and Pd (a = 3.89).

6.3.4 Photodeposition of Pt on Au-TiO₂

The last test to be performed is the photodeposition of Pt on Au-TiO$_2$ NPs. TEM images of Au-TiO$_2$ before and after the second photodeposition process were shown in Figure 6.7a and b, respectively.

In the second photodeposition, we add the Pt precursor (0.2 µmol) into the solution of Au-TiO$_2$ NPs, expecting to get a metal size of 18.4 nm for the Au@Pd NPs, assuming that the Pt^{4+} ions are completely reduced on the existing Au cores and thus forming a core-shell structured hemisphere shape at the surface.
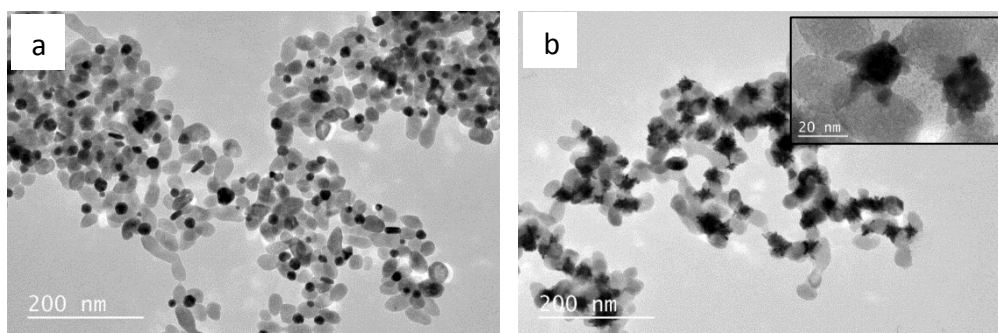
Figure 6.7 TEM images of (a) Au-TiO₂ and (b) (Au@Pt)-TiO₂ nanoparticles; inset shows magnified Au@Pt nanoparticles.

Interestingly, we failed to obtain a core-shell structured metal NPs with a fine shell around the

core as in the previous cases; instead, we got a much rougher system with star-like shapes. The magnified TEM image in Figure 6.7b clearly shows that Pt nanoparticles formed clusters, mainly around the Au NPs deposited on the surface of TiO$_2$. Fernando et al.[13] reported that this is due to the lattice mismatch between the (111) planes of Au and Pt is 5.3 % which leads to the anisotropic growth of Pt NPs on the Au cores. After initial nucleation and growth, Pt seeds themselves could act as seeds for further deposition of Pt, leading to clusterlike structures.[13] It is highly expected that the hybrid nanoparticles in this clusterlike morphology give rise to a better catalytic activity due to its relatively high specific surface area.

An XPS study was then performed to probe the surface chemistry of the metal NPs on the TiO$_2$. Figure 6.8 shows the high-resolution XPS spectra of (Au@Pt)-TiO$_2$ NPs obtained within the binding energy region of 537-528 eV for O1s, 68-90 eV for the Au4f and Pt4f elements. On the left-hand side of Figure 6.8 (a) (c) are recorded before any etching process while (b) (d) were etched for 6 s. Let's first note, besides the presence of titanium and oxygen, both gold and platinum are detected on the sample.
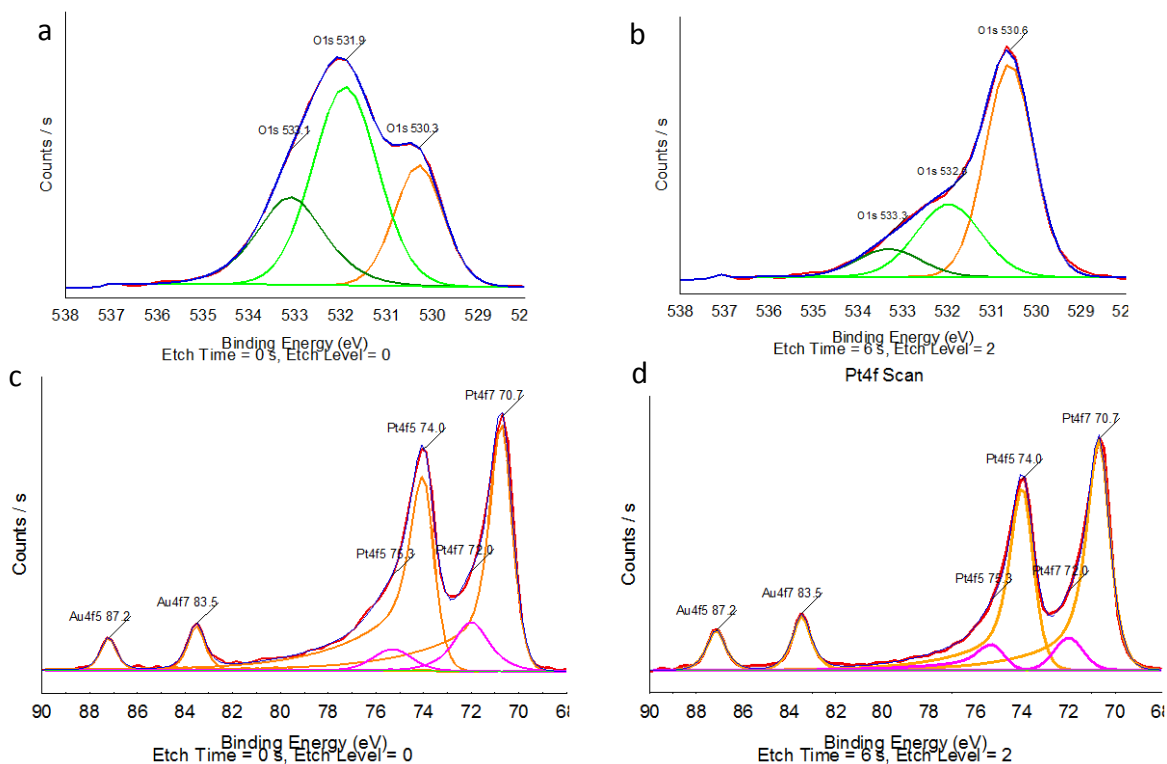
Figure 6.8 XPS spectra of Ti$_{2p}$, O$_{1s}$, Au$_{4f}$ and Pt$_{4f}$ in the (Au@Pt)-TiO$_2$ nanoparticles (a) (c) before and (b) (d) after 6 s of etching.

The O 1s peaks located at binding energies 530.3$\pm$ 0.2 eV in all samples correspond to the

lattice oxygen in TiO₂. These peaks are polluted with strong asymmetric contributions at higher binding energies ascribed to oxygen in surface hydroxyl groups as well as pollution sources. This was effectively confirmed after the etching which strongly decreased contribution due to the pollution (Figure 6.8b).

The fit of Au 4f identified two binding energy peaks, which are attributed to respectively the Au^0 4f$_{7/2}$ (83.5 eV) and Au^0 4f$_{5/2}$ (87.2 eV) electronic states,[14] and does not change whatever the etching time from 3 to 16s (Figure 6.9). The fit of Pt 4f revealed two dominant peaks at 70.7 and 74.0 eV, which are due to metallic Pt^0 4f$_{7/2}$ and Pt^0 4f$_{5/2}$, respectively.[15] These two peaks are slightly asymmetric on their left due to the contribution by Pt^{II} 4f$_{7/2}$ and Pt^{II} 4f$_{5/2}$ at 75.3 eV and 72.0 eV, respectively, which correspond to a thin layer of PtO on the surface of the Pt nanodots. This contribution tends to decrease with etching (compare Figure 6.8c and d).

Additionally, the etching process (from 0 to 16 s) also tends to show that the peak position show no change for Pt and gold (Figure 6.9). Furthermore, the ratio of the intensity between the Au and Pt peaks increases from 0.32 to 0.53 with etching times, indicating that more Au sites are exposed and excited to generate more photoelectrons, suggesting the core-shell structure of the (Au@Pt)on TiO₂ NPs.
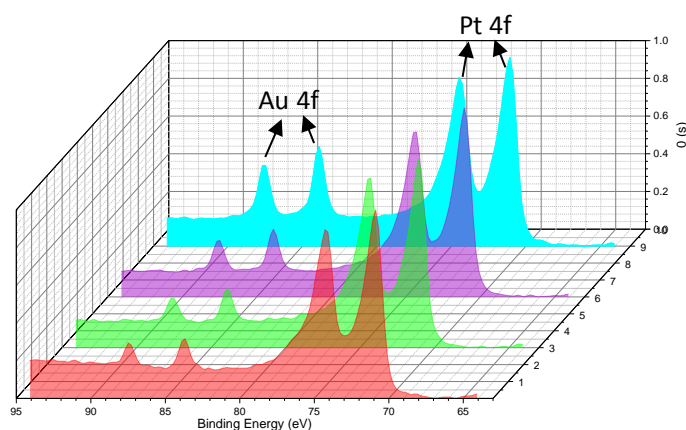
Figure 6.9 XPS spectra of Au4f and Pt4f in the (Au@Pt)-TiO₂ nanoparticles with etching times (upside direction).

It should be nonetheless mentioned that these core-shell structured objects were recently obtained by Naya et al.[16] coupling the deposition-precipitation method with a selective Pt photodeposition on the Au surface of the preformed Au-TiO₂ species to yield what they call Au (core)-Pt (shell) BNPs-loaded TiO₂ particles. In Au (core)@Pt (shell)-TiO₂, the mean Pt-shell thickness was controlled at an atomic layer level by the irradiation time. This approach

involves a drying step with a calcination at 400 ^{o}C for 4 h in air; approach we want to avoid in order to keep the TiO$_2$ size as small as it is, and elude any sintering between NPs.[8] It should be noted here that the photochemical deposition of Pt^{4+} on Au-TiO$_2$ provided Pt NDs with metallic binding energy analogues to those found in the literature.[17-22] as opposite to what was found in chapter 5. This offers new perspectives to this work developing new sets of experiments to understand the differences.

6.4 Conclusions

In this chapter, bimetallic core-shell structured (Au@M)-TiO$_2$ (M=Ag, Pd, Au, Pt) nanoobjects have been successfully synthesized by a simple two-step photodeposition method in the cuvette setup using UV laser. The metallic Au can be firstly deposited on the surface of TiO$_2$, followed by deposition of another metal on Au-TiO$_2$ in the second step. The techniques including TEM, XPS and EDS mapping have confirmed the existence of core-shell structure for most of them. For both the Au@Au and Au@Ag systems, a fine shell with around 1 nm thickness is formed on the Au core, due to their similar lattice constants between Ag and Au, while, in the case of Pd and Pt, the chosen conditions led to less defined shell in the case of Pd and a star-like configuration in the case of Pt. The extension from monometallic to bimetallic nanoparticles favours the investigations of design and synthesis of hybrid structured composites and the study of the potential applications in the future.

6.4 Conclusions

6.5 Bibliography

1.   Zaleska-Medynska, A.; Marchelek, M.; Diak, M.; Grabowska, E., Noble metal-based bimetallic nanoparticles: the effect of the structure on the optical, catalytic and photocatalytic properties. *Adv. Colloid Interface Sci.* **2016,** *229*, 80-107.

2.   Wenderich, K.; Mul, G., Methods, Mechanism, and Applications of Photodeposition in Photocatalysis: A Review. *Chem. Rev.* **2016,** *116*, 14587-14619.

3.   Patra, K. K.; Gopinath, C. S., Bimetallic and Plasmonic Ag-Au on TiO₂ for Solar Water Splitting: An Active Nanocomposite for Entire Visible-Light-Region Absorption. *ChemCatChem* **2016,** *8*, 3294-3311.

4.   Yang, D.; Feng, W.; Wu, G.; Li, L.; Guan, N., Nitrate hydrogenation on Pd–Cu/TiO₂ catalyst prepared by photo-deposition. *Catal.Today* **2011,** *175*, 356-361.

5.   Zhou, J.; Zhou, X.; Li, L.; Chen, Q., Enhanced liquid phase catalytic hydrogenation reduction of bromate over Pd-on-Au bimetallic catalysts. *Appl. Catal., A* **2018,** *562*, 142-149.

6.   Sun, J.; Han, Y.; Fu, H.; Qu, X.; Xu, Z.; Zheng, S., Au@Pd/TiO₂ with atomically dispersed Pd as highly active catalyst for solvent-free aerobic oxidation of benzyl alcohol. *Chem. Eng. J.* **2017,** *313*, 1-9.

7.   Han, Y.; Zhou, J.; Wang, W.; Wan, H.; Xu, Z.; Zheng, S.; Zhu, D., Enhanced selective hydrodechlorination of 1,2-dichloroethane to ethylene on Pt–Ag/TiO₂ catalysts prepared by sequential photodeposition. *Appl. Catal., B* **2012,** *125*, 172-179.

8.   Tada, H.; Suzuki, F.; Ito, S.; Akita, T.; Tanaka, K.; Kawahara, T.; Kobayashi, H., Au-Core/Pt-Shell Bimetallic Cluster-Loaded TiO₂. 1. Adsorption of Organosulfur Compound. *J. Phys. Chem. B* **2002,** *106*, 8714-8720.

9.   Ren, S.; Liu, W., One-step photochemical deposition of PdAu alloyed nanoparticles on TiO₂ nanowires for ultra-sensitive H₂ detection. *J. Mater. Chem. A* **2016,** *4*, 2236-2245.

10.   Tanaka, A.; Fuku, K.; Nishi, T.; Hashimoto, K.; Kominami, H., Functionalization of Au/TiO₂ plasmonic photocatalysts with pd by formation of a core-shell structure for effective dechlorination of chlorobenzene under irradiation of visible light. *J. Phys. Chem. C* **2013,** *117*, 16983-16989.

11.   Jones, W.; Su, R.; Wells, P. P.; Shen, Y.; Dimitratos, N.; Bowker, M.; Morgan, D.; Iversen, B. B.; Chutia, A.; Besenbacher, F.; Hutchings, G., Optimised photocatalytic hydrogen production using core-shell AuPd promoters with controlled shell thickness. *Phys. Chem. Chem. Phys.* **2014,** *16*, 26638-26644.

12.   Kwon, K.-W.; Shim, M., γ-Fe₂O₃/II–VI Sulfide Nanocrystal Heterojunctions. *J. Am. Chem. Soc.* **2005,** *127*, 10269-10275.

13.   Fernando, J. F. S.; Shortell, M. P.; Firestein, K. L.; Zhang, C.; Larionov, K. V.; Popov, Z. I.; Sorokin, P. B.; Bourgeois, L.; Waclawik, E. R.; Golberg, D. V., Photocatalysis with Pt-Au-ZnO and Au-ZnO Hybrids: Effect of Charge Accumulation and Discharge Properties of Metal Nanoparticles. *Langmuir* **2018,** *34*, 7334-7345.

14.   Wang, D.; Bi, Q.; Yin, G.; Wang, P.; Huang, F.; Xie, X.; Jiang, M., Photochemical Preparation of Anatase Titania Supported Gold Catalyst for Ethanol Synthesis from CO₂ Hydrogenation. *Catal. Lett.* **2018,** *148*, 11-22.

15.   Fang, W.; Qin, Z.; Liu, J.; Wei, Z.; Jiang, Z.; Shangguan, W., Photo-switchable pure water splitting under visible light over nano-Pt@P25 by recycling scattered photons. *Appl. Catal., B* **2018,** *236*, 140-146.

16.   Naya, S. I.; Miki, S.; Yamauchi, J.; Teranishi, M.; Kobayashi, H.; Tada, H., Au (Core)-Pt (Shell)

Nanocatalysts with the Shell Thickness Controlled at a Monolayer Level: Extremely High Activity for Hydrogen Peroxide Decomposition. *J. Phys. Chem. C* **2018,** *122*, 22953-22958.

17. Camposeco, R.; Castillo, S.; Mejía-Centeno, I.; Navarrete, J.; Marín, J., Characterization of physicochemical properties of Pd/TiO₂ nanostructured catalysts prepared by the photodeposition method. *Mater. Charact.* **2014,** *95*, 201-210.

18. Velmurugan, R.; Krishnakumar, B.; Swaminathan, M., Synthesis of Pd co-doped nano-TiO2–SO42– and its synergetic effect on the solar photodegradation of Reactive Red 120 dye. *Materials Science in Semiconductor Processing* **2014,** *25*, 163-172.

19. Espino-Estévez, M. R.; Fernández-Rodríguez, C.; González-Díaz, O. M.; Araña, J.; Espinós, J. P.; Ortega-Méndez, J. A.; Doña-Rodríguez, J. M., Effect of TiO₂-Pd and TiO₂-Ag on the photocatalytic oxidation of diclofenac, isoproturon and phenol. *Chem. Eng. J.* **2016,** *298*, 82-95.

20. Wang, J.; Rao, P.; An, W.; Xu, J.; Men, Y., Boosting photocatalytic activity of Pd decorated TiO₂ nanocrystal with exposed (001) facets for selective alcohol oxidations. *Appl. Catal., B* **2016,** *195*, 141-148.

21. López-Tenllado, F. J.; Hidalgo-Carrillo, J.; Montes, V.; Marinas, A.; Urbano, F. J.; Marinas, J. M.; Ilieva, L.; Tabakova, T.; Reid, F., A comparative study of hydrogen photocatalytic production from glycerol and propan-2-ol on M/TiO₂ systems (M=Au, Pt, Pd). *Catal. Today* **2017,** *280*, 58-64.

22. Hou, W.; Dong, X.; Li, Y.; Zhang, H.; Xu, L.; Tian, Y.; Jiao, A.; Chen, M., Ultraviolet laser beam-assisted one-step synthesis of clean PtPd nanoarchitectures with excellent electrocatalytic properties for direct methanol fuel cells. *Mater. Chem. Phys.* **2019,** *221*, 409-418.

Conclusions and Perspectives

The goal of my thesis is :(1) to photochemically reduce metal ions (Ag^+, Pd^{2+}, Au^{3+} and Pt^{4+}) on the surface of TiO_2 in a microchannel or cuvette setup by a photodeposition method using UV laser at 364 nm, (2) to study the growth law of metal nanoparticles (NPs) during the photodeposition process, and (3)to control the photochemistry step in terms of generation of number of metal dots per TiO_2 particle.

In this context, I have accomplished the hydrothermal synthesis of TiO_2 NPs and controlled their size and shapes (Chapter 2). By adjusting the composition of a mixture of surface directing agents or pH of the reactant solution, TiO_2 NPs were prepared with a range of sizes and morphologies. Two types of laser deposition approach, including microchannel and cuvette setup, have been built to control the photodeposition process (Chapter 3). Specifically, the use of a high-intensity UV laser and well-controlled fluidic flow system in the microchannel setup provides accurate control of various physical parameters including, exposure intensity and time, which are important in the growth law of metal NPs. A model is proposed to predict the growth behaviour of metal particles on the surface of TiO_2 (Appendix 2). In Chapter 4, I succeeded in synthesizing Ag-TiO_2 heterodimers in both microchannel and cuvette setup. I determined that not only the concentration of the hole scavenger but also the pH have a strong influence on the number of dots on the TiO_2 surface. Higher pH values favor more nucleation sites and lead to multi Ag dots on each TiO_2 NP. High intensity and long exposure time result in better Janus yield and larger Ag size. The proposed growth model perfectly predicts the growth of Ag NPs. Other metal deposited TiO_2 NPs such as Pd-TiO_2, Au-TiO_2 and Pt-TiO_2 are also synthesized (Chapter 5). The effect of hole scavengers on the size and morphology of product particles is discussed. The growth of Au NPs generally follows the proposed growth model, while the growth of Pd or Pt NPs is not fitted by the proposed model; more study needs to clarify the results. In Chapter 6, I extend the topic of monometallic photodeposition to bimetallic photodeposition. Using Au-TiO_2 as core support, Ag, Pd, Au and Pt could be reduced on the Au site by a second photodeposition process, forming a core-shell structure attached to the surface of TiO_2. The uniformity of the shell element distribution depends on the lattice mismatch between the metal and Au.
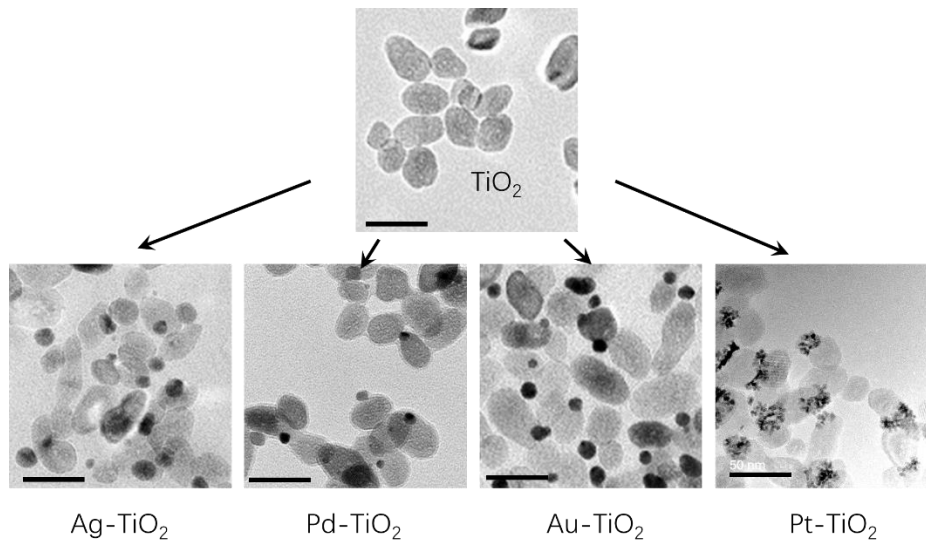
Figure 1 Evolution from TiO₂ to metal-TiO₂ heterodimers

For the perspective of the project, other metals in the valence state of 2 are prospected to be deposited on TiO$_2$, including Cu^{2+} or Ni^{2+} ions. The preliminary result of the photodeposition of Cu on TiO$_2$ is shown in Figure 2. However, some more work need be done to solve the stability problem since the formed Cu nanoparticles can easily be oxidized and dissolved into solution.
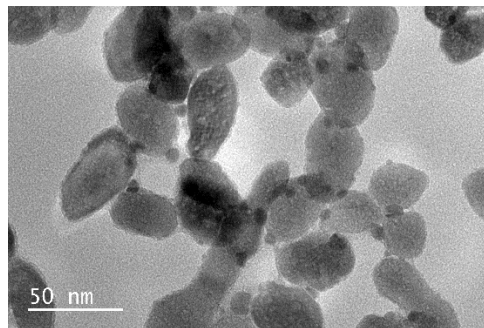
Figure 2 TEM image of Cu-TiO₂ nanoparticles made in cuvette setup. Experimental conditions are: c[Cu(NO₃)₂]= 1 mM, c[TiO₂]=5.5 mM, HCOONa as a hole scavenger, pH = 3, power 56.1 mW, exposure time 4 min, 6 uM polyvinylpyrrolidone as stabilizer to maintain Cu nanoparticles.

We expect that not only the electrons but also the holes generated by TiO$_2$ excitation can be used in the photodeposition process. Some preliminary results show that Ru^{3+} ions have been oxidized into RuO$_2$ in the photodeposition process (Figure 3), while more study remains to be performed as well.
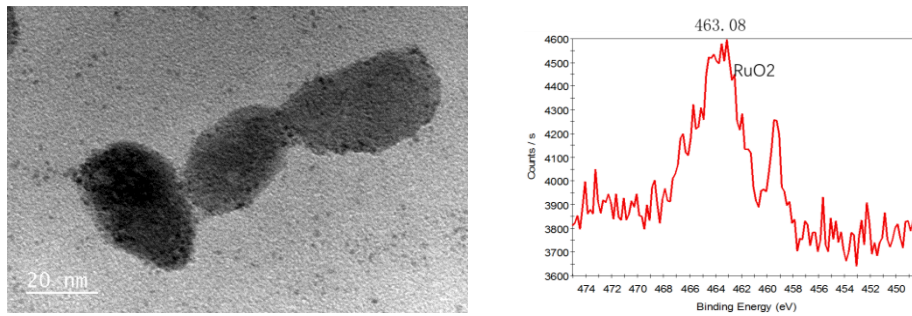
Figure 3 TEM images of RuO$_2$-TiO$_2$ nanoparticles made in cuvette setup and the corresponding XPS spectra. Experimental conditions are: c[RuCl$_3$] = 0.5 mM, c[TiO$_2$] = 5.5 mM, power 56.1 mW, exposure time 8 min, pH = 3, H$_2$O as a hole scavenger.

Beyond the above preliminary results, other research possibilities concerning photodeposition using UV laser also include, the simultaneous photodeposition of Ru^{3+} and metal ions on TiO$_2$ to form RuO$_2$-TiO$_2$-M type hybrid materials at the same time without any external sacrificial agents; also foreseen are the bimetallic or trimetallic photodeposition, for instance, (Pd@Ag)-TiO$_2$, (Au@Pd@Pt)-TiO$_2$, respectively. Some extension to photodeposition on other semiconductors such as ZnO is also planned. Last but not least，some catalytic performances should be tested in the near future.

Appendix 1

Optical absorption and laser heating of TiO$_2$ nanoparticle suspensions

A1.1 Optical absorption of the TiO$_2$ solution at 364 nm

For a small sphere of radius R<<λ_0 and of dielectric constant ε immersed in a medium of dielectric constant ε_m (with $\varepsilon_m \in \Re$ and $\varepsilon_m = n_m{}^2$), its absorption cross-section[1] is given by:

$$\sigma_{abs} = K.Im(p)$$

Where K is defined as $K = \dfrac{2\pi n_m}{\lambda_0}$, $Im()$ is an imaginary part and the polarizability

$$p = 4\pi R^3 \frac{\varepsilon - \varepsilon_m}{\varepsilon + 2\varepsilon_m} \; .$$

As the particle absorbs light, the dielectric constant presents an imaginary part, $\varepsilon = \varepsilon_1 + i\varepsilon_2 \equiv (n + ik)^2 = (n^2 - k^2) + i2nk$. After insertion and some calculation, we find:

$$\frac{\varepsilon - \varepsilon_m}{\varepsilon + 2\varepsilon_m} = \frac{(\varepsilon_1 - \varepsilon_m)(\varepsilon_1 + 2\varepsilon_m) + \varepsilon_2{}^2}{(\varepsilon_1 + 2\varepsilon_m)^2 + \varepsilon_2{}^2} + i\frac{3\varepsilon_2\varepsilon_m}{(\varepsilon_1 + 2\varepsilon_m)^2 + \varepsilon_2{}^2}$$

And then: $Im(p) = 12\pi R^3 \dfrac{\varepsilon_2\varepsilon_m}{(\varepsilon_1 + 2\varepsilon_m)^2 + \varepsilon_2{}^2}$ and $\sigma_{abs} = \dfrac{24\pi^2 n_m}{\lambda_0} R^3 \dfrac{\varepsilon_2\varepsilon_m}{(\varepsilon_1 + 2\varepsilon_m)^2 + \varepsilon_2{}^2}$

We use the wavelength dependence of refractive indices for $\lambda_0 = 364nm$ and T=25°C from the following website (https://refractiveindex.info/).

Application for TiO$_2$ NPs of diameter 20 nm in water

TiO$_2$: n=2.8877 ε_1=8.3386

TiO$_2$: k=0.019701 ε_2=0.11378

Water: n$_m$=1.3419 ε_m=1.8006 (k=0 assumed as k=5*10^{-9})

Then the absorption cross-section of a TiO$_2$ NP is $(\sigma_{abs})_{TiO_2} = 1.2548 \; 10^{-18} m^2$

To calculate the optical absorption of the laser within the microchannel, we suppose a diluted suspension of TiO$_2$ NPs with length L and cross section S (Figure A1.1).
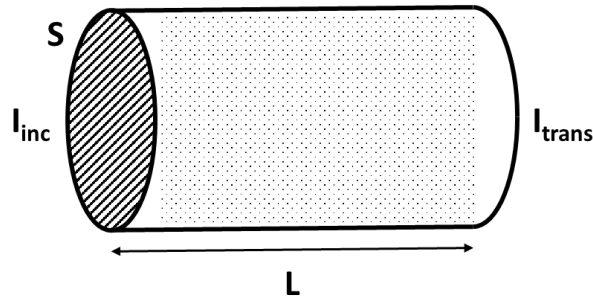
Figure A1.1 Illustration of laser pass through TiO$_2$ suspension with length L and cross section S.

On the one hand, $P_{abs} = S.I_{abs}$ and neglecting the scattering intensity, we get:

$I_{abs} = I_{trans} - I_{inc} = I_{inc}\left(1 - e^{\alpha L}\right) \approx \alpha L I_{inc}$ where α is the optical absorption of the solution by definition.

If V is a unit volume, we deduce $P_{abs} \approx S\alpha L I_{inc} = \alpha V I_{inc}$.

On the other hand, by definition of the absorption, $P_{abs} = N\sigma_{abs}I_{inc}$, where N is the number of absorbing NPs in the solution.

We deduce $\alpha V = N\sigma_{abs}$ and then $\alpha = \dfrac{N}{V}\sigma_{abs}$ where N/V is the number of NPs per unit volume of the flowing solution.

When it applies to the TiO$_2$ suspension:

Application to the solution of TiO$_2$ NPs

The concentration of TiO$_2$ in the global solution: 5.5 mM, which means 440 mg/L

Density of TiO$_2$: ρ = 3.9 g/cm^3.

The volume of a TiO$_2$ NP of diameter 20 nm: v=4.2* 10^{-24} m^3.

Mass of a NP: m=ρv=1.64*10^{-14} mg

Number of NPs per unit volume: N/V=440/m=1.64*10^{16} particles/l=2.7*10^{19} particles/m^3

Then the absorption of the TiO$_2$ solution at 364 nm is: $\left(\alpha_{TiO_2}\right)_{solution} = \dfrac{N}{V}\sigma_{abs} = 0.337\ cm^{-1}$

A1.2. Laser heating in a liquid layer of TiO$_2$ solution

Here is the scheme of calculation:

Considering the microchannel geometry, we analyze a thin layer of an absorbing solution of TiO$_2$ NPS sandwiched between two glass walls assumed as semi-infinite (Figure A1.2). We also assume the TiO$_2$ suspension to be sufficiently diluted (5.5mM) to assimilate the thermal

conductivity of the solution to that of water, i.e. $\Lambda_w \approx \Lambda_{water} = 0.61\ WK^{-1}m^{-1}$.
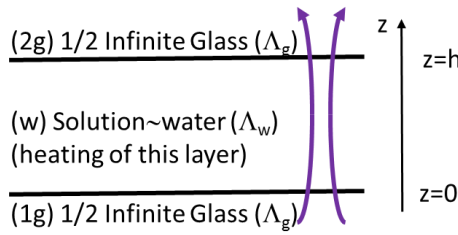
Figure A1.2 Illustration of a layer of solution between two glasses.

For a microchannel on thickness L = 600 µm, we find that: $\left(\alpha_{TiO_2}\right)_{solution} L = 2\ 10^{-2} << 1$, so that

laser attenuation in the channel is very weak and we can linearize $I_{abs}/I_{inc} \approx \alpha L$.

Moreover, as we have a flowing solution within the microchannel (with a typical mean velocity

v≈960 µm/s), we need to estimate the Peclet number (Pe) that compares the effects of the

flow ($v.\nabla T$) to the thermal diffusion ($\chi \nabla^2 T$):

$$Pe = vL/\chi$$

Where χ=1.43*10^{-7} m^2/s is the thermal diffusivity of water. The characteristic length L of the

heating in the flow direction is the beam waist ω$_0$=95 µm. Thus we get Pe=0.65, which is

slightly smaller than one and show that diffusion of temperature remains larger that flow

transport effects. Then, at a first order approximation, we neglect in the following these

possible flow effect. Looking for stationary solutions, heat equations are:

$$(\text{in 1g space})\ \left(\nabla_r^2 + \frac{\partial^2}{\partial z^2}\right) T_{1g}(r,z) = 0$$

$$(\text{in w space})\ \left(\nabla_r^2 + \frac{\partial^2}{\partial z^2}\right) T_W(r,z) + \frac{\alpha}{\Lambda_w}\frac{2P}{\pi\omega_0^2}G(r) = 0$$

$$(\text{in 2g space})\ \left(\nabla_r^2 + \frac{\partial^2}{\partial z^2}\right) T_{2g}(r,z) = 0$$

Where ∇_r^2 is the radial part of the Laplacian operator., the Fourier-Bessel decomposition will

be used as the resolution methods use considering the cylindrical symmetry. In the Fourier-

Bessel space, the temperature field is defined as: $T(k,z) = \int_0^\infty T(r,z) J_0(kr) r dr$, with $J_0(kr)$

the zeroth order Bessel function of the first kind. Heat equations in the Fourier-Bessel space

become:

$$(\text{1g})\ \left(\frac{\partial^2}{\partial z^2} - k^2\right) T_1(k,z) = 0$$

233

$$(w) \quad \left(\frac{\partial^2}{\partial z^2} - k^2 \right) T_2(k,z) + \frac{\alpha}{\Lambda_w} \frac{2P}{\pi \omega_0^2} G(k) = 0$$

$$(2g) \quad \left(\frac{\partial^2}{\partial z^2} - k^2 \right) T_3(k,z) = 0$$

Where $G(k) = \left(\frac{\omega_0}{2} \right)^2 e^{-k^2 \omega_0^2 / 8}$ corresponds to the Fourier-Bessel transform of the Gaussian

laser beam.

We impose the following interfacial boundary conditions:

1) continuity of the temperature fields,

$$T_2(k,z=0) = T_3(k,z=0)$$

$$T_2(k,z=h) = T_1(k,z=h)$$

and 2) continuity of the heat fluxes across the solution/microchannel interface,

$$\Lambda_w \left(\frac{\partial T_2}{\partial z} \right)_{(k,z=0)} = \Lambda_g \left(\frac{\partial T_1}{\partial z} \right)_{(k,z=0)} \quad \text{at z=0}$$

$$\Lambda_w \left(\frac{\partial T_2}{\partial z} \right)_{(k,z=h)} = \Lambda_g \left(\frac{\partial T_3}{\partial z} \right)_{(k,z=h)} \quad \text{at z=h}$$

Solutions of the heat equations are:

(1g) $T_{1g}(k,z) = A_{1g}(k) e^{kz}$

(w) $T_w(k,z) = A_w(k) e^{kz} + B_w(k) e^{-kz} + T(k)$

(2g) $T_{2g}(k,z) = B_{2g}(k) e^{-kz}$

With $T(k) = \frac{\alpha}{\Lambda_w} \frac{I(k)}{k^2}$ and $I(k) = \frac{2P}{\pi \omega_0^2} G(k)$, leading to $T(k) = \frac{\alpha}{\Lambda_w} \frac{P}{2\pi} \frac{e^{-k^2 \omega_0^2 / 8}}{k^2}$. The constants

of integration A(k) and B(k) are determined from the boundary conditions. For the water

solution layer, we get:

$$T_w(k,z) = T(k) \left[1 + \Phi_+(k) e^{kz} + \Phi_-(k) e^{-kz} \right] \quad \text{with}$$

$$\Phi_+(k) = \frac{-\left(1 + \Lambda_w/\Lambda_g\right) + \left(1 - \Lambda_w/\Lambda_g\right) e^{-kh}}{\left(1 + \Lambda_w/\Lambda_g\right)^2 e^{kh} - \left(1 - \Lambda_w/\Lambda_g\right)^2 e^{-kh}}, \quad \Phi_-(k) = \frac{\left(1 - \Lambda_w/\Lambda_g\right) - \left(1 + \Lambda_w/\Lambda_g\right) e^{kh}}{\left(1 + \Lambda_w/\Lambda_g\right)^2 e^{kh} - \left(1 - \Lambda_w/\Lambda_g\right)^2 e^{-kh}}$$

As $T(r,z)=\int_0^\infty T(k,z)J_0(kr)kdk$, we finally find in real space the following general solution for

the heating induced by the laser absorption in the TiO$_2$ flowing suspension:

$$T(r,z)=\frac{\alpha}{\Lambda_w}\frac{P}{2\pi}\int_0^\infty\frac{e^{-k^2\omega_0^2/8}}{k}\Big[1+\Phi_+(k)e^{kz}+\Phi_-(k)e^{-kz}\Big]J_0(kr)dk$$

If we want to estimate the largest overheating due to laser absorption, we need to estimate

$T\left(r=0,z=\dfrac{h}{2}\right)$, i.e., at the middle of the microchannel where the temperature is at its

maximum value, i.e.:

$$T(r,z)_{max}=T\left(r=0,z=\frac{h}{2}\right)=\frac{\alpha}{\Lambda_w}\frac{P}{2\pi}\int_0^\infty\frac{e^{-k^2\omega_0^2/8}}{k}\left[1+\Phi_+(k)e^{\frac{kh}{2}}+\Phi_-(k)e^{-\frac{kh}{2}}\right]dk$$

For $\Lambda_w=0.61\ WK^{-1}m^{-1}$, $\Lambda_g=1.38\ WK^{-1}m^{-1}$, ω_0=95 µm and h=600 µm, we find that

$$\frac{2\pi\Lambda_w}{\alpha P}T\left(r=0,z=\frac{h}{2}\right)=\int_0^\infty\frac{e^{-k^2\omega_0^2/8}}{k}\left[1+\Phi_+(k)e^{\frac{kh}{2}}+\Phi_-(k)e^{-\frac{kh}{2}}\right]dk=2.13$$

With $\alpha=33.7\ m^{-1}$, we finally get $T\left(r=0,z=\dfrac{h}{2}\right)\Big/P=0.0188\ K/mW$

and for a mean power P= 10 mW, we obtain $T\left(r=0,z=\dfrac{h}{2}\right)=0.188K$, which shows that laser

heating of the solution is very weak and can be neglected.

A1.3 Bibliography

1.   Bohren, C. F.; Huffman, D. R., *Absorption and scattering of light by small particles*. John Wiley & Sons: 2008.

Appendix 2

A growth prediction model of metallic nanodots photodeposited on TiO$_2$ nanoparticles

Table of contents

The developments of a growth prediction model will be performed with the example of silver nanodots photodeposited on TiO$_2$ nanoparticles, and then generalized to the photodeposition of other metals.

The sketch of the physical processes involved in the photodeposition is the following:

(a) Light absorption by TiO$_2$ induces production of electron-hole pairs in the bulk and at the surface of the particle.

(b) Electrons may recombine with holes, may be trapped on defects and may reach the surface to reduce metal ions, let us say silver ions, at the surface of TiO$_2$; the same may happen for the holes in TiO$_2$ with oxidation of a hole scavenger at the surface of TiO$_2$.

(c) Reduction of Ag$^+$ ions produces Ag^0 atoms and beyond a certain amount of Ag^0 atoms, an Ag^0 cluster is nucleated and grows at the surface of TiO$_2$ as a function of (i) the production of electrons related to the laser absorption and intensity, (ii) the Ag$^+$ concentration and (iii) the exposure time. Two growth mechanisms, (i) growth under a flux of metal atoms or (ii) growth by diffusion of metal atoms are possible, and the experimental measured growth laws will allow differentiating between the two. We will show that silver metal growth is compatible with the growth under a flux of metal atoms, considering time variation and scaling.

After obtaining a description of the growth of Ag^0 nanodots onto TiO$_2$ nanoparticles, we generalize the calculation to the reduction of other metallic ions.

A2.1 Methods to determine the concentration of silver atoms

The first stage consists in setting the different equations allowing the determination of the electron production due to light absorption in order to determine the Ag^0 concentration at the surface of TiO$_2$. In a second step, the Ag^0 concentration will be used to predict the growth of a silver nanodot deposited onto the TiO$_2$ surface.

A2.1.1 Kinetic equations, involved parameters, and hypotheses for calculations

A2.1.1.1 Kinetic equations in the photodeposition process

Figure A2.1 gives a schematic of the main aspects upon band gap excitation, which consists of two major processes[1].
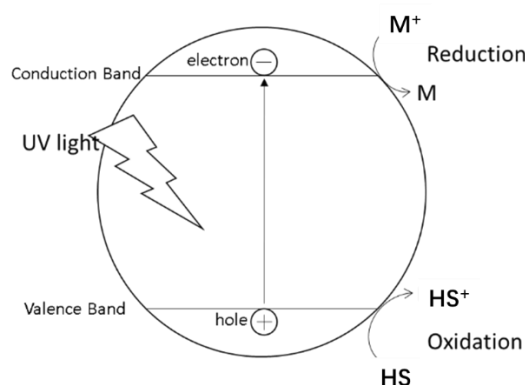
Figure A2.1. Band gap excitation process in a TiO₂ nanoparticle. Note that TiO₂ is, in fact, an indirect semiconductor. M: metal, HS: hole scavenger.

(a) Formation of charge carriers by photon absorption; they may cause a recombination process. Here, we neglect the charge carriers trapped in the bulk and at interface defects, because the number of these carriers is negligibly small compared to the total number of carriers produced when using a focused laser; this is related to the flux of photons (the beam intensity), which can be tremendously larger than that issued from any UV lamp. The primary step to be considered is the photonic generation of electrons and holes in TiO₂:

$$TiO_2 + h\nu \xrightleftharpoons[k_r]{g=\alpha I} TiO_2\left(e_{CB}^-, h_{VB}^+\right)$$

<div align="right">Equation A2.1</div>
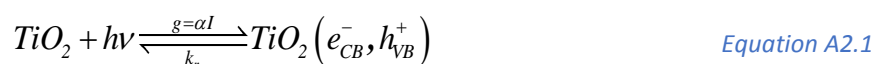
where g is the absorbed energy, expressed as the product of the colloid absorption coefficient and the beam intensity,[2] where α is the optical absorption and I is the light intensity. This charge carriers generation is immediately followed by the intra-particle electron-hole recombination at a rate k_r.

(b) Interfacial redox reactions take place at the TiO₂ surface. We mainly use methanol or formate as hole scavengers in our research. The oxidized product HS⁺ are dependent on different reaction conditions, which are not our focus point in this thesis. One could refer to literature concerning methanol[3-8] and formate[9-13] for the detailed reaction mechanism. The reaction scheme on the surface of TiO₂ is the following[14-16]:

$$Ag^+ + e^- \xrightarrow{\ k_{Ag}\ } Ag^0 \qquad\qquad \text{Equation A2.2}$$

$$HS + h^+ \xrightarrow{\ k_{HS}\ } HS^+ \qquad\qquad \text{Equation A2.3}$$

where k_{Ag} and k_{HS} are the silver atom production rate and the hole scavenging rate, respectively. We also neglect reverse reactions, which are negligible. Then, we can set the following equations[2]:

$$\frac{d[e]}{dt} = \left\{ D_e \Delta[e] + g - k_r[e][h] \right\}_{Bulk} - \left\{ k_{Ag}[e]\left[Ag^+\right] \right\}_{Interface} \qquad \text{Equation A2.3}$$

$$\frac{d[h]}{dt} = \left\{ D_h \Delta[h] + g - k_r[e][h] \right\}_{Bulk} - \left\{ k_{HS}[h][HS] \right\}_{Interface} \qquad \text{Equation A2.4}$$

$$\frac{d[Ag]}{dt} = \left\{ D_{Ag} \Delta[Ag] + k_{Ag}[e]\left[Ag^+\right] \right\}_{Interface} \qquad \text{Equation A2.5}$$

$$\frac{d\left[HS^+\right]}{dt} = \left\{ D_{HS^+} \Delta\left[HS^+\right] + k_{HS}[h][HS] \right\}_{Interface} \qquad \text{Equation A2.6}$$

D_i is the diffusion coefficient of species $i\left(e,\ h,\ Ag\ or\ HS^+\right)$, which are in bulk for e⁻ and h⁺, and at the TiO₂ surface for Ag⁰, called later on Ag, and oxidized hole scavengers (HS⁺). Δ is the Laplacian in two dimensions.

In order to find the metallic Ag atom concentration [Ag], which is a prerequisite to predict the growth of a silver nanodot, we need to calculate [e] and [h]. To do so, we first raise some insights on several constant values involved, as these equations are nonlinear.

A2.1.1.2 The values and orders of magnitude of the involved constants

(a) Diffusion of electrons within a TiO₂ sphere.

It is interesting to calculate the time required for a carrier to transit from the interior of a crystallite to its surface. The electron mobility μ in TiO₂ has been determined as $0.5\ cm^2V^{-1}s$ at room temperature[17]. Since

$$D_e = \frac{\mu kT}{e} \qquad\qquad \text{Equation A2.7}$$

where k, T are Boltzmann constant and temperature, respectively. Here e is the electron energy. This corresponds to a diffusion coefficient of $1.3\times10^{-6}\ m^2 s^{-1}$. For a TiO₂ sphere, Grätzel gave the expression of the average diffusion time of electrons:[17]

$$\tau_e = \frac{r_0^{\ 2}}{\pi^2 D_e} \qquad\qquad \text{Equation A2.8}$$

Thus, for a colloidal TiO₂ particle with a radius r_0=20 nm, the average diffusion time for electrons from the interior to the surface of the particle is $\tau_e = 32\,ps$. This value is also retrieved by Enright's work[18]. Instead of tens of picoseconds diffusion time for 20 nm TiO₂, Tamaki nonetheless measured a much shorter diffusion time,[19] *170 fs*, leading to a diffusion coefficient of $D_e = 2.4 \times 10^{-4}\,m^2 s^{-1}$. The discrepancy can be explained by the fact that only the electrons generated near the surface may reach the surface, while the rest of the electrons may be trapped in the bulk TiO₂ under classical exposure.

(b) Diffusion of holes within a TiO₂ sphere

Adopting a similar approach as mentioned above, it is possible to calculate a value for the hole mobility in TiO₂. Specifically, values of $\mu_h = 1.6 \times 10^{-3}\,m^2 V^{-1} s^{-1}$ and $D_h = 4 \times 10^{-5}\,m^2 s^{-1}$ are obtained for the hole mobility and diffusion coefficient, respectively[18, 19]. Using Equation A2.8 above with r_0=20 nm, we find diffusion time of holes $\tau_h = 1\,ps$.

(c) Electron-hole recombination time and rate

Performing femtosecond spectroscopy on bare TiO₂-P25 diluted in water, Ohtani et al. [20] measured the bulk electron-hole recombination rate: $k_r = (0.72 \pm 0.06) \times 10^{10}\,M^{-1} s^{-1}$. Ohtani et al. [20] also investigated the case of TiO₂-P25 loaded by Pt diluted in water, and they measured the bulk electron-hole recombination rate: $(k_r)_{load} = 0.18 \times 10^{10}\,M^{-1} s^{-1}$, which is a factor four smaller than the value for bare TiO₂-P25, showing a smaller recombination likely due to a faster decay of trapped electrons by their transfer to the Pt site.

(d) The concentration of hole scavengers and rate of hole scavenging at the surface of TiO₂ in the presence of methanol

1. <u>The concentration of hole scavengers at the surface of TiO₂ in the presence of methanol</u>

The direct reaction between positive holes and the hole scavenger (methanol for example) is only possible if the hole scavenger is strongly adsorbed on the TiO₂ surface, (discussed by Tamaki et al.[21]). The adsorbed hole scavenger species concentration $[HS]_{Interface}$ may be obtained by a Langmuir-Hinshelwood-type model for adsorption:

$$[HS]_{ads} = C_T \frac{K_{ads}[HS]_{Bulk}}{\left(1 + K_{ads}[HS]_{Bulk}\right)}$$, where $K_{ads}(M^{-1})$ is the adsorption equilibrium constant,

and $C_T(M)$ is the total concentration of active sites at the TiO₂ surface. $C_T = q.N_{HS}$, where q (g L^{-1}) is the fixed TiO₂ load of the solution and N_{HS} is the total moles of active sites for hole scavenging per unit mass of TiO₂ (mol g^{-1}).

For instance, Matthews et al.[22] measured on bare TiO₂-P25: $K_{ads} = 1118.1 M^{-1}$.

Measurements of N_{HS}, corresponding to the number of OH sites, reported in the literature for TiO₂-P25 are $N_{HS} = 2.74 \times 10^{-4}$ mol g^{-1} from reference[23] and $N_{HS} = 3.98 \times 10^{-4}$ mol g^{-1} for TiO₂-P25 from reference[24]. As these data are very close together, we will consider their mean value. We get: $N_{HS} = (3.36 \pm 0.62) \times 10^{-4}$ mol g^{-1}.

Considering the measured TiO₂-P25 value $K_{ads} = 1118.1 M^{-1}$ and an initial bulk methanol concentration $[HS]_{Bulk} = 12.34\ M$, we find that $K_{ads}[HS]_{Bulk} \gg 1$, and

$$[HS]_{ads} = C_T \frac{K_{ads}[HS]_{Bulk}}{\left(1 + K_{ads}[HS]_{Bulk}\right)} \approx C_T = qN_{HS}$$, which becomes independent of K_{ads} and

$[HS]_{Bulk}$ means that the surface of our TiO₂ NPs is totally saturated. Using our TiO₂ load $q = 0.439\ g/L$ (from $[TiO_2] = 5.5 \times 10^{-3} M$) and $N_{HS} = 3.36\ 10^{-4}$ mol.g^{-1}, we finally deduce:

$$[HS]_{ads} = qN_{HS} = (1.475 \pm 0.272) \times 10^{-4}\ M^{-1}.$$

2.   Rate of hole scavenging at the surface of TiO₂ in presence of methanol

For bare TiO₂ anatase of diameter 4.28 nm at pH=3.5, Dimitrijevic et al. [25] found a mean value:

$$k_{HS} = 1.4 \times 10^9 M^{-1} s^{-1}$$

(e) The concentration of Ag⁺ at the surface of TiO₂ and Rate of the equation

$$Ag^+ + e^- \xrightarrow{\ k_{Ag}\ } Ag^0$$
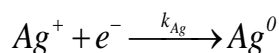
Silver ions also adsorb at the TiO₂ surface for electron transfer, even both positively charged at pH<5. The adsorbed silver ions concentration $\left[Ag^+\right]_{ads}$ may be obtained as well by a Langmuir-Hinshelwood-type model for adsorption:

$$\left[Ag^+\right]_{ads} = C_T \frac{K_{ads}\left[Ag^+\right]_{Bulk}}{\left(1 + K_{ads}\left[Ag^+\right]_{Bulk}\right)}$$

where $K_{ads}(M^{-1})$ is the adsorption equilibrium constant, and $C_T(M)$ is the total concentration of active sites for Ag^+ adsorption at the TiO₂ surface. $C_T = q. N_{Ag}$ where q (g L^{-1}) is the fixed TiO₂ load of the solution and N is the total moles of active sites per unit mass of TiO₂ (mol g^{-1}). In our experiments $q = 0.439\,g/L$ with a typical concentration [Ag⁺]=2 10^{-3} M

Using data measured by Kominami et al.[26], we deduce the number N_{Ag} of mole of Ag⁺/g=1.91x10^{-4} mol g^{-1}. Using our value $q = [TiO_2]M_{TiO_2} = 0.439\,g/L$ we finally get

$C_T = qN_{Ag^+} = 8.38 \times 10^{-5} M$. Kominami also measured K$_{ads}$= 205 M^{-1}.

With our typical concentration [Ag⁺]=2×10^{-3} M, we deduce

$$\left[Ag^+\right]_{ads} = C_T \frac{K_{ads}\left[Ag^+\right]_{Bulk}}{\left(1 + K_{ads}\left[Ag^+\right]_{Bulk}\right)} = 2.44 \times 10^{-5} M$$

Which leads to $\left[Ag^+\right]_{ads}/\left[Ag^+\right]_{Bulk} = 1.22 \times 10^{-2}\ (1\%)$ and

$$\left(\left[Ag^+\right]/[HS]\right)_{ads} = 2.44\ 10^{-5}/1.475\ 10^{-4} = 1.65 \times 10^{-2}\ (16.5\%)$$

<u>Rate of the equation</u> $Ag^+ + e^- \xrightarrow{\ k_{Ag}\ } Ag^0$

Mostafavi performed an experiment in methanol according to the following procedure [27] and found:

$$k_{Ag} = (2.6 \pm 0.6) \times 10^{10} M^{-1} s^{-1}$$

(f) Expression of *g*

g is the source term and corresponds to the energy deposited due to optical absorption, written as αI, where α is the absorption coefficient (in m^{-1}) and I is the beam intensity. The variation of the number density of photons as $\dfrac{dn}{dt} = \dfrac{\alpha(n)I}{\hbar\omega} +$ other terms [28] can help to understand this term, where $\hbar$ and ω indicate reduced Planck constant and Angular frequency, respectively; Since I is expressed in $J/(s.m^2)$ and $\hbar\omega$ is in J , then $g \equiv \dfrac{\alpha(n)I}{\hbar\omega}$, which represents the number of photons per unit volume. When working in Molar units, as for all species, then

$$g \equiv \frac{\alpha(n)I}{10^3 \mathbb{N} \hbar \omega}$$

where $\mathbb{N}$ is the Avogadro number.

Here is an example, considering the calculation of the optical absorption described in Appendix 1,

$$\alpha = \frac{\sigma_{abs}}{V_{TiO_2}} = \frac{1.2548 \times 10^{-18}}{4.19 \times 10^{-24}} m^{-1} = 3.0 \times 10^5 \, m^{-1}$$ where σ_{abs} and V_{TiO_2} are absorption cross

section and average volume of a TiO₂ nanoparticle, respectively.

$$I = \frac{2P}{\pi \omega_x \omega_y} = \frac{2 \times 10^{-2}}{\pi \times (55 \times 110).10^{-12}} W/m^2 = 1.0 \times 10^6 \, W/m^2 \quad \text{for} \quad P = 10 \, mW, \quad \text{where } \omega \text{ is}$$

the radius of the laser beam in *x* and *y* direction.

$$\hbar \omega = hc/\lambda = 6.62 \times 10^{-34} \times 3 \times 10^8 / (0.364 \times 10^{-6}) = 5.45 \times 10^{-19} \, J, \mathbb{N} = 6.02 \times 10^{23}$$

Then $g = \dfrac{\alpha(n)I}{10^3 \mathbb{N} \hbar \omega} = 9.6 \times 10^2 \, Ms^{-1}$

Table A2.1 summarizes the above parameters that fix the order of magnitude of the different processes involved for a TiO₂ –P25:

Term	values or range of the term
The diffusion time of electrons from interior to the surface	$\tau_e = 170 \, fs - 30 \, ps$
The diffusion time of holes from interior to the surface	$\tau_h = 1 \, ps$
Hole scavenging rate	$k_{HS} = 1.4 \times 10^9 \, M^{-1}s^{-1}$
Recombination rate in presence of metal load	$k_r = 0.18 \times 10^{10} \, M^{-1}s^{-1}$
Silver atom production rate	$k_{Ag} = (2.6 \pm 0.6) \times 10^{10} \, M^{-1}s^{-1}$
Source term *g*	$g = 9.6 \times 10^2 \, Ms^{-1}$ at *P*=10 mW

Table A2.1 Summary of several terms discussed above from (a) to (f).

A2.1.1.3 Hypotheses and simplifications for calculations

In order to simplify our reaction equations, several hypotheses and simplifications are made in the following.

(a) We first neglect the diffusion of charge carriers inside TiO₂.

When looking at the lifetime of the charge carriers in a TiO₂ sphere shown in Table A2.1, and if we consider the value $\tau_e = 170\,fs$, compared to the value of $\tau_r = 23\,ps$ and $\tau_h = 1\,ps$, we can assume that electron diffusion remains the fastest process inside a TiO₂ sphere.

Consequently, electron and hole profiles within a TiO₂ nanoparticle of diameter 40 nm can be assumed as homogeneous spatially at the larger time scales involved for growth processes. Thus the diffusion terms in Equation A2.3 and Equation A2.4, respectively, are considered as negligible.

Another consequence is that there is no need to make any difference between bulk and surface concentration of [e] and [h]. We just have to consider a thin two-phase "shell" below and above the interface, of a thickness corresponding to one molecular size on each side of the interface.

Then, the kinetics of electrons and holes, originally shown in Equation A2.3 and Equation A2.4, respectively, can be simply described by:

$$\frac{d[e]}{dt} = g - k_r[e][h] - k_{Ag}[e]\left[Ag^+\right]_{ads} \qquad \textit{Equation A2.10}$$

$$\frac{d[h]}{dt} = g - k_r[e][h] - k_{HS}[h][HS]_{ads} \qquad \textit{Equation A2.11}$$

(b) We assume that the concentration of $[Ag^+]_{ads}$ and $[HS]_{ads}$ are constant over the whole reaction.

We assume the $[Ag^+]$ and $[HS]$ are present in large quantities in the solution (thus no starving effect), so that $[Ag^+]_{ads}$ and $[HS]_{ads}$ may be assumed as constant and equal to their initial values, all over the photodeposition and the growth of silver dots.

Then we can set $k'_{Ag} = k_{Ag}\left[Ag^+\right]_{ads}$ and $k'_{HS} = k_{HS}\left[HS\right]_{ads}$ in order to reduce the order of reactions.

Consequently, equations can be written as:

$$\frac{d[e]}{dt} = g - k_r[e][h] - k'_{Ag}[e] \qquad \textit{Equation A2.12}$$

$$\frac{d[h]}{dt} = g - k_r[e][h] - k'_{HS}[h] \qquad \textit{Equation A2.13}$$

$$\frac{d[Ag]}{dt} = D_{Ag}\Delta[Ag] + k'_{Ag}[e]$$

<div align="right">*Equation A2.14*</div>

(c) We assume that the number of electron-hole pairs is conserved during the whole process.

As Boxall argued in his investigation of Photoelectrophoresis of colloidal semiconductors,[2, 29] the number of electron-hole pairs is thought to be conserved during the whole process, i.e.

$$\frac{d[e]}{dt} = \frac{d[h]}{dt}$$

<div align="right">*Equation A2.15*</div>

leading to $\qquad\qquad k'_{HS}[h] - k'_{Ag}[e] = 0$

<div align="right">*Equation A2.16*</div>

In a different context, Curran did the same approximation using slightly different arguments.[30] This approximation is coherent with the time scale associated to photodeposition, much larger than diffusion processes and even much larger than the kinetics of any molecular process associated to photo-excitation and relaxation on the one hand, and trapping-dissociating at TiO₂ defects on the other hand.

Consequently, $k'_{HS}[h] = k'_{Ag}[e]$ since bulk and interface do not matter anymore.

A2.1.2 Calculation of the electron concentration

As a result of the above simplifications, the equation to be solved for the electron concentration is:

$$\frac{d[e]}{dt} = g - \frac{k_r k'_{Ag}}{k'_{HS}}[e]^2 - k'_{Ag}[e]$$

<div align="right">*Equation A2.17*</div>

alternatively, after factorization

$$\frac{d[e]}{dt} = g - k'_{Ag}[e]\left(\frac{k_r}{k'_{HS}}[e] + 1\right)$$

<div align="right">*Equation A2.18*</div>

On the right hand of Equation A2.17, the first term *g* represents the rate of electrons produced by light, the second is related to the losses due to electron-hole recombination and the third to the consumption of electrons due to reaction with Ag⁺.

The equation can be straightforwardly solved analytically. Nonetheless, as our main actuation parameter is the light intensity, i.e. here *g*, it is quite relevant to discuss the solutions of this equation in terms of low and high field regime.

<div align="center">249</div>

A2.1.2.1 Electron concentration in the low field regime

At low field, i.e. for small values of g, the production of electrons is small as is the case of excitation by a UV lamp. Thus, the concentration of electrons can be described by

$$\frac{d[e]}{dt} = g - k'_{Ag}[e]$$

Equation A2.19

The low field regime also means $k_r[e]/k'_{HS} << 1$, indicating that recombination is negligible in this case.

The solution to Equation A2.19 is:

$$[e] = \frac{g}{k'_{Ag}}\left[1 - exp\left(-k'_{Ag}\,t\right)\right]$$

Equation A2.20

A2.1.2.2 Electron concentration in the high field regime

At high field, i.e. at large values of g, the production of electrons is significant as is the case of the excitation by a focused laser beam in a microchannel. The concentration of electrons can be described by

$$\frac{d[e]}{dt} = g - \frac{k_r k'_{Ag}}{k'_{HS}}[e]^2$$

Equation A2.21

The high field regime also corresponds to $k_r[e]/k'_{HS} >> 1$ which shows that recombination becomes the limiting factor in this case. The solution of Equation A2.21 is:

$$[e] = \sqrt{\frac{g k'_{HS}}{k_r k'_{Ag}}}\, tanh\left(\sqrt{\frac{k_r k'_{Ag}\, g}{k'_{HS}}}t\right)$$

Equation A2.22

A2.1.3 Calculation of the Ag⁰ concentration at the surface of the TiO₂ nanoparticle

The production of electrons is then used to produce silver atoms at the surface of TiO₂ nanoparticles. Consequently, we need to solve Equation A2.14

$$\frac{d[Ag]}{dt} = D_{Ag}\Delta_S[Ag]_{ads} + k'_{Ag}[e]$$

where Δ_S is the Laplacian in two dimensions and describes the diffusion of Ag atoms at the

surface of TiO₂, and D_{Ag} is the associated diffusion constant. Whether the diffusion part is significant or not depends on the time scale of Ag diffusion compared to that of reaction $Ag^+ + e^- \xrightarrow{k_{Ag}} Ag^0$. Liu found that the diffusion coefficient of Ag atom D_{Ag} follows an Arrhenius law (with an activation energy 1 eV at 500 K), and the value ranges from 5×10^{-17} to $1 \times 10^{-14} m^2 s^{-1}$.[31] For a TiO₂ particle with radius of 20 nm, the shortest diffusion time over half a hemisphere is calculated to be $t_{diff} = 4 \times 10^{-3} s$, which is tremendously large compared to the reaction time $\tau_{Ag} = \left(\left[Ag^+ \right]_{ads} k_{Ag} \right)^{-1} \approx 6.5 \times 10^{-7} s$ ($k_{Ag} = \left(2.6 \pm 0.6 \right) \times 10^{10} M^{-1} s^{-1}$, $\left[Ag^+ \right]_{ads} = 5.94 \times 10^{-5} M$). Thus the Ag diffusion at the surface of TiO₂ should be negligible compared to direct adsorption on a cluster. The Equation A2.14 to be solved is simplified as:

$$\frac{d\left[Ag \right]}{dt} = k'_{Ag} \left[e \right] \qquad \text{Equation A2.23}$$

where the electron concentration depends on either the low or the high field regime of production.

A2.1.3.1 Silver atom concentration at low field regime

At low field regime, $k_r \left[e \right] / k'_{HS} \ll 1$, we obtained from Equation A2.20, $\left[e \right] = \frac{g}{k'_{Ag}} \left[1 - exp\left(-k'_{Ag} t \right) \right]$, leading to Equation A2.24:

$$\frac{d\left[Ag \right]}{dt} = k'_{Ag} \left[e \right] = g \left[1 - exp\left(-k'_{Ag} t \right) \right] \qquad \text{Equation A2.24}$$

By defining a rescaled time $T = k'_{Ag} t$, the solutions are the following:

$$\begin{cases} \left[Ag \right]_{T \ll 1} \approx \left(\dfrac{g k'_{Ag}}{2} \right) t^2, & \text{at short time} \qquad \text{Equation A2.25} \\[2em] \left[Ag \right]_{T \gg 1} \approx gt, & \text{at large time} \qquad \text{Equation A2.26} \end{cases}$$

A2.1.3.2 Silver atom concentration at high field regime

At high field regime, $k_r \left[e \right] / k'_{HS} \gg 1$, we obtained from Equation A2.22, i.e.

$$[e] = \sqrt{\frac{gk'_{HS}}{k_r k'_{Ag}}} \tanh\left(\sqrt{\frac{k_r k'_{Ag} g}{k'_{HS}}} t\right), \text{ leading to Equation A2.27:}$$

$$\frac{d[Ag]}{dt} = k'_{Ag}[e] = \frac{k'_{HS}}{k_r}\sqrt{\frac{k_r k'_{Ag} g}{k'_{HS}}} \tanh\left[\sqrt{\frac{k_r k'_{Ag} g}{k'_{HS}}} t\right] \qquad \textit{Equation A2.27}$$

By defining a rescaled time $T = \sqrt{\dfrac{k_r k'_{Ag} g}{k'_{HS}}} t$, the solutions are the following:

$$\begin{cases} [Ag]_{T \ll 1} \approx \left(\dfrac{gk'_{Ag}}{2}\right) t^2 & \textit{at short time} \qquad \textit{Equation A2.28} \\[4mm] [Ag]_{T \gg 1} \approx \sqrt{\dfrac{k'_{HS} k'_{Ag} g}{k_r}} t & \textit{at large time} \qquad \textit{Equation A2.29} \end{cases}$$

At this stage of the calculation, we can make an important remark for the generalization to the deposition of other metals. By inserting the steady-state value of the production of electrons, either $[e]_{Steady} = \dfrac{g}{k'_{Ag}}$ at low field or $[e]_{Steady} = \sqrt{\dfrac{gk'_{HS}}{k_r k'_{Ag}}}$ at high field (obtained from setting $\dfrac{d[e]}{dt} = 0$ in Equation A2.19 and Equation A2.21), instead of its time variation, in the rate of production of [Ag], we directly get the late stage regime $T \gg 1$ of [Ag](t). The reason is related to the fact that steady state is closely reached at T=1.

As a short summary, in order to understand the photodeposition of silver, we first determined the rate of production of electrons due to the photoexcitation of TiO$_2$, and considered this electron production governed the rate of production of silver atoms at the surface of TiO$_2$.

$$\frac{d[e]}{dt} = g - \frac{k_r k'_{Ag}}{k'_{HS}}[e]^2 - k'_{Ag}[e]$$

$$\frac{d[Ag]}{dt} = k'_{Ag}[e]$$

In a second step, we solved these equations in the low and high excitation field regime, and we found that:

$$\text{At low field} \begin{cases} [Ag]_{T \ll 1} \approx \left(\dfrac{gk'_{Ag}}{2}\right) t^2, & \textit{at short time} \\[4mm] [Ag]_{T \gg 1} \approx gt, & \textit{at large time} \end{cases}$$

252

$$\text{At high field} \begin{cases} \left[Ag\right]_{T \ll 1} \approx \left(\dfrac{gk'_{Ag}}{2}\right)t^2 & \text{at short time} \\[4mm] \left[Ag\right]_{T \gg 1} \approx \sqrt{\dfrac{k'_{HS}\,k'_{Ag}\,g}{k_r}}\,t & \text{at large time} \end{cases}$$

Orders of magnitude

Considering a concentration $\left[Ag^+\right]_{ads} = 5.94\ 10^{-5}\ M$ often used in this work, we find that

the time scale of production of silver atoms $\tau = \dfrac{1}{k'_{Ag}}$ is ~ 1 μs. This time scale is considerably

short compared to any characteristic time t involved in the photodeposition experiments

from a few tens of milliseconds to tens of minutes, i.e. $t \gg \tau$. Thus, it appears that a very

large majority of our experiments will be concerned by the so-called late stage regime.

Moreover, using typical values of our experiments, we find that the electron concentration

at steady state is $\left[e\right]_{steady} = \sqrt{\dfrac{gk'_{HS}}{k_r k'_{Ag}}} = 4.2 \times 10^{-4}\ M$, and then $\dfrac{k_r}{k'_{HS}}\left[e\right]_{steady} = 3.6$ which does

not satisfy very well the high field condition $k_r\left[e\right]/k'_{HS} \gg 1$.

To conclude, the model of the production of the silver atom is not well justified by the high

field conditions, but we still obtain silver nanodot on TiO₂ nanoparticles in microchannel

setup (assumed at high field regime).

A2.2 Growth of an Ag⁰ deposit at TiO₂ surface

After solving the question of the production of silver atoms, we now come to consider the

growth mode of the silver atoms into a silver cluster. The calculation is inspired by the work

of Tavassoli on dew growth on solid substrates.[32] This means that we will not take into

account the effects of the atomic interactions between metallic nanodots and TiO₂

substrates as well as the exact nature of the interface and the mutual compatibility. As

displayed in Figure A2.2, we consider an immobile three-dimensional dot (here an Ag⁰ cluster)

deposited on a two-dimensional plane substrate (here the surface of TiO₂) on which the

produced Ag⁰ atoms, of volume v_a, may diffuse with the diffusion constant D_A or behave as a

sort of flux of matter; the size of the TiO₂ nanoparticle is supposed to be large compared to

that of the Ag nanodot in order to suppose that locally it can be assumed as flat at the scale

of the silver nanodot.
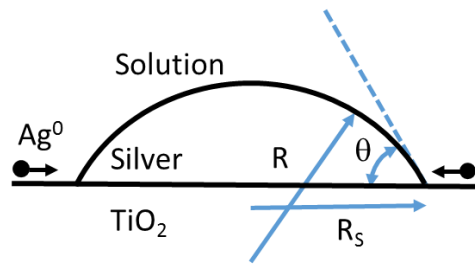
Figure A2.2 A scheme of an immobile silver dot at interface on the surface of TiO₂.

Then, the concentration of silver atoms at point r and at time t, $[Ag](r,t)$, is described by the following reaction-diffusion equation for $r \geq R_S$, where R_S is the nanodot radius at the surface of TiO₂:

$$\frac{\partial [Ag]_S (r,t)}{\partial t} = D_{Ag} \Delta_S [Ag]_S + k'_{Ag} [e]$$

$\qquad$ *Equation A2.30*

Δ_S is the Laplacian in two dimensions in circular symmetry and $[Ag]_S$ is a concentration expressed in $\dfrac{number\ of\ Ag^0\ atoms\ @surface}{surface\ unity}$. We finally find:

$$\frac{\partial [Ag]_S (r,t)}{\partial t} = D_A \frac{1}{r} \frac{\partial}{\partial r} \left(r \frac{\partial}{\partial r} [Ag]_S (r,t) \right) + k'_{Ag} [e]$$

$\qquad$ *Equation A2.31*

$R(t)$ is the radius of the immobile growing silver dot. The initial conditions are given by: $[Ag](r,t=0)=0$, which corresponds to the initial silver concentration and $R(t=0)=0$, thus indicating that the dot is not present at the beginning of the process. We consider an adsorption boundary condition at the perimeter of the silver dot, i.e. $[Ag](r=R,t>0)=0$ (meaning that a silver atom is automatically absorbed by the nanodot when close to it), and we assume that at infinity on the TiO₂ substrate, the concentration of silver atoms is finite and equal to 0.

Concentration gradients in the neighbourhood of the silver dot create a flux of silver atoms on the two-dimensional substrate. This flux feeds the silver dot, triggering its growth. Therefore, the volume increase rate of the silver dot is related to the total flux of atoms at its perimeter, and by mass conservation,

$$\Phi(t) = \frac{dV}{dt} \equiv \kappa R^2 \frac{dR}{dt}$$

$\qquad$ *Equation A2.32*

254

where the total flux is

$$\Phi(t) = v_a \left[2\pi R D_{Ag} \left. \frac{\partial [Ag]_s}{\partial r} \right|_R \right]$$

and corresponds to the concentration of atoms incorporated at the perimeter of the silver dot. κ is a dimensionless factor related to the contact angle of the silver dot on the TiO₂ surface.

Note nonetheless that experimentally, this is the radius R_s at an interface, which is measured. Then the volume of a spherical cap is given by

$$V = \frac{2\pi}{3} R_s{}^3 K(\theta)$$

where $K(\theta) = \dfrac{2 \sin^3 \theta}{\cos^3 \theta - 3 \cos \theta + 2}$. [33]

and,

$$\frac{dV}{dt} = 2\pi K(\theta) R_s{}^2 \frac{dR_s}{dt}$$

According to both Equation A2.34 and Equation A2.35, we thus find $\kappa = 2\pi K(\theta)$. As we experimentally measure R_s, we will use R to denote R_s in the following for the sake of simplicity.

Silver dot growth may happen according to two mechanisms, (i) silver atoms diffusion on the TiO₂ surface and aggregation or (ii) Constant flux boundary condition. Diffusion growth is not described in this work because the obtained growth exponents for the metallic nanodot is the low and high field regimes are far too large compared to those we obtained experimentally. Consequently, the following sections are dedicated to the description of growth by constant flux boundary conditions.

A2.3 Constant flux boundary condition

In this case, we impose a condition on the flux of the silver atoms, assuming that the total flux of atoms at the silver dot perimeter is constant. Therefore, $\Phi(t) = Q$ at $r = R$, where $\Phi(t) = \kappa R^2 \dfrac{dR}{dt}$ and Q, in m³s⁻¹, expresses the volume of Ag arriving at the perimeter of the silver dot per unit of time. Here we assume that the band gap excitation of TiO₂ produces a

flux of electrons, which react at the interface to produce a flux of Ag⁰. So, in this scheme, $\Phi(t)$ should be proportional to $\dfrac{d[Ag]}{dt}$.

The number of atoms N_a at the surface S of a TiO₂ particle is $[Ag]10^3 S v_a^{1/3} \mathbb{N}$ where all lengths are expressed in m. Then $[Ag]_S = [Ag]10^3 v_a^{1/3} \mathbb{N}$ and the flux is

$$\Phi = \frac{dV}{dt} = \frac{d}{dt}[v_a \times N_a] = \frac{d}{dt}\Big[v_a \times [Ag] \cdot 10 \cdot S v_a^{1/3} \cdot \mathbb{N}\Big] = \frac{d[Ag]}{dt}10 \cdot S v_a^{4/3}\mathbb{N} \equiv \Omega^2 \frac{d[Ag]}{dt}$$

where $\Omega = \sqrt{10^3 S_T v_a^{4/3}\mathbb{N}}$ is set as a volume.

Consequently: $\Phi(t) = \kappa R^2 \dfrac{dR}{dt} = \Omega^2 \dfrac{d[Ag]}{dt}$,   which leads to $\dfrac{\kappa R^3}{3} = \Omega^2 [Ag]$ with

$$[Ag] = k'_{Ag} \int_0^{[e]} [e]\, dt$$

Assuming $R(t=0) = [Ag](t=0) = [e](t=0) = 0$, we finally find:

$$R^3(t) = \frac{3\Omega^2}{\kappa}[Ag](t).$$

A growth by constant flux boundary conditions shows that growth is directly proportional to the time variation of the concentration [Ag].

A2.3.1 Remarks about this modelling at low field

Then, according to the previous equations, at low field, we get:

$$R^3(T \ll 1) \approx \frac{3\Omega^2}{\kappa}\left(\frac{g k'_{Ag}}{2}\right)t^2$$

$$R^3(T \gg 1) \approx \frac{3\Omega^2}{\kappa} g t$$

At first, at a short time, the expected behaviour is $R^3 \sim t^2$, which was never predicted nor observed in the past.[34] Moreover at large time, $R^3(T \gg 1)$ becomes independent of $[Ag^+]$, which is not consistent with our experimental results, likely because none of our laser experiments belongs to this low field regime. Finally, at large time $R \sim t^{1/3}$ which is currently measured in our experiments.

A2.3.2 Remarks about this modelling at high field

Then, according to the previous equations, at high field, we get:

$$R^3 \left(T << 1 \right) \approx \frac{3 \Omega^2}{\kappa} \left(\frac{g k'_{Ag}}{2} \right) t^2$$

$$R^3 \left(T >> 1 \right) \approx \frac{3 \Omega^2}{\kappa} \sqrt{\frac{k'_{HS} k'_{Ag} g}{k_r}} t$$

Still surprisingly is that at a short time $R \sim t^{2/3}$, while this behaviour was never predicted nor observed[34, 35] for the same reasons as in the low field case. Moreover, at large time $R^3 \left(T >> 1 \right) \sim \left(g \left[Ag^+ \right]_{ads} \right)^{1/2}$, which represents a new behaviour that deserves confrontation with the experimental results. We also retrieve the behaviour $R \sim t^{1/3}$ at large time, which is currently measured. As a final general remark, let us notice that up to now, we have assumed that $R(t=0)=0$ for the sake of simplicity (here the critical radius R_C is expected to be very small). If nonetheless, we consider critical nuclei R_C nucleated at short time, or further growth of an already present nanodot then we straightforwardly find:

$$R^3 (t) - R_C{}^3 = \frac{3 \Omega^2}{\kappa} \left[Ag \right] (t)$$

So we can account for an initial radius, critical or not, if required, by fitting the volume of the deposited dot instead of its radius.

A2.4 Generalization to the photoreduction of metallic ions Mⁿ⁺

In this case, we need to generalize the rate equation for [e], [h] and [Mⁿ⁺] (for metal) and solve:

$$\frac{d[e]}{dt} = g - k_r [e][h] - k'_M [e]^n \qquad \textit{Equation A2.36}$$

$$\frac{d[h]}{dt} = g - k_r [e][h] - k'_{HS} [h] \qquad \textit{Equation A2.37}$$

$$\frac{d[M]}{dt} = k'_M [e]^n \qquad \textit{Equation A2.38}$$

$$\frac{d\left[HS^{+}\right]}{dt} = k'_{HS}\left[h\right]$$

<div align="right">Equation A2.39</div>

We suppose here that the electrons in the number of "n" ("n" indicates valence in M^{n+}) are transferred at the same time to the metallic ion. This constrains implies that the deposition yield should decrease with an increase of the reduction order. With the same hypotheses as for Ag, we find:

$$\frac{d\left[e\right]}{dt} = g - \frac{k_r k'_M}{k'_{HS}}\left[e\right]^{n+1} - k'_M\left[e\right]^n$$

<div align="right">Equation A2.40</div>

Which can be rewritten as:

$$\frac{d\left[e\right]}{dt} = g - k'_M\left[e\right]^n\left(\frac{k_r}{k'_{HS}}\left[e\right]+1\right)$$

<div align="right">Equation A2.41</div>

Where for Ag^+, n=1; for Pd^{2+} or Ni^{2+}, n=2; for Au^{3+}, n=3; for Pt^{4+}, n=4, etc. We have seen that using our different setups we may simplify the problem by considering either a low or a high field approximation. Moreover, considering estimations of time scales, we can even concentrate on the late stage regime, which can be simply retrieved by considering the steady-state production of electrons. We will use this scheme in the following.

A2.4.1 Generalization of photoreduction of metal ions at low field regime

For the low field regime, we have seen that $k_r\left[e\right]/k'_{HS} \ll 1$. Then the electron production is described by:

$$\frac{d\left[e\right]}{dt} = g - k'_M\left[e\right]^n$$

<div align="right">Equation A2.42</div>

Looking for the late time solution, we have seen that using the stationary solution $\left[e\right]_{Steady}$ allows retrieving the right late stage behaviour of [Ag]. Considering $\left[e\right]_{Steady}$, we get:

$k'_M\left[e\right]^n_{Steady} = g$, which means that $\frac{d\left[M\right]}{dt} = k'_M\left[e\right]^n = g$ and then $\left[M\right] = gt$.

Consequently, at low field, the late stage variation of the metallic dot is invariant with the reduction order of the reaction:

$$R^3\left(t \gg\right) = \frac{3\Omega^2}{\kappa}\left[M\right](t) = \frac{3\Omega^2}{\kappa}gt$$

<div align="right">Equation A2.43</div>

A2.4.2 Generalization of photoreduction of metal ions at high field regime

For the high field regime, we have seen that $k_r / k'_{HS}[e] \gg 1$. Then the electron production is described by:

$$\frac{d[e]}{dt} = g - \frac{k_r k'_M}{k'_{HS}}[e]^{n+1} \qquad \text{Equation A2.44}$$

Looking again for the late stage solution, we consider the stationary solution $[e]_{Steady}$ and get:

$$\frac{k_r k'_M}{k'_{HS}}[e]^{n+1} = g \qquad , \qquad \text{which} \qquad \text{means} \qquad \text{that} \qquad [e]^n = \left(\frac{gk'_{HS}}{k_r k'_M}\right)^{\frac{n}{n+1}} \qquad \text{and}$$

$$\frac{d[M]}{dt} = k'_M [e]^n = k'_M \left(\frac{gk'_{HS}}{k_r k'_M}\right)^{\frac{n}{n+1}} \text{, then } [M] = k'_M \left(\frac{gk'_{HS}}{k_r k'_M}\right)^{\frac{n}{n+1}} t$$

Consequently, at high field, the late stage variation of the metallic dot varies with the reduction order of the reaction:

$$R^3(t \gg) = \frac{3\Omega^2}{\kappa}[M](t) = \frac{3\Omega^2}{\kappa} k'_M \left(\frac{gk'_{HS}}{k_r k'_M}\right)^{\frac{n}{n+1}} t \qquad \text{Equation A2.45}$$

In conclusion, we expect the following high field late stage regime of growth depending on the reduction order of the metallic ions:

For n=1, M=Ag,

$$R^3(t \gg) = \frac{3\Omega^2}{\kappa}[Ag](t) = \frac{3\Omega^2}{\kappa} k'_{Ag} \left(\frac{gk'_{HS}}{k_r k'_{Ag}}\right)^{\frac{1}{2}} t = \frac{3\Omega^2}{\kappa} \frac{k'_{HS}}{k_r} \left(\frac{k_r k'_{Ag} g}{k'_{HS}}\right)^{\frac{1}{2}} t \sim g^{\frac{1}{2}} \left(k'_{Ag}\right)^{\frac{1}{2}} t \qquad \text{Equation A2.46}$$

For n=2, M=Pd,

$$R^3(t \gg) = \frac{3\Omega^2}{\kappa}[Pd](t) = \frac{3\Omega^2}{\kappa} k'_{Pd} \left(\frac{gk'_{HS}}{k_r k'_{pd}}\right)^{\frac{2}{3}} t = \frac{3\Omega^2}{\kappa} \frac{k'_{HS}}{k_r} \left(\frac{k_r k'_{pd} g^2}{k'_{HS}}\right)^{1/3} t \sim g^{\frac{2}{3}} k'^{\frac{1}{3}}_{Pd} t \qquad \text{Equation A2.47}$$

For n=3, M=Au,

$$R^3(t \gg) = \frac{3\Omega^2}{\kappa}[Au](t) = \frac{3\Omega^2}{\kappa} k'_{Au} \left(\frac{gk'_{HS}}{k_r k'_{Au}}\right)^{\frac{3}{4}} t = \frac{3\Omega^2}{\kappa} \frac{k'_{HS}}{k_r} \left(\frac{k_r k'_{Au} g^3}{k'_{HS}}\right)^{1/4} t \sim g^{\frac{3}{4}} k'^{\frac{1}{4}}_{Au} t \qquad \text{Equation A2.48}$$

For n=4, M=Pt,

$$R^3\left(t>>\right)=\frac{3\Omega^2}{\kappa}\left[Pt\right](t)=\frac{3\Omega^2}{\kappa}k'_{Pt}\left(\frac{gk'_{HS}}{k_rk'_{Pt}}\right)^{\frac{4}{5}}t=\frac{3\Omega^2}{\kappa}\frac{k'_{HS}}{k_r}\left(\frac{k_rk'_{pt}g^4}{k'_{HS}}\right)^{1/5}t\sim g^{\frac{4}{5}}k'_{Pt}{}^{\frac{1}{5}}t$$

<div align="right">Equation
A2.49</div>

This is these predictions that will be confronted with experiments with silver (n=1), palladium (n=2), gold (n=3) and platinum (n=4).

A2.5 Comparison to growth data from the literature

Very few publications describe the growth of metallic dots onto semiconductor nanoparticles. There were all obtained using a photo-excitation by a UV lamp over variable exposure time. In this section, we confront the corresponding growth laws measurements to our model in order to get some early insights on its validity.

A2.5.1 Photodeposition of silver and gold

Lu et al.[36] developed a photocatalytic strategy to synthesize colloidal Ag-TiO₂ nanorod composites with a single Ag nanoparticle on each TiO₂ nanorod. They used a 6 W UV lamp (wavelength 365 nm) positioned 10 cm from the reaction vial. They performed experiments where they vary the UV exposure time for three concentration of hole scavenger, here 1-hexadecanol, from zero to low (0.1 mM) and high (0.5 mM) concentration. Consequently, depending on the low or high field hypothesis, a law of the form $R\left(t>>\right)\propto t^{1/3}$ (low field) or $R\left(t>>\right)\propto\sqrt{\left[HS\right]_{ads}}\,t^{1/3}$ (high field). Results are presented in Figure A2.3.

As illustrated, the three growth laws verify well a 1/3 power law in time as expected from the model. Moreover, we also observe an increase of the growth rate with the concentration in hole scavenger as expected for the high field case but the consideration of just three concentrations prevent us from performing a reasonable fit.

<div align="center">260</div>
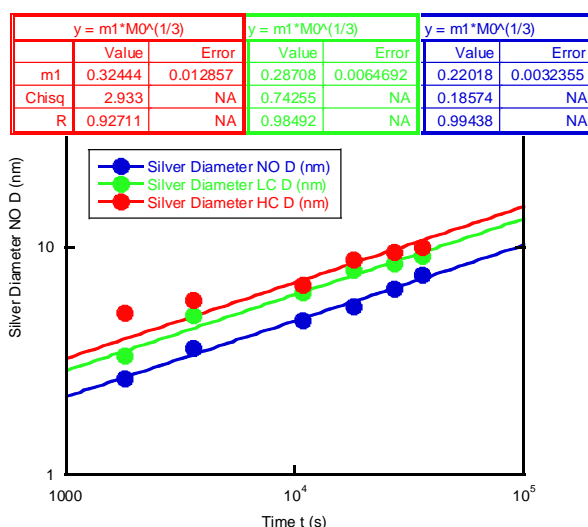
Figure A2.3 Silver diameter as a function of exposure time using three concentrations of 1- hexadecanol. Data are took from ref.[36]

Gold deposition on TiO$_2$ nanoparticles is very poorly documented. We just found one publication by Chang et al.[37] The experiment was performed using a 400 W mercury lamp with chloroauric acid as the gold precursor and commercially available TiO$_2$ from Degussa (P25). Figure A2.4 shows that a power law fit of the three only available data gives a temporal exponent 0.67, slightly far from the expected exponent of 1/3.
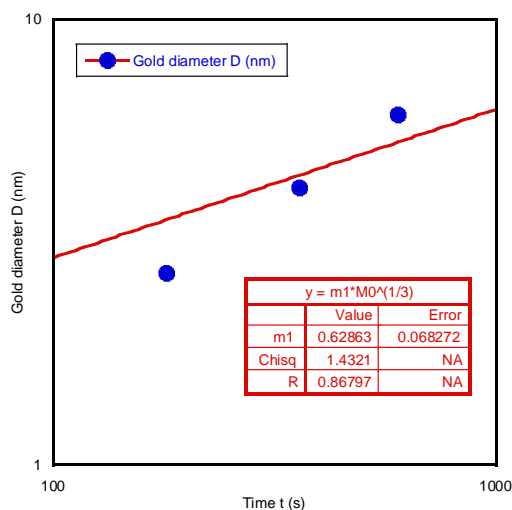
Figure A2.4 Gold diameter as a function of exposure time. Data are taken from ref.[37]

Gold photodeposition on II-VI semiconductors such as CdS and CdSe/CdS is slightly more documented. On the one hand, Carbone et al.[38] investigated the gold deposition on CdS and CdSe(core)/CdS(shell) nanorods using an ordinary UV lamp (2-3 mW/cm^2) with chloroauric acid as gold precursor and CHCl$_3$/Ethanol (90:10 v/v) as a hole scavenger; a chloroformic solution of HAuCl$_4$, (di-n-dodecyl)dimethylammonium bromide (DDABr), and dodecylamine (DDA) was dropwise injected. Figure A2.5 shows that a power law fit of the growth is highly

compatible with the expected exponent of 1 for the volume of the gold dot for both CdSe(core)/CdS(shell) and CdS nanorods substrates, respectively in red and in blue.
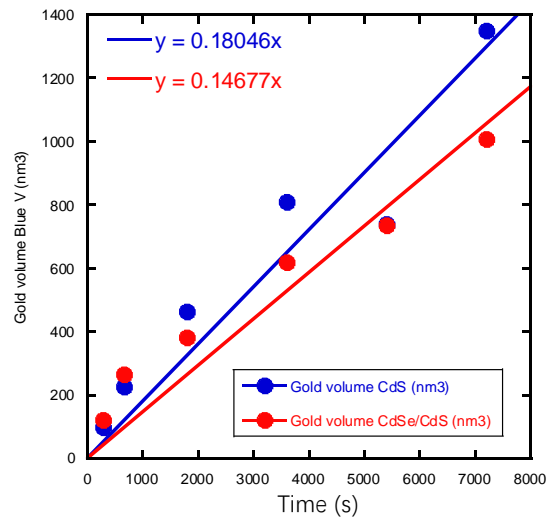
Figure A2.5 Gold diameter as a function of exposure time on both CdS and CdSe/CdS. Data are taken from ref[38].

On the other hand, Dermotière et al.[39] also investigated the gold deposition on CdSe/CdS nanorods using a UV lamp (1 mW/cm² and distance lamp/sample of 15 cm). The gold salt solution was prepared from a mixture of 10 mg of AuCl₃, 70 mg of dodecyldimethylammonium bromide (DDAB) and 50 mg of dodecylamine (DDA), dissolved in 10 mL of toluene. Figure A2.6 shows that a power law fit of the growth is highly compatible with the expected exponent of 1/3 for the diameter of the gold dot.
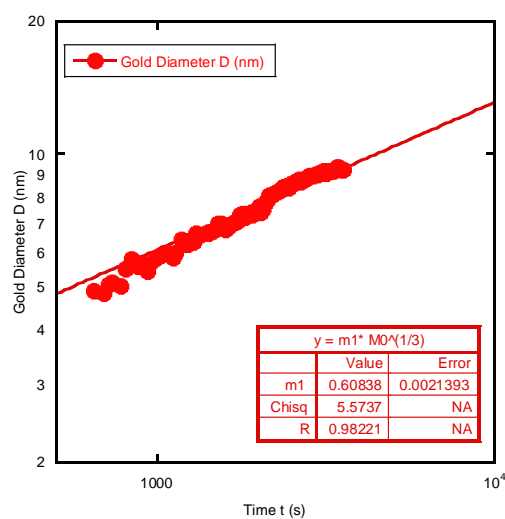
Figure A2.6 Gold diameter as a function of exposure time on CdSe/CdS. Data are taken from ref[39].

A2.5.2 Photodeposition of palladium and platinum

Unfortunately, we fail to find any experiment on the growth of palladium dots on semiconductor nanoparticles by photodeposition. Concomitantly we found one experiment involving photodeposition of platinum on TiO_2 nanoparticles. Murcia et al[40] used a mild intensity of 60 W/m^2 from a Osram Ultra-Vitalux UV lamp (300 W) at 365 nm, hexachloroplatinic acid (H_2PtCl_6, Aldrich 99.9%) as the metal precursor and isopropanol as a sacrificial donor, the final pH of the suspensions was 3. Figure A2.7 shows that a power law fit of the growth is compatible with expectation when forcing the exponent of 1/3 (a pure power law gives an exponent 0.24).

y = m1* M0^(1/3)		
	Value	Error
m1	0.25146	0.010311
Chisq	0.61278	NA
R^2	0.88198	NA
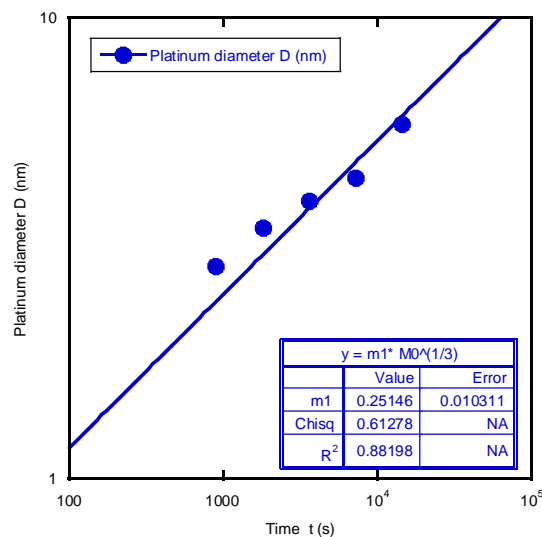
Figure A2.7 Platinum diameter as a function of exposure time. Data are taken from ref.[40]

As a conclusion, despite the weakness of data available in the literature, it seems that the growth laws of the metallic dot on semiconductor nanoparticles by photodeposition are all compatible, and sometimes in total agreement, with our predictions in terms of power-law exponents. Nonetheless, it was impossible to get some more insights from the existing literature, in particular on growth law amplitudes, considering the amount of available data.

References page 264

A2.6 Bibliography

1. Schneider, J.; Matsuoka, M.; Takeuchi, M.; Zhang, J.; Horiuchi, Y.; Anpo, M.; Bahnemann, D. W., Understanding TiO₂ Photocatalysis: Mechanisms and Materials. *Chem. Rev.* **2014**, *114*, 9919-9986.

2. Boxall, C.; Kelsall, G. H., Photoelectrophoresis of colloidal semiconductors. Part 2. Transient experiments on TiO₂ particles. *J. Chem. Sco., Faraday Trans.* **1991**, *87*, 3547-3556.

3. Migani, A.; Blancafort, L., Excitonic Interfacial Proton-Coupled Electron Transfer Mechanism in the Photocatalytic Oxidation of Methanol to Formaldehyde on TiO₂ (110). *J. Am. Chem. Soc.* **2016**, *138*, 16165-16173.

4. Zhang, J.; Nosaka, Y., Photocatalytic oxidation mechanism of methanol and the other reactants in irradiated TiO₂ aqueous suspension investigated by OH radical detection. *Appl. Catal. B* **2015**, *166-167*, 32-36.

5. Yamakata, A.; Vequizo, J. J. M.; Matsunaga, H., Distinctive Behavior of Photogenerated Electrons and Holes in Anatase and Rutile TiO₂ Powders. *J. Phys. Chem. C* **2015**, *119*, 24538-24545.

6. Liu, S.; Liu, A. A.; Wen, B.; Zhang, R.; Zhou, C.; Liu, L. M.; Ren, Z., Coverage Dependence of Methanol Dissociation on TiO₂ (110). *J. Phys. Chem. Lett.* **2015**, 3327-3334.

7. Xu, C.; Yang, W.; Guo, Q.; Dai, D.; Chen, M.; Yang, X., Molecular hydrogen formation from photocatalysis of methanol on anatase-TiO₂ (101). *J. Am. Chem. Soc.* **2014**, *136*, 602-605.

8. Shen, M.; Henderson, M. A., Identification of the Active Species in Photochemical Hole Scavenging Reactions of Methanol on TiO₂. *J. Phys. Chem. Lett.* **2011**, *2*, 2707-2710.

9. Liu, H.; Imanishi, A.; Nakato, Y., Mechanisms for Photooxidation Reactions of Water and Organic Compounds on Carbon-Doped Titanium Dioxide, as Studied by Photocurrent Measurements. *J. Phys. Chem. C* **2007**, *111*, 8603-8610.

10. Monllor-Satoca, D.; Borja, L.; Rodes, A.; Gomez, R.; Salvador, P., Photoelectrochemical behavior of nanostructured WO₃ thin-film electrodes: The oxidation of formic acid. *Chemphyschem* **2006**, *7*, 2540-2551.

11. Dijkstra, M. F. J.; Panneman, H. J.; Winkelman, J. G. M.; Kelly, J. J.; Beenackers, A. A. C. M., Modeling the photocatalytic degradation of formic acid in a reactor with immobilized catalyst. *Chem. Eng. Sci.* **2002**, *57*, 4895-4907.

12. Cornu, C. J. G.; Colussi, A. J.; Hoffmann, M. R., Quantum Yields of the Photocatalytic Oxidation of Formate in Aqueous TiO₂ Suspensions under Continuous and Periodic Illumination. *J. Phys. Chem. B* **2001**, *105*, 1351-1354.

13. Pelizzetti, E.; Minero, C., Mechanism of the photo-oxidative degradation of organic pollutants over TiO₂ particles. *Electrochim. Acta* **1993**, *38*, 47-55.

14. Miller, K. L.; Lee, C. W.; Falconer, J. L.; Medlin, J. W., Effect of water on formic acid photocatalytic decomposition on TiO₂ and Pt/TiO₂. *J. Catal.* **2010**, *275*, 294-299.

15. Muggli, D. S.; Falconer, J. L., Role of Lattice Oxygen in Photocatalytic Oxidation on TiO₂. *J. Catal.* **2000**, *191*, 318-325.

16. Sá, J.; Agüera, C. A.; Gross, S.; Anderson, J. A., Photocatalytic nitrate reduction over metal modified TiO₂. *Appl. Catal., B* **2009**, *85*, 192-200.

17. Graetzel, M.; Frank, A. J., Interfacial electron-transfer reactions in colloidal semiconductor dispersions. Kinetic analysis. *J. Phys. Chem.* **1982**, *86*, 2964-2967.

18. Enright, B.; Fitzmaurice, D., Spectroscopic Determination of Electron and Hole Effective Masses in a Nanocrystalline Semiconductor Film. *J. Phys. Chem.* **1996**, *100*, 1027-1035.

19. Tamaki, Y.; Furube, A.; Murai, M.; Hara, K.; Katoh, R.; Tachiya, M., Dynamics of efficient electron–hole separation in TiO$_2$ nanoparticles revealed by femtosecond transient absorption spectroscopy under the weak-excitation condition. *Phys. Chem. Chem. Phys.* **2007,** *9*, 1453-1460.

20. Bunsho, O.; M., B. R.; Philip, C. J. D.; Hiroshi, K.; Hidenori, N.; Kohei, U., Femtosecond Diffuse Reflectance Spectroscopy of Aqueous Titanium(IV) Oxide Suspension: Correlation of Electron-Hole Recombination Kinetics with Photocatalytic Activity. *Chem. Lett.* **1998,** *27*, 579-580.

21. Tamaki, Y.; Furube, A.; Murai, M.; Hara, K.; Katoh, R.; Tachiya, M., Direct Observation of Reactive Trapped Holes in TiO$_2$ Undergoing Photocatalytic Oxidation of Adsorbed Alcohols: Evaluation of the Reaction Rates and Yields. *J. Am. Chem. Soc.* **2006,** *128*, 416-417.

22. Matthews, R. W., Kinetics of photocatalytic oxidation of organic solutes over titanium dioxide. *J. Catal.* **1988,** *111*, 264-272.

23. Vohra, M. S.; Selimuzzaman, S. M.; Al‐Suwaiyan, M. S., NH$_4$$^+$‐NH$_3$ removal from simulated wastewater using UV‐TiO$_2$ photocatalysis: effect of co‐pollutants and pH. *Environm. Technol.* **2010,** *31*, 641-654.

24. Mueller, R.; Kammler, H. K.; Wegner, K.; Pratsinis, S. E., OH Surface Density of SiO$_2$ and TiO$_2$ by Thermogravimetric Analysis. *Langmuir* **2003,** *19*, 160-165.

25. Dimitrijevic, N. M.; Shkrob, I. A.; Gosztola, D. J.; Rajh, T., Dynamics of Interfacial Charge Transfer to Formic Acid, Formaldehyde, and Methanol on the Surface of TiO$_2$ Nanoparticles and Its Role in Methane Production. *J. Phys. Chem. C* **2012,** *116*, 878-885.

26. Kominami, H.; Murakami, S.-y.; Kato, J.-i.; Kera, Y.; Ohtani, B., Correlation between Some Physical Properties of Titanium Dioxide Particles and Their Photocatalytic Activity for Some Probe Reactions in Aqueous Systems. *J. Phys. Chem. B* **2002,** *106*, 10501-10507.

27. Mostafavi, M.; Dey, G. R.; François, L.; Belloni, J., Transient and Stable Silver Clusters Induced by Radiolysis in Methanol. *J. Phys. Chem. A* **2002,** *106*, 10184-10194.

28. Kull, M.; Coutaz, J.-L., Intensity-dependent absorption and luminescence in semiconductor-doped glasses. *J. Opt. Soc. Am. B* **1990,** *7*, 1463-1472.

29. Boxall, C.; Kelsall, G. H., Photoelectrophoresis of colloidal semiconductors. Part 1.—The technique and its applications. *J. Chem. Sco., Faraday Trans.* **1991,** *87*, 3537-3545.

30. Curran, J. S.; Lamouche, D., Transport and kinetics in photoelectrolysis by semiconductor particles in suspension. *J. Phys. Chem.* **1983,** *87*, 5405-5411.

31. Liu, Z.; Destouches, N.; Vitrant, G.; Lefkir, Y.; Epicier, T.; Vocanson, F.; Bakhti, S.; Fang, Y.; Bandyopadhyay, B.; Ahmed, M., Understanding the Growth Mechanisms of Ag Nanoparticles Controlled by Plasmon-Induced Charge Transfers in Ag-TiO$_2$ Films. *J. Phys. Chem. C* **2015,** *119*, 9496-9505.

32. Tavassoli, Z.; Rodgers, G. J., Diffusive growth of a single droplet with three different boundary conditions. *Eur. Phys. J. B* **2000,** *14*, 139-144.

33. Rogers, T. M.; Elder, K. R.; Desai, R. C., Droplet growth and coarsening during heterogeneous vapor condensation. *Phys. Rev. A* **1988,** *38*, 5303-5309.

34. Beysens, D.; Knobler, C. M.; Schaffar, H., Scaling in the growth of aggregates on a surface. *Phys. Rev. B* **1990,** *41*, 9814-9818.

35. Lazzari, R.; Jupille, J., Growth kinetics and size-dependent wetting of Ag/α-Al$_2$O$_3$(0001) nanoparticles studied via the plasmonic response. *Nanotechnology* **2012,** *23*, 135707.

36. Lu, Q.; Lu, Z.; Lu, Y.; Lv, L.; Ning, Y.; Yu, H.; Hou, Y.; Yin, Y., Photocatalytic Synthesis and Photovoltaic Application of Ag-TiO$_2$ Nanorod Composites. *Nano Lett.* **2013,** *13*, 5698-5702.

37. Chang, L.-H.; Yeh, Y.-L.; Chen, Y.-W., Preferential oxidation of CO in hydrogen stream over

265

nano-gold catalysts prepared by photodeposition method. *Int. J. Hydrogen Energy* **2008,** *33*, 1965-1974.

38. Carbone, L.; Jakab, A.; Khalavka, Y.; Sönnichsen, C., Light-controlled one-sided growth of large plasmonic gold domains on quantum rods observed on the single particle level. *Nano Lett.* **2009,** *9*, 3710.

39. Demortiere, A.; Schaller, R. D.; Li, T.; Chattopadhyay, S.; Krylova, G.; Shibata, T.; dos Santos Claro, P. C.; Rowland, C. E.; Miller, J. T.; Cook, R.; Lee, B.; Shevchenko, E. V., In situ optical and structural studies on photoluminesence quenching in CdSe/CdS/Au heterostructures. *J. Am. Chem. Soc.* **2014,** *136*, 2342-2350.

40. Murcia, J. J.; Hidalgo, M. C.; Navío, J. A.; Vaiano, V.; Ciambelli, P.; Sannino, D., Ethanol partial photoxidation on Pt/TiO₂ catalysts as green route for acetaldehyde synthesis. *Catal. Today* **2012,** *196*, 101-109.

Appendix 3

Prediction of metal size deposited on TiO$_2$ polyhedrons

A3.1 Prediction of metal size after one-step photodeposition process

In this part, we introduce a general approach to theoretically estimate the expected metal size deposited during the photodeposition process using various metal precursors. First, we use Au-TiO$_2$ as an example to show the calculation procedure of Au size; then, a general equation is deduced for all the other metals.

A3.1.1 Assumptions:

For the sake of simplicity, we first assume a volume of a reactant mixture solution of 1 mL. Then, for the photodeposition of metal at the surface of TiO$_2$, we neglect the contact angle mentioned in Appendix 2 and assume a hemispherical shape, that is, we consider a metal particle with a diameter D at the surface, and a contact angle of 90°; the volume of the metal

dot is then $V_{M(1)} = \dfrac{2}{3}\pi(\dfrac{D}{2})^3 = \dfrac{\pi D^3}{12}$.

A3.1.2 Fixed conditions of TiO$_2$ part:

All the calculations are based on TiO$_2$ polyhedron support, with an average diameter of 16.5 nm (roughly 20, 15 and 15 nm in three axes); the mass of a single TiO$_2$ polyhedron is then

$$m_{TiO_2(1)} = \rho_{TiO_2}V_{TiO_2} = 3.9 \times \left(\frac{4}{3}\pi \times 20 \times 15 \times 15 \times 10^{-21}\right) = 7.35 \times 10^{-17}\,g \ .$$

The concentration of TiO$_2$ polyhedrons is 5.5 mM (atomic concentration), and the total mass of TiO$_2$ polyhedrons in V$_{sol}$=1 mL solution is

$$m_{TiO_2} = c_{TiO_2}V_{sol}M_{TiO_2} = 5.5 \times 1 \times 79.87 \times 10^{-6}\,g = 4.39 \times 10^{-4}\,g \ .$$

The number of TiO$_2$ polyhedrons is also given by

$$N_{TiO_2} = \frac{m_{TiO_2}}{m_{TiO_2(1)}} = \frac{4.39 \times 10^{-4}\,g}{7.35 \times 10^{-17}\,g} = 6 \times 10^{12} \ .$$

In conclusion, the number density D' of TiO$_2$ polyhedrons is fixed to $D' = 6 \times 10^{12}\,/\,mL$.

A3.1.3 Example of M-TiO$_2$ (M=Au)

For the synthesis of Au-TiO$_2$ NPs, let us assume first that the metal precursor is reduced to metallic gold, that is, the consumption rate ε = 100%.

For a solution with volume V$_{sol}$ =1 mL and concentration c_{Au3+}=0.5 mM, the total mass of reduced gold is

$$m_{Au} = \varepsilon c_{Au^{3+}} V_{sol} M_{Au} = 100\% \times 0.5 \times 1 \times 197 \times 10^{-6} g = 9.85 \times 10^{-5} g$$

Then, according to the TEM results, we obtained a Janus yield **Y** =50 % of Au-TiO$_2$ (by counting more than 200 NPs), which means a ratio between Au-TiO$_2$ NPs and the total TiO$_2$ NPs of 50%. The total number of Au NPs after the photodeposition process is:

$$N_{Au} = Y N_{TiO_2} = 50\% \times 6 \times 10^{12} = 3 \times 10^{12}$$

The mass of a single Au NP is then

$$m_{Au(1)} = \frac{m_{Au}}{N_{Au}} = 3.28 \times 10^{-17} g$$

The volume of a single Au NP is then

$$V_{Au(1)} = \frac{m_{Au(1)}}{\rho_{Au}} = \frac{3.28 \times 10^{-17}}{19.3} \times \left(10^{-7}\right)^3 = 1700 \ nm^3$$

As assumed before, this value is equal to the volume of the metal hemisphere, that is

$$V_{M(1)} = \frac{\pi D_1^3}{12} = 1700 \ nm^3$$

Then, in the case of the gold consumption rate ε=100% and a Janus yield **Y** = 50%, a reasonable estimation of the largest expected diameter of Au NPs (Au size) is in average D$_1$=18.7 nm.

A3.1.4 Generalization

We can now generalize the calculation for other metals (M = Ag, Pd or Pt).

The total mass of the reduced metal in solution is

$$m_M = \varepsilon c_M V_{sol} M_M 10^{-6}$$

where c_M is the concentration in mM, V$_{sol}$ is the solution volume in mL, and M_M is the molar mass in g/mol.

The number of Au NPs is

$$N_{M(1)} = YD'V_{sol}$$

Where D' is the number density of TiO₂ polyhedrons in mL⁻¹, which is fixed at

$$D' = 6 \times 10^{12} / mL$$

The mass of a single metal NP is

$$m_{M(1)} = \frac{m_M}{N_{M(1)}} = \frac{\varepsilon c_M V_{sol} M_M 10^{-6}}{YD'V_{sol}} = \frac{\varepsilon c_M M_M 10^{-6}}{YD'}$$

The volume of a single metal NP is

$$V_{M(1)} = \frac{m_{M(1)}}{\rho_M} = \frac{\varepsilon c_M M_M 10^{-6}}{\rho_M YD'}$$

where ρ_M is in the density of the metal in g/cm³.

With the assumption, we suppose $V_{M(1)} = \dfrac{\pi D_1^3}{12}$

so $\dfrac{\pi D_1^3}{12} = \dfrac{\varepsilon c_M M_M 10^{-6}}{\rho_M YD'}$

and finally, we get a diameter of the photodeposited metal $D_{M(1)} = \left(\dfrac{1.2 \times 10^6 \varepsilon c_M M_M}{\pi YD' \rho_M} \right)^{1/3}$

A summary for each metal investigated in this work is given in Table A3.1, where the last column corresponds to the optimized case where ε=1 and Y=100%:

metal NP	M_M (g/mol)	ρ_M (g/cm³)	expected metal size (c_M in mM)	expected metal size ($Y=1$, $\varepsilon = 1$, c_M in mM)
Ag	107.87	10.49	$D_{Ag} = \left[18.7 \times \left(\dfrac{\varepsilon c_{Ag}}{Y} \right)^{1/3} \right] nm$	$D_{Ag} = \left[18.7 \times \left(c_{Ag} \right)^{1/3} \right] nm$
Pd	106.42	12.02	$D_{Pd} = \left[17.8 \times \left(\dfrac{\varepsilon c_{Pd}}{Y} \right)^{1/3} \right] nm$	$D_{Pd} = \left[17.8 \times \left(c_{Pd} \right)^{1/3} \right] nm$
Au	196.97	19.30	$D_{Au} = \left[18.7 \times \left(\dfrac{\varepsilon c_{Au}}{Y} \right)^{1/3} \right] nm$	$D_{Au} = \left[18.7 \times \left(c_{Au} \right)^{1/3} \right] nm$
Pt	195.08	21.45	$D_{Pt} = \left[18.0 \times \left(\dfrac{\varepsilon c_{Pt}}{Y} \right)^{1/3} \right] nm$	$D_{Pt} = \left[18.0 \times \left(c_{Pt} \right)^{1/3} \right] nm$

Table A3.1 Estimation of metal size after the first photodeposition process.

A3.2 Prediction of metal size after two-step photodeposition process

In a following step, we want to estimate the size of metal NPs after photodeposition of a shell of a second metal. As illustrated in Chapter 6, we firstly synthesized Au-TiO₂ NPs using one-step photodeposition, and in a second step, we added another metal precursor to be reduced on the Au core site. As observed experimentally, the second metal is photoreduced onto the existing Au site rather than nucleated elsewhere on the surface of TiO₂. Consequently, the Janus yield does not change at all. The calculation of the new core-shell metal NPs, is performed with the same assumptions as before.

A3.2.1 Assumptions

We still assume the first Au NPs deposition on the surface TiO₂ present a hemisphere shape. As deposition of the second metal occurs on the first one, we continue to suppose that all the second metal precursor is reduced onto the Au NPs, forming a metallic shell on the Au hemispheres.

A3.2.2 Calculation of the quantity of the second metal, deposited as a shell on Au-TiO₂ NPs (M=Ag, Pd, Au and Pt)

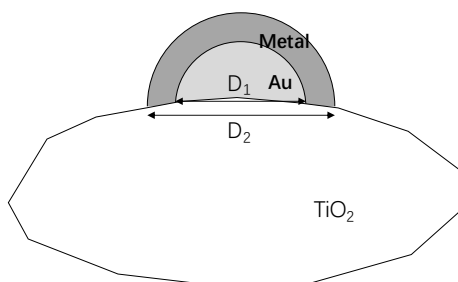

Figure A3.1 metal deposited on Au-TiO₂ NP.

As shown in Figure A3.1, In one Au@M-TiO₂ NP, the volume of the metal shell can be calculated as

$$V_{M(2)} = \frac{2}{3}\pi\left(\left(\frac{D_2}{2}\right)^3 - \left(\frac{D_1}{2}\right)^3\right) = \frac{\pi}{12}\left(D_2^3 - D_1^3\right)$$

Where D_1 and D_2 are the diameter of Au and {Au@metal} NP, respectively.

then the mass of a single metal shell is

$$m_{M(2)} = \rho_M V_M = \frac{\pi \rho_M}{12}\left(D_2^3 - D_1^3\right)$$

In the reaction solution of V_{sol}, the number of shell structure is

$$N_{M(2)} = YD'V_{sol}$$

Where Y is the yield of Au-TiO_2, D' is the number density of TiO_2 polyhedrons in mL^{-1}, which

is fixed at $D' = 6 \times 10^{12} / mL$, V_{sol} is the solution volume in mL.

The total mass of metal added from the precursor at the beginning

$$m_M = c_M V_{sol} M_M$$

We would have

$$m_M = N_{M(2)} \times m_{M(2)}$$

Thus we obtained the following equation

$$D_2 = \left(D_1^3 + \frac{1.2 \times 10^6 \, \varepsilon c_M M_M}{\pi YD' \rho_M}\right)^{1/3}$$

Using this equation, we summarize the expected largest whole metal size (discussed in

Chapter 6) in Table A3.2 shown below.

Metal 2	C_M (mM)	M_M (g/mol)	ρ_M (g/cm³)	Y*	D_1* (nm)	D_2 (nm)
Ag	0.5	107.87	10.49	46%-53%	15.9	21.9
Pd	0.5	106.42	12.02	49%	15.9	21.3
Au	0.5	196.97	19.30	47%-49%	15.5	21.7
Pt	0.2	195.08	21.45	50%	15.8	18.4

Table A3.2 Expected whole metal size after the second photodeposition process. "*" denotes the Au
diameter and Janus yield of Au-TiO_2 after the first photodeposition step.

Experimentally, we verify that our photodeposited core-shell metallic NPs are always smaller

than these estimations

Appendix 4

Characterization techniques

Transmission electron microscopy (TEM) experiments were carried out with two machines, a JEOL JEM1400 Plus microscope and MET HITACHI H7650 microscope, both operating at 120 kV.

High-resolution (HR) TEM images were obtained with a TEM-FEG HR (JEOL 2200FS) at 200 kV. Chemical analysis (elemental mapping) was carried out by STEM coupled to EDX with a JEOL 2200 FS equipped with a field emissive gun, operating at 200 kV and with a point resolution of 0.23 nm. High-resolution transmission electron microscopy micrographs and videos were acquired with a Gatan Ultrascan CCD 2k-2k, and digital diffractograms were calculated using the Gatan Digital Micrograph program.

X-ray photoelectron spectroscopy (XPS) surface analysis was obtained using a ThermoFisher Scientific K-ALPHA spectrometer with a monochromatized Al Kα source (hv = 1486.6 eV) and a 200 μm spot size. Before insertion of samples in the analysis chamber, a pressure of $3 \cdot 10^{-7}$ mbar was always reached in the load lock chamber. C1s, O1s, N1s, Cl2p, Ti2p, Au4f, Cu2p, Pt4f, Pd3d, Ag3d and Ru3d high-resolution spectra were acquired by using a constant pass energy of 40 eV although surveys in the 0–1100 eV range were first obtained at a constant pass energy of 200 eV. Sputtering was achieved with low energy argon ions. Charge neutralization was applied during analysis. High-resolution spectra were fitted and quantified using the AVANTAGE® software provided by ThermoFisher Scientific.

The UV-vis absorption spectra were recorded with a SHIMADZU UV-3600 Uv-Vis-Nir spectrophotometer using 10 mm cuvettes.

The Zeta potential was performed with a NANOPLUS Particulate Systems Analyzer using a standard cell with Dome Electrode 0.7 mL.

X-ray diffraction (XRD) measurements were carried out at room temperature with a PANalytical X'pert Pro MPD diffractometer using a Cu Kα1 radiation, λ = 1.540 598 Å. and Bragg-Brentano geometry. 2 theta was in the range between 8° and 80° with a step size of 0.02°.

Titre: Synthèse de nano-hétérodimères par photodéposition laser de nanoplots métalliques sur des nanoparticules de TiO$_2$

Résumé:

Deux configurations différentes, à savoir en microcanal et en cuve de spectroscopie utilisant un laser UV, sont conçues pour effectuer la photodéposition de plots métalliques uniques sur du TiO$_2$. Des nanoparticules cristallines d'anatase de formes et de tailles variées sont synthétisées à dessein et utilisées comme semi-conducteurs pour cette réaction photochimique. Quatre précurseurs de métaux avec différents états de valence (Ag (I), Au (III), Pd (II) et Pt (IV)), sont réduits de manière photochimique à la surface de TiO$_2$. Plusieurs techniques, notamment XPS, TEM / HRTEM, spectroscopie UV-vis, sont utilisées pour caractériser l'état chimique, la distribution en taille et en nombre des points métalliques et le comportement d'absorption des nanoparticules Metal-TiO$_2$. On obtient des nano-hétérodimères avec un plot Ag, Au, Pd et Pt par TiO$_2$, ce qui montre que le dépôt au laser semble être beaucoup plus efficace dans ce cas que celui de la photodéposition par lampe UV habituelle, suggérant que le flux de photons compte beaucoup plus que l'énergie déposée. Les hétérodimères Ag-TiO$_2$ sont synthétisés avec succès par les deux méthodes de dépôt au laser. Le nombre et la distribution de taille des plots d'Ag dépendent des capteurs de trous, du pH et du précurseur métallique. Un modèle de croissance prédit bien la variation de la taille de l'argent dans le processus de photodéposition. L'extension de la synthèse à d'autres précurseurs métalliques (KAuCl$_4$, Na$_2$PdCl$_4$ et H$_2$PtCl$_6$) à l'aide des deux configurations a conduit à la formation d'hétérodimères de TiO$_2$ à base d'or, de palladium et de platine. La loi de croissance de l'or peut aussi être raisonnablement prédite, bien qu'elle ne soit pas aussi bonne que dans le cas de l'Ag, alors que notre modèle ne fonctionne pas dans le cas de Pd et de Pt. Enfin, des nanoobjets bimétalliques à structure coeur-écorce (Au@M)-TiO$_2$ (M = Ag, Pd, Au et Pt) ont été synthétisés avec succès par une méthode de dépôt simple par laser UV en deux étapes en configuration cuve de spectroscopie.

Mots clés: Nano Hétérodimères, laser, photodéposition de nanoplots de métaux noble, nanoparticules de TiO$_2$

Title: Synthesis of nano heterodimers by laser photodeposition of metal nanodots on TiO$_2$ nanoparticles

Abstract :

Two different setups, namely microchannel and cuvette setups using UV laser, are built to perform the photodeposition of a single metal dotson TiO$_2$. Crystal anatase TiO$_2$ nanoparticles with various shapes and sizes, are synthesized on purpose and used as semiconductors for this photochemical reaction. Four metal precursors with different valence states, i.e. Ag(I), Au (III), Pd(II) and Pt(IV) ions, are photochemically reduced on the surface of TiO$_2$. Several techniques, including XPS, TEM/HRTEM, UV-vis spectroscopy, are performed to characterize the chemical state, size and number distribution of metal dots, and the absorption behaviours of the Metal-TiO$_2$ nanoparticles. Nano-heterodimers with one Ag, Au, Pd and Pt per TiO$_2$ are obtained showing that laser deposition seems to be much more efficient in this case than of the usual UV lamp photodeposition, suggesting that the flux of photons matters much more than the deposited energy. Ag-TiO$_2$ heterodimer nanoparticles are successfully synthesized by the two laser deposition methods. The number and size distribution of Ag dots are dependent on hole scavengers, pH and metal precursor. A growth model well predicted the silver size variation in the photodeposition process. Extending the synthesis to other metal precursors (KAuCl$_4$, Na$_2$PdCl$_4$ and H$_2$PtCl$_6$) using both setups led to the formation of gold, palladium and platinum-based heterodimers with TiO$_2$. The growth law of gold can reasonably be predicted as well, although it is not as good as in the case of Ag, while our model did not work in the case of Pd and Pt. Finally, bimetallic core-shell structured (Au@M)-TiO$_2$ (M=Ag, Pd, Au and Pt) nanoobjects were successfully synthesized by a simple two-step UV laser deposition method in the cuvette setup.

Keywords: Nano heterodimers, laser, photodeposition of noble metal nanodots, TiO$_2$ nanoparticles

---

Unité de recherche

Institut de Chimie de la Matière Condensée de Bordeaux (ICMCB), UMR5026